Spatial Damping Identification

Thesis submitted in accordance with the requirements of
the University of Liverpool
for the degree of Doctor in Philosophy

by
Marco Prandina

February 2010

To Didona

Abstract

This dissertation reports a study on the identification of damping in multiple degree-of-freedom systems with particular attention to the spatial location of the sources of energy dissipation. The main focus is in developing practical tools which can be used in real problems to obtain valuable information about the amplitude, the location and the way energy is dissipated in a structure.

The physical phenomena involved in the energy dissipation of real vibrating structures are various. All these mechanisms have been studied separately with success by several authors, but there is still considerable doubt on how the damping behaviour should be represented in a suitable manner for engineering applications. Despite viscous damping being widely utilised in software and applications, it is a mathematical approximation of reality and therefore has to be used with an awareness of this limitation.

The initial research focuses on the analysis of the existing damping models and identification methods. From the knowledge gained, a new and improved method is developed. The advantages and limitations of each method identified in the literature are considered and used to develop a new method based on the balance between the energy input by external forces and the energy dissipated by damping. This method is able to spatially identify different sources of damping and does not require any information about the inertial and elastic properties of the system provided the full set of measurements is available. This new method has been tested and validated by numerical simulations and by two different experiments on real structures.

Nessuno vuole la realtà
(No one wants reality)

Gareth A. Vio

Acknowledgements

I would like to thank my supervisor, Professor John Mottershead, for his continuous encouragement and support from the very beginning of my PhD. Despite being a very busy man, he has always found the time to answer all the questions that I asked him every time I went to his office, often without notice. He carefully and patiently listened to all my incorrect theories before pointing me in the right direction. I am also extremely grateful to him for encouraging me to attend and to present in important international conferences despite my initial worries, allowing me to become more independent and self-confident.

A special thanks goes to Dr Maryam Tehrani, who helped me a lot in the first months with everything that is necessary to start a new life in a foreign country. She has been selflessly helpful for many practical everyday things as well as very helpful in my research, giving advice about Frequency Response Function measurements and PhD bureaucracy. Most importantly, she is a very good friend.

All the experimental work would not have been possible without the help of Dr Simon James. His experience in designing, building and running experiments saved me a lot of time and without his support I would have probably never finished my tests in time for deadlines. Even if I will never understand why he still uses imperial units in 2010, I am grateful to him for teaching me many secret tips for successful experiments.

I am also very thankful to Dr Gareth Vio, my personal Matlab guru who taught me commands that the people at MathWorks have probably never heard of and Dr Hamed Khodaparast who helped me any time I had doubts on the fundamental theory of vibration and dynamics. I consider you two my third and fourth supervisors.

I am grateful to all the members of the ECERTA project. In particular, I thank

Professor Ken Badcock who built and managed our international team and oversaw our research successfully. Our project meetings helped me to improve my communication and presentation skills as well as my knowledge in aeroelasticity. Dr Simão Marques has been not only a valid team member but also a good friend and my favourite football interlocutor every Monday. Being part of this project has been an honour for me.

I want to thank Dr Elvio Bonisoli from Politecnico di Torino for encouraging me to start the PhD and the whole academic adventure. I was an unmotivated engineer in industry and now I am an international researcher thanks to him.

Another thanks goes to my friends Jonathan Griffiths and Paul Fitzsimons for checking the spelling and grammar of this dissertation. If any mistake is found, it is their fault.

A big thanks goes to all my coffee break and lunch break mates, especially my friend Yazdi. We talked of many things together and I really appreciated every second of these breaks; work and career are important but the thing that I will really miss when I leave will be these random chats. I invented an additional coffee break at 5.30 pm in order to spend more time with these friends and some of them worked overtime to attend these precious moments. I hope they will continue this tradition when I leave.

The last and most important thanks goes to my family, who always supported me despite some of them initially not wanting me to be so far away from home, and particularly to my girlfriend Didona who left the most beautiful country in the world to join and help me in the most rainy country in the world. Thank you very much, this work is fully dedicated to you.

This work is founded by the European Union for the Marie Curie Excellence Team ECERTA under contract number MEXT-CT-2006 042383.

Contents

Abstract iii

Acknowledgements vii

Contents xii

List of Figures xv

List of Tables xvii

List of Symbols xix

List of Acronyms xxiii

1 Introduction 1

1.1 Historical background 1

1.2 Classification of damping 4

1.2.1 Material damping 4

1.2.2 Non-material damping 5

1.3 Scope of the thesis 7

1.4 Closure 9

2 Models for damping in vibrating systems 11

2.1 Dynamics of mechanical systems 11

2.2 Single degree-of-freedom systems 11

2.2.1 Undamped systems 11

2.2.2 Viscously damped systems 12

Effect of viscous damping on the FRF 15

Effect of viscous damping on the Nyquist plot 17

Effect of viscous damping on the hysteresis loop 18

Energy dissipated by viscous damping 19

2.2.3 Non-viscously damped systems 21

Hysteretic damping 21
Coulomb friction 25
Velocity n^{th} power damping 28
Fractional time derivatives models 28
2.3 Multiple degree-of-freedom systems 29
2.3.1 Undamped systems 29
2.3.2 Viscously damped systems 33
Classical viscous damping 37
Effect of viscous damping on the FRF 39
2.4 Closure 41

3 Damping identification **43**
3.1 The inverse problem 43
3.2 SDOF and modal identification 44
3.2.1 Logarithmic decrement 44
3.2.2 Half-power bandwidth method 46
3.2.3 Energy-dissipation method 48
3.2.4 Other methods 50
3.3 MDOF spatial identification 50
3.3.1 Preliminary calculations 51
3.3.2 FRF-based methods 52
Chen et al. 52
Lee and Kim 54
Instrumental variable 55
Considerations on the inversion of the FRF 56
3.3.3 Modal parameters methods 59
Lancaster 59
Pilkey and Inman 60
Ibrahim 61
Minas and Inman 63
Adhikari and Woodhouse 64
Considerations on the perturbation method 65
3.3.4 Time histories methods 65
Liang 66
3.3.5 Hybrid and other methods 67
Srikantha Phani and Woodhouse 67
Other methods 68

3.3.6 Numerical comparison 69
3.4 Closure 75

4 Energy balance method **77**
4.1 Advantages and drawbacks of the existing method 77
4.2 The energy balance method 78
4.2.1 Theory 78
4.2.2 Parameterisation of the damping matrix 79
4.2.3 Expansion of incomplete measurements 84
4.2.4 Localisation of damping 86
4.2.5 Solution of the energy equation 88
4.3 Energy method and inverse FRF equivalence 89
4.4 Closure 92

5 Numerical simulations **93**
5.1 Introduction 93
5.2 Cantilever beam 93
5.2.1 Case 1: same damping coefficients 93
5.2.2 Case 1a: same damping coefficients with known location . 100
5.2.3 Case 2: different damping coefficients 101
5.2.4 Case 3: Viscous and Coulomb friction 102
5.3 Goland wing 107
5.4 Closure 114

6 Experiments **117**
6.1 Introduction 117
6.2 Design of experiment 1: cantilever beam 117
6.3 Damping sources 121
6.3.1 Magnetic eddy current dashpot 121
6.3.2 Air viscous dashpot 123
6.3.3 Coulomb friction device 124
6.4 Test procedure 124
6.5 Results for experiment 1 128
6.5.1 Case 1: undamped cantilever beam 129
6.5.2 Case 2: single magnetic dashpot 131
6.5.3 Case 3: single air dashpot 133
6.5.4 Case 4: single Coulomb friction device 135
6.5.5 Case 5: multiple air dashpot 137

6.6 Conclusions for experiment 1 139
6.7 Design of experiment 2: five masses system 141
6.8 Test procedure 144
6.9 Results for experiment 2 145
6.9.1 Case 1: undamped system 145
6.9.2 Case 2: single air dashpot 147
6.9.3 Case 3: multiple air dashpots 149
6.9.4 Case 4: combined viscous and friction dashpots 152
6.10 Conclusions for experiment 2 154
6.11 Closure 155

7 Conclusions and future work **157**
7.1 Summary of the contributions made 157
7.2 Suggestions for future work 160
7.3 List of publications 162

Bibliography **163**

List of Figures

2.1 Single degree-of-freedom system 13
2.2 Free vibration time response to an initial unitary displacement . . 15
2.3 Effect of viscous damping on the FRF 16
2.4 Effect of viscous damping on the Nyquist plot of receptance . . . 17
2.5 Effect of viscous damping on the Nyquist plot of mobility 18
2.6 Effect of viscous damping on the hysteresis loop 19
2.7 Effect of hysteretic damping on the FRF 22
2.8 Effect of hysteretic damping on the Nyquist plot of receptance . . 23
2.9 Effect of hysteretic damping on the hysteresis loop 24
2.10 Coulomb friction force 25
2.11 Coulomb friction force with stiction 26
2.12 Coulomb friction force with Stribeck friction 27
2.13 Effect of Coulomb friction on the hysteresis loop 27
2.14 Undamped multi degree-of-freedom system 30
2.15 Mode shapes of a cantilever beam 32
2.16 Viscously damped multi degree-of-freedom system 33
2.17 Receptance of an undamped MDOF system 39
2.18 Receptance of a viscously damped system varying c_2 40
2.19 Receptance of a viscously damped system varying c_3 40

3.1 Free vibration time response 45
3.2 Half power points definition 47
3.3 Effect of modal incompleteness on the FRF 57
3.4 Effect of modal incompleteness on the DSM 58
3.5 Cantilever beam 69
3.6 MAC error for Lancaster's formula 72
3.7 MAC error for inversion of FRF 72
3.8 MAC error for first-order perturbation 72
3.9 Identified damping matrix using Lancaster's formula 73
3.10 Identified damping matrix using inversion of FRF 73

3.11 Identified damping matrix using first-order perturbation 73
3.12 Error ε_C for the three methods 74
3.13 Error by first-order perturbation 74

4.1 Absolute dashpot 82
4.2 Relative dashpot 82
4.3 Identical relative dashpots 83

5.1 Cantilever beam and DOFs numbering 94
5.2 Cantilever beam with viscous dashpots 94
5.3 Cantilever beam with viscous dashpots and Coulomb friction . . . 103
5.4 Finite element model of the Goland wing 108
5.5 Location of viscous dashpots on the Goland wing 109
5.6 Location of the identified viscous dashpots on the Goland wing . . 111
5.7 Diagonal elements of the identified and original damping matrices 112
5.8 Modal damping ratio comparison 113

6.1 Cantilever beam experimental setup 118
6.2 Effect of the length of the beam on natural frequencies 118
6.3 Effect of added mass on natural frequencies 119
6.4 Experiment 1: DOFs numbering 120
6.5 Experimental setup 121
6.6 Eddy current dashpot model 122
6.7 Magnetic eddy current dashpot 122
6.8 Air dashpot 123
6.9 Coulomb friction device 124
6.10 Measured force versus harmonic fitted force 125
6.11 Measured acceleration versus harmonic fitted acceleration 127
6.12 Identified damping matrix for case 1 129
6.13 Energy DOF contribution for case 1 130
6.14 Case 2: magnetic dashpot location 131
6.15 Identified damping matrix for case 2 132
6.16 Energy DOF contribution for case 2 132
6.17 Identified damping matrix for case 3 134
6.18 Energy DOF contribution for case 3 134
6.19 Case 4: Coulomb friction device location 135
6.20 Identified damping matrix for case 4 136
6.21 Energy DOF contribution for case 4 137

6.22 Case 5: Multiple air dashpots location 138
6.23 Case 5: air dashpots at DOF 6 and 8 138
6.24 Identified damping matrix for case 5 139
6.25 Energy DOF contribution for case 5 139
6.26 Experiment 2: Scheme and DOF numbering 141
6.27 Experiment 2 design 142
6.28 Experimental setup 143
6.29 FRF of the undamped system 144
6.30 Mode shapes for experiment 2 145
6.31 Identified damping matrix for the undamped system 146
6.32 Viscous dashpot between DOFs 4 and 5 147
6.33 FRF of the undamped system versus case 2 148
6.34 Identified damping matrix for case 2 149
6.35 FRF of the undamped system versus case 3 150
6.36 Identified damping matrix for case 3 151
6.37 FRF of the undamped system versus case 3b 151
6.38 Identified damping matrix for case 3b 152
6.39 Coulomb friction device between DOFs 3 and 4 153
6.40 Identified damping matrix for case 4 154

List of Tables

3.1 Identified natural frequencies 70
3.2 Identified damping ratios 71

5.1 Dashpots configuration for case 1. 94
5.2 Selection of smallest angles. 97
5.3 Results for case 1. 99
5.4 Damping ratios for case 1 100
5.5 Results for case 1a. 101
5.6 Dashpots configuration for case 2. 102
5.7 Results for case 2. 102
5.8 Damping sources configuration for case 3. 103
5.9 Results for case 3. 106
5.10 Nominal values of thicknesses for the Goland wing FEM. 107
5.11 Nominal values of areas for the Goland wing FEM. 108
5.12 Frequencies and damping ratios of the Goland Wing 110
5.13 Identified versus original modal damping comparison 114

6.1 Natural frequencies for three different wing configurations 120
6.2 Mass and stiffness values for experiment 2 142
6.3 Natural frequencies for experiment 2 143
6.4 Comparison of damping ratios for case 1 147

List of Symbols

a_p	Modal parameter a
b_p	Modal parameter b
c	Viscous damping coefficient
c_{cr}	Critical damping coefficient
c_{eq}	Equivalent viscous damping coefficient
$c(\omega)$	Frequency dependent damping coeff.
$f(t)$	Excitation force
f_0	Amplitude of excitation
$f(\omega)$	Fourier transform of excitation force
$h(\omega)$	Receptance
i	Imaginary unit ($\sqrt{-1}$)
k	Stiffness of ideal massless spring
k_p	Modal stiffness
m	Mass
m_p	Modal mass
$q_i(t)$	Modal coordinate displacement
$\dot{q}_i(t)$	Modal coordinate velocity
$\ddot{q}_i(t)$	Modal coordinate acceleration
s	Laplace variable
u_p	Modal coordinate
x_0	Amplitude of displacement
x_s	Static amplitude of displacement
$x(t)$	Displacement
$\dot{x}(t)$	Velocity
$\ddot{x}(t)$	Acceleration
$x(\omega)$	Fourier transform of response
A	Harmonic series coefficient A
B	Harmonic series coefficient B
E_c	Energy of conservative components
E_d	Energy dissipated by damping
E_f	Energy input by external forces
F_d	Damping force
F_n	Normal force
F_s	Static friction force
Q	Amplification factor

$P(s)$	Second-order pencil
T	Period of the harmonic force
V	Potential energy
δ	Logarithm decrement
ε_C	Modal incompleteness error
ε_p	Projection error
ζ	Damping ratio
η	Loss factor
η_0	Frequency independent loss factor
λ_p	Complex eigenvalue
μ	Kinetic coefficient of friction
μ_s	Static coefficient of friction
ϕ	Phase angle
τ_d	Damped period
ω	Frequency
ω_d	Damped natural frequency
ω_n	Natural frequency
$\mathbf{c}$	Damping parameters vector
$\mathbf{d}_v$	Viscous damping force
$\mathbf{d}_c$	Coulomb friction force
$\mathbf{e}$	Energy vector
$\mathbf{e}_{id}$	Identified energy vector
$\mathbf{f}(t)$	Forces vector
$\mathbf{f}(\omega)$	Fourier transform of excitation force
$\mathbf{g}_i$	Column of matrix $\mathbf{G}$
$\mathbf{g}(\mathbf{x}, \dot{\mathbf{x}}, \ddot{\mathbf{x}})$	Generic damping function
$\mathbf{u}(t)$	Modal coordinates vector
$\mathbf{u}_n$	Unity vector
$\mathbf{x_0}$	Amplitudes vector
$\mathbf{x}(t)$	Displacements vector
$\dot{\mathbf{x}}(t)$	Velocities vector
$\dot{\mathbf{x}}_f(t)$	Full velocities vector
$\ddot{\mathbf{x}}(t)$	Accelerations vector
$\ddot{\mathbf{x}}_f(t)$	Full accelerations vector
$\ddot{\mathbf{x}}_m(t)$	Measured accelerations vector
$\mathbf{x}(\omega)$	Fourier transform of response
$\boldsymbol{\epsilon}_{\mathbf{EE}}$	Equation error
$\boldsymbol{\xi}_{\mathbf{p}}$	State-space eigenvector
$\boldsymbol{\phi}_{\mathbf{p}}$	Mode shape
$\boldsymbol{\psi}_{\mathbf{p}}$	Damped mode shape
$\mathbf{A}$	State-space matrix A
$\mathbf{B}$	State-space matrix B

$\mathbf{B}_m$	Magnetic flux density
$\mathbf{C}$	Viscous damping matrix
$\mathbf{C}_{id}$	Identified damping matrix
$\mathbf{D}$	Generic damping matrix
$\mathbf{D}_c$	Coulomb friction matrix
$\mathbf{D}_s$	Structural damping matrix
$\mathbf{E}_\mu$	MAC error array
$\mathbf{G}$	Matrix of velocity integrals
$\mathbf{H}(\omega)$	Receptance matrix
$\mathbf{I}$	Identity matrix
$\mathbf{K}$	Stiffness matrix
$\mathbf{L}_i$	Localisation matrix
$\mathbf{M}$	Mass matrix
$\mathbf{P}_D$	Matrix of phase differences cosines
$\mathbf{W}_p$	Modal Weight
$\mathbf{Z}(\omega)$	Dynamic stiffness matrix
$\mathbf{\Lambda}$	Complex eigenvalues matrix
$\mathbf{\Lambda_R}$	Real part of matrix $\mathbf{\Lambda}$
$\mathbf{\Lambda_I}$	Imaginary part of matrix $\mathbf{\Lambda}$
$\mathbf{\Xi}$	State-space modal matrix
$\mathbf{\Phi}$	Modal matrix
$\tilde{\mathbf{\Phi}}$	Mass-normalized modal matrix
$\mathbf{\Psi}$	Damped modal matrix
$\mathbf{\Omega}$	Natural frequencies matrix
$\Im$	Imaginary part
$\Re$	Real part
$^{\mathrm{T}}$	Transpose
*	Complex conjugate
$^+$	Pseudo-inverse

List of Acronyms

DOF	Degree of freedom.
DSM	Dynamic stiffness matrix.
FEM	Finite element model.
FFT	Fast Fourier transform.
FRF	Frequency response function.
MDOF	Multiple degree-of-freedom.
SDOF	Single degree-of-freedom.

Chapter 1

Introduction

1.1 Historical background

The dynamic behaviour of vibrating mechanical systems is mainly governed by the cyclic transformation between kinetic and potential energy which is associated with inertia and elastic properties [1]. These properties have been well known since the 17th century; inertia forces were formally defined in Newton's second law of motion in 1687 [2] whereas elastic forces were described by Hooke's law in 1679 [3]. Mass and stiffness discrete elements are normally used to represent these properties in mathematical models which allow the explanation and estimation of important characteristics of vibrating systems, such as natural frequencies and mode shapes. Several methods are already well established for modelling or identifying these elements and they are used everyday in various applications with a relatively small level of uncertainty.

There are other aspects of vibration, such as the limited response of a vibratory system excited at resonance or the decay of free vibrations, which can be explained only by accounting for mechanisms which remove energy from the system [4], i.e. the damping. Since in the majority of mechanical systems the damping is considered light and the dynamical behaviour is principally determined by the relatively large elastic or inertial forces [5], it is often oversimplified or totally neglected in many engineering designs. However, damping can be very important in systems where the dynamic behaviour is dominated by the energy dissipation. If a model is to be used to predict transient responses, dynamic instabilities or decay times, a good understanding of damping is necessary. Defining an accurate damping model requires an higher degree of complexity than a mass and stiffness

system. The difficulty lies in representing all the sources of damping, which are very different in terms of nature, extent and distribution within the structure. Even if each physical energy dissipation phenomenon had been studied separately with success, there still remains many different theories on how damping should be represented by mathematical models for engineering applications.

The first attempt to study damping was probably made by Poisson in 1831 while analysing the theory of friction for the case of a compressible fluid [6]. In 1851, Stokes derived an equation for the motion of pendulums which considers the *vis viva* (from the Latin for *living force*) lost by internal friction [7]; Maxwell measured the coefficient of viscosity or fluid internal friction of air and other gasses in 1866 [8]. The first important and famous model of damping is the linear viscous damping, introduced by Lord Rayleigh [9] in 1878 by grouping the coefficients of a quadratic energy dissipation function into a symmetric matrix called *the damping matrix*. Lord Rayleigh also developed the so-called *proportional damping* which considers the damping matrix as a linear combination of the stiffness and mass matrices. A large number of theories and models of damping have been developed since Lord Rayleigh, but in a large number of standard applications his model is still used to approximate the energy dissipated in a system. This approximation is attractive computationally because it results in systems of second order differential equations with solutions that are readily available by well-understood techniques.

The modern engineering design of structures demands a damping model which is capable of accurately reproducing the response of large structures within the frequency range of interest and this is not always possible by using the viscous damping model only. At the same time, the model should not be too complex since the analysis must be performed in a reasonable computational time. Consequently, the various physical damping mechanisms must be approximated to a mathematical representation which takes into consideration the predominant sources of damping which affect a particular structure subjected to a certain type of excitation within a specific range of frequencies. For this reason, a reasonably good damping model for one application could give completely unreliable results for a different system. Moreover, spatial agreement between the mathematical

model and the real system is also important, since it could help the implementation of the model in the Finite Element Model (FEM) approach.

Damping could be a significant factor in many different fields: the instabilities in aircraft wings, the design of buildings in seismic areas, bridges in windy regions, the dynamic behaviour of rotors, acoustics, geophysics and astronomy, the design of musical instruments and audio systems or the prediction of earthquake effects are just a few examples. Damping can also be deliberately introduced in a system to reduce the amplitude of vibration at frequencies close to resonance: vehicles or simpler structures like washing machines usually contain damping mechanisms in order to increase the comfort of passengers, to reduce the acoustic noise or to avoid unwanted movements. These damping devices can be divided into passive and active mechanisms. The passive mechanisms include applying layers of high damping materials (usually viscoelastic polymers, synthetic rubbers) over the surface of the structure, or within the core of a sandwich-type structure [10], the attachment of mechanical vibration absorbers such as viscous fluid dampers or magnetic eddy current dashpots [11, 12, 13] in strategic locations, applying piezoelectric materials shunted with passive electric circuits [14, 15] or tuned mass dampers [16, 17]. It is also theoretically possible to increase the initial structural damping by appropriate heat treatment (of metallic copper-manganese alloys typically) to modify the material damping, but this inevitably changes other important mechanical properties and so may not be totally advantageous [10].

Acoustic (or radiation) damping can also be increased by changing the surrounding medium (e.g. immersing the structure in water) or varying the shape or size of the structure itself. In these cases there will be obvious changes in the inertial and elastic properties too. The influence of damping on the performance of passive vibration isolation were discussed by Ruzicka [5] including several idealized isolators (viscous, Coulomb friction, quadratic, velocity-n^{th} power and hysteretic damping) and their effect on transmissibilities. Active and semi-active methods usually include the use of actuators along with sensors and feedback controllers (analog or digital) to produce an actuation with the right timing to counteract the resonant oscillation. These techniques comprise active constrained-layer damping [18], the use of controlled circuits with piezoelectric materials [19] as well as

traditional actuators or shakers [20, 21].

1.2 Classification of damping

Separating and evaluating all the sources of damping in a structure is practically impossible but it can be interesting to classify them into categories in order to understand which kinds of damping can be the most relevant and which ones can be neglected in a particular application. Damping phenomena can be initially divided into two main categories: material and non-material damping.

1.2.1 Material damping

Material damping can be found in the literature under various different names: internal or hysteretic damping and internal friction are the most common. Material damping is related to the energy dissipated in a volume of continuous media; Lazan [22] used the term *macro-continuous* media to exclude the damping generated at interfaces between separated recognizable parts of a structure, yet include the damping originated at interfaces between internal micro and sub-micro structures.

Muszynska [23] listed several types of internal energy dissipation mechanisms by classifying the different internal structure reorganizations which are associated with these mechanisms and separating between linear and non-linear sources. Without going into the details of each mechanism, it could be useful to name some of these phenomena in order to have an idea of the complexity of the problem. Included are electronic mechanisms (electronic absorption of ultrasounds, phonon and phonoelectronic mechanisms), damping depending on solvent atoms (Snoek's damping, ordering in solid solutions, Koester's damping, damping caused by phase processed in solid solutions), relaxation on point defects, damping from dislocations (relaxation of dislocations, dislocation resonance, dislocation hysteresis, damping depending on history of deformation, deformation hysteresis), relaxation on grain boundaries, irreversible intercrystal heat flux, viscoelastic delay micro-creep, thermoelastic damping, thermal hysteresis, magnetoelastic relaxation, eddy currents and ferromagnetic hysteresis.

For practical reasons it is not possible to account for all the precise physical mechanisms but it is important to know that they exist and that all materials dissipate a certain amount of energy during cyclic deformations. Generally these behaviours in engineering problems are experimentally estimated by measuring the energy dissipated per unit volume per cycle for a number of samples of each material or by extracting information from the hysteresis loops, again from experimental measurements [24, 25]. Bert [26] described some of the mathematical models and experimental techniques for the rheological behaviour of a solid. Rheology is defined as "the science dealing with the deformation and flow of matter" [27, 25]. The term *rheological* has been used by Lazan and then by others to include deformation, flow and all stress-strain-time properties of material systems. The mathematical models for material damping include the Maxwell model (a spring and a dashpot in series), the Kelvin-Voigt model (a spring in parallel with a dashpot) and the Kimball-Lovell complex stiffness model. Koeller [28] modelled the viscoelastic behaviour of polymers including fractional or viscoelastic elements called *springpots*, which constitute an intermediate device between a spring and a dashpot. Schmidt and Gaul [29] provided a finite element formulation of the viscoelastic constitutive equations using fractional time derivatives. There are also models which combines the Kelvin-Voigt and Maxwell model in different ways to obtain three-parameter models [30] or add even more elements to obtain the so-called Kelvin chain or the generalized Maxwell model [31].

1.2.2 Non-material damping

Non-material damping includes all the energy dissipation mechanisms acting on the interfaces between parts of the structure and the interactions with the surrounding medium. The main sources of non-material damping include the effects of friction in joints, radiation into surrounding fluid, air pumping and squeeze film damping. A series of experiments by Beards [32] showed that the energy dissipated in joints is generally much larger than the dissipations due to material damping; bolted, riveted and welded connections are often the main source of damping in a structure. Two papers by Ungar [33, 34] offer a comprehensive and exhaustive overview of the mechanisms involved, the magnitudes and the status

of the engineering knowledge.

The physical phenomena experienced in joints are described in an article by Goodman [35], which focus on interfacial slip damping: the friction in joints dissipates energy in two different ways, known as microslip and macroslip. Since friction forces depend on the normal force, and since the actual normal pressure distribution is not uniform when the structure is loaded dynamically, there could be an initial behaviour when the shearing forces are not sufficient to create global sliding and some of the surfaces in contact are sticking and some others have local slip: i.e. the microslip [36, 37]. When loads and the relative displacements increase, slip takes place over the entire surface and the so-called macroslip happens [38]. An approach to the mathematical modelling of frictional joints is the Iwan network model [39] which consists of springs and sliders in a parallel-series or series-parallel configuration. A *slider* is a dissipation element which follows Coulomb friction properties when the excitation is greater than a break-free force [40]. Other approaches includes the Valanis model [41], based on a first order differential equation originally intended for plasticity in order to unify the isotropic hardening models and kinematic [42] and the Bouc-Wen model [43].

A different non-material form of damping is the acoustic radiation damping, which is due to the coupling of the response of a structure with the surrounding fluid medium, normally the air, which reduces vibrations and produces noise and sounds [9, 33]. This kind of damping depends both on the characteristic of the fluid (density, etc.) and on the properties of the structure (mass, stiffness, shape, size, etc.). Its order of magnitude is usually too small to be considered in most engineering structures, but can be important for specific applications (i.e. musical instruments). However, the amount of acoustic damping can be in theory estimated by fluid-structure equations [24].

Another mechanism involving the fluid surrounding the structure is the air pumping damping. Air can be entrapped inside some parts of the structure or in joints; when the structure vibrates, the air can be compressed and rarefied and forced to flow through leaks by laminar or turbulent motion, depending on a multitude of factors [33]. This kind of damping can have a small effect at low frequencies but generally appears to be negligible in most cases.

1.3 Scope of the thesis

The scope of this thesis is to provide a brief but comprehensive survey on the main spatial damping identification techniques currently available and to develop and validate a new improved method. The main interest is in the location and identification of the main sources of damping in multiple degree-of-freedom systems using a practical method supported by engineering knowledge. Traditional modal damping identification methods normally used in standard vibration problems are certainly well-established techniques which are easier to apply and reliable but they provide information which are more difficult to link to a specific region of the structure or to a specific physical phenomenon. Having an idea of the spatial distribution and amplitude of damping sources in a structure gives several advantages: for example, if the equivalent viscous damping coefficient of a particular joint is known, it can be used as an element of the damping matrix of a larger structure and, if the location of these joints is known, it can easily be implemented in FEM. Accurate information on the location of the sources of energy dissipation could also help the solution of local problems that cannot be properly addressed by knowing the modal damping ratio only as well as detecting other kinds of malfunctions in a particular region.

In chapter 2, basic notions on modal analysis and on the effect of damping in vibrations are given in order to provide the necessary knowledge to understand the methods presented afterward; the effect of viscous damping on the frequency response function, time response, hysteresis loop, energy dissipation and Nyquist plot of a single degree-of-freedom system is discussed together with other forms of damping as hysteretic damping or Coulomb friction. The effect on the eigenvalues and the eigenvectors of multiple degree-of-freedom systems and considerations on classical or proportional damping are addressed.

In chapter 3 some modal damping and single degree-of-freedom identification techniques are explained and a literature review of the main spatial multiple degree-of-freedom damping identification techniques is presented, with some critical observations on some aspects of the philosophy and performance of different approaches. The different techniques have been classified into three main groups:

methods based on the inversion of the receptance matrix, methods based on modal parameters and methods based on time histories. The survey includes the works of several authors with different approaches and a numerical simulation in order to compare the performance of the methods when dealing with the problem of modal incompleteness; a common issue in experiments on real structures.

In chapter 4 the theory and details of the proposed identification method based on the balance between the energy input in the system by external forces and the energy dissipated by damping is presented. After deriving the energy equation, some techniques are proposed in order to improve the identification by addressing issues such as the damping matrix parameterisation, the spatial and modal incompleteness of measurements and the underdetermination of the system of equations. How to solve the energy equation in order to obtain sensitive parameters with physical meaning is considered, with particular attention to the non-negative definiteness of the identified viscous damping matrix.

In chapter 5 the results of numerical simulations on a finite element model of a cantilever beam is presented to validate the theory, to show how the energy method deals with spatial and modal incompleteness and to illustrate the meaning of "energy-equivalent viscous damping". A simulation on the beam damped with a Coulomb friction device and a larger structure (the Goland wing) are also presented in order to demonstrate the versatility of the method.

In chapter 6 the design and the results of two different experiments are presented and discussed. The first one consists of an aluminium cantilever beam with several different sources of damping attached to it. These sources are magnetic dashpots, air dashpots and friction devices located between the different degrees of freedom of the beam and the ground. The aim of the experiment is to locate and estimate the value of damping using the measurements of ten accelerometers equally spaced along the length of the beam when exciting it by a set of single frequency harmonic forces. In this case the sources of damping are called "absolute" and they dissipate the energy of the system to the ground directly. The second experiment is a five degree-of-freedom system with "relative" sources of damping between two or more degrees of freedom of the structure. The results of the identification method and some practical issues on the integration of measurements are given

and considerations on the viscous equivalent damping and the physical meaning of this approximation are discussed.
Chapter 7 summarises the main outcomes of the research with particular attention to the practical aspects of the study from an engineering point of view. Some new ideas on future work and possible extensions of the method proposed are also given.

1.4 Closure

It appears from this introduction why damping remains one of the most unpredictable and difficult aspects of mechanical vibrations. Being aware of the complexity of the problem is the first step in trying to develop a simple procedure or a model in order to obtain the necessary amount of information from standard measurements. The difficulty lies in choosing a priori the sufficient level of accuracy for each application, in deciding when damping can be neglected or when efforts must be spent to estimate certain parameters which can be crucial in the dynamic behaviour of the system in the range of frequency of interest. In the next chapter, basic notions on modal analysis and on the effect of damping in vibrations are given in order to provide the necessary knowledge to understand the methods presented afterward.

Chapter 2

Models for damping in vibrating systems

2.1 Dynamics of mechanical systems

Modelling the dynamics of a real mechanical system does not mean describing how all the features of the system interact with one another. In most cases, it is sufficient to consider the basic properties separated into simple discrete elements which can represent the dynamic properties of the system to desired accuracy. These properties are mass, stiffness and damping which are responsible for inertia, elastic and dissipative forces respectively [44]. Depending on the number of degrees of freedom (DOF) of the discretised model, systems can be classified into single degree-of-freedom (SDOF) and multiple degree-of-freedom (MDOF) systems.

2.2 Single degree-of-freedom systems

2.2.1 Undamped systems

In an undamped SDOF system, the dynamic properties are usually represented in the first place by an infinitely rigid constant mass m and an ideal massless spring of constant stiffness k. The equation of motion is written as

$$m\ddot{x}(t) + kx(t) = f(t) \tag{2.1}$$

where $x(t)$, $\ddot{x}(t)$ are respectively the displacement and the acceleration response of the system induced by the time dependent excitation force $f(t)$. The free

vibration solution is obtained considering the system with no external forcing

$$m\ddot{x}(t) + kx(t) = 0. \tag{2.2}$$

Excluding the trivial solution where $x(t) = 0$, which corresponds to no motion at all, it is known that the solution of eq. (2.2) is of the form

$$x(t) = x_0 e^{i\omega t} \tag{2.3}$$

where i is the imaginary unit ($\sqrt{-1}$), x_0 represents the amplitude of the displacement and ω the frequency of vibration. By substituting eq. (2.3) into eq. (2.2) and solving for ω, the natural frequency ω_n is obtained

$$\omega_n = \sqrt{\frac{k}{m}} \tag{2.4}$$

which represents the frequency at which the system naturally vibrates once it has been set into motion. In the case of forced vibration, considering an harmonic excitation of the form

$$f(t) = f_0 e^{i\omega t} \tag{2.5}$$

where f_0 represents the amplitude of the force, it is a common procedure to study the behaviour of the system by looking at the Frequency Response Function (FRF) which relates the output (displacement, velocity or acceleration) to the input $f(t)$. For an undamped system excited with an harmonic force, the FRF can be calculated as

$$h(\omega) = \frac{x_0}{f_0} = \frac{1}{k - \omega^2 m} \tag{2.6}$$

where $h(\omega)$ is the receptance of the system. Alternative forms of FRF can be obtained by relating velocity or acceleration to the excitation force, called respectively mobility and accelerance.

2.2.2 Viscously damped systems

The simplest and commonest approach to modelling damping in SDOF systems is representing the dissipative forces by an ideal massless dashpot with constant viscous damping coefficient c. A viscous dashpot is a linear device which produces

a force F_d proportional to the relative instantaneous velocity $\dot{x}(t)$ across the damper, as

$$F_d = c\dot{x}(t) \tag{2.7}$$

which, in a physical sense, corresponds to the force obtainable by certain types of laminar flow of a fluid through a restriction [5]. The system is schematically represented in figure 2.1. The equation of motion of the viscously damped SDOF

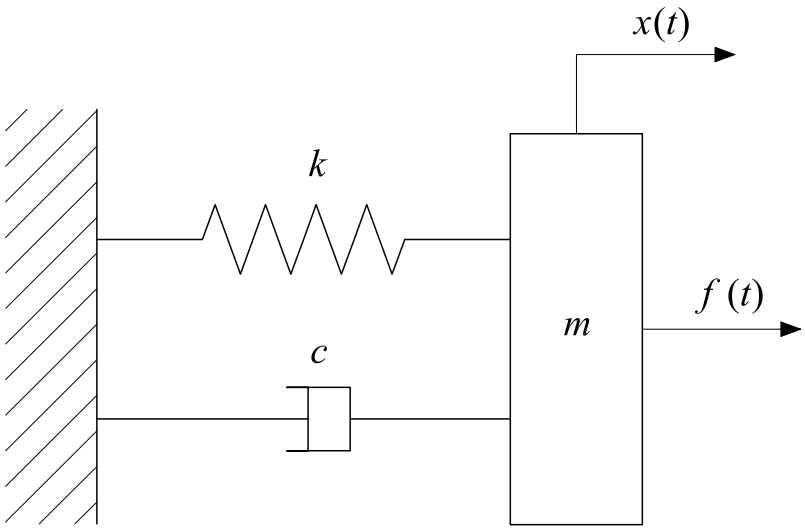

Figure 2.1: Single degree-of-freedom system

system becomes

$$m\ddot{x}(t) + c\dot{x}(t) + kx(t) = f(t) \tag{2.8}$$

whose solution is of the form

$$x(t) = x_0 e^{st} \tag{2.9}$$

where s is a complex quantity, sometimes referred as the Laplace variable [44]. Considering the free vibration

$$m\ddot{x}(t) + c\dot{x}(t) + kx(t) = 0 \tag{2.10}$$

by substituting eq. (2.9) in eq. (2.10), the characteristic equation is obtained

$$ms^2 + cs + k = 0 \tag{2.11}$$

and solving for s

$$s_{1,2} = -\frac{c}{2m} \pm \sqrt{\left(\frac{c}{2m}\right)^2 - \frac{k}{m}} \tag{2.12}$$

two roots are obtained. When the term inside the square root is equal to zero, the system is said to be critically damped and the critical damping coefficient c_{cr} is defined as

$$c_{cr} = 2\sqrt{km}. \tag{2.13}$$

The viscous damping present in the system c divided by c_{cr} gives the damping ratio ζ

$$\zeta = \frac{c}{c_{cr}} \tag{2.14}$$

which can be used to determine if a system is critically damped ($\zeta = 1$), underdamped ($\zeta < 1$) or overdamped ($\zeta > 1$). Substituting eq. (2.4) and eq. (2.14) into eq. (2.10), the equation of motion can be expressed in the form

$$\ddot{x}(t) + 2\zeta\omega_n\dot{x}(t) + {\omega_n}^2 x(t) = 0 \tag{2.15}$$

and the two roots becomes

$$s_{1,2} = -\omega_n\zeta \pm i\omega_n\sqrt{\zeta^2 - 1}. \tag{2.16}$$

It can be seen from eq. (2.16) that the roots of the characteristic equation are real and equal if the system is critically damped, real and distinct if it is overdamped and complex conjugate if it is underdamped. Figure 2.2 shows the time responses of a SDOF system to an initial unitary displacement: the critically damped system converges to zero faster than any other, and without oscillating; the overdamped system will take longer to return to the equilibrium position, again without oscillating, whereas the underdamped system will oscillate at a frequency which is lower than the natural frequency of the system, defined as the damped natural frequency ω_d,

$$\omega_d = \omega_n\sqrt{1 - \zeta^2} \tag{2.17}$$

for a certain number of cycles until it converges to zero. The undamped system ($\zeta = 0$) will instead vibrates at its natural frequency forever since the initial energy cannot be dissipated in any way.

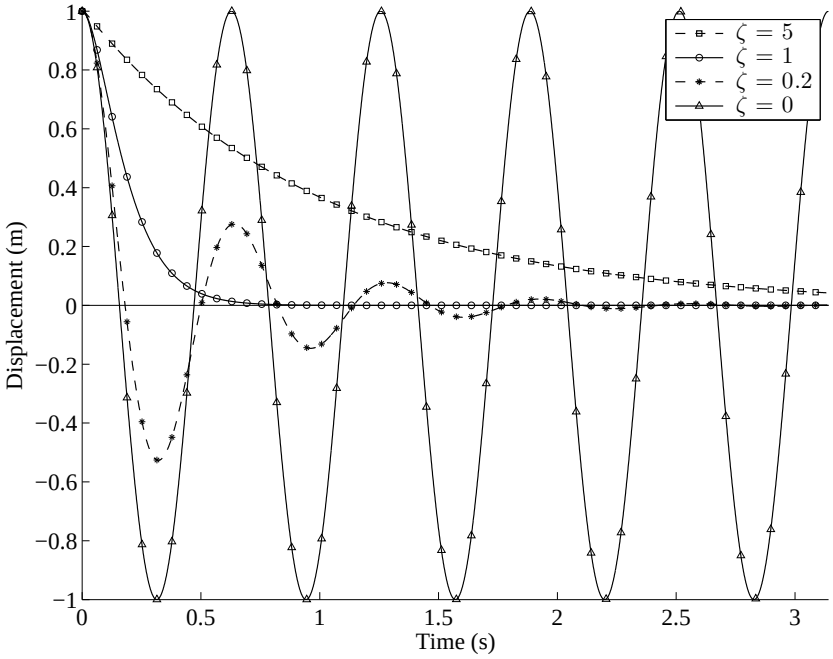

Figure 2.2: Free vibration time response to an initial unitary displacement for different values of ζ. $\omega_n = 10$ rad/s.

Effect of viscous damping on the FRF

The receptance of a viscously damped system excited by a harmonic force as eq. (2.5) is given by

$$h(\omega) = \frac{1}{k + i\omega c - \omega^2 m} \tag{2.18}$$

and it is generally a complex quantity. The FRF is normally plotted in two distinct figures showing the magnitude and the phase angle of $h(\omega)$ versus the frequency, also know as the Bode plot. The phase angle ϕ of the FRF is defined as

$$\phi = \tan^{-1}\left(\frac{\Im\left(h(\omega)\right)}{\Re\left(h(\omega)\right)}\right) \tag{2.19}$$

where $\Im$ and $\Re$ respectively indicates the imaginary and real part. The effect of viscous damping is shown in figure 2.3: the FRF of the undamped system ($\zeta = 0$) presents a high peak when $\omega = \omega_n$ since the denominator of eq. (2.18) is zero and the amplitude of the response is infinite. This will never happen in real systems since a small source of damping is always present in practice, but the amplitude of the response can be very large. The term *resonance* is used to indicate when a structure is excited with a harmonic force at a frequency close

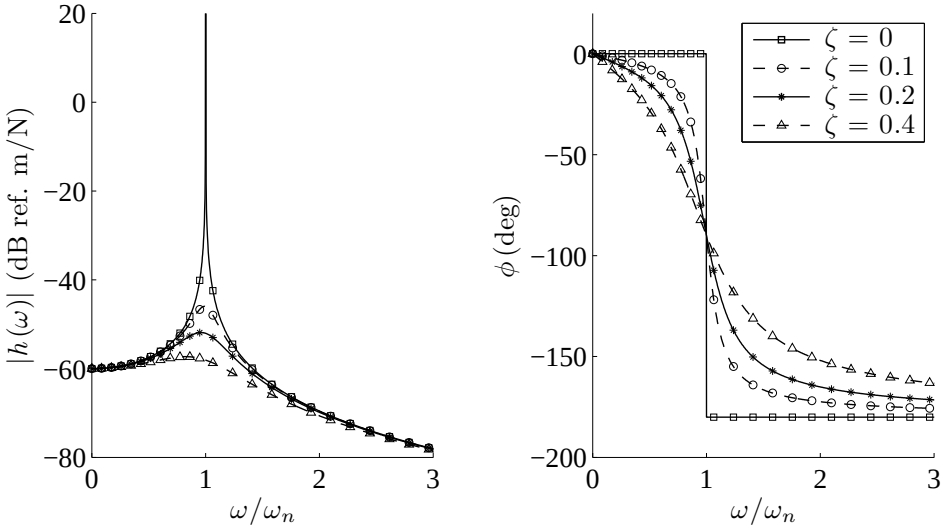

Figure 2.3: Amplitude and phase of the FRF (receptance) of a viscously damped SDOF system for different values of ζ. $m = 2$ kg, $k = 1000$ N/m.

to the natural frequency; in normal structures, this situation is usually avoided since large displacements can lead to destructive events. The effect of viscous damping is much more visible in the proximity of resonance: from the amplitude plot it can be seen that the magnitude of the resonance peak is reduced when the amount of damping is increased. Moreover, the maximum amplitude occurs now at ω_d and not at ω_n. The phase shift of the response, which in the theoretical undamped case happens from $0°$ to $-180°$ instantaneously when the frequency of the excitation passes through resonance, becomes gradual when damping is present, with a value of $-90°$ at resonance.

The way the FRF is displayed can help the identification of damping. The Bode plot is only one of the possibilities to plot a complex value versus frequency using two separate figures; another way is to plot the real part and the imaginary part versus frequency, again in two separate figures, or plotting the real part versus the imaginary part in the Argand plane [45]. The latter case is also known as the Nyquist plot and it can be particularly helpful to visualize the damping properties.

Effect of viscous damping on the Nyquist plot

The Nyquist plot consists of displaying the real part versus the imaginary part of the FRF in the Argand plane. One of the advantages of this plot is the fact that

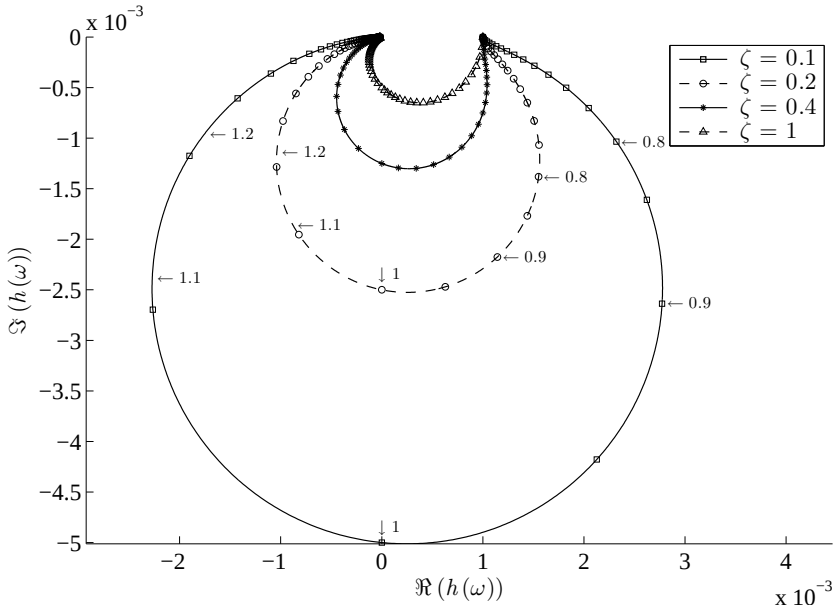

Figure 2.4: Nyquist plot of the receptance of a viscously damped SDOF system for different values of ζ. The numbers appearing in the plot indicate the ω/ω_n ratio. $m = 2$ kg, $k = 1000$ N/m.

the frequencies close to resonance are clearly identified and well separated on the plot and the size of the curves obtained is related to damping. Depending on the type of damping, the choice of which FRF (receptance, mobility or accelerance) is displayed in the Nyquist plot is important. The Nyquist plot of the receptance of a viscously damped system showed in figure 2.4 can be related to the viscous damping coefficient but it is difficult to extract precise values from the plot. The plot of mobility (figure 2.5) is instead the right choice if the interest is in viscous damping: the mobility of a viscously damped system excited by a harmonic force as eq. (2.5) is given by

$$b(\omega) = \frac{i\omega}{k + i\omega c - \omega^2 m} \tag{2.20}$$

its real and imaginary part are respectively

$$\Re(b(\omega)) = \frac{\omega^2 c}{(k - \omega^2 m)^2 + (\omega c)^2} \tag{2.21}$$

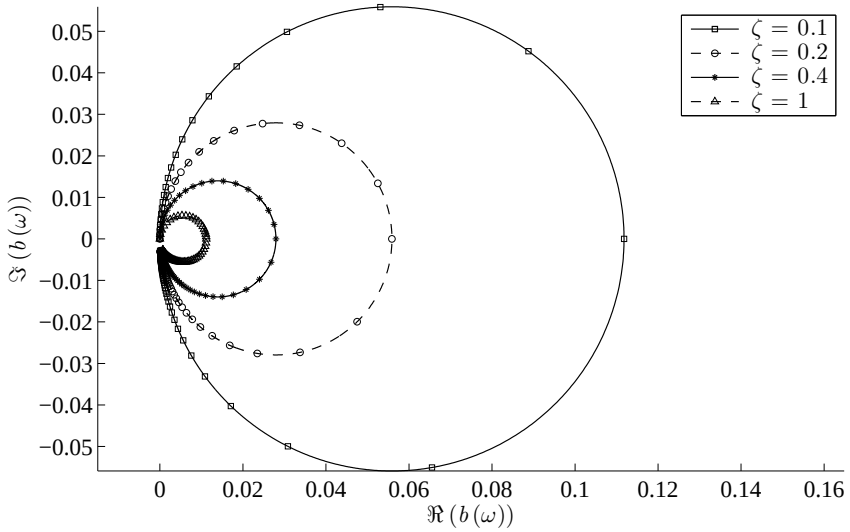

Figure 2.5: Nyquist plot of the mobility of a viscously damped SDOF system for different values of ζ. $m = 2$ kg, $k = 1000$ N/m.

$$\Im(b(\omega)) = \frac{\omega(k - \omega^2 m)}{(k - \omega^2 m)^2 + (\omega c)^2} \tag{2.22}$$

The two equations can be arranged in the following equation

$$\left(\Re(b(\omega)) - \frac{1}{2c}\right)^2 + (\Im(b(\omega)))^2 = \left(\frac{1}{2c}\right)^2 \tag{2.23}$$

which is the equation of a circle in the Argand plane centred at point $(1/2c, 0)$ with a radius of $1/2c$ allowing an easy estimation of the damping simply by measuring the diameter of the circle of the mobility plot.

Effect of viscous damping on the hysteresis loop

The hysteresis loop is a plot of instantaneous force versus instantaneous displacement of a system during steady state forced vibration [24] often used to display the viscoelastic behaviour of materials (in that case, stress versus strain is a more common version). In an undamped system this plot is simply a line segment in the first and third quadrant and the slope depends on the mass and the stiffness of the system. Lazan [25] showed that the hysteresis loop of a viscously damped system (figure 2.6) is elliptical and the area enclosed by the ellipse represents the energy dissipated per cycle. This property make it a valid instrument to experimentally estimate the global energy dissipated in a system.

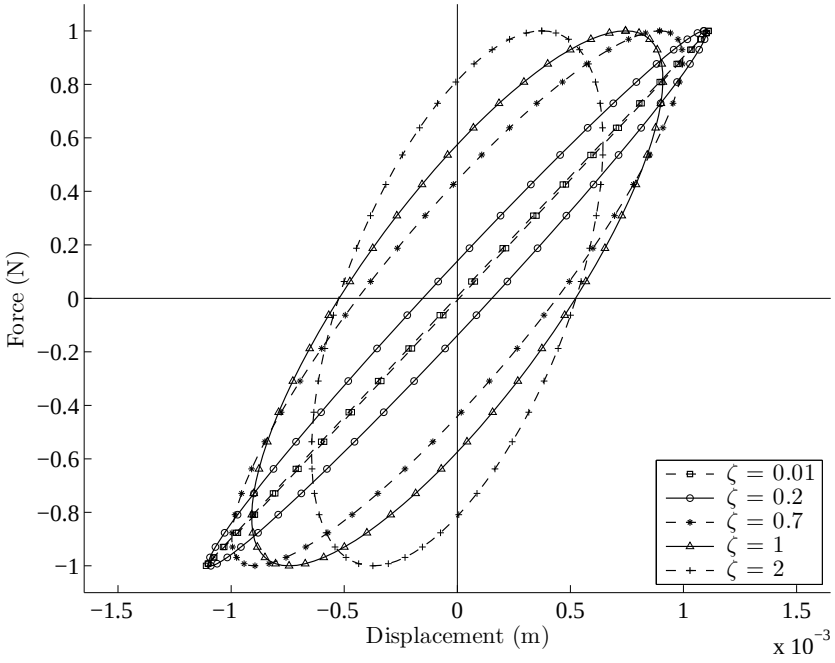

Figure 2.6: Hysteresis loop of a viscously damped SDOF system for different values of ζ. $f_0 = 1$ N, $\omega = 10$ rad/s, $m = 1$ kg, $k = 1000$ N/m.

Energy dissipated by viscous damping

The energy lost per cycle E_d by a general damping force F_d can be calculated by

$$E_d = \oint F_d \, dx \tag{2.24}$$

and it might depend on multiple factors, such as amplitude, frequency or temperature [46]. Considering a viscously damped SDOF system, substituting eq. (2.7) in eq. (2.24) it becomes

$$E_d = \oint c\dot{x} \, dx = \oint c\dot{x}^2 \, dt \tag{2.25}$$

If the system is excited by a single frequency harmonic force in the form

$$f(t) = f_0 \sin(\omega t) \tag{2.26}$$

the steady state velocity will assume the form

$$\dot{x}(t) = \omega x_0 \cos(\omega t - \phi) \tag{2.27}$$

Substituting eq. (2.27) in eq. (2.25)

$$E_d = \oint c\dot{x}^2 \, dt = \oint c\left(\omega x_0 \cos(\omega t - \phi)\right)^2 \, dt \tag{2.28}$$

The period T of the response is the same as that of the excitation force

$$T = \frac{2\pi}{\omega} \tag{2.29}$$

so the energy dissipated per cycle becomes

$$E_d = c\omega^2 x_0^2 \int_0^T \cos^2(\omega t - \phi)\, dt = \pi c \omega x_0^2 \tag{2.30}$$

Crandall [4] defined the loss factor η by dividing the energy lost in a cycle by the peak potential energy V stored in the system during that cycle

$$\eta = \frac{E_d}{2\pi V} \tag{2.31}$$

giving a convenient measure of the structural damping. In real structures, the values for η typically vary in a range from 10^{-5} to 10^{-1} but it can be larger for specific applications. For an ideal viscous dashpot, the loss factor becomes

$$\eta = \frac{c\omega}{k} \tag{2.32}$$

It can be seen from eq. (2.30) and eq. (2.32) that the energy dissipated per cycle by viscous damping and the loss factor are proportional to the frequency of the vibration. It is observed in experiments that this frequency dependence is not so pronounced in most common materials and real structures [44, 4]. The actual behaviour is closer to a frequency independent or weakly dependent dissipation mechanism. This fact suggests that other models of damping, different from viscous, could be more suitable to represent damping in a real structure. Jacobsen [47] introduced an approximation, known as *equivalent viscous damping*, based on the energy dissipated per cycle within a system. If the frequencies at which damping is important are known and the damping can be considered light, which is the case in most engineering applications, it is a common assumption to consider an ideal equivalent viscous dashpot by equating eq. (2.30) to the actual energy dissipated by the real, and probably non-viscous, system at those frequencies (usually at resonances) and calculating an equivalent viscous damping coefficient c_{eq}. This coefficient is used to represent the energy dissipated at a specific frequency only, but it can be considered an acceptable approximation

in a wider range of frequencies. If a more reliable model is required or if critical instabilities and frequencies are not known in advance then a different and more accurate model becomes necessary.

2.2.3 Non-viscously damped systems

As stated previously, viscous damping is just one of the possible models for energy dissipation in vibrating systems which is often chosen for mathematical reasons rather than for accurate representation of the physical system. Potentially, any model which guarantees that the energy dissipation rate is non-negative can represent the damping of a given system [48]. The most common models of non-viscous damping include hysteretic damping, Coulomb friction and velocity n$^{\text{th}}$ power damping.

Hysteretic damping

The idea of hysteretic damping was introduced with the aim of describing the material damping properties of solids by Kimball and Lovell [49]. Theodorsen and Garrick [50] introduced a linear structural friction model of damping with frequency independent dissipated energy per cycle to obtain results closer to the experimental behaviour of real structures while studying the flutter problem. This model provides a damping force "proportional to the displacement, but in phase with the velocity" and was labelled *hysteretic damper* by Bishop and Johnson [51]. Crandall [52] points out that the behaviour of the hysteretic damper model can be described by a transfer function in the frequency domain, but deriving the differential equation linking the physical variables is not so straightforward as for the viscous damping. Using the same notation used by Crandall [4], a frequency dependent dashpot parameter can be defined as

$$c(\omega) = \frac{k\eta(\omega)}{|\omega|} \tag{2.33}$$

which leads to the frequency domain equation of motion for the SDOF system

$$\left[-m\omega^2 + ic(\omega)\omega + k\right] x(\omega) = f(\omega) \tag{2.34}$$

or

$$\left[-m\omega^2 + k\left(1 + i\eta(\omega)\mathrm{sgn}(\omega)\right)\right] x(\omega) = f(\omega) \tag{2.35}$$

where $x(\omega)$ and $f(\omega)$ are the Fourier transforms of the response and excitation respectively. Many authors have then wrongly derived time domain equations from eq. (2.34) such as

$$m\ddot{x}(t) + c(\omega)\dot{x}(t) + kx(t) = f(t) \tag{2.36}$$

and used it directly to calculate transient motions. Crandall [4] calls eq. (2.36) "non-equation" since it mixes time-domain and frequency-domain operations without properly inverting the frequency dependent damping.

Eq.(2.33) is a general expression for the frequency dependent dashpot. If the loss factor is assumed to be a constant η_0 independent of frequency, it becomes

$$c(\omega) = \frac{k\eta_0}{|\omega|} \tag{2.37}$$

known as the ideal hysteretic damper [52]. The unit impulse response function for a SDOF system with ideal hysteretic damping has been derived [53, 54, 55] as

$$h(t) = \frac{1}{\pi k \eta_0 t} \qquad (-\infty < t < \infty) \tag{2.38}$$

showing a non-physical behaviour since it violates causality. This means that the

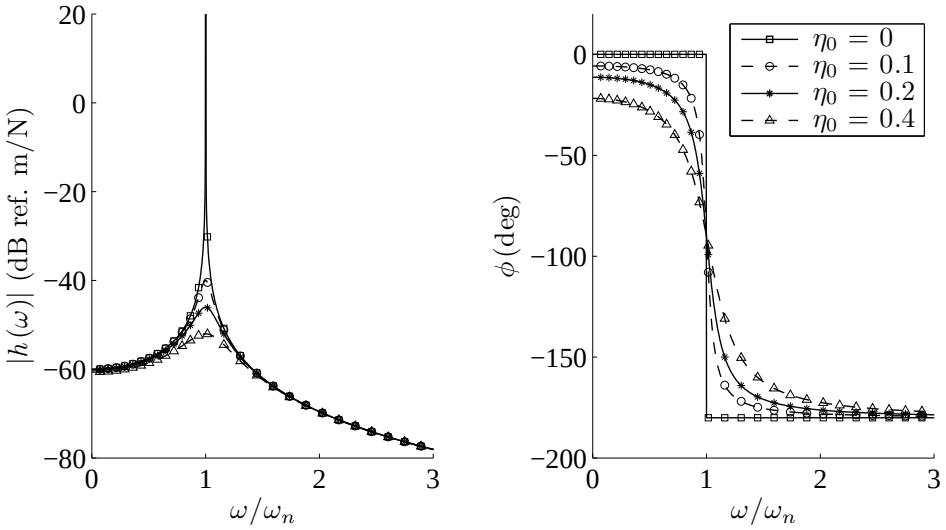

Figure 2.7: Amplitude and phase of the FRF (receptance) of a SDOF system with ideal hysteretic damper for different values of η_0. m = 2 kg, k = 1000 N/m.

state of the system at a given point of time is affected not only by the events

in the past but also by the events in the future [56] so that the response may anticipate the excitation. This flaw put some limitation to this model, which can be anyway used in some common applications such as steady state oscillation in instability analysis or stationary random vibration. For a harmonically excited ($\omega > 0$) SDOF system with an ideal hysteretic damper, the receptance becomes

$$h(\omega) = \frac{1}{-m\omega^2 + k\,(1 + i\eta_0)} \tag{2.39}$$

and the effect on the FRF is shown in figure 2.7. An important aspect which can be noticed in comparison with figure 2.3 for the viscous damper, is that the maximum amplitude of the FRF now is always obtained when $\omega = \omega_n$, regardless of the amount of damping. This behaviour is in contrast with real structures experiments, showing again how it is difficult to accurately represent real damping mechanisms using a mathematical model. Another difference is the presence of a non-zero phase angle when ω approaches zero [44]. If the damping is

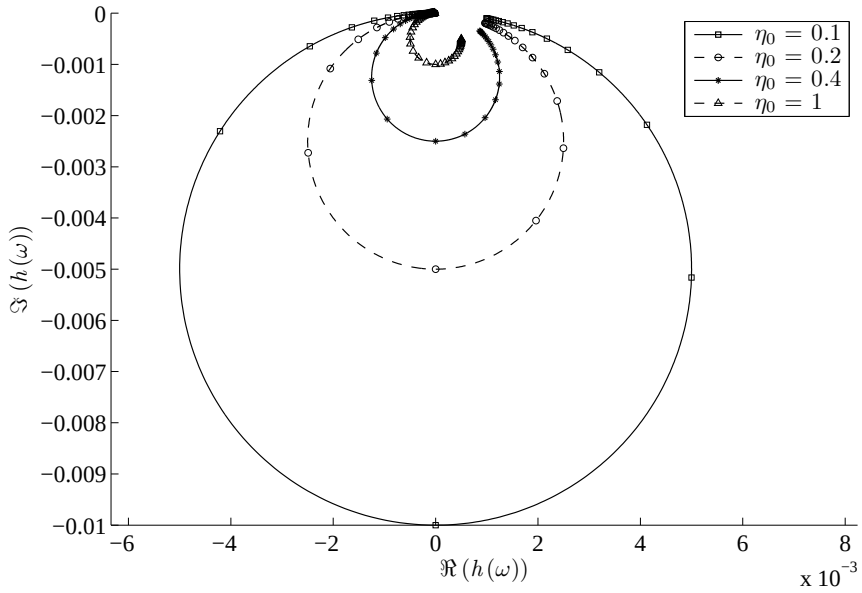

Figure 2.8: Nyquist plot of the receptance of a SDOF system with ideal hysteretic damper for different values of η_0. $m = 2$ kg, $k = 1000$ N/m.

low, however, the two models (viscous and hysteretic) at resonance are sufficiently close to be assumed equivalent and it can be proven that the constant loss factor of the ideal hysteretic damper η_0 and the damping ratio ζ of the viscous dashpot

at resonance are related by

$$\eta_0 \approx 2\zeta \tag{2.40}$$

On the Nyquist plot, following a similar procedure to the one used to derive eq. (2.23), the equation of a circle can now be obtained on the receptance plot as

$$\Re\left(h(\omega)\right)^2 + \left(\Im(h(\omega)) + \frac{1}{2\eta_0 k}\right)^2 = \left(\frac{1}{2\eta_0 k}\right)^2 \tag{2.41}$$

The circle, shown in figure 2.8, is now centred at point $(0, -1/2\eta_0 k)$ with a radius of $1/2\eta_0 k$. The hysteresis loop (figure 2.9) is still elliptical and, as it is plotted in this case, it cannot actually give any useful information about the nature of damping, since it shows the loop for a harmonic excitation at a certain fixed frequency so that the frequency dependence of $c(\omega)$ is not visible. If equation

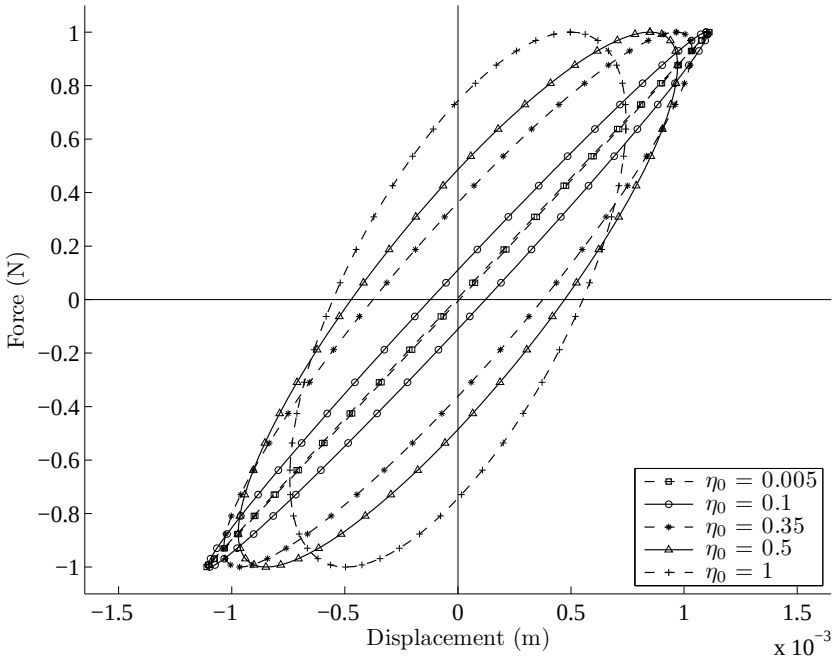

Figure 2.9: Hysteresis loop of a hysteretically damped SDOF system for different values of η_0. $f_0 = 1$ N, $\omega = 10$ rad/s, $m = 1$ kg, $k = 1000$ N/m.

eq.(2.40) holds and the hysteresis plot of the two equivalent systems is plotted for an exciting force at a frequency close to resonance, then the size of the loops will be approximately the same. Away from resonance, the size of the two loops will be considerably different.

Other forms of non-ideal hysteretic damping can be found in literature as, for example, the *band-limited hysteretic damper* suggested by Bishop and Price [57], which is defined by transfer functions within certain frequencies which vanish outside these bands, or combinations of hysteretic dampers with springs like the *modified hysteretic model* and the *quasi hysteretic model* introduced by Muravskii [58, 59].

Coulomb friction

Coulomb friction is a non-linear damping mechanism attainable from the relative motion of two contacting dry surfaces which slide relatively to each other with a normal force F_n holding them together [5], so that

$$F_d = \mu F_n \text{sgn}(\dot{x}) \tag{2.42}$$

where μ is the coefficient of friction, which is mainly a function of the material and of the roughness of the two surfaces. The damping force described by eq. (2.42) is shown in figure 2.10. This model of friction presents two main problems: firstly,

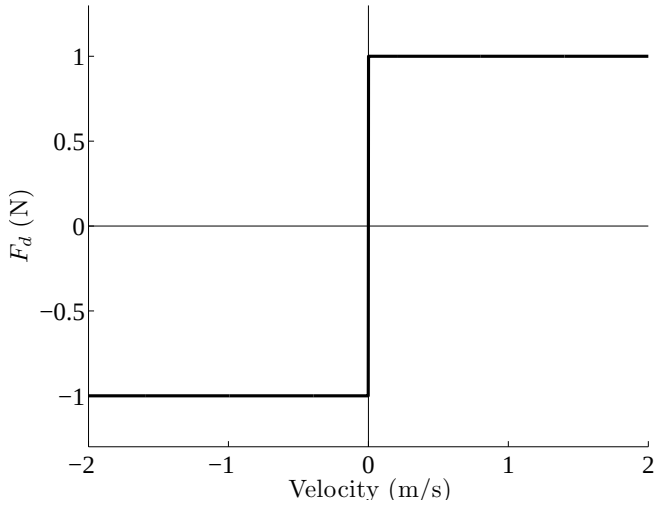

Figure 2.10: Coulomb friction force. $F_n = 1$ N, $\mu = 1$.

nonlinearity and discontinuity cause numerical stiffness when the change in the direction of relative velocity occurs. This results in very small integration time steps in simulations and high computational costs. It is also possible, with certain time-integration methods, for numerical instabilities to develop [60]. Second,

the actual behaviour of the friction forces is not as simple as the one shown in figure 2.10.

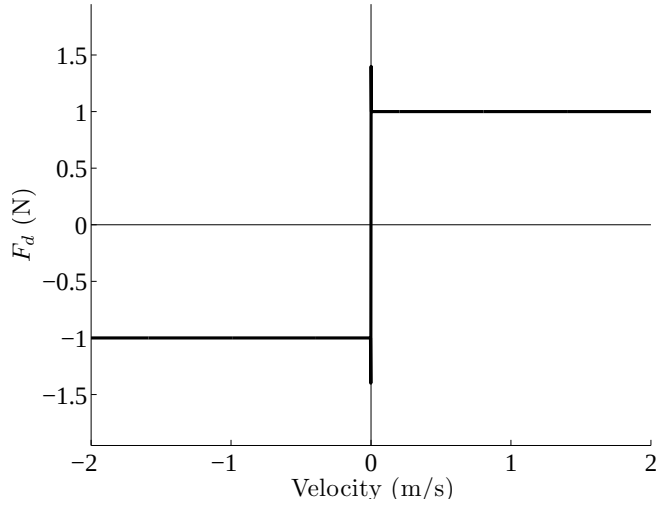

Figure 2.11: Coulomb friction force with stiction. $F_n = 1$ N, $\mu = 1$. $\mu_s = 1.5$.

Morin [61] suggested the existence of a static friction force F_s at rest which is larger than the Coulomb friction of eq. (2.42) when there is motion. In trying to represent this force, a slightly more elaborate model includes two different coefficients: the *kinetic coefficient of friction*, which is used exactly as in eq. (2.42) for all velocities different from zero, and the *static coefficient of friction* μ_s which is used to represent the equilibrium force during static friction or *stiction*. The two parameters model produces the force shown in figure 2.11.

Stribeck [62] showed that the static friction force does not decrease discontinuously as in figure 2.11, but that there is a velocity dependence which is continuous. A common model for this behaviour is shown in figure 2.12. The latter model is fairly representative of the actual behaviour but it still contains an important discontinuity when the velocity changes direction. Several authors have tried to reduce this discontuinity by considering a small region close to the zero velocity where the change from negative to positive force is not a vertical line but it is replaced by a slope or by a hyperbolic tangent or logarithmic curve [60].

A common way of dealing with Coulomb friction in complex structures is to define an energy equivalent viscous model as explained in section 2.2.2. By assuming that under forced harmonic excitation the velocity is sinusoidal in the form of

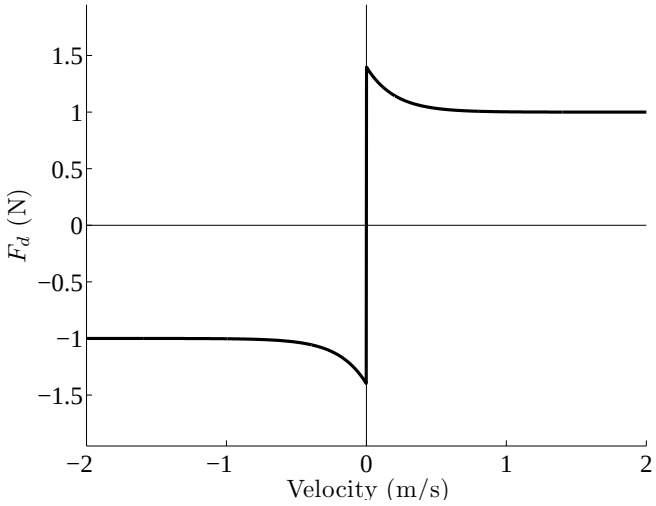

Figure 2.12: Coulomb friction force with Stribeck friction. $F_n = 1$ N, $\mu = 1$. $\mu_s = 1.5$.

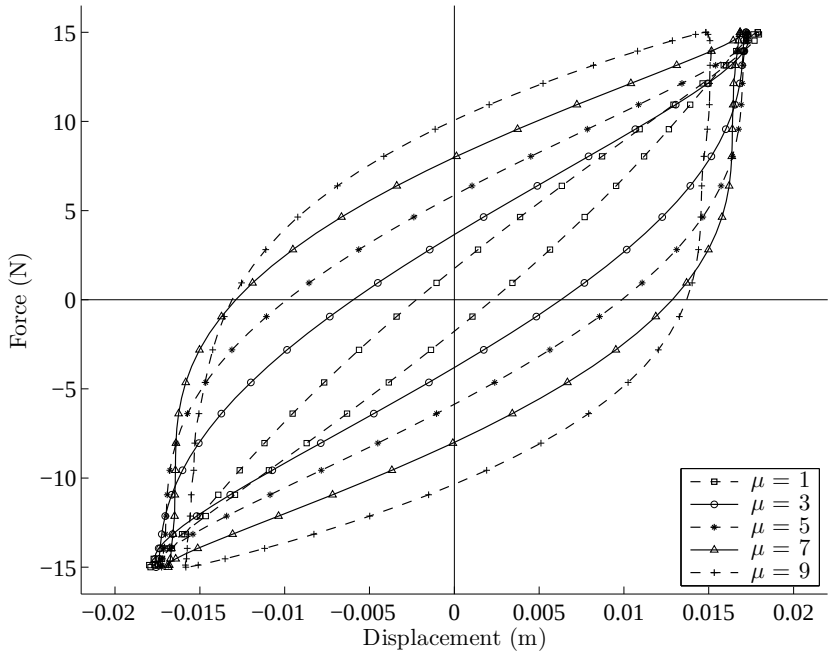

Figure 2.13: Hysteresis loop of a SDOF system with Coulomb friction for different values of μ. $f_0 = 15$ N, $F_n = 1$ N, $\omega = 13$ rad/s, $m = 1$ kg, $k = 1000$ N/m.

eq. (2.27), the energy dissipated per cycle [46] by the Coulomb friction force of eq. (2.42) is given by

$$E_d = \oint F_d \, dx = \oint F_d \, \dot{x} \, dt = 4\mu F_n x_0 \tag{2.43}$$

By equating eq. (2.43) and eq. (2.30)

$$\pi c_{eq} \omega x_0^2 = 4\mu F_n x_0 \tag{2.44}$$

the equivalent viscous damping coefficient c_{eq} can be estimated as

$$c_{eq} = \frac{4\mu F_n}{\pi \omega x_0} \tag{2.45}$$

This approximation means that the equivalent system with a viscous dashpot with damping coefficient c_{eq} dissipates the same amount of energy per cycle of the original system with Coulomb friction as eq. (2.42), but only at the specific frequency ω. Since usually the importance of damping is visible only in the proximity of resonance, this method allows a simpler calculation of the resonant amplitude of a Coulomb friction damped system using well known linear solutions used for viscous damping. The hysteresis loop for a SDOF system with Coulomb friction (figure 2.13) is no longer an ellipse and shows the non-linear behaviour of this type of energy dissipation.

Velocity n$^{\text{th}}$ power damping

In a more general sense, the damping force can be assumed to be proportional to the n$^{\text{th}}$ power of the relative velocity as

$$F_d = c_n \dot{x} \left|\dot{x}\right|^{n-1} \tag{2.46}$$

Eq. (2.46) includes viscous damping ($n = 1$) and Coulomb friction ($n = 0$) as special cases but also quadratic damping ($n = 2$) obtainable from the turbulent flow of a fluid through an orifice [5], cubic damping ($n = 3$) and other kinds of damping, included fractional values for n too. Whereas for some value of n there is a corresponding physical phenomenon, the n$^{\text{th}}$ power damping model can be used as an abstract mathematical model in inverse problems where c_n and n becomes the identification parameters [63].

Fractional time derivatives models

Fractional derivatives have been formally and mathematically defined by several authors in different ways; the most common definitions are known as the

Riemann-Liouville and the *Grünwald–Letnikov derivatives* [64]. Practically speaking, a fractional derivative is a derivative of order n for n being a fraction. The physical meaning of such an operator is not straightforward: for example, it is known that velocity is the order 1 derivative of displacement with respect to time but the meaning of order 1/2 derivative of displacement is quite obscure. A detailed geometric and physical interpretation of several fractional derivatives has been suggested by Podlubny [65].

Fractional time derivatives offer a powerful and versatile instrument in dynamics, especially for the curve-fitting of experimental data. One of the first applications of fractional derivatives to mechanics was the modelling of stress relaxation of some materials by Nutting [66] in 1921. Koeller [28] modelled the viscoelastic behaviour of polymers including fractional or viscoelastic elements called *springpots*, which constitute an intermediate device between a spring and a dashpot. Schmidt and Gaul [29] provided a finite element formulation of the viscoelastic constitutive equations using fractional time derivatives.

2.3 Multiple degree-of-freedom systems

Normally the behaviour of a real structure cannot be represented by a SDOF model, unless it is a very simple system. However, even if a real structure is a continuous system and has an infinite number of degrees of freedom, a good approximation of the real structure can be a model with a finite number of elements representative of the most important properties from a dynamic point of view. Most commonly, models consider discretised masses (known as lumped-mass model) connected with springs and dashpots similarly to the SDOF system.

2.3.1 Undamped systems

The equations of motion of a MDOF system are usually written in a matrix form. Considering, for example, the system shown in figure 2.14, the equilibrium

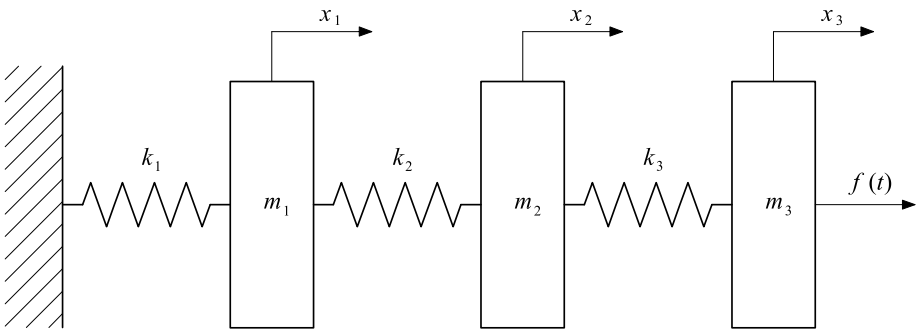

Figure 2.14: Undamped multi degree-of-freedom system

equations can be written as

$$\begin{aligned} &m_1\ddot{x}_1(t) + (k_1 + k_2)x_1(t) - k_2x_2(t) = 0 \\ &m_2\ddot{x}_2(t) - k_2x_1(t) + (k_2 + k_3)x_2(t) - k_3x_3(t) = 0 \\ &m_3\ddot{x}_3(t) - k_3x_2(t) + k_3x_3(t) = f(t) \end{aligned} \tag{2.47}$$

or, in a more compact form

$$\mathbf{M}\ddot{\mathbf{x}}(t) + \mathbf{K}\mathbf{x}(t) = \mathbf{f}(t) \tag{2.48}$$

where $\mathbf{M} \in \mathbb{R}^{n\times n}$ is the mass matrix, $\mathbf{K} \in \mathbb{R}^{n\times n}$ is the stiffness matrix, $\mathbf{x}(t)$ and $\ddot{\mathbf{x}}(t) \in \mathbb{R}^{n\times 1}$ respectively represent the vector of displacements and accelerations and $\mathbf{f}(t) \in \mathbb{R}^{n\times 1}$ is the forces vector. n represents the number of degrees of freedom. The mass and stiffness matrices are symmetric and positive definite. In this example:

$$\mathbf{M} = \begin{bmatrix} m_1 & 0 & 0 \\ 0 & m_2 & 0 \\ 0 & 0 & m_3 \end{bmatrix} \qquad \mathbf{K} = \begin{bmatrix} k_1 + k_2 & -k_2 & 0 \\ -k_2 & k_2 + k_3 & -k_3 \\ 0 & -k_3 & k_3 \end{bmatrix}$$

$$\mathbf{x}(t) = \begin{Bmatrix} x_1(t) \\ x_2(t) \\ x_3(t) \end{Bmatrix} \qquad \ddot{\mathbf{x}}(t) = \begin{Bmatrix} \ddot{x}_1(t) \\ \ddot{x}_2(t) \\ \ddot{x}_3(t) \end{Bmatrix} \qquad \mathbf{f}(t) = \begin{Bmatrix} 0 \\ 0 \\ f(t) \end{Bmatrix}$$

Similarly to the SDOF system, the solution of eq.(2.48) when exciting the system with a harmonic force is in the form

$$\mathbf{x}(t) = \mathbf{x_0}e^{i\omega t} \tag{2.49}$$

where $\mathbf{x_0} \in \mathbb{R}^{n\times 1}$ is the vector of displacement amplitudes. Substituting eq.(2.49) into eq.(2.48) and considering the free motion, an eigenvalue problem is obtained:

$$\left(\mathbf{K} - \omega^2\mathbf{M}\right)\mathbf{x_0} = 0 \tag{2.50}$$

The non-trivial solution can be calculated when

$$\det\left(\mathbf{K} - \omega^2\mathbf{M}\right) = 0 \tag{2.51}$$

yielding n solutions ω_1^2, ω_2^2, ..., ω_n^2 which are the eigenvalues of eq.(2.50) whose square roots represents the natural frequencies of the MDOF system. By solving eq.(2.50) for each natural frequency, n vector solutions $\boldsymbol{\phi}_1$, ..., $\boldsymbol{\phi}_n$ are obtained, known as the eigenvectors of eq.(2.50), representing the mode shapes of the dynamic system. Mode shapes are usually grouped into the modal matrix $\boldsymbol{\Phi}$

$$\boldsymbol{\Phi} = [\boldsymbol{\phi}_1 \quad \dots \quad \boldsymbol{\phi}_n] \tag{2.52}$$

A mode shape $\boldsymbol{\phi_p}$ describes the way the system vibrates for a particular natural frequency ω_p and it is useful for visualizing the dynamic behaviour of the structure. The absolute magnitude of a mode shape is not definite since it only describes the shape of the vibration and the relative quantities between the different degrees of freedom. For this reason it can be arbitrarily scaled by multiplying it by any constant. For example, figure 2.15 shows the first 6 mode shapes of a cantilever beam scaled so that the maximum value is equal to 1. The eigenvectors of the undamped system possess orthogonality properties so that for two distinct modes p and q where $p \neq q$

$$\begin{aligned}\boldsymbol{\phi}_p^{\mathrm{T}}\mathbf{M}\boldsymbol{\phi}_q &= 0\\ \boldsymbol{\phi}_p^{\mathrm{T}}\mathbf{K}\boldsymbol{\phi}_q &= 0\end{aligned} \tag{2.53}$$

whereas if $q = p$

$$\begin{aligned}\boldsymbol{\phi}_p^{\mathrm{T}}\mathbf{M}\boldsymbol{\phi}_p &= m_p\\ \boldsymbol{\phi}_p^{\mathrm{T}}\mathbf{K}\boldsymbol{\phi}_p &= k_p\end{aligned} \tag{2.54}$$

where m_p and k_p are respectively the modal mass and the modal stiffness of mode $\boldsymbol{\phi_p}$ and $^{\mathrm{T}}$ indicates the transpose. The orthogonality properties of the undamped mode shapes can be summarised by the two equations

$$\begin{aligned}\boldsymbol{\Phi}^{\mathrm{T}}\mathbf{M}\boldsymbol{\Phi} &= \mathrm{diag}(m_1, \dots, m_n)\\ \boldsymbol{\Phi}^{\mathrm{T}}\mathbf{K}\boldsymbol{\Phi} &= \mathrm{diag}(k_1, \dots, k_n)\end{aligned} \tag{2.55}$$

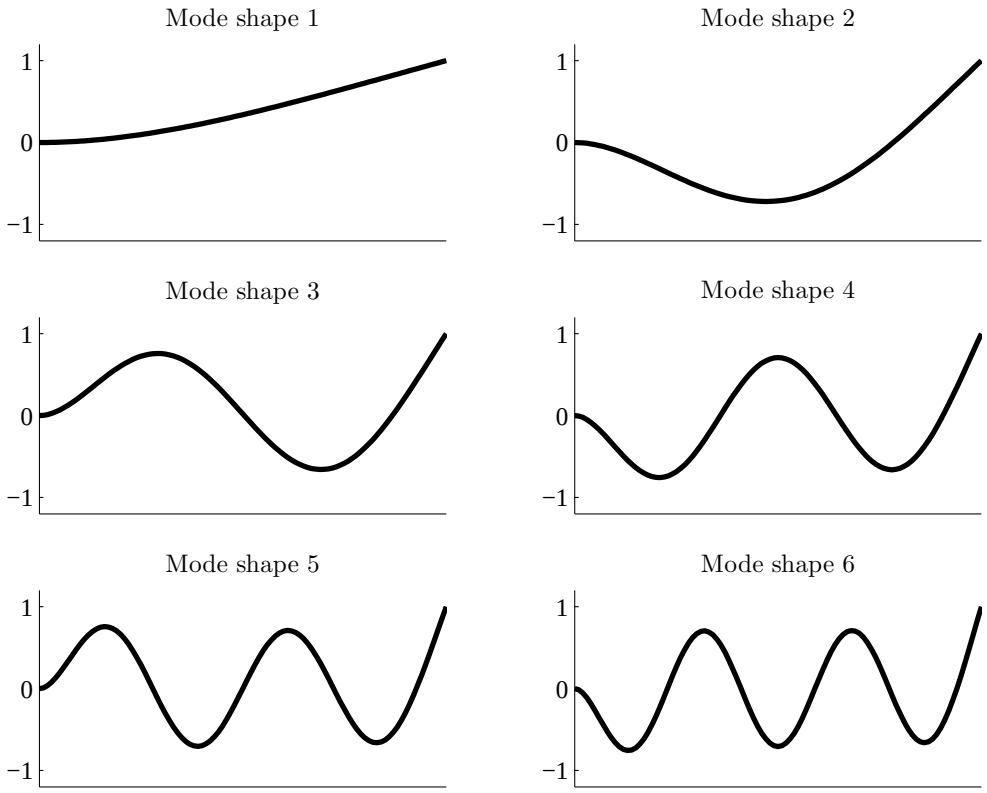

Figure 2.15: Mode shapes of a cantilever beam

where diag() indicates a matrix $\in \mathbb{R}^{n\times n}$ with the modal quantities on the diagonal and zero elsewhere. These orthogonality properties are important since they allow the uncoupling of the equations of motion so that they can be solved as n uncoupled SDOF equations. A common way to normalize the eigenvectors is

$$\begin{aligned} \tilde{\mathbf{\Phi}}^{\mathrm{T}}\mathbf{M}\tilde{\mathbf{\Phi}} &= \mathbf{I} \\ \tilde{\mathbf{\Phi}}^{\mathrm{T}}\mathbf{K}\tilde{\mathbf{\Phi}} &= \mathrm{diag}(\omega_1^2, \ldots, \omega_n^2) \end{aligned} \tag{2.56}$$

where $\tilde{\mathbf{\Phi}}$ is now the mass-normalised modal matrix and $\mathbf{I}$ is the identity matrix. To uncouple the equations of motion, define the coordinate transformation

$$\mathbf{x}(t) = \tilde{\mathbf{\Phi}}\mathbf{u}(t) \tag{2.57}$$

where $\mathbf{u}(t)$ is the vector of modal coordinates. Substituting eq.(2.57) into eq.(2.48), premultiplying by $\tilde{\mathbf{\Phi}}^{\mathrm{T}}$, using the orthogonality properties and considering the free vibration

$$\ddot{\mathbf{u}}(t) + \mathbf{\Omega}^2\mathbf{u}(t) = 0 \tag{2.58}$$

where $\mathbf{\Omega}$ is defined as

$$\mathbf{\Omega} = \mathrm{diag}(\omega_1, \ldots, \omega_n) \tag{2.59}$$

obtaining n uncoupled SDOF equations for each modal coordinate u_p in the form

$$\ddot{u}_p(t) + \omega_p^2 u_p(t) = 0 \tag{2.60}$$

Natural frequencies, mode shapes and orthogonality properties represent the basis of *modal analysis* which is at the present time one of the most powerful tools in vibration engineering.

2.3.2 Viscously damped systems

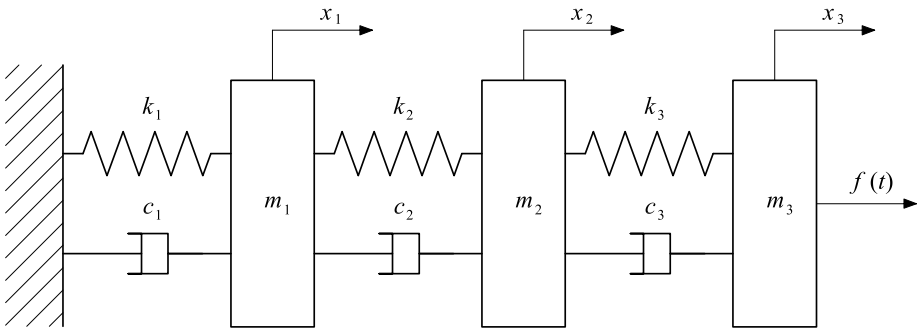

Figure 2.16: Viscously damped multi degree-of-freedom system

Considering the system in figure 2.16, the equations of motion become

$$\begin{aligned}
&m_1\ddot{x}_1 + (k_1 + k_2)x_1 + (c_1 + c_2)\dot{x}_1 - k_2 x_2 - c_2\dot{x}_2 = 0 \\
&m_2\ddot{x}_2 - k_2 x_1 - c_2\dot{x}_1 + (k_2 + k_3)x_2 + (c_2 + c_3)\dot{x}_2 - k_3 x_3 - c_3\dot{x}_3 = 0 \\
&m_3\ddot{x}_3 - k_3 x_2 - c_3\dot{x}_2 + k_3 x_3 + c_3\dot{x}_3 = f
\end{aligned} \tag{2.61}$$

which can be written in the matrix form

$$\mathbf{M}\ddot{\mathbf{x}}(t) + \mathbf{C}\dot{\mathbf{x}}(t) + \mathbf{K}\mathbf{x}(t) = \mathbf{f}(t) \tag{2.62}$$

where $\dot{\mathbf{x}}(t) \in \mathbb{R}^{n\times 1}$ represents the vector of velocities and $\mathbf{C} \in \mathbb{R}^{n\times n}$ is the viscous damping matrix. In this example

$$\mathbf{C} = \begin{bmatrix} c_1 + c_2 & -c_2 & 0 \\ -c_2 & c_2 + c_3 & -c_3 \\ 0 & -c_3 & c_3 \end{bmatrix} \qquad \dot{\mathbf{x}}(t) = \begin{Bmatrix} \dot{x}_1(t) \\ \dot{x}_2(t) \\ \dot{x}_3(t) \end{Bmatrix}$$

The viscous damping matrix is symmetric and non-negative definite. Considering the free vibration

$$\mathbf{M}\ddot{\mathbf{x}}(t) + \mathbf{C}\dot{\mathbf{x}}(t) + \mathbf{K}\mathbf{x}(t) = 0 \tag{2.63}$$

the solution [44] can be found in the form

$$\mathbf{x}(t) = \mathbf{x_0}e^{st} \tag{2.64}$$

The dynamics of the system is governed by the second-order matrix pencil $P(s)$ as

$$P(s) = \mathbf{M}s^2 + \mathbf{C}s + \mathbf{K} \tag{2.65}$$

the eigenvalues and eigenvectors of which satisfy

$$P(\lambda_p)\boldsymbol{\psi}_p = 0 \tag{2.66}$$

or

$$(\mathbf{M}\lambda_p^2 + \mathbf{C}\lambda_p + \mathbf{K})\boldsymbol{\psi}_p = 0 \tag{2.67}$$

This is a complex eigenproblem so the solution is usually found using a different approach. Adding the equation

$$\mathbf{M}\dot{\mathbf{x}}(t) - \mathbf{M}\dot{\mathbf{x}}(t) = 0 \tag{2.68}$$

to eq.(2.63) and using the symmetric state-space arrangement [67] by defining

$$\mathbf{A} = \begin{bmatrix} \mathbf{0} & \mathbf{M} \\ \mathbf{M} & \mathbf{C} \end{bmatrix} \qquad \mathbf{B} = \begin{bmatrix} -\mathbf{M} & \mathbf{0} \\ \mathbf{0} & \mathbf{K} \end{bmatrix} \qquad \mathbf{y}(t) = \begin{Bmatrix} \dot{\mathbf{x}}(t) \\ \mathbf{x}(t) \end{Bmatrix}$$

where $\mathbf{A}$ and $\mathbf{B} \in \mathbb{R}^{2n\times 2n}$ and $\mathbf{y}(t) \in \mathbb{R}^{2n\times 1}$, another matrix equation is obtained

$$\mathbf{A}\dot{\mathbf{y}}(t) + \mathbf{B}\mathbf{y}(t) = 0 \tag{2.69}$$

The size of the problem is doubled but eq.(2.69) is a first order differential equation leading to a simpler eigenvalue problem

$$(\mathbf{A}\lambda + \mathbf{B})\mathbf{y_0} = 0 \tag{2.70}$$

The eigenvalues λ_p and the eigenvectors $\boldsymbol{\xi}_\mathbf{p} \in \mathbb{C}^{2n\times 1}$ of eq.(2.70) are generally complex quantities and they are related to the eigenvectors $\boldsymbol{\psi}_\mathbf{p} \in \mathbb{C}^{n\times 1}$ of eq.(2.66) by

$$\boldsymbol{\xi}_p = \begin{Bmatrix} \boldsymbol{\psi}_p\lambda_p \\ \boldsymbol{\psi}_p \end{Bmatrix} \tag{2.71}$$

In case of underdamped systems, the eigenvectors of eq.(2.70) appear in complex conjugate pairs and so do the eigenvalues, so that

$$\boldsymbol{\xi}_p^* = \left\{ \begin{array}{c} \boldsymbol{\psi}_p^* \lambda_p^* \\ \boldsymbol{\psi}_p^* \end{array} \right\} \tag{2.72}$$

where * indicates the complex conjugate, is also an eigenvector of the problem. The eigenvectors still have orthogonality properties as in the undamped case but with respect to the matrices $\mathbf{A}$ and $\mathbf{B}$. If the state-space modal matrix $\boldsymbol{\Xi}$ is defined as

$$\boldsymbol{\Xi} = [\boldsymbol{\xi}_1 \;\; \boldsymbol{\xi}_2 \;\; \ldots \;\; \boldsymbol{\xi}_{2n}] \tag{2.73}$$

and the coordinate transformation as

$$\mathbf{y}(t) = \boldsymbol{\Xi}\mathbf{u}(t) \tag{2.74}$$

the orthogonality properties can be expressed by

$$\begin{aligned} \boldsymbol{\Xi}^{\mathrm{T}}\mathbf{A}\boldsymbol{\Xi} &= \mathrm{diag}(a_1, \ldots, a_{2n}) \\ \boldsymbol{\Xi}^{\mathrm{T}}\mathbf{B}\boldsymbol{\Xi} &= \mathrm{diag}(b_1, \ldots, b_{2n}) \end{aligned} \tag{2.75}$$

where a_p and $b_p \in \mathbb{C}$, leading to $2n$ SDOF equations for each modal coordinate u_p in the form

$$a_p \dot{u}_p(t) + b_p u_p(t) = 0 \tag{2.76}$$

whose solution can be found in the form

$$u_p(t) = \bar{u}_p e^{\lambda_p t} \tag{2.77}$$

where

$$\lambda_p = -\frac{b_p}{a_p} \tag{2.78}$$

and $\bar{u}_p$ represents the amplitude of the modal coordinate and depends on the initial conditions. The free vibration response can be calculated considering the separate contributions of each mode as

$$\mathbf{u}(t) = \sum_{p=1}^{2n} \boldsymbol{\xi}_p \bar{u}_p e^{\lambda_p t} \tag{2.79}$$

Taking as analogy the SDOF case, each eigenvalue λ_p can be written in the form

$$\lambda_p = -\omega_p \zeta_p \pm i\omega_p \sqrt{1 - \zeta_p^2} \tag{2.80}$$

which allows the calculation of the modal damping ratio of each mode by

$$\zeta_p = \frac{-\Re(\lambda_p)}{|\lambda_p|} \tag{2.81}$$

From an engineering point of view, the state-space analysis presents several drawbacks when compared to the classical modal analysis used for the undamped system. The doubled size of the eigenvalue problem results, especially in the case of large structure, in high computational effort to solve it; the physical meaning of complex mode shapes is less straightforward than the classical normal modes. Plots like figure 2.15 are meaningless for the damped system, since the complex nature of eigenvectors introduces a phase shift which causes the maximum displacement for each DOF to be reached at different instants [44] so that a static mode shape is not representative of the dynamic behaviour and an animated mode shape is required. In order to apply classic modal analysis to damped systems, the modal matrix $\mathbf{\Psi}$ of the eigenproblem in eq.(2.66) should be real and able to diagonalise simultaneously $\mathbf{M}$, $\mathbf{K}$ and $\mathbf{C}$. The real eigenvectors obtained from the undamped system do not necessarily diagonalize the damping matrix, i.e. $\mathbf{\Phi}^{\mathrm{T}}\mathbf{C}\mathbf{\Phi}$ does not yield a diagonal matrix. The additional coupling due to damping does not allow a direct use of the modal analysis theory to the damped system unless approximations or constraints on the viscous damping matrix are introduced. A common procedure, when damping is considered small, simply consists in neglecting the off-diagonal terms of $\mathbf{\Phi}^{\mathrm{T}}\mathbf{C}\mathbf{\Phi}$, known as the decoupling approximation [56]. Several studies were focused on understanding the effects of this approximation on the dynamic behaviour [68, 69] and on the best way for obtaining the optimal diagonal matrix from the non-diagonal matrix [70].

A different strategy can be applied to the normalization of the mode shapes measured in real experiments, since it causes a transfer of information between the real and imaginary parts of eigenvectors. Ibrahim and Sestieri [71] proposed a way to normalize the eigenvectors so that the real part holds most of the information; by doing so, the error produced by using the real part of the mode shape in place of the full complex mode shape is minimized. The normalization is obtained using the equations

$$\mathbf{\Psi}^{\mathrm{T}}\mathbf{M}\mathbf{\Psi}\mathbf{\Lambda} + \mathbf{\Lambda}\mathbf{\Psi}^{\mathrm{T}}\mathbf{M}\mathbf{\Psi} + \mathbf{\Psi}^{\mathrm{T}}\mathbf{C}\mathbf{\Psi} = 2i\mathbf{\Lambda}_I \tag{2.82}$$

and

$$\mathbf{\Lambda \Psi}^{\mathrm{T}}\mathbf{M\Psi\Lambda} + \mathbf{\Psi}^{\mathrm{T}}\mathbf{K\Psi} = 2i\mathbf{\Lambda}_I\mathbf{\Lambda} \tag{2.83}$$

where $\mathbf{\Lambda}$ is defined as

$$\mathbf{\Lambda} = \mathrm{diag}(\lambda_1, \ldots, \lambda_n) = \mathbf{\Lambda}_R + i\mathbf{\Lambda}_I \tag{2.84}$$

and $\mathbf{\Lambda_R}$ and $\mathbf{\Lambda_I}$ respectively represent the real and imaginary part of $\mathbf{\Lambda}$. This normalization can be useful, for example, in the identification of the real modes of an undamped FEM model associated with the complex modes of experiments. The classical approach, however, is to select a damping matrix $\mathbf{C}$ which is diagonalisable by the normal modes of the undamped system.

Classical viscous damping

Lord Rayleigh [9] introduced proportional damping (or Rayleigh damping) in order to apply the concept of classical modal analysis of undamped systems to damped systems. The damping matrix is assumed to be proportional to the stiffness and mass matrix and becomes

$$\mathbf{C} = \alpha\mathbf{K} + \beta\mathbf{M} \tag{2.85}$$

where α and β are constants. From a physical point of view there are no reasons for the damping matrix to have this kind of relation with the other two matrices, but from a mathematical point of view this formulation offers two important advantages: the mode shapes are always real and they uncouple the equations of motion by simultaneously diagonalizing the three matrices $\mathbf{M}$, $\mathbf{C}$ and $\mathbf{K}$. By substituting eq.(2.85) into eq.(2.63) using the coordinate transformation (2.57), previously applied to the undamped system, and premultiplying by $\tilde{\mathbf{\Phi}}^{\mathrm{T}}$

$$\tilde{\mathbf{\Phi}}^{\mathrm{T}}\mathbf{M}\tilde{\mathbf{\Phi}}\ddot{\mathbf{u}}(t) + \tilde{\mathbf{\Phi}}^{\mathrm{T}}\left(\alpha\mathbf{K} + \beta\mathbf{M}\right)\tilde{\mathbf{\Phi}}\dot{\mathbf{u}}(t) + \tilde{\mathbf{\Phi}}^{\mathrm{T}}\mathbf{K}\tilde{\mathbf{\Phi}}\mathbf{u}(t) = 0 \tag{2.86}$$

remembering the normalization (2.56)

$$\ddot{\mathbf{u}}(t) + \mathrm{diag}(\alpha\omega_1^2 + \beta, \ldots, \alpha\omega_n^2 + \beta)\dot{\mathbf{u}}(t) + \mathrm{diag}(\omega_1^2, \ldots, \omega_n^2)\mathbf{u}(t) = 0 \tag{2.87}$$

leading to n uncoupled equations

$$\ddot{u}_p(t) + (\alpha\omega_p^2 + \beta)\dot{u}_p(t) + \omega_p^2 u(t) = 0 \tag{2.88}$$

By analogy with eq.(2.15) for the viscously damped SDOF system, it is possible to write eq.(2.88) in the form

$$\ddot{u}_p(t) + 2\zeta_p\omega_p\dot{x}_p(t) + {\omega_p}^2 u_p(t) = 0 \tag{2.89}$$

where ζ_p is the modal damping ratio of mode p

$$\zeta_p = \frac{\alpha\omega_p}{2} + \frac{\beta}{2\omega_p} \tag{2.90}$$

Using this formulation, each mode can be studied separately from the other ones as a simple SDOF system. Proportional damping is widely used in simulations since it is computationally efficient and it reduces the number of identification parameters for the damping matrix to two (α and β) in inverse problems. Proportional damping is only a special case of classical viscous damping. Necessary and sufficient conditions for a viscously damped linear system to possess classical normal modes were established by Caughey [72] and Caughey and O'Kelly [73] and can be expressed by the equation

$$\mathbf{K}\mathbf{M}^{-1}\mathbf{C} = \mathbf{C}\mathbf{M}^{-1}\mathbf{K} \tag{2.91}$$

Unfortunately, real systems normally possess complex modes so proportional damping, despite the unquestionable advantages just mentioned, is not always accurate enough to represent damping in certain applications. Different strategies were developed in order to obtain forms of damping which allow complex modes but are still affordable from a computational point of view. Link [74] proposed an interesting parameterisation applied to model updating. His idea is to use a proportional damping matrix for each substructure, reducing considerably the number of parameters compared to a fully populated viscous matrix, and then assemble the global damping matrices as

$$\mathbf{C} = \sum_{i}^{q} \alpha_i \mathbf{K_i} + \sum_{i}^{q} \beta_i \mathbf{M_i} \tag{2.92}$$

where q is the number of substructures considered and $\mathbf{M_i}$ and $\mathbf{K_i}$ are the mass and stiffness matrices of the i^{th} substructure. In this way the updating parameters are reduced to $2q$ and the global viscous matrix $\mathbf{C}$ is not classical and can possess complex modes.

Effect of viscous damping on the FRF

The FRF of a MDOF system subjected to a harmonic input force can be calculated by

$$\mathbf{H}(\omega) = \left[\mathbf{K} + i\omega\mathbf{C} - \omega^2\mathbf{M}\right]^{-1} \tag{2.93}$$

where $\mathbf{H}(\omega) \in \mathbb{C}^{n\times n}$ is the receptance matrix of the system. The element $H_{p,q}$

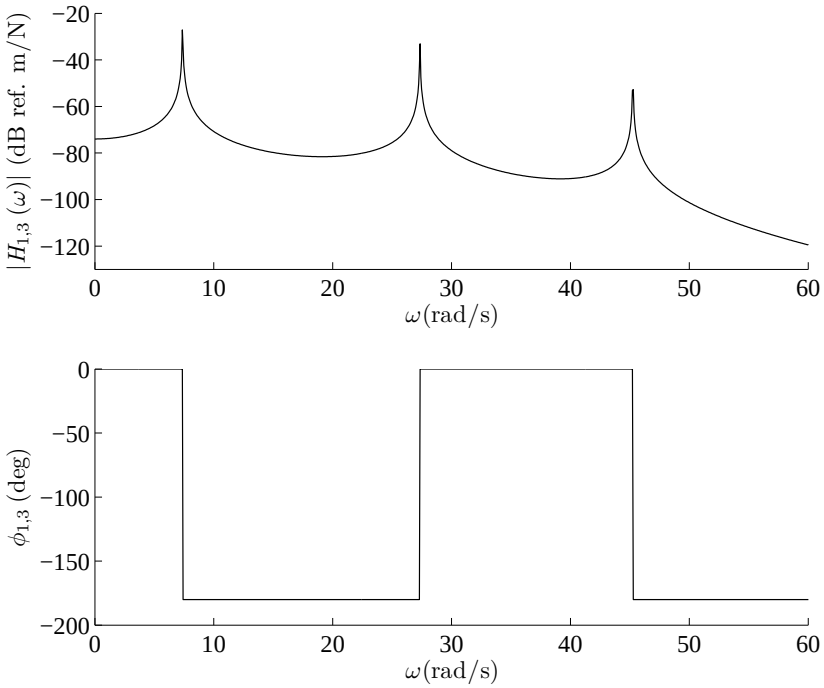

Figure 2.17: Receptance of an undamped MDOF system. $m_1 = 3$ kg, $m_2 = 5$ kg, $m_3 = 8$ kg, $k_1 = 5000$ N/m, $k_2 = 2000$ N/m, $k_3 = 1000$ N/m.

of the receptance matrix represents the response of the system at the degree of freedom p when the system is excited at the degree of freedom q. The amplitude and phase of the receptance $H_{1,3}$ of the undamped system in figure 2.14 are displayed in figure 2.17. The three peaks in the amplitude plot correspond to the three natural frequencies of the system, where a 180° phase shift occurs as for the SDOF system. Depending on the location and on the type of damping, the effect on the FRF can be different for each mode. For example, in figure 2.18 the effect of adding a viscous dashpot between DOF 1 and DOF 2 (figure 2.16) with three different damping coefficient is shown. The dashpot in this particular location does not seem to affect too much mode 1 and mode 2 whereas it seems

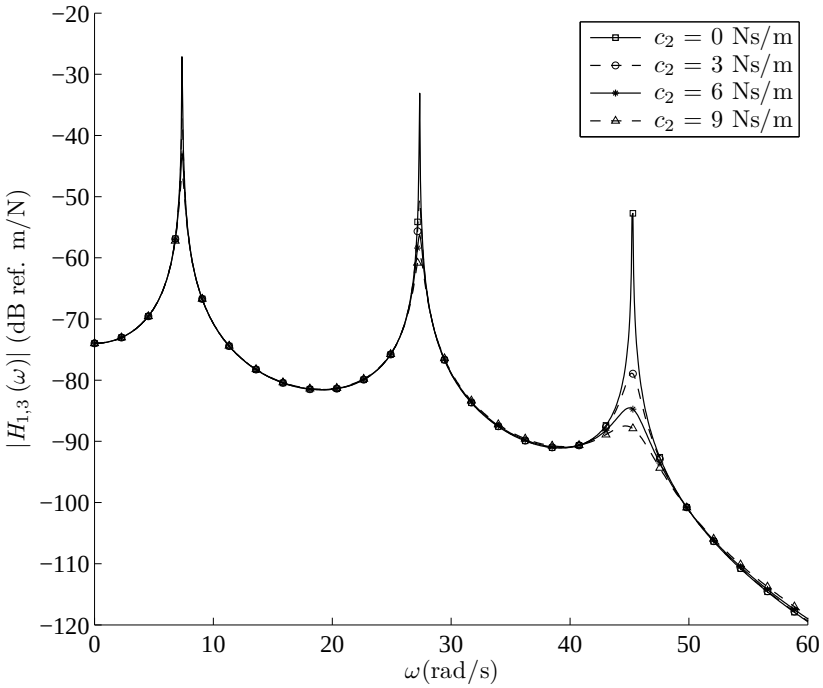

Figure 2.18: Receptance of a viscously damped system varying c_2. $m_1 = 3$ kg, $m_2 = 5$ kg, $m_3 = 8$ kg, $k_1 = 5000$ N/m, $k_2 = 2000$ N/m, $k_3 = 1000$ N/m.

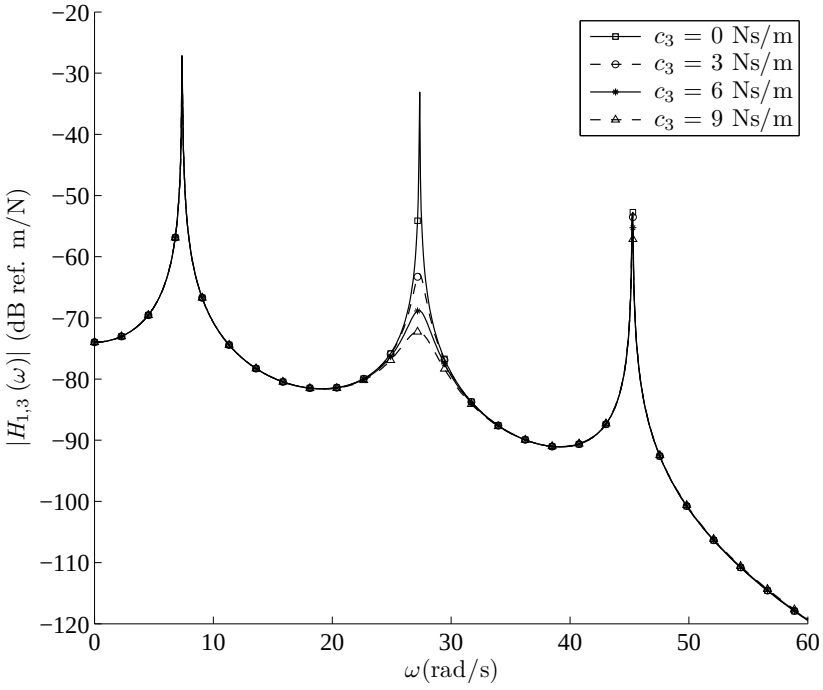

Figure 2.19: Receptance of a viscously damped system varying c_3. $m_1 = 3$ kg, $m_2 = 5$ kg, $m_3 = 8$ kg, $k_1 = 5000$ N/m, $k_2 = 2000$ N/m, $k_3 = 1000$ N/m.

to be very important for the amplitude of the response at frequencies close to the natural frequency of mode 3. Figure 2.19 shows the effect of adding a viscous dashpot between DOF 2 and DOF 3. In this case, mode 1 and mode 3 seems unaffected whereas mode 2 is highly affected by the dashpot. The same results can be obtained by comparing the values of the modal damping ratios calculated using eq.(2.81). Considering the most damped configuration in figure 2.19, with $c_1 = 0$ Ns/m, $c_2 = 0$ Ns/m and $c_3 = 9$ Ns/m, we obtain the modal damping ratios for the three modes respectively $\zeta_1 = 0.0028$, $\zeta_2 = 0.0571$ and $\zeta_3 = 0.0009$ confirming that the second mode is the most affected by the dashpot in DOF 3. These results can be justified by looking at the mode shapes of the system, since the viscous damping force is proportional to the relative velocities between the DOFs where the dashpot is connected. If the dashpot is located between two DOFs which do not have relative displacement for a particular mode shape, it will not dissipate any energy so the effect on the FRF at the frequency of that mode will be very small.

2.4 Closure

The basic notions on modal analysis and on the effect of damping in vibrations have been provided in order to give the necessary grounding for a better understanding of the rest of the dissertation. In the next chapter, some modal damping and SDOF identification techniques are explained and a literature review of the main MDOF damping identification techniques is presented, with some critical observations on aspects of the philosophy and performance of different approaches.

Chapter 3

Damping identification

3.1 The inverse problem

Damping identification is a typical engineering inverse problem. The aim is to use the information collected by experiments in order to infer the values of the parameters of the model characterizing the system under investigation. This kind of problems can be very difficult to solve for many reasons; firstly, the identified model parameters could be wrong or insufficiently detailed, resulting in meaningless values which cannot be used to represent the real system in simulations. Secondly, the inverse problem can be underdetermined, so that different values for the parameters could be consistent with the data but not necessarily with the physical system. The inverse problem could also be overdetermined, so that a least squares approximation would be necessary and the parameters identified by the solution are a sort of equivalent average of the values of the real system under certain conditions.

Given the complexity of the damping mechanism listed in chapter 1, the methods considered have been restricted to linear damping models and specifically viscous damping. However, some of the analysed methods are capable of identifying other kinds of linear and non-linear damping too. The techniques presented in this chapter can be divided into two main categories: the identification of modal damping, which estimates the values of the damping ratio ζ for each mode or the loss factor η, and the spatial identification of damping, which aims to identify the location and the value of the coefficients of the damping matrix. In this thesis the main interest is in the location and the identification of the main sources of damping in a MDOF system, so most of the work has been done on the spatial

identification. In engineering problems, however, the value of ζ is often sufficient for the analysis of most structures, especially when the damping is considered light.

In this chapter, after a short description of some modal damping and SDOF identification techniques, a literature review of the main MDOF damping identification techniques is presented, with some critical observations on some aspects of the philosophy and performance of different approaches.

3.2 SDOF and modal identification

The identification of damping in SDOF systems can be performed in several different ways; the most famous are the logarithmic decrement method and the half-power bandwidth method which are used to identify the damping ratio ζ or the loss factor η. Other methods include the energy method, whose modification leads to the MDOF improved method proposed in chapter 4, and the estimation of damping from the Nyquist plot and from the hysteresis loop as already mentioned in chapter 2. All these method can be adapted to the identification of the modal damping ratio in MDOF systems when the modes are well separated and can be treated as separate SDOF systems.

3.2.1 Logarithmic decrement

The logarithmic decrement technique is based on the measurement of the rate of decay of free oscillations [46]. Starting from the general solution of eq. (2.11), given by

$$x(t) = a_1 e^{s_1 t} + a_2 e^{s_2 t} \tag{3.1}$$

where a_1 and a_2 are constants determined by the initial conditions, and remembering eq. (2.16), the solution can be written in the form

$$x(t) = e^{-\omega_n \zeta t} \left(a_1 e^{i\omega_n t\sqrt{1-\zeta^2}} + a_2 e^{-i\omega_n t\sqrt{1-\zeta^2}} \right) \tag{3.2}$$

or

$$x(t) = x_0 e^{-\omega_n \zeta t} \sin\left(\omega_n t\sqrt{1-\zeta^2} + \phi \right) \tag{3.3}$$

The logarithmic decrement δ is defined as

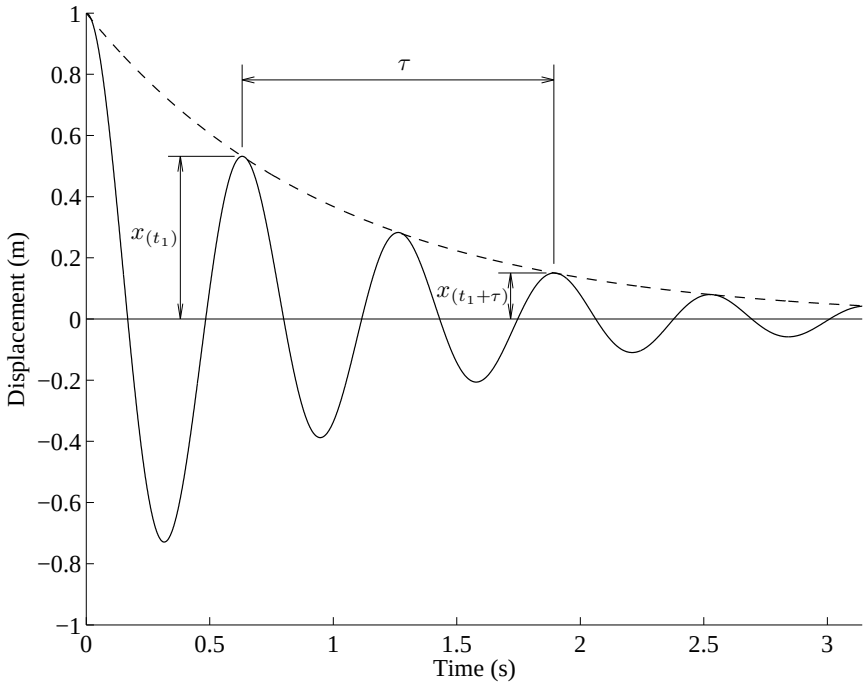

Figure 3.1: Free vibration response. $\zeta = 0.2$.

$$\delta = \ln \frac{x(t_1)}{x(t_1 + \tau)} \tag{3.4}$$

where $x(t_1)$ is the amplitude of the peak of the free vibration at a certain instant t_1 and τ is an integer multiple of the damped period τ_d defined as

$$\tau_d = \frac{2\pi}{\omega_d} = \frac{2\pi}{\omega_n \sqrt{1 - \zeta^2}} \tag{3.5}$$

The values of $x(t_1)$ and $x(t_1 + \tau)$ can be easily extracted from the plot of a simple free vibration test as in figure 3.1 and δ can be directly estimated. Assuming $\tau = n\tau_d$, where n is an integer, and substituting eq. (3.3) into eq. (3.4) the expression for the logarithmic decrement becomes

$$\delta = \ln \frac{e^{-\omega_n \zeta t_1} \sin\left(\omega_n t_1 \sqrt{1 - \zeta^2} + \phi\right)}{e^{-\omega_n \zeta (t_1 + n\tau_d)} \sin\left(\omega_n (t_1 + n\tau_d) \sqrt{1 - \zeta^2} + \phi\right)} \tag{3.6}$$

The values of the sines are equal after each period τ_d, then

$$\delta = \ln \frac{e^{-\omega_n \zeta t_1}}{e^{-\omega_n \zeta (t_1 + n\tau_d)}} = \zeta \omega_n n \tau_d \tag{3.7}$$

Substituting eq. (3.5) into eq. (3.7) leads to

$$\delta = \frac{2n\pi\zeta}{\sqrt{1 - \zeta^2}} \tag{3.8}$$

which can be used to estimate the value of ζ knowing n and δ. For lightly damped systems, eq. (3.8) is often simplified as

$$\delta = 2n\pi\zeta \tag{3.9}$$

so that the damping ratio is simply obtained by

$$\zeta = \frac{\delta}{2n\pi} \tag{3.10}$$

3.2.2 Half-power bandwidth method

The half-power bandwidth method is based on the data obtainable from the plot of the FRF of a SDOF system, but it can be used in MDOF systems too, provided that the modes are well separated in the FRF plot. Theoretically, the value of damping could be extracted directly from the receptance plot without using the half-power bandwidth method [44]; defining the amplification factor Q for the SDOF system as

$$Q = \frac{x_0}{x_s} \tag{3.11}$$

where x_0 is the amplitude of the displacement under dynamic load and x_s is the amplitude of the displacement under static load, equal to f_0/k. From the definition of receptance

$$|h(\omega)| = \frac{Q}{k} \tag{3.12}$$

which leads to

$$\log(Q) = \log|h(\omega)| - \log\left(\frac{1}{k}\right) \tag{3.13}$$

The amplification factor Q on the FRF is represented by the distance between a point of the FRF and the horizontal stiffness line. If the value of Q_{max} at resonance can be measured and the damping is light, the value of the damping ratio ζ can be derived directly from

$$\log(Q_{max}) = \log\left(\frac{1}{2k\zeta}\right) - \log\left(\frac{1}{k}\right) = -\log(2\zeta) \tag{3.14}$$

or

$$Q_{max} = \frac{1}{2\zeta} \tag{3.15}$$

Unfortunately, the precise value of the resonance peak amplitude is very difficult to measure so the half-power bandwidth method is usually preferred. As

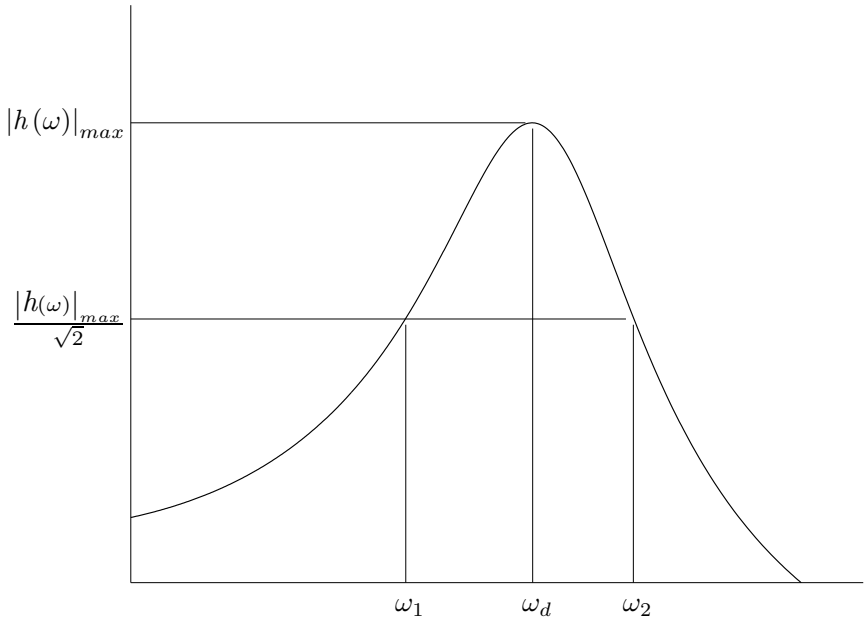

Figure 3.2: Half power points definition

previously stated damping is mainly effective at the resonance frequency, but also in the proximity where the amplitude is easier to measure. Consider a hysteretically damped SDOF system under steady-state harmonic vibration [44], the energy dissipated per cycle of oscillation at resonance is

$$E_{d(max)} = \pi x_{0(max)}^2 k\eta = \pi \left|h(\omega)\right|_{max}^2 f_0 k\eta \tag{3.16}$$

the half-power points are defined at frequencies where the energy dissipated per cycle is half of the maximum energy dissipated at the resonance frequency ω_d. Since the energy is proportional to the square power of the amplitude of the receptance, the half-power frequencies are found where

$$\left|h(\omega)\right|_{1,2} = \frac{|h(\omega)|_{max}}{\sqrt{2}} \tag{3.17}$$

and are indicated with ω_1 and ω_2. It can be demonstrated [45] that the loss factor can be calculated by

$$\eta = \frac{\omega_2^2 - \omega_1^2}{2\omega_d} \tag{3.18}$$

Recalling eq. (2.40), at resonance it is possible to write

$$\zeta \approx \frac{\omega_2^2 - \omega_1^2}{4\omega_d} \tag{3.19}$$

since the peak at resonance down to the half-power points is quite symmetric, a reasonable approximation is to consider

$$\omega_2 + \omega_1 \approx 2\omega_d \tag{3.20}$$

and therefore the damping ratio ζ can be calculated as

$$\zeta \approx \frac{\omega_2 - \omega_1}{2\omega_d} \tag{3.21}$$

3.2.3 Energy-dissipation method

The energy-dissipation method or energy-balance method in SDOF was proposed and experimentally validated by Liang and Feeny [75] in 2006. The method is based on the balance between the energy input by an external force and the energy dissipated by damping and results in the "equivalent viscous and Coulomb damping" parameters identification. Consider the SDOF system

$$m\ddot{x} + kx + d(x, \dot{x}, \ddot{x}) = f(t) \tag{3.22}$$

where $d(x, \dot{x}, \ddot{x})$ represents a generic damping function of displacements, velocities and accelerations. The energy-balance equation is obtained by an integration along a motion path C as

$$\int_C \left(m\ddot{x} + kx + d(x, \dot{x}, \ddot{x})\right) \mathrm{d}x = \int_C f(t)\mathrm{d}x \tag{3.23}$$

or, changing the integration variable to time

$$\int_t^{t+T_1} \left(m\ddot{x} + kx + d(x, \dot{x}, \ddot{x})\right) \dot{x}\mathrm{d}t = \int_t^{t+T_1} f(t)\dot{x}\mathrm{d}t \tag{3.24}$$

where T_1 is a finite time interval. Defining

$$\begin{aligned} E_c &= \int_t^{t+T_1} \left(m\ddot{x} + kx\right) \dot{x}\mathrm{d}t \\ E_d &= \int_t^{t+T_1} d(x, \dot{x}, \ddot{x})\dot{x}\mathrm{d}t \\ E_f &= \int_t^{t+T_1} f(t)\dot{x}\mathrm{d}t \end{aligned} \tag{3.25}$$

where E_c is the energy contribution of the conservative components of the system, E_d is the energy dissipated by damping and E_f is the energy input by the external force $f(t)$. Eq. (3.24) can be now expressed as

$$E_d = E_f - E_c \tag{3.26}$$

In case of a periodic excitation $f(t)$ and a response $x(t)$ of the same period T, if the integration is performed over a cycle of periodic motion or an integer multiple of that period, E_c is equal to zero from the definition of conservative force. The energy-balance equation in this case becomes

$$\int_0^T d(x, \dot{x}, \ddot{x})\dot{x}\mathrm{d}t = \int_0^T f(t)\dot{x}\mathrm{d}t \tag{3.27}$$

which represents the base of the identification method: the energy dissipated by damping in a cycle of periodic motion equals the energy input by the external force. Viscous damping is a special case where

$$d(x, \dot{x}, \ddot{x}) = c\dot{x} \tag{3.28}$$

In this case, eq. (3.27) is reduced to

$$c\int_0^T \dot{x}^2\mathrm{d}t = \int_0^T f(t)\dot{x}\mathrm{d}t \tag{3.29}$$

By measuring the input force and the response, the viscous damping coefficient c can be estimated by

$$c = \frac{\int_0^T f(t)\dot{x}\mathrm{d}t}{\int_0^T \dot{x}^2\mathrm{d}t} \tag{3.30}$$

In order to obtain the "equivalent viscous and Coulomb damping" parameters, Liang and Feeny [75] apply this method to a system with a damping function of the type

$$d(x, \dot{x}, \ddot{x}) = c\dot{x} + \mu F_n \mathrm{sgn}(\dot{x}) \tag{3.31}$$

so that the energy equation becomes

$$c\int_0^T \dot{x}^2\mathrm{d}t + \mu F_n \int_0^T \mathrm{sgn}(\dot{x})\dot{x}\mathrm{d}t = \int_0^T f(t)\dot{x}\mathrm{d}t \tag{3.32}$$

In order to identify the two parameters (c and the product μF_n), at least two different excitations are necessary. Multiple tests measurements will lead to a least-squares version of eq. (3.32) which provides the equivalent parameters which are representative of the system in the frequency range and force amplitude used in the tests. A more detailed study of this method will be given in chapter 4 leading to the improved MDOF method proposed.

3.2.4 Other methods

Besides the three techniques just described, there is a large amount of literature on the identification of damping in SDOF systems or modal damping ratios. It has already been mentioned how to extract information about damping from the Nyquist plot and from the hysteresis loop; other techniques, which will not be treated in this dissertation, include different methods based on free decay vibrations measurements [76, 77], other energy-related methods [78] and method based on modulations of responses [79] and wavelets [80, 81, 82]. The present study is more concerned with the spatial identification of damping in MDOF systems rather than the damping ratio identification; the next section presents a summary of the main MDOF damping identification techniques.

3.3 MDOF spatial identification

There are several MDOF damping identification methods available in literature, each of them has its own advantages and drawbacks. Regarding linear viscous damping identification, the methods can be classified into three main groups depending on the input data used: methods based on the FRF matrix, methods based on modal parameters (frequencies and mode shapes) and methods based on time histories.

There are review papers which present surveys on the existing methods to identify the linear viscous damping matrix. Srikantha Phani and Woodhouse have compared the performance of a number of specific identification routines using a numerical simulation [83] and an experiment [84]. In particular, they try to determine which are the best methods for a given vibration measurements from

a test structure, what is the sensitivity of the damping identification methods to noise and truncation and what is the influence of modal and spatial incompleteness of data. The study is performed by comparing indices based on numerical accuracy and spatial distribution. Prandina *et al.* [85] concentrated particularly on the philosophy of the methods and not so much with the performance of particular implementations and routines; important considerations are focussed on the effects of modal truncation which is an inevitable consequence of modal testing over a limited frequency range. Pilkey and Inman [86] listed and explained the main features of a number of different methods showing the theories of the different approaches.

3.3.1 Preliminary calculations

Before starting the literature review, some calculations are presented in order to draw conclusions in the next sections. Recalling the eigenproblem of the damped MDOF system in eq. (2.66), the eigenvalues and eigenvectors forming self-conjugate sets can be arranged to form the spectral and modal matrices as

$$\begin{bmatrix} \mathbf{\Lambda} & \mathbf{0} \\ \mathbf{0} & \mathbf{\Lambda}^* \end{bmatrix} = \begin{bmatrix} \mathrm{diag}(\lambda_p) & \mathbf{0} \\ \mathbf{0} & \mathrm{diag}(\lambda_p^*) \end{bmatrix} \in \mathbb{C}^{2n\times 2n} \tag{3.33}$$

$$[\mathbf{\Psi}\ \mathbf{\Psi}^*] = [\boldsymbol{\psi}_1\ \ldots\ \boldsymbol{\psi}_n\ \boldsymbol{\psi}_1^*\ \ldots\ \boldsymbol{\psi}_n^*] \in \mathbb{C}^{n\times 2n} \tag{3.34}$$

Using the symmetric state-space arrangement [67] it can be shown that

$$\begin{bmatrix} \mathbf{\Lambda}\mathbf{\Psi}^{\mathrm{T}} & \mathbf{\Psi}^{\mathrm{T}} \\ \mathbf{\Lambda}^*\mathbf{\Psi}^{*\mathrm{T}} & \mathbf{\Psi}^{*\mathrm{T}} \end{bmatrix} \left(s \begin{bmatrix} \mathbf{0} & \mathbf{M} \\ \mathbf{M} & \mathbf{C} \end{bmatrix} + \begin{bmatrix} -\mathbf{M} & \mathbf{0} \\ \mathbf{0} & \mathbf{K} \end{bmatrix} \right) \begin{bmatrix} \mathbf{\Psi}\mathbf{\Lambda} & \mathbf{\Psi}^*\mathbf{\Lambda}^* \\ \mathbf{\Psi} & \mathbf{\Psi}^* \end{bmatrix} = \\ = \begin{bmatrix} s\mathbf{I} - \mathbf{\Lambda} & \mathbf{0} \\ \mathbf{0} & s\mathbf{I} - \mathbf{\Lambda}^* \end{bmatrix} \tag{3.35}$$

where $\mathbf{\Psi}$ is normalised so that

$$\begin{bmatrix} \mathbf{\Lambda}\mathbf{\Psi}^{\mathrm{T}} & \mathbf{\Psi}^{\mathrm{T}} \\ \mathbf{\Lambda}^*\mathbf{\Psi}^{*\mathrm{T}} & \mathbf{\Psi}^{*\mathrm{T}} \end{bmatrix} \begin{bmatrix} \mathbf{0} & \mathbf{M} \\ \mathbf{M} & \mathbf{C} \end{bmatrix} \begin{bmatrix} \mathbf{\Psi}\mathbf{\Lambda} & \mathbf{\Psi}^*\mathbf{\Lambda}^* \\ \mathbf{\Psi} & \mathbf{\Psi}^* \end{bmatrix} = \mathbf{I} \tag{3.36}$$

$$\begin{bmatrix} \mathbf{\Lambda}\mathbf{\Psi}^{\mathrm{T}} & \mathbf{\Psi}^{\mathrm{T}} \\ \mathbf{\Lambda}^*\mathbf{\Psi}^{*\mathrm{T}} & \mathbf{\Psi}^{*\mathrm{T}} \end{bmatrix} \begin{bmatrix} -\mathbf{M} & \mathbf{0} \\ \mathbf{0} & \mathbf{K} \end{bmatrix} \begin{bmatrix} \mathbf{\Psi}\mathbf{\Lambda} & \mathbf{\Psi}^*\mathbf{\Lambda}^* \\ \mathbf{\Psi} & \mathbf{\Psi}^* \end{bmatrix} = - \begin{bmatrix} \mathbf{\Lambda} & \mathbf{0} \\ \mathbf{0} & \mathbf{\Lambda}^* \end{bmatrix} \tag{3.37}$$

Expanding eqs.(3.36) and (3.37) leads to the orthogonality relationships given by Lancaster [87]

$$\begin{bmatrix} \boldsymbol{\Psi}^{\mathrm{T}} \\ \boldsymbol{\Psi}^{*\mathrm{T}} \end{bmatrix} \mathbf{M} \begin{bmatrix} \boldsymbol{\Psi} & \boldsymbol{\Psi}^{*} \end{bmatrix} \begin{bmatrix} \boldsymbol{\Lambda} & \mathbf{0} \\ \mathbf{0} & \boldsymbol{\Lambda}^{*} \end{bmatrix} + \begin{bmatrix} \boldsymbol{\Lambda} & \mathbf{0} \\ \mathbf{0} & \boldsymbol{\Lambda}^{*} \end{bmatrix} \begin{bmatrix} \boldsymbol{\Psi}^{\mathrm{T}} \\ \boldsymbol{\Psi}^{*\mathrm{T}} \end{bmatrix} \mathbf{M} \begin{bmatrix} \boldsymbol{\Psi} & \boldsymbol{\Psi}^{*} \end{bmatrix} + \\ + \begin{bmatrix} \boldsymbol{\Psi}^{\mathrm{T}} \\ \boldsymbol{\Psi}^{*\mathrm{T}} \end{bmatrix} \mathbf{C} \begin{bmatrix} \boldsymbol{\Psi} & \boldsymbol{\Psi}^{*} \end{bmatrix} = \mathbf{I} \tag{3.38}$$

$$- \begin{bmatrix} \boldsymbol{\Lambda} & \mathbf{0} \\ \mathbf{0} & \boldsymbol{\Lambda}^{*} \end{bmatrix} \begin{bmatrix} \boldsymbol{\Psi}^{\mathrm{T}} \\ \boldsymbol{\Psi}^{*\mathrm{T}} \end{bmatrix} \mathbf{M} \begin{bmatrix} \boldsymbol{\Psi} & \boldsymbol{\Psi}^{*} \end{bmatrix} \begin{bmatrix} \boldsymbol{\Lambda} & \mathbf{0} \\ \mathbf{0} & \boldsymbol{\Lambda}^{*} \end{bmatrix} + \begin{bmatrix} \boldsymbol{\Psi}^{\mathrm{T}} \\ \boldsymbol{\Psi}^{*\mathrm{T}} \end{bmatrix} \mathbf{K} \begin{bmatrix} \boldsymbol{\Psi} & \boldsymbol{\Psi}^{*} \end{bmatrix} = \\ = - \begin{bmatrix} \boldsymbol{\Lambda} & \mathbf{0} \\ \mathbf{0} & \boldsymbol{\Lambda}^{*} \end{bmatrix} \tag{3.39}$$

3.3.2 FRF-based methods

The first category of identification methods considered uses the FRF matrix (typically the receptance matrix) as the input data to identify the viscous damping matrix. The equations of motion of a viscously damped MDOF system

$$\mathbf{M}\ddot{\mathbf{x}}(t) + \mathbf{C}\dot{\mathbf{x}}(t) + \mathbf{K}\mathbf{x}(t) = \mathbf{f}(t) \tag{3.40}$$

described in section 2.3.2 can be written in the frequency domain as

$$\mathbf{x}(\omega) \left[\mathbf{K} + i\omega\mathbf{C} - \omega^2\mathbf{M}\right] = \mathbf{f}(\omega) \tag{3.41}$$

where $\mathbf{x}(\omega)$ and $\mathbf{f}(\omega)$ are respectively the Fourier transform of $\mathbf{x}(t)$ and $\mathbf{f}(t)$. The receptance matrix is defined as

$$\mathbf{H}(\omega) = \left[\mathbf{K} + i\omega\mathbf{C} - \omega^2\mathbf{M}\right]^{-1} \tag{3.42}$$

and can be directly measured from experiments. The element $H_{p,q}$ of the receptance matrix represents the response of the system at the degree of freedom p when the system is excited at the degree of freedom q. For a linear conservative system, Maxwell's Rule of Reciprocity applies [44] so that $H_{p,q} = H_{q,p}$ and the FRF matrix is symmetric. This property is often used to check the quality of the measured data by reciprocity checks.

Chen et al.

A method based on FRF measurements was proposed by Chen *et al.* [88]. The frequency response function generated from the normal modes $\mathbf{H}^N(\omega)$ is defined

as

$$\mathbf{H}^N(\omega) = \left[\mathbf{K} - \omega^2\mathbf{M}\right]^{-1} \tag{3.43}$$

eq. (3.41) can be rewritten as

$$\mathbf{H}^N(\omega)^{-1}\mathbf{x}(\omega) + i\omega\mathbf{C}\mathbf{x}(\omega) = \mathbf{f}(\omega) \tag{3.44}$$

and premultiplying eq. (3.44) by $\mathbf{H}^N(\omega)$ yields

$$\mathbf{x}(\omega) + i\mathbf{G}(\omega)\mathbf{x}(\omega) = \mathbf{H}^N(\omega)\mathbf{f}(\omega) \tag{3.45}$$

where

$$\mathbf{G}(\omega) = \omega\mathbf{H}^N(\omega)\mathbf{C} \ \in \mathbb{R}^{n\times n} \tag{3.46}$$

recalling that

$$\mathbf{x}(\omega) = \mathbf{H}(\omega)\mathbf{f}(\omega) \tag{3.47}$$

and using eq. (3.45), the relationship between the FRFs generated from the normal modes $\mathbf{H}^N(\omega)$ and the complex modes $\mathbf{H}(\omega)$ can be written as

$$\mathbf{H}^N(\omega) = \left[\mathbf{I} + i\mathbf{G}(\omega)\right]\mathbf{H}(\omega) \tag{3.48}$$

By separating $\mathbf{H}(\omega)$ into real and imaginary parts

$$\mathbf{H}^N(\omega) = \left[\mathbf{I} + i\mathbf{G}(\omega)\right]\left(\Re\left(\mathbf{H}(\omega)\right) + i\Im\left(\mathbf{H}(\omega)\right)\right) \tag{3.49}$$

Expanding eq. (3.49) yields

$$\mathbf{H}^N(\omega) = \left[\Re\left(\mathbf{H}(\omega)\right) - \mathbf{G}(\omega)\Im\left(\mathbf{H}(\omega)\right)\right] + i\left[\mathbf{G}(\omega)\Re\left(\mathbf{H}(\omega)\right) + \Im\left(\mathbf{H}(\omega)\right)\right] \tag{3.50}$$

Since $\mathbf{H}^N(\omega)$ is real, the imaginary part of the right hand side of eq (3.50) can be set to zero and $\mathbf{G}(\omega)$ can be obtained from the FRF as

$$\mathbf{G}(\omega) = -\Im\left(\mathbf{H}(\omega)\right)\left[\Re\left(\mathbf{H}(\omega)\right)\right]^{-1} \tag{3.51}$$

The viscous damping matrix can be obtained directly from eq. (3.46) and eq. (3.48) as

$$\mathbf{C} = \frac{1}{\omega}\left[\mathbf{H}^N(\omega)\right]^{-1}\mathbf{G}(\omega) \tag{3.52}$$

Symmetry of the damping matrix is then imposed and the equation can be solved in a least squares sense over the frequency range measured.

Lee and Kim

Lee and Kim [89] proposed a method based on the inversion of the receptance matrix measured from experiments. The method considers the identification of the viscous damping matrix $\mathbf{C}$ and the structural damping matrix $\mathbf{D}_s$ considered as complex-stiffness damping. In this case the equations of motion in the frequency domain become

$$\left[\mathbf{K} + i\left(\omega\mathbf{C} + \mathbf{D}_s\right) - \omega^2\mathbf{M}\right]\mathbf{x}(\omega) = \mathbf{f}(\omega) \tag{3.53}$$

and the receptance matrix

$$\mathbf{H}(\omega) = \left[\mathbf{K} + i\left(\omega\mathbf{C} + \mathbf{D}_s\right) - \omega^2\mathbf{M}\right]^{-1} \tag{3.54}$$

The dynamic stiffness matrix (DSM) $\mathbf{Z}(\omega)$ can be obtained from the inversion of $\mathbf{H}(\omega)$

$$\mathbf{Z}(\omega) = \left[\mathbf{H}(\omega)\right]^{-1} = \mathbf{K} - \omega^2\mathbf{M} + i\left(\omega\mathbf{C} + \mathbf{D}_s\right) \tag{3.55}$$

By separating the real and imaginary part

$$\Re\left(\mathbf{Z}(\omega)\right) = \mathbf{K} - \omega^2\mathbf{M} \tag{3.56}$$

$$\Im\left(\mathbf{Z}(\omega)\right) = \omega\mathbf{C} + \mathbf{D}_s \tag{3.57}$$

eq. (3.57) can be written in the form

$$\begin{bmatrix} \mathbf{I} & \omega \end{bmatrix} \begin{bmatrix} \mathbf{D}_s \\ \mathbf{C} \end{bmatrix} = \Im\left(\mathbf{Z}(\omega)\right) \tag{3.58}$$

Eq. (3.58) can be solved for the range of frequencies at which the FRF has been measured, so that the two damping matrices $\mathbf{C}$ and $\mathbf{D}_s$ can be determined in a least squares sense from

$$\begin{bmatrix} \mathbf{D}_s \\ \mathbf{C} \end{bmatrix} = \begin{bmatrix} \mathbf{I} & \omega_1\mathbf{I} \\ \mathbf{I} & \omega_2\mathbf{I} \\ \dots & \dots \\ \mathbf{I} & \omega_{max}\mathbf{I} \end{bmatrix}^{+} \begin{bmatrix} \Im\left(\mathbf{Z}(\omega_1)\right) \\ \Im\left(\mathbf{Z}(\omega_2)\right) \\ \dots \\ \Im\left(\mathbf{Z}(\omega_{max})\right) \end{bmatrix} \tag{3.59}$$

where $^{+}$ indicates the pseudo-inverse of the matrix.

Instrumental variable

Fritzen [90] proposed an iterative method based on the minimisation of the error $\boldsymbol{\epsilon}_{\mathbf{EE}}$ of the equation of motion defined as

$$\boldsymbol{\epsilon}_{EE} = \mathbf{f}(\omega) - \left(\mathbf{K} + i\omega\mathbf{C} - \omega^2\mathbf{M}\right)\mathbf{x}(\omega) \tag{3.60}$$

by applying the instrumental variable method, initially developed for parameter estimation in econometrics. Srikantha and Woodhouse [83] applied the same concepts on the error $\mathbf{E}$ between the dynamic stiffness $\mathbf{Z}(\omega)$ and the inverse of the measured Frequency Response Function $\mathbf{H}(\omega)$, which can be expressed as

$$\mathbf{E} = \mathbf{H}(\omega)\mathbf{Z}(\omega) - \mathbf{I} \tag{3.61}$$

It is possible to separate the real and imaginary part as

$$\begin{bmatrix} \Re(-\omega^2\mathbf{H} & i\omega\mathbf{H} & \mathbf{H}) \\ \Im(-\omega^2\mathbf{H} & i\omega\mathbf{H} & \mathbf{H}) \end{bmatrix} \begin{bmatrix} \mathbf{M} \\ \mathbf{C} \\ \mathbf{K} \end{bmatrix} = \begin{bmatrix} \mathbf{I} \\ \mathbf{0} \end{bmatrix} + \begin{bmatrix} \Re(\mathbf{E}) \\ \Im(\mathbf{E}) \end{bmatrix} \tag{3.62}$$

and then use the instrumental variable method to estimate the three matrices $\mathbf{M}$, $\mathbf{C}$ and $\mathbf{K}$. The instrument variable method is able to significantly reduce bias when noise is present and Fritzen [90], after several examples, concluded that the accuracy is better than least squares methods. The iterative solution is of the form

$$\begin{bmatrix} \mathbf{M} & \mathbf{C} & \mathbf{K} \end{bmatrix}^{\mathrm{T}}_{m+1} = \left[\mathbf{W}_m^{\mathrm{T}}\mathbf{A}\right]^{-1}\mathbf{W}_m^{\mathrm{T}}\bar{\mathbf{I}} \tag{3.63}$$

where

$$\mathbf{A} = \left[\mathbf{A}_1 \ \ldots \ \mathbf{A}_k \ \ldots \ \mathbf{A}_n\right]^{\mathrm{T}} \tag{3.64}$$

$$\mathbf{A_k} = \begin{bmatrix} \Re(-\omega_k^2\mathbf{H} & i\omega_k\mathbf{H} & \mathbf{H}) \\ \Im(-\omega_k^2\mathbf{H} & i\omega_k\mathbf{H} & \mathbf{H}) \end{bmatrix} \tag{3.65}$$

$$\bar{\mathbf{I}} = \left[\begin{bmatrix} \mathbf{I} \\ \mathbf{0} \end{bmatrix} \cdots \begin{bmatrix} \mathbf{I} \\ \mathbf{0} \end{bmatrix}\right] \tag{3.66}$$

and $\mathbf{W}$ is the "instrumental variable" matrix. The choice of $\mathbf{W}$ is particularly important and has restrictions such that $\mathbf{W}$ and the error are not correlated. Srikantha and Woodhouse suggest to use the dynamic stiffness matrix obtained using the matrices $\mathbf{M}_m$, $\mathbf{C}_m$ and $\mathbf{K}_m$ identified in each previous iteration as

$$\mathbf{W}_{m+1} = \mathbf{K}_m - \omega^2\mathbf{M}_m + i\omega\mathbf{C}_m \tag{3.67}$$

after an initial estimate which can be based on the least square solution from the inverse of the FRF matrix similar to Lee and Kim's method. The iteration is performed until convergence is reached according to various criteria based on the norms of the identified matrices, natural frequencies or minimisation of the error between the measured and reconstructed FRFs.

Considerations on the inversion of the FRF

The three methods described are representative of the large number of techniques which extract damping information from FRF measurements. Most of these methods are based on the inversion of the FRF matrix. There is an important aspect which has to be considered when using these methods in real experiments [85]. Considering a system with viscous damping only, the receptance matrix can be written in the form

$$\mathbf{H}(s) = \sum_{p=1}^{n} \left(\frac{\boldsymbol{\psi}_p \boldsymbol{\psi}_p^{\mathrm{T}}}{(s - \lambda_p)} + \frac{\boldsymbol{\psi}_p^* \boldsymbol{\psi}_p^{*\mathrm{T}}}{\left(s - \lambda_p^*\right)} \right) \tag{3.68}$$

where $\boldsymbol{\psi}_\mathbf{p}$ and λ_p have been defined in section 2.3.2. When $s = i\omega$

$$\mathbf{H}(i\omega) = \sum_{p=1}^{n} \left(\frac{\boldsymbol{\psi}_p \boldsymbol{\psi}_p^{\mathrm{T}}}{(i\omega - \lambda_p)} + \frac{\boldsymbol{\psi}_p^* \boldsymbol{\psi}_p^{*\mathrm{T}}}{\left(i\omega - \lambda_p^*\right)} \right) \tag{3.69}$$

or, in a more compact form

$$\mathbf{H}(i\omega) = \boldsymbol{\Psi}^{\mathrm{T}} \left(i\omega \mathbf{I} - \boldsymbol{\Lambda}\right)^{-1} \boldsymbol{\Psi} + \boldsymbol{\Psi}^{*\mathrm{T}} \left(i\omega \mathbf{I} - \boldsymbol{\Lambda}^*\right)^{-1} \boldsymbol{\Psi}^* \tag{3.70}$$

where

$$\boldsymbol{\Psi} = [\boldsymbol{\psi}_1 \quad \dots \quad \boldsymbol{\psi}_n] \tag{3.71}$$

and

$$\boldsymbol{\Lambda} = \mathrm{diag}(\lambda_1, \dots, \lambda_n) \tag{3.72}$$

From eq. (3.69) it is observable that $\mathbf{H}(i\omega)$ is dominated by the eigenvalues closest to the frequency ω where the denominator goes to zero (Figure 3.3). Considering the dynamic stiffness expressed in state-space form

$$\mathbf{Z}'(i\omega) = \begin{bmatrix} \mathbf{Z'}_{11}(i\omega) & \mathbf{Z'}_{12}(i\omega) \\ \mathbf{Z'}_{21}(i\omega) & \mathbf{Z'}_{22}(i\omega) \end{bmatrix} = \left(i\omega \begin{bmatrix} \mathbf{0} & \mathbf{M} \\ \mathbf{M} & \mathbf{C} \end{bmatrix} + \begin{bmatrix} -\mathbf{M} & \mathbf{0} \\ \mathbf{0} & \mathbf{K} \end{bmatrix} \right) \tag{3.73}$$

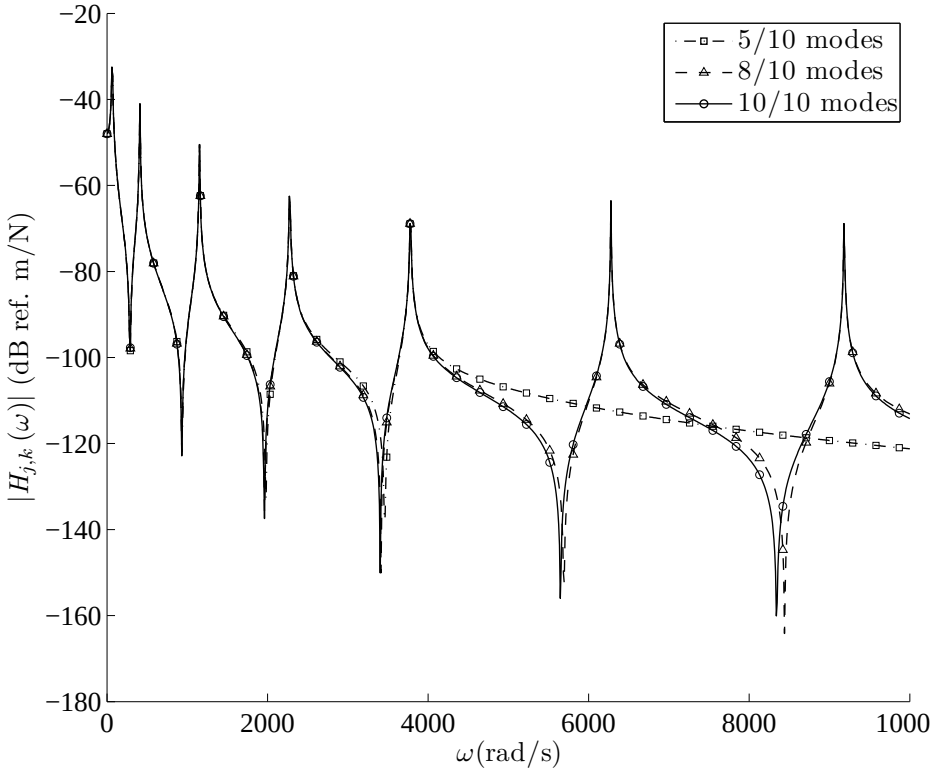

Figure 3.3: Effect of modal incompleteness on the FRF of a 10 degree-of-freedom system.

and in terms of the modal and spectral matrices

$$\mathbf{Z}'(i\omega) = \begin{bmatrix} \mathbf{\Lambda\Psi}^{\mathrm{T}} & \mathbf{\Psi}^{\mathrm{T}} \\ \mathbf{\Lambda}^{*}\mathbf{\Psi}^{*\mathrm{T}} & \mathbf{\Psi}^{*\mathrm{T}} \end{bmatrix}^{-1} \begin{bmatrix} i\omega\mathbf{I} - \mathbf{\Lambda} & \mathbf{0} \\ \mathbf{0} & i\omega\mathbf{I} - \mathbf{\Lambda}^{*} \end{bmatrix} \begin{bmatrix} \mathbf{\Psi\Lambda} & \mathbf{\Psi}^{*}\mathbf{\Lambda}^{*} \\ \mathbf{\Psi} & \mathbf{\Psi}^{*} \end{bmatrix}^{-1} \tag{3.74}$$

By combining eqs. (3.74) and (3.36)

$$\mathbf{Z}'(i\omega) = \begin{bmatrix} \mathbf{0} & \mathbf{M} \\ \mathbf{M} & \mathbf{C} \end{bmatrix} \begin{bmatrix} \mathbf{\Psi\Lambda} & \mathbf{\Psi}^{*}\mathbf{\Lambda}^{*} \\ \mathbf{\Psi} & \mathbf{\Psi}^{*} \end{bmatrix} \begin{bmatrix} i\omega\mathbf{I} - \mathbf{\Lambda} & \mathbf{0} \\ \mathbf{0} & i\omega\mathbf{I} - \mathbf{\Lambda}^{*} \end{bmatrix} \begin{bmatrix} \mathbf{\Lambda\Psi}^{\mathrm{T}} & \mathbf{\Psi}^{\mathrm{T}} \\ \mathbf{\Lambda}^{*}\mathbf{\Psi}^{*\mathrm{T}} & \mathbf{\Psi}^{*\mathrm{T}} \end{bmatrix} \begin{bmatrix} \mathbf{0} & \mathbf{M} \\ \mathbf{M} & \mathbf{C} \end{bmatrix} \tag{3.75}$$

and the dynamic stiffness matrix $\mathbf{Z}(i\omega)$ can be expressed from eq. (3.73) in the form

$$\mathbf{Z}(i\omega) = \mathbf{K} - \omega^2\mathbf{M} + i\omega\mathbf{C} = \omega^2\mathbf{Z}'_{11}(i\omega) + \mathbf{Z}'_{22}(i\omega) \tag{3.76}$$

By expanding the product of the three central matrices on the right-hand side of eq. (3.75)

$$\begin{bmatrix} \mathbf{\Psi\Lambda} & \mathbf{\Psi}^{*}\mathbf{\Lambda}^{*} \\ \mathbf{\Psi} & \mathbf{\Psi}^{*} \end{bmatrix} \begin{bmatrix} i\omega\mathbf{I} - \mathbf{\Lambda} & \mathbf{0} \\ \mathbf{0} & i\omega\mathbf{I} - \mathbf{\Lambda}^{*} \end{bmatrix} \begin{bmatrix} \mathbf{\Lambda\Psi}^{\mathrm{T}} & \mathbf{\Psi}^{\mathrm{T}} \\ \mathbf{\Lambda}^{*}\mathbf{\Psi}^{*\mathrm{T}} & \mathbf{\Psi}^{*\mathrm{T}} \end{bmatrix} = \begin{bmatrix} \mathbf{Q}_{11} & \mathbf{Q}_{12} \\ \mathbf{Q}_{21} & \mathbf{Q}_{22} \end{bmatrix} \tag{3.77}$$

where

$$\mathbf{Q}_{11} = \sum_p \left(\boldsymbol{\psi}_p \lambda_p^2 (i\omega - \lambda_p) \boldsymbol{\psi}_p^{\mathrm{T}} + \boldsymbol{\psi}_p^* \lambda_p^{*2} (i\omega - \lambda_p^*) \boldsymbol{\psi}_p^{*\mathrm{T}} \right) \tag{3.78}$$

$$\mathbf{Q}_{12} = \sum_p \left(\boldsymbol{\psi}_p \lambda_p (i\omega - \lambda_p) \boldsymbol{\psi}_p^{\mathrm{T}} + \boldsymbol{\psi}_p^* \lambda_p^* (i\omega - \lambda_p^*) \boldsymbol{\psi}_p^{*\mathrm{T}} \right) \tag{3.79}$$

$$\mathbf{Q}_{21} = \sum_p \left(\boldsymbol{\psi}_p \lambda_p (i\omega - \lambda_p) \boldsymbol{\psi}_p^{\mathrm{T}} + \boldsymbol{\psi}_p^* \lambda_p^* (i\omega - \lambda_p^*) \boldsymbol{\psi}_p^{*\mathrm{T}} \right) \tag{3.80}$$

$$\mathbf{Q}_{22} = \sum_p \left(\boldsymbol{\psi}_p (i\omega - \lambda_p) \boldsymbol{\psi}_p^{\mathrm{T}} + \boldsymbol{\psi}_p^* (i\omega - \lambda_p^*) \boldsymbol{\psi}_p^{*\mathrm{T}} \right) \tag{3.81}$$

It can be seen that the elements of $\mathbf{Z}'(i\omega)$ which are present in eq. (3.76) de-

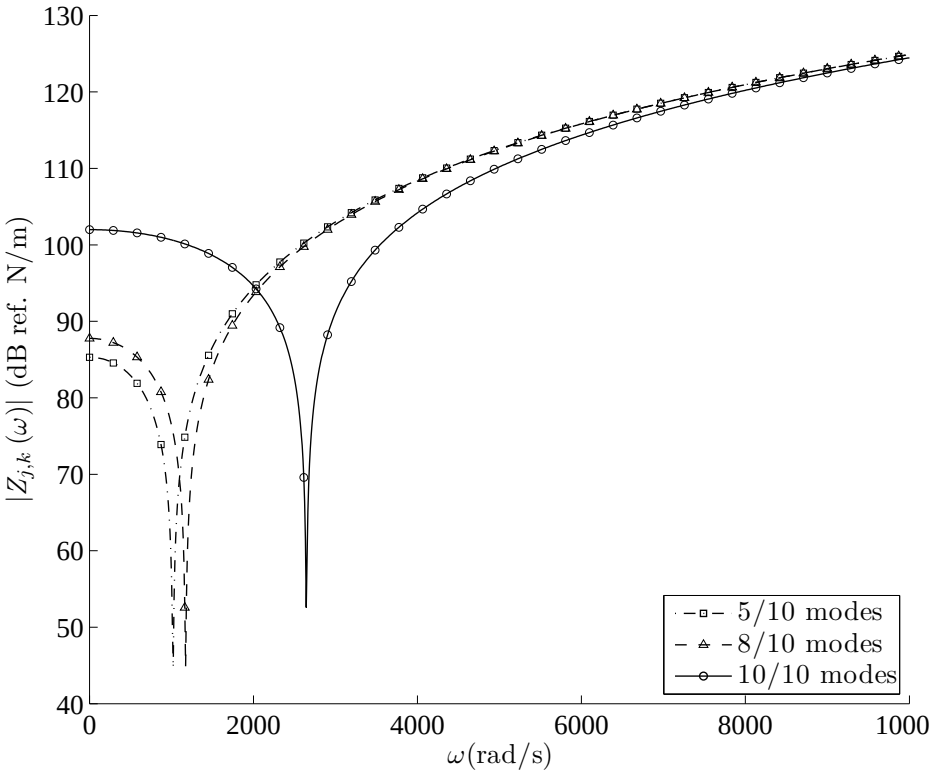

Figure 3.4: Effect of modal incompleteness on the DSM of a 10 degree-of-freedom system.

pends on the summations from eqs. (3.78-3.81) which show that the contribution of the p$^{\text{th}}$ mode vanishes as $i\omega$ approaches λ_p and the high-frequency poles become very significant through squaring in $\mathbf{Q}_{11}$. Thus the low-frequency dynamic stiffness matrix is dominated by the high-frequency eigenvalues far away from the frequency ω (Figure 3.4). Berman [91, 92] explained the meaning of this result; that it is impossible to invert the receptance matrix of a practical structure with

many modes, measured over a limited frequency range, in order to estimate the matrices $\mathbf{M}$, $\mathbf{C}$ and $\mathbf{K}$. Consequently, a damping matrix identified by extracting the imaginary part of an inverted matrix of measured receptances will only be correct if all the modes are present in the measurements. This is possible in simulation but never happens in practical case of mechanical systems with distributed mass and stiffness.

3.3.3 Modal parameters methods

Methods based on modal parameters consider complex mode shapes and natural frequencies extracted from modal analysis tests as input for the identification. Information about damping is often extracted from the imaginary part of the modal parameters, since the mode shapes of an undamped system are real. Partial information about the mass and stiffness matrices are often required and usually extracted from FEM.

Lancaster

Lancaster's formula [87] appeared in 1961 without proof as a derivation from a previous article [93], although a proof was given subsequently by Lancaster and Prells [94] using the theory of matrix polynomials. The formula states that if the eigenvectors are normalized so that

$$\boldsymbol{\psi}_p^{\mathrm{T}} \left(2\mathbf{M}\lambda_p + \mathbf{C}\right) \boldsymbol{\psi}_p = 1 \tag{3.82}$$

the damping matrix can be obtained by

$$\mathbf{C} = -\mathbf{M} \left(\boldsymbol{\Psi} \boldsymbol{\Lambda}^2 \boldsymbol{\Psi}^{\mathrm{T}} + \boldsymbol{\Psi}^* \boldsymbol{\Lambda}^{*2} \boldsymbol{\Psi}^{*\mathrm{T}} \right) \mathbf{M} \tag{3.83}$$

The formula can be alternatively developed [85] from eq. (3.36) in a few simple steps as demonstrated below. By inverting eq. (3.36)

$$\left(\begin{bmatrix} \boldsymbol{\Lambda}\boldsymbol{\Psi}^{\mathrm{T}} & \boldsymbol{\Psi}^{\mathrm{T}} \\ \boldsymbol{\Lambda}^*\boldsymbol{\Psi}^{*\mathrm{T}} & \boldsymbol{\Psi}^{*\mathrm{T}} \end{bmatrix} \begin{bmatrix} \mathbf{0} & \mathbf{M} \\ \mathbf{M} & \mathbf{C} \end{bmatrix} \begin{bmatrix} \boldsymbol{\Psi}\boldsymbol{\Lambda} & \boldsymbol{\Psi}^*\boldsymbol{\Lambda}^* \\ \boldsymbol{\Psi} & \boldsymbol{\Psi}^* \end{bmatrix} \right)^{-1} = \mathbf{I} \tag{3.84}$$

Expanding the inverse on the left hand side and rearranging leads to

$$\begin{bmatrix} \mathbf{0} & \mathbf{M} \\ \mathbf{M} & \mathbf{C} \end{bmatrix}^{-1} = \begin{bmatrix} \boldsymbol{\Psi}\boldsymbol{\Lambda} & \boldsymbol{\Psi}^*\boldsymbol{\Lambda}^* \\ \boldsymbol{\Psi} & \boldsymbol{\Psi}^* \end{bmatrix} \begin{bmatrix} \boldsymbol{\Lambda}\boldsymbol{\Psi}^{\mathrm{T}} & \boldsymbol{\Psi}^{\mathrm{T}} \\ \boldsymbol{\Lambda}^*\boldsymbol{\Psi}^{*\mathrm{T}} & \boldsymbol{\Psi}^{*\mathrm{T}} \end{bmatrix} \tag{3.85}$$

or

$$\begin{bmatrix} \mathbf{0} & \mathbf{M} \\ \mathbf{M} & \mathbf{C} \end{bmatrix}^{-1} = \begin{bmatrix} \boldsymbol{\Psi}\boldsymbol{\Lambda}^2\boldsymbol{\Psi}^{\mathrm{T}} & \boldsymbol{\Psi}\boldsymbol{\Lambda}\boldsymbol{\Psi}^{\mathrm{T}} \\ \boldsymbol{\Psi}\boldsymbol{\Lambda}\boldsymbol{\Psi}^{\mathrm{T}} & \mathbf{0} \end{bmatrix} + \begin{bmatrix} \boldsymbol{\Psi}^*\boldsymbol{\Lambda}^{*2}\boldsymbol{\Psi}^{*\mathrm{T}} & \boldsymbol{\Psi}^*\boldsymbol{\Lambda}^*\boldsymbol{\Psi}^{*\mathrm{T}} \\ \boldsymbol{\Psi}^*\boldsymbol{\Lambda}^*\boldsymbol{\Psi}^{*\mathrm{T}} & \mathbf{0} \end{bmatrix} \tag{3.86}$$

it can be proven using the Schur complement [95] that the left hand side matrix inverse is

$$\begin{bmatrix} \mathbf{0} & \mathbf{M} \\ \mathbf{M} & \mathbf{C} \end{bmatrix}^{-1} = \begin{bmatrix} -\mathbf{M}^{-1}\mathbf{C}\mathbf{M}^{-1} & \mathbf{M}^{-1} \\ \mathbf{M}^{-1} & \mathbf{0} \end{bmatrix} \tag{3.87}$$

by comparing the right hand side in eq. (3.86) and eq. (3.87) it is seen that

$$-\mathbf{M}^{-1}\mathbf{C}\mathbf{M}^{-1} = \boldsymbol{\Psi}\boldsymbol{\Lambda}^2\boldsymbol{\Psi}^{\mathrm{T}} + \boldsymbol{\Psi}^*\boldsymbol{\Lambda}^{*2}\boldsymbol{\Psi}^{*\mathrm{T}} \tag{3.88}$$

or

$$\mathbf{C} = -\left(\mathbf{M}\boldsymbol{\Psi}\boldsymbol{\Lambda}^2\boldsymbol{\Psi}^{\mathrm{T}}\mathbf{M} + \mathbf{M}\boldsymbol{\Psi}^*\boldsymbol{\Lambda}^{*2}\boldsymbol{\Psi}^{*\mathrm{T}}\mathbf{M}\right) \tag{3.89}$$

which is Lancaster's formula. This formula can be expanded in order to show the contribution of each mode as

$$\mathbf{C} = -\mathbf{M}\sum_p \left(\boldsymbol{\psi}_p\lambda_p^2\boldsymbol{\psi}_p^{\mathrm{T}} + \boldsymbol{\psi}_p^*\lambda_p^{*2}\boldsymbol{\psi}_p^{*\mathrm{T}}\right)\mathbf{M} \tag{3.90}$$

or

$$\mathbf{C} = -2\mathbf{M}\sum_p \Re\left(\boldsymbol{\psi}_p\lambda_p^2\boldsymbol{\psi}_p^{\mathrm{T}}\right)\mathbf{M} \tag{3.91}$$

To apply this method the mass matrix must be known, which may be an acceptable restriction, and we see that the damping matrix is constructed mode-by-mode. This means that if we know an incomplete set of eigenvalues and eigenvectors corresponding to the limited frequency range of a vibration test and no others, then the same eigenvalues and eigenvectors will be returned exactly from eq. (2.66) when $\mathbf{C}$ is computed using the truncated series in eq. (3.91). The same equation ensures that the identified damping matrix is strictly real. Therefore the damping matrix $\mathbf{C}$ appears to be computed correctly by the truncated series for the frequency range in question and for example will reproduce exactly the modal damping ratios obtained in the test.

Pilkey and Inman

Pilkey and Inman [96] proposed two methods based on Lancaster's formula; one iterative and one direct. The iterative method is due to the fact that Lancaster's

formula requires the normalization in eq. (3.82) but the damping matrix $\mathbf{C}$ is unknown at first, so the eigenvectors are normalized using an initial guess $\mathbf{C}_0$ for the viscous damping matrix

$$\boldsymbol{\psi}_p^{\mathrm{T}} \left(2\mathbf{M}\lambda_p + \mathbf{C}_0\right) \boldsymbol{\psi}_p = 1 \tag{3.92}$$

then the matrix $\mathbf{C}_1$ is computed using Lancaster's formula

$$\mathbf{C}_1 = -\mathbf{M} \left(\boldsymbol{\Psi}\boldsymbol{\Lambda}^2\boldsymbol{\Psi}^{\mathrm{T}} + \boldsymbol{\Psi}^*\boldsymbol{\Lambda}^{*2}\boldsymbol{\Psi}^{*\mathrm{T}}\right) \mathbf{M} \tag{3.93}$$

and compared to the initial guess according to convergence criteria. If the criteria are not satisfied, a new normalization is performed using $\mathbf{C}_1$ as

$$\boldsymbol{\psi}_p^{\mathrm{T}} \left(2\mathbf{M}\lambda_p + \mathbf{C}_1\right) \boldsymbol{\psi}_p = 1 \tag{3.94}$$

and so on until convergence is reached. The direct method avoids the iteration but implies knowledge of the stiffness matrix $\mathbf{K}$. The eigenvalue problem in eq. (2.67) can be written as

$$\boldsymbol{\psi}_p^{\mathrm{T}}\mathbf{C}\boldsymbol{\psi}_p = -\boldsymbol{\psi}_p^{\mathrm{T}} \left(\mathbf{K}\frac{1}{\lambda_p} + \mathbf{M}\lambda_p\right) \boldsymbol{\psi}_p \tag{3.95}$$

which, substituted into the normalization eq. (3.82) yields a normalization condition which does not contain the damping matrix as

$$\boldsymbol{\psi}_p^{\mathrm{T}} \left(\mathbf{M}\lambda_p^2 - \mathbf{K}\right) \boldsymbol{\psi}_p = \lambda_p \tag{3.96}$$

The two normalizations in eq. (3.92) and eq. (3.96) are essentially the same equations as eq. (3.38) and eq. (3.39) obtained directly [85] from the eigenproblem of the viscously damped MDOF system described in eq. (2.66).
By measuring the complex mode shapes and knowing the mass and stiffness matrices it is then possible to normalize the eigenvectors and estimate the damping matrix using Lancaster's formula directly without iteration.

Ibrahim

Ibrahim [97] proposed a method to identify the viscous damping matrix from measured complex modes together with an analytical mathematical model of the structure under investigation that needs improvements. The data extracted from the experiments consists of: m complex eigenvectors $\boldsymbol{\psi}_1 \ldots \boldsymbol{\psi}_m$ measured at n

points on the structure where $n > m$, the damped natural frequencies $(\omega_d)_i$ and the damping factors ζ_i. The data extracted from the mathematical model consists of the analytical mass matrix $\mathbf{M}_A \in \mathbb{R}^{n\times n}$, the n normal modes $\boldsymbol{\phi}_1 \dots \boldsymbol{\phi}_n$ and the natural frequencies $(\omega_n)_i$. If the structure is linear, the measured parameters satisfy the equation

$$\left[\begin{array}{cc} \mathbf{M}^{-1}\mathbf{K} & \mathbf{M}^{-1}\mathbf{C} \end{array} \right] \left\{ \begin{array}{c} \boldsymbol{\psi}_i \\ \lambda_i \boldsymbol{\psi}_i \end{array} \right\} = -\lambda_i^2 \boldsymbol{\psi}_i \tag{3.97}$$

for $i = 1, \dots, m$, where λ_i is the i$^{\text{th}}$ characteristic root of the system which is related to the i$^{\text{th}}$ damping factor and the i$^{\text{th}}$ damped natural frequency through the equation

$$\lambda_i = (\omega_d)_i \left(\frac{\zeta_i}{\sqrt{1-\zeta_i^2}} + i \right) \tag{3.98}$$

These equations are not sufficient to compute the two matrices $\mathbf{M}^{-1}\mathbf{K}$ and $\mathbf{M}^{-1}\mathbf{C}$, since $n > m$. The remaining equations regarding the unmeasured modes out of the frequency range over which the modal test was conducted are assumed to satisfy

$$\left[\begin{array}{cc} \mathbf{M}^{-1}\mathbf{K} & \mathbf{M}^{-1}\mathbf{C} \end{array} \right] \left\{ \begin{array}{c} \boldsymbol{\Phi}_i \\ \lambda_i \boldsymbol{\Phi}_i \end{array} \right\} = -\lambda_i^2 \boldsymbol{\Phi}_i \tag{3.99}$$

for $i = m+1, \dots, n$, where λ_i is now defined as

$$\lambda_i = -(\omega_n)_i \zeta + i(\omega_n)_i \sqrt{1-\zeta^2} \tag{3.100}$$

where ζ is the average damping factor of the m measured modes. Combining eq. (3.97) and eq. (3.99), the equation obtained can be solved for $\mathbf{M}^{-1}\mathbf{K}$ and $\mathbf{M}^{-1}\mathbf{C}$. These two matrices have been obtained from data derived from both the modal test and analytical model. The matrix $\mathbf{M}^{-1}\mathbf{K}$ can now be used to compute the experimental normal modes by means of the equation

$$\left[\mathbf{M}^{-1}\mathbf{K}\right] \boldsymbol{\phi} = \omega^2 \boldsymbol{\phi} \tag{3.101}$$

The first m eigenvectors obtained from eq. (3.101) are the computed normal modes obtained from the measured complex modes, the remaining eigenvectors are the higher analytical modes previously used. The mass matrix can now be corrected using an approach based on minimum changes [98] by computing a mass

matrix that satisfies the orthogonality condition of the computed experimental normal modes. The orthogonality relation of the analytical mass matrix

$$\mathbf{\Phi}^{\mathrm{T}}\mathbf{M}_A\mathbf{\Phi} = \mathrm{diag}(m_1, \ldots, m_n) = \mathbf{M}_m \tag{3.102}$$

can be used to obtain the corrected mass matrix

$$\mathbf{M} = \mathbf{M}_A + \mathbf{M}_A\mathbf{\Phi}\mathbf{M}_m^{-1}\left[\mathbf{I} - \mathbf{M}_m\right]\mathbf{M}_m^{-1}\mathbf{\Phi}^{\mathrm{T}}\mathbf{M}_A \tag{3.103}$$

which can be used to derive the stiffness and damping matrix using the previously identified matrices

$$\mathbf{K} = \mathbf{M}\left[\mathbf{M}^{-1}\mathbf{K}\right] \tag{3.104}$$

$$\mathbf{C} = \mathbf{M}\left[\mathbf{M}^{-1}\mathbf{C}\right] \tag{3.105}$$

Minas and Inman

The method proposed by Minas and Inman [99] assumes knowledge of the analytical stiffness and mass matrices from a FEM and measurement of an incomplete set of eigenvalues and eigenvectors from experiments. The mass and stiffness matrices are then reduced to the size of the modal data measured. The eigenvalue problem in eq. (2.67) can be written as

$$\mathbf{C}\boldsymbol{\psi}_p = -\frac{1}{\lambda_p}\left(\lambda_p^2\mathbf{M} + \mathbf{K}\right)\boldsymbol{\psi}_p = \mathbf{f}_p \tag{3.106}$$

and its complex conjugate transpose is

$$\boldsymbol{\psi}_p^*\mathbf{C} = \mathbf{f}_p^* \tag{3.107}$$

which can be solved by separating the real and imaginary parts and rearranging, obtaining the equation

$$\mathbf{G}_p\mathbf{d} = \mathbf{b}_p \tag{3.108}$$

where $\mathbf{G}_p$ contains the real and imaginary parts of the eigenvectors, $\mathbf{d}$ contains the $(n^2 - n)/2$ unknown parameters of the symmetric damping matrix and $\mathbf{b}_p$ contains the real and imaginary parts of $\mathbf{f}_p$. Eq. (3.108) can be solved using the least-squares approach or other optimization procedures depending on the size of the modal data available which can lead to an overdetermined or underdetermined problem.

Adhikari and Woodhouse

Adhikari and Woodhouse [100] introduced a damping identification method based on perturbation analysis. A similar approach with a comparison of perturbation and exact solutions of a system with non-classical damping can be found in a paper by Lees [101]. This method is based on the following expressions, originally developed by Lord Rayleigh [9], of the complex eigenvalues λ_p and eigenvectors $\boldsymbol{\psi}_\mathbf{p}$ in terms of undamped eigenvalues ω_p and eigenvectors $\boldsymbol{\phi}_p$

$$\lambda_p = -\frac{\boldsymbol{\phi}_p^{\mathrm{T}}\mathbf{C}\boldsymbol{\phi}_p}{2} \pm i\omega_p \tag{3.109}$$

$$\boldsymbol{\psi}_p = \boldsymbol{\phi}_p \pm i\omega_p \sum_j \frac{\boldsymbol{\phi}_p^{\mathrm{T}}\mathbf{C}\boldsymbol{\phi}_j}{\omega_p^2 - \omega_j^2}\boldsymbol{\phi}_j \tag{3.110}$$

From the matrix of measured complex eigenvectors $\boldsymbol{\Psi}$, matrices $\mathbf{U} = \Re(\boldsymbol{\Psi})$ and $\mathbf{V} = \Im(\boldsymbol{\Psi})$ are extracted and it is assumed that the columns of $\mathbf{V}$ are given by a linear combination of the columns of $\mathbf{U}$, so that

$$\mathbf{V} = \mathbf{U}\mathbf{B} \tag{3.111}$$

and

$$\mathbf{B} = \left(\mathbf{U}^{\mathrm{T}}\mathbf{U}\right)^{-1}\mathbf{U}^{\mathrm{T}}\mathbf{V} \tag{3.112}$$

for an incomplete set of frequencies and modes. From eq. (3.110) and eq. (3.111) it can be seen that

$$c'_{jp} = \boldsymbol{\phi}_p^{\mathrm{T}}\mathbf{C}\boldsymbol{\phi}_j = \frac{\left(\omega_p^2 - \omega_j^2\right) b_{jp}}{\omega_p} \qquad j \neq p \tag{3.113}$$

and from eq. (3.109)

$$c'_{pp} = \boldsymbol{\phi}_p^{\mathrm{T}}\mathbf{C}\boldsymbol{\phi}_p = 2\Re(\lambda_p) \tag{3.114}$$

Eqs. (3.113) and (3.114) complete the matrix $\mathbf{C}'$, which is the fully populated damping matrix in the modal coordinates of the undamped system. The matrix $\mathbf{C}$ in physical coordinates is then computed as

$$\mathbf{C} = \mathbf{U}\left(\mathbf{U}^{\mathrm{T}}\mathbf{U}\right)^{-1}\mathbf{C}'\left(\mathbf{U}^{\mathrm{T}}\mathbf{U}\right)^{-1}\mathbf{U}^{\mathrm{T}} \tag{3.115}$$

It is seen that the matrices $\mathbf{C}$ and $\mathbf{C}'$ are generally not symmetric. Adhikari and Woodhouse [102] modified their formulation by placing a constraint on the solution of $\mathbf{B}$ that ensured a symmetric solution for $\mathbf{C}'$ and hence for $\mathbf{C}$.

Considerations on the perturbation method

The method depends on pseudo inversions of the undamped eigenvectors $\mathbf{U}$ in eqs. (3.112) and (3.115). By combining eqs. (3.111) and (3.112) the projection of $\mathbf{V}$ onto the columns of $\mathbf{U}$ is obtained as

$$\mathbf{U}\left(\mathbf{U}^{\mathrm{T}}\mathbf{U}\right)^{-1}\mathbf{U}^{\mathrm{T}}\mathbf{V} = \mathbf{V}' \neq \mathbf{V} \tag{3.116}$$

This means that the matrix $\mathbf{B}$ obtained from eq. (3.112) results in the projection $\mathbf{V}'$ when substituted into eq. (3.111). The error $\mathbf{E} = (\mathbf{V} - \mathbf{V}')$ is therefore carried into eq. (3.113) which in turn produces erroneous values for $\mathbf{C}'$. The Frobenius norm ε_p of this error,

$$\varepsilon_p = \frac{\|\mathbf{E}\|_F}{\|\mathbf{V}\|_F} \cdot 100\% \tag{3.117}$$

may be used as an indicator to assess whether or not enough modes have been included in $\mathbf{U}$ and $\mathbf{V}$. In eq. (3.115) pseudo inverses are used in the transformation from modal to physical coordinates, of $\mathbf{C}'$ to $\mathbf{C}$. By pre and postmultiplying eq. (3.115) by $\mathbf{U}^{\mathrm{T}}$ and $\mathbf{U}$, thereby reversing the transformation, then

$$\mathbf{U}^{\mathrm{T}}\mathbf{U}\left(\mathbf{U}^{\mathrm{T}}\mathbf{U}\right)^{-1}\mathbf{C}'\left(\mathbf{U}^{\mathrm{T}}\mathbf{U}\right)^{-1}\mathbf{U}^{\mathrm{T}}\mathbf{U} = \mathbf{C}' \tag{3.118}$$

It can be seen that if the damping matrix in modal coordinates $\mathbf{C}'$ is known exactly it is converted to physical coordinates with perfect accuracy by eq. (3.115). Thus it is the pseudo inverse in eq. (3.112) that introduces errors into the damping estimate and not the pseudo inversion in eq. (3.115). Moreover, since eqs. (3.109) and (3.110) are developed using the undamped orthogonality equation, it is clear that the first order perturbation method requires a known mass matrix too.

3.3.4 Time histories methods

The last group of damping identification techniques consists in methods which use measurements in the time domain as input to estimate the damping matrix. These measurements are usually obtained from force transducers and accelerometers from which velocities and displacements are derived.

Liang

The method proposed by Liang [103] extends the technique introduced in the previous paper [75] by Liang and Feeny presented in section 4.2 to MDOF systems. The concept is the same: balancing the energy input by the external forces with the energy dissipated by damping. Starting from the equation of motion of a MDOF system with viscous damping and Coulomb friction

$$\mathbf{M}\ddot{\mathbf{x}} + \mathbf{K}\mathbf{x} + \mathbf{C}\dot{\mathbf{x}} + \mathbf{D}(\dot{\mathbf{x}})\mathbf{f}_k = \mathbf{f}(t) \tag{3.119}$$

where $\mathbf{f}_k \in \mathbb{R}^{n\times 1}$ represents a vector consisting of Coulomb elements such that $\mathbf{D}(\dot{\mathbf{x}})\mathbf{f}_k$ models the Coulomb damping. Assuming some of the damping coefficients are known, eq (3.119) can be rearranged as

$$\mathbf{M}\ddot{\mathbf{x}} + \mathbf{K}\mathbf{x} + \mathbf{e}(\mathbf{x}, \dot{\mathbf{x}}) + \mathbf{B}(\dot{\mathbf{x}})\mathbf{c}' + \mathbf{G}(\dot{\mathbf{x}})\mathbf{f}'_k = \mathbf{f}(t) \tag{3.120}$$

where $\mathbf{e}(\mathbf{x}, \dot{\mathbf{x}}) \in \mathbb{R}^{n\times 1}$ contains all the known damping forces and $\mathbf{c}'$ and $\mathbf{f}'_k$ contains all the viscous damping and Coulomb friction coefficients to be identified. These coefficients are multiplied by $\mathbf{B}(\dot{\mathbf{x}})$ and $\mathbf{G}(\dot{\mathbf{x}})$ which represent the associated state functions (velocities and sign functions). As for the SDOF method, the excitation and the response must have a common fundamental period T. Premultiplying eq. (3.120) by $\dot{\mathbf{x}}_i^{\mathrm{T}}$, where $\dot{\mathbf{x}}_i = [0 \ldots \dot{x}_i \ldots 0]^{\mathrm{T}} \in \mathbb{R}^{n\times 1}$ and integrating over a full cycle of vibration, an energy equation is obtained

$$\begin{aligned}\int_t^{t+T} \dot{\mathbf{x}}_i^{\mathrm{T}}\mathbf{M}\ddot{\mathbf{x}}\mathrm{d}t + \int_t^{t+T} \dot{\mathbf{x}}_i^{\mathrm{T}}\mathbf{K}\mathbf{x}\mathrm{d}t + \int_t^{t+T} \dot{\mathbf{x}}_i^{\mathrm{T}}\mathbf{e}(\mathbf{x}, \dot{\mathbf{x}})\mathrm{d}t + \\ + \int_t^{t+T} \dot{\mathbf{x}}_i^{\mathrm{T}}\mathbf{B}(\dot{\mathbf{x}})\mathbf{c}'\mathrm{d}t + \int_t^{t+T} \dot{\mathbf{x}}_i^{\mathrm{T}}\mathbf{G}(\dot{\mathbf{x}})\mathbf{f}'_k\mathrm{d}t = \int_t^{t+T} \dot{\mathbf{x}}_i^{\mathrm{T}}\mathbf{f}(t)\mathrm{d}t\end{aligned} \tag{3.121}$$

Repeating the premultiplication by all the vectors $\dot{\mathbf{x}}_i^{\mathrm{T}}$ with $i = 1, \ldots, n$, assuming $\mathbf{M}$ is diagonal, remembering that the integration of conservative components over a cycle of periodic motion are zeros and rearranging leads to n equations of the type

$$c'_1\tau_{i1} + \ldots + c'_p\tau_{ip} + F'_{k1}\gamma_{i1} + \ldots + F'_{kq}\gamma_{iq} = \beta_i \tag{3.122}$$

where, for $i = 1, \ldots, n$

$$\tau_{ij} = \int_t^{t+T} b_{ij}(\dot{\mathbf{x}})\dot{x}_i\mathrm{d}t \quad j = 1, \ldots, p \tag{3.123}$$

$$\gamma_{ij} = \int_t^{t+T} g_{ij}(\dot{\mathbf{x}})\dot{x}_i \mathrm{d}t \quad j = 1, \ldots, q \tag{3.124}$$

$$\beta_i = \int_t^{t+T} f_i(t)\dot{x}_i \mathrm{d}t - \int_t^{t+T} \left(\sum_{j \neq i}^{n} k_{ij} x_j \right) \dot{x}_i \mathrm{d}t - \int_t^{t+T} e_i(\dot{\mathbf{x}})\dot{x}_i \mathrm{d}t \tag{3.125}$$

Eq. (3.122) can be rearranged to obtain a least squares problem with a solution which gives a column vector of the unknown damping parameters. From eq. (3.125) it can be seen that knowledge of the stiffness matrix is required together with some known damping coefficients and the assumption of a diagonal mass matrix in order to obtain enough equations to identify the unknown damping parameters.

3.3.5 Hybrid and other methods

To conclude the literature review, there are other methods which differ from the three main groups and use different types of input together in order to improve the performance of the identification.

Srikantha Phani and Woodhouse

Srikantha Phani and Woodhouse [83] proposed a method which relies on both FRF measurements and modal parameters. The philosophy of the method is to combine the results from the perturbational method described in section 3.3.3 by Adhikari and Woodhouse [100] developed from the equations by Lord Rayleigh [9] with a series expansion for the FRF matrix of a viscously damped system. First, the diagonal part of the modal damping matrix $\mathbf{C}'$ is obtained using the modal parameters and then the off-diagonal terms are obtained from a perturbation expansion. The FRF can be written in modal coordinates as

$$\mathbf{H}(\omega) = \left[-\omega^2 \mathbf{I} + i\omega \mathbf{C}' + \mathbf{\Lambda} \right]^{-1} \tag{3.126}$$

where $\mathbf{\Lambda}$ in this case is a diagonal matrix with squared undamped natural frequencies. From the experiments the modal damping factors determine the diagonal elements of $\mathbf{C}'$ whereas a standard series expansion is used to identify the off-diagonal terms. Defining

$$\mathbf{A}(\omega) = \mathbf{\Lambda} - \omega^2 \mathbf{I} + i\omega \mathbf{C}'_d \tag{3.127}$$

where $\mathbf{C}'_d$ is the diagonal part of $\mathbf{C}'$, it is possible to approximate $\mathbf{H}(\omega)$ as

$$\mathbf{H}(\omega) = [\mathbf{A}(\omega) + i\omega\mathbf{C}'_0]^{-1} \approx \mathbf{A}^{-1}(\omega) - i\omega\mathbf{A}^{-1}(\omega)\mathbf{C}'_0\mathbf{A}^{-1}(\omega) \tag{3.128}$$

where $\mathbf{C}'_0$ is the off-diagonal part of $\mathbf{C}'$. At this point, the full FRF matrix $\mathbf{H}(\omega)$ can be measured on the test structure and the matrix of real modes $\mathbf{U}$, damping amplification factors Q_n and natural frequencies ω_n for each mode can be extracted using standard modal identification techniques. The diagonal terms of $\mathbf{C}'$ is obtained by

$$\mathbf{C}'_{d_{nn}} = \frac{\omega_n}{Q_n} \tag{3.129}$$

the off-diagonal terms are given by

$$\mathbf{C}'_0 \approx \frac{\mathbf{A}(\omega) - \mathbf{A}(\omega)\mathbf{H}(\omega)\mathbf{A}(\omega)}{i\omega} \tag{3.130}$$

Matrix $\mathbf{C}'$ can then be converted to physical coordinates by

$$\mathbf{C} = \left[\mathbf{U}^{\mathrm{T}}\right]^{-1}\mathbf{C}'\mathbf{U} \tag{3.131}$$

Since in eq. (3.130) $\mathbf{C}'$ is frequency dependent, a least squares solution is required and can be obtained by considering the range of frequency of interest.

Other methods

In this section some other approaches which have been found in literature and have not been studied in details are listed for the sake of completeness. Caravani and Thomson [104] proposed an iterative method where the aim is to minimize the difference between the response vector of the identified system and the real system. Beliveau [105] used a Bayesian approach based on perturbation and a Newton-Raphson scheme. Fabunmi *et al.* [106] used mobility and the knowledge of mass and stiffness matrices as input of the identification method based on the transformation of the response vector as a linear combination of orthonormal basis vectors. Other useful references can be found in the works by Hasselman [107], Starek and Inman [108], Wang [109], Gaylard [110], Mottershead and Foster [111] and Roemer and Mook [112].

3.3.6 Numerical comparison

Three of the identification methods listed in this chapter (Lancaster's formula, perturbational method and inversion of the FRF matrix) have been compared [85] in a numerical simulation in order to estimate the effect of modal incompleteness on the performance of the identification. The cantilever beam shown in figure 3.5 is used for this purpose. The beam, of length 0.56 m and cross section 0.04 m

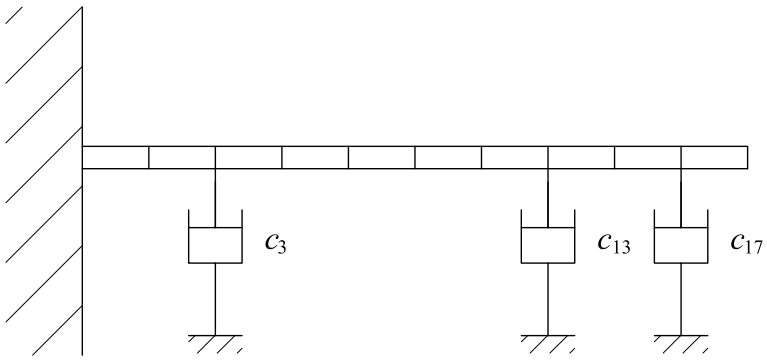

Figure 3.5: Cantilever beam with three dashpots in DOF 3, 13 and 17

(breadth) × 0.004 m (depth) has the standard material properties of aluminium. In-plane bending vibrations are considered. Grounded dashpots are connected at coordinates 3, 13 and 17 with damping coefficients of 0.2, 0.5 and 0.15 Ns/m respectively. The beam model consists of ten Euler-Bernoulli beams, having twenty coordinates and the same number of damped modes of vibration. One way of assessing the effectiveness of the identified damping matrix is to compute the eigenvalues of the system, using the known **M**, **K** and the identified **C**.
Natural frequencies and modal damping ratios determined for the computed eigenvalues are shown in tables 3.2 and 3.1 using the identified damping matrix from data consisting of five measured modes. All three methods produce estimates very close to the exact natural frequencies. In table 3.2 all three methods return estimated damping ratios that exactly reproduce the damping ratios for the first five modes. Since the data is restricted to the first five modes, the remaining modes should be undamped. It is seen that Lancaster's formula and inverse do indeed correctly reproduce the undamped modes. The perturbation method identifies damping in modes 6-20 that should not be present.

Mode	Exact	Lancaster	FRF inverse	Perturbation
1	65.45	65.45	65.45	65.45
2	410.16	410.16	410.16	410.16
3	1148.71	1148.71	1148.71	1148.71
4	2252.59	2252.59	2252.59	2252.60
5	3729.53	3729.53	3729.53	3729.53
6	5587.26	5587.26	5587.26	5587.31
7	7839.20	7839.20	7839.20	7839.24
8	10502.37	10502.37	10502.37	10502.46
9	13579.43	13579.43	13579.43	13579.51
10	16881.19	16881.19	16881.19	16881.35
11	22468.11	22468.12	22468.11	22468.32
12	27144.31	27144.30	27144.31	27145.03
13	32905.22	32905.22	32905.22	32906.51
14	39714.40	39714.40	39714.40	39718.82
15	47722.70	47722.70	47722.70	47743.74
16	57076.72	57076.73	57076.73	57189.76
17	67741.22	67741.23	67741.22	67789.80
18	79084.58	79084.65	79084.63	79272.22
19	89058.18	89058.08	89058.11	88698.73
20	111455.14	111455.07	111455.15	111265.52

Table 3.1: Identified natural frequencies (rad/s). Five measured modes.

The modes determined from the identified C and those with exact damping are compared using a generalised MAC correlation,

$$\mathrm{MAC}(j,k) = \frac{\left| \left\{ \begin{array}{c} \lambda_k \boldsymbol{\psi}_k \\ \boldsymbol{\psi}_k \end{array} \right\}^{\mathrm{T}} \mathbf{W}_j \left\{ \begin{array}{c} \lambda_j \boldsymbol{\psi}_j \\ \boldsymbol{\psi}_j \end{array} \right\} \left\{ \begin{array}{c} \lambda_j \boldsymbol{\psi}_j \\ \boldsymbol{\psi}_j \end{array} \right\}^{\mathrm{T}} \mathbf{W}_k \left\{ \begin{array}{c} \lambda_k \boldsymbol{\psi}_k \\ \boldsymbol{\psi}_k \end{array} \right\} \right|}{\left| \left\{ \begin{array}{c} \lambda_j \boldsymbol{\psi}_j \\ \boldsymbol{\psi}_j \end{array} \right\}^{\mathrm{T}} \mathbf{W}_j \left\{ \begin{array}{c} \lambda_j \boldsymbol{\psi}_j \\ \boldsymbol{\psi}_j \end{array} \right\} \left\{ \begin{array}{c} \lambda_k \boldsymbol{\psi}_k \\ \boldsymbol{\psi}_k \end{array} \right\}^{\mathrm{T}} \mathbf{W}_k \left\{ \begin{array}{c} \lambda_k \boldsymbol{\psi}_k \\ \boldsymbol{\psi}_k \end{array} \right\} \right|} \tag{3.132}$$

where the modal weight $\mathbf{W}_p$ is given by

$$\mathbf{W}_p = |\lambda_p| \begin{bmatrix} \mathbf{0} & \mathbf{M} \\ \mathbf{M} & \tilde{\mathbf{C}} \end{bmatrix} + \begin{bmatrix} -\mathbf{M} & \mathbf{0} \\ \mathbf{0} & \mathbf{K} \end{bmatrix} \tag{3.133}$$

where $\tilde{\mathbf{C}}$ is the identified damping matrix. The modal properties for the identified $\tilde{\mathbf{C}}$ and the exact $\mathbf{C}$ are denoted by the subscripts j and k respectively. This generalised MAC returns an identity matrix when $\tilde{\mathbf{C}} = \mathbf{C}$. The array given by

$$\mathbf{E}_\mu = |\mathbf{I} - \mathbf{MAC}| \tag{3.134}$$

Mode	Exact	Lancaster	FRF inverse	Perturbation
1	0.036247	0.036247	0.036247	0.036247
2	0.002208	0.002208	0.002208	0.002208
3	0.002140	0.002140	0.002140	0.002140
4	0.000711	0.000711	0.000711	0.000711
5	0.000281	0.000281	0.000281	0.000281
6	0.000433	0.000000	0.000000	0.000553
7	0.000243	0.000000	0.000000	0.000292
8	0.000097	0.000000	0.000000	0.000301
9	0.000224	0.000000	0.000000	0.000201
10	0.000186	0.000000	0.000000	0.000195
11	0.000022	0.000000	0.000000	0.000171
12	0.000027	0.000000	0.000000	0.000304
13	0.000066	0.000000	0.000000	0.000428
14	0.000031	0.000000	0.000000	0.000729
15	0.000027	0.000000	0.000000	0.002977
16	0.000040	0.000000	0.000000	0.009675
17	0.000015	0.000000	0.000000	0.004627
18	0.000004	0.000000	0.000000	0.004859
19	0.000004	0.000000	0.000000	0.134941
20	0.000006	0.000000	0.000000	0.007014

Table 3.2: Identified damping ratios. Five measured modes.

results in the null matrix for exact damping identification.

$\mathbf{E}_\mu$ computed with different numbers of measured modes are shown in figures 3.6-3.8. The method based on the inverse of the FRF consistently returns the most accurate eigenvectors and the least accurate are those given by first-order perturbation. It is seen that inverting $\mathbf{H}(i\omega)$ returns the first five eigenvectors with excellent accuracy even when only five modes are measured. The contents of the identified damping matrix determined by the three methods using different numbers of measured modes are shown in figures 3.9-3.11.

It is seen that inverting $\mathbf{H}(i\omega)$ produces three prominent peaks at the correct locations of the grounded dampers, DOFs 3, 13 and 17, even when only five modes are measured. A very accurate representation of the damping matrix is obtained using 10 modes. Lancaster's formula also produces a good estimate of $\mathbf{C}$, but not quite as good as the inverse FRF method. The first-order perturbation method results in a fully populated damping matrix with the damping distributed over

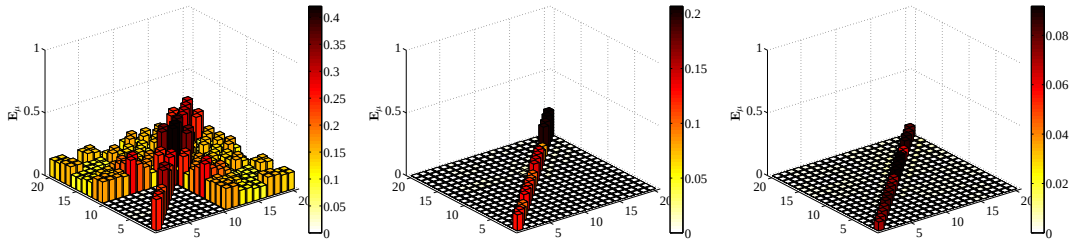

(a) 5 modes (b) 10 modes (c) 15 modes

Figure 3.6: MAC error for Lancaster's formula with different numbers of measured modes.

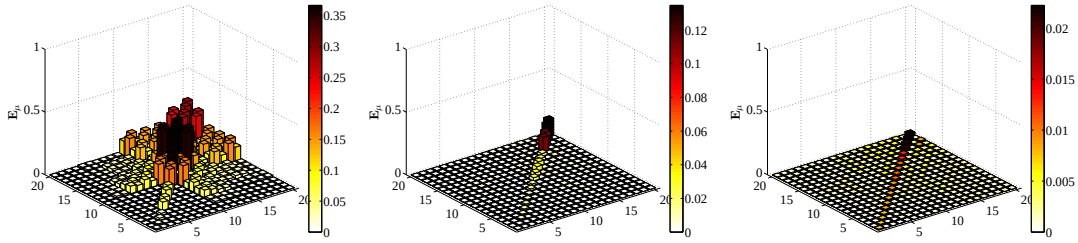

(a) 5 modes (b) 10 modes (c) 15 modes

Figure 3.7: MAC error for inversion of FRF with different numbers of measured modes.

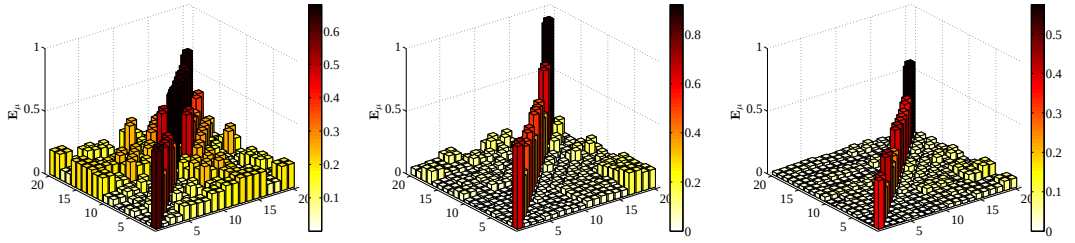

(a) 5 modes (b) 10 modes (c) 15 modes

Figure 3.8: MAC error for first-order perturbation with different numbers of measured modes.

almost all of the system coordinates. It is seen in figure 3.11 that the identified damping terms are very small for the cases of 5 and 10 measured modes. Figures 3.9-3.11 are all shown with the same scale on the vertical axis. When fifteen modes are measured prominent peaks begin to appear at coordinates 3 and 13. The error in the damping matrix is assessed in figure 3.12 using ε_C

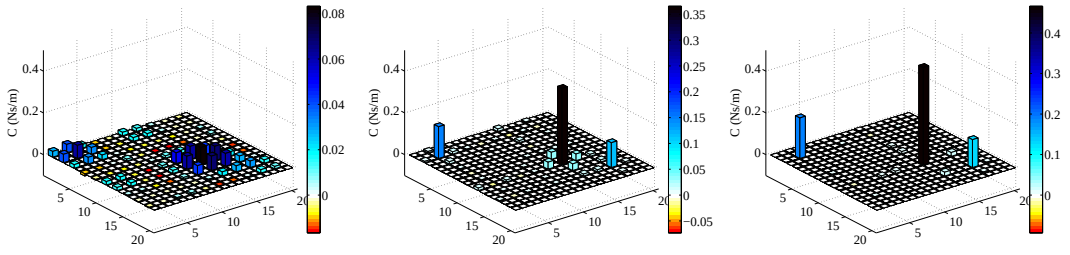

(a) 5 modes (b) 10 modes (c) 15 modes

Figure 3.9: Identified damping matrix using Lancaster's formula with different numbers of measured modes.

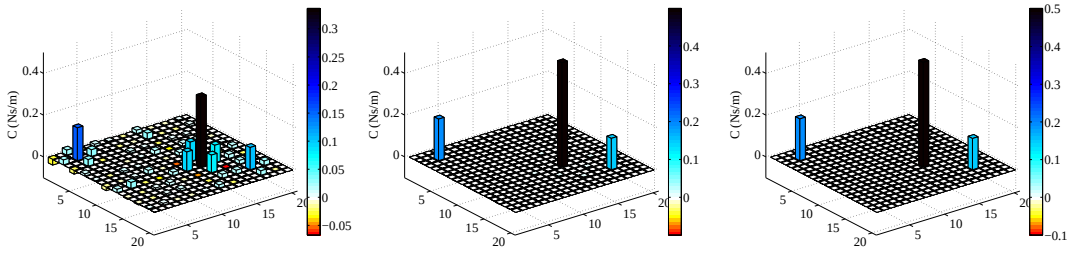

(a) 5 modes (b) 10 modes (c) 15 modes

Figure 3.10: Identified damping matrix using inversion of FRF with different numbers of measured modes.

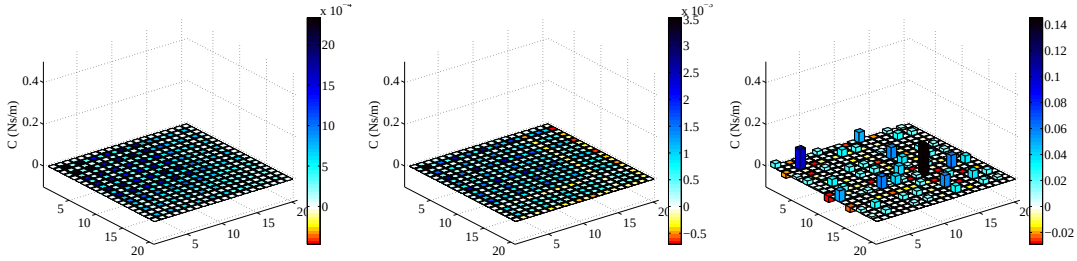

(a) 5 modes (b) 10 modes (c) 15 modes

Figure 3.11: Identified damping matrix using first-order perturbation with different numbers of measured modes.

defined as

$$\varepsilon_C = \frac{\left\|\mathbf{C} - \tilde{\mathbf{C}}\right\|_F}{\|\mathbf{C}\|_F} \cdot 100\% \tag{3.135}$$

It is seen that the inverse of $\mathbf{H}(i\omega)$ method converges most rapidly. All three methods converge to the correct damping matrix when all the modes are available for measurement. The first-order perturbation approach is investigated further in figure 3.13 where the projection error ε_p, described in section 3.3.3, is shown

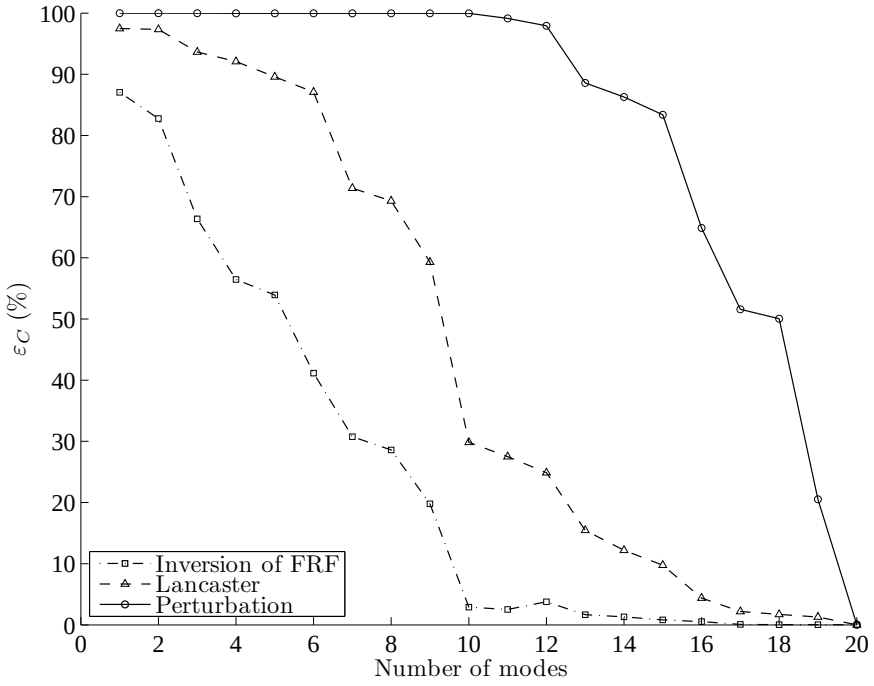

Figure 3.12: Error ε_C for the three methods

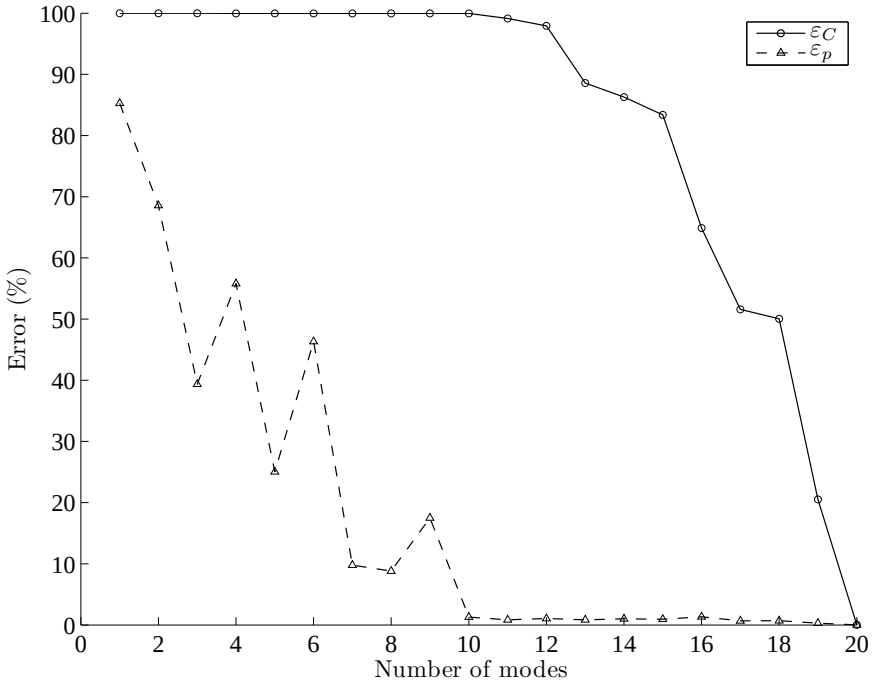

Figure 3.13: Error by first-order perturbation

together with ε_C. Even when the projection error is reduced to a very small amount, when ten or more modes are measured, a significant error persists in the terms of the damping matrix and their distribution on the beam. Prandina *et*

al. [85] demonstrated that the energy method described in section 3.3.4 and its modifications described in the following chapters are equivalent to the method based on the inversion of the FRF for the case of viscous damping. For this reason, the energy method also produces a good estimate of $\mathbf{C}$ when dealing with modal incompleteness.

3.4 Closure

Some modal damping and SDOF identification techniques have been described and a literature review of the main MDOF damping identification techniques has been presented. A numerical comparison between three of the main techniques has been performed with particular interest in the accuracy of the results when dealing with the problem of modal incompleteness, which is an unavoidable issue in most vibration tests. The MDOF identification method based on energy proposed by Liang [103] in section 3.3.4 gives the basis for the new method presented in the next chapter.

Chapter 4

Energy balance method

4.1 Advantages and drawbacks of the existing method

In this chapter a multi degree-of-freedom damping identification method based on the balance between the input energy and the energy dissipated by damping is presented. The identified damping matrix parameterisation, the spatial and modal incompleteness of measurements and the underdetermination of the system of equations are also addressed in order to improve the results of the identification. The MDOF identification methods based on energy, such as the one proposed by Liang [103], are powerful tools since they present some important advantages compared to the majority of the other techniques considered. The most important advantage is that they are able to identify different forms of damping as opposed to just viscous damping. Liang considered viscous damping and Coulomb friction but the method can be applied, for example, to quadratic damping with a few small changes in the equations. Another advantage is that from the results of the numerical simulation presented by Prandina *et al.* [85] it was found that the error in the identification of the viscous damping matrix when dealing with modal incompleteness is smaller than the one from methods based on Lancaster's formula or perturbational approach.

Unfortunately, the method proposed in [103] also presents some drawbacks. Firstly, it assumes the knowledge of the stiffness matrix which is not always available and it is also a source of uncertainty. Secondly, the assumption of having a diagonal mass matrix is valid for certain types of structures only and cannot be applied to

every case. Even if this problem can be avoided by using a similar formulation to the one for the stiffness matrix, in that case the mass matrix must be known too. Finally, the method requires some known damping coefficients which are difficult to estimate a priori.
In order to avoid these disadvantages but maintain the versatility and performance of the method, a different energy approach is proposed in this chapter.

4.2 The energy balance method

The energy balance method theory is presented in this section; after deriving the energy equation, some techniques are proposed in order to improve the identification by addressing issues such as the damping matrix parameterisation, spatial incompleteness of measurements and the underdetermination of the system of equations.

4.2.1 Theory

The equations of motion of a damped multi degree-of-freedom system can be written in the matrix form

$$\mathbf{M}\ddot{\mathbf{x}} + \mathbf{K}\mathbf{x} + \mathbf{D}\ \mathbf{g}(\mathbf{x}, \dot{\mathbf{x}}, \ddot{\mathbf{x}}) = \mathbf{f}(t) \tag{4.1}$$

where $\mathbf{D} \in \mathbb{R}^{n \times n}$ represents a generic damping matrix of coefficients multiplied by $\mathbf{g}(\mathbf{x}, \dot{\mathbf{x}}, \ddot{\mathbf{x}})$ $\mathbb{R}^{n \times 1}$, a function of displacements, velocities and accelerations. This is a generic formulation for damping, which includes viscous damping, Coulomb friction, quadratic damping and many other models. If eq. (4.1) is integrated along the motion path C, an energy equation is obtained as

$$\int_C \mathbf{M}\ddot{\mathbf{x}}\mathrm{d}x + \int_C \mathbf{K}\mathbf{x}\mathrm{d}x + \int_C \mathbf{D}\ \mathbf{g}(\mathbf{x}, \dot{\mathbf{x}}, \ddot{\mathbf{x}})\mathrm{d}x = \int_C \mathbf{f}(t)\mathrm{d}x \tag{4.2}$$

and changing the integration variable into time

$$\int_t^{t+T} \dot{\mathbf{x}}^{\mathrm{T}}\mathbf{M}\ddot{\mathbf{x}}\mathrm{d}t + \int_t^{t+T} \dot{\mathbf{x}}^{\mathrm{T}}\mathbf{K}\mathbf{x}\mathrm{d}t + \int_t^{t+T} \dot{\mathbf{x}}^{\mathrm{T}}\mathbf{D}\ \mathbf{g}(\mathbf{x}, \dot{\mathbf{x}}, \ddot{\mathbf{x}})\mathrm{d}t = \int_t^{t+T} \dot{\mathbf{x}}^{\mathrm{T}}\mathbf{f}(t)\mathrm{d}t \tag{4.3}$$

The main difference between this formulation and the one presented in [103] is the premultiplication by the full vector of velocities $\dot{\mathbf{x}}^{\mathrm{T}}$, instead of the vector

$\dot{\mathbf{x}}_i^{\mathrm{T}} = [0 \dots \dot{x}_i \dots 0]$. This modification, together with the assumption that the excitation and the response have a common fundamental period T, allows the simplification of the energy equation by removing the integration of conservative components over a full cycle of periodic motion. The kinetic and potential energy over this period

$$\int_t^{t+T} \dot{\mathbf{x}}^{\mathrm{T}} \mathbf{M} \ddot{\mathbf{x}} \mathrm{d}t = \int_t^{t+T} \dot{\mathbf{x}}^{\mathrm{T}} \mathbf{K} \mathbf{x} \mathrm{d}t = 0 \tag{4.4}$$

are equal to zero and eq. (4.3) becomes

$$\int_t^{t+T} \dot{\mathbf{x}}^{\mathrm{T}} \mathbf{D}\ \mathbf{g}(\mathbf{x}, \dot{\mathbf{x}}, \ddot{\mathbf{x}}) \mathrm{d}t = \int_t^{t+T} \dot{\mathbf{x}}^{\mathrm{T}} \mathbf{f}(t) \mathrm{d}t \tag{4.5}$$

Eq. (4.5) represents the balance between the energy dissipated by damping mechanisms on the left hand side of the equation and the energy input to the system by external forces on the right hand side. This equation is the base of the identification method proposed. An important remark is that the mass and stiffness matrices are no longer required and there are no particular restrictions on $\mathbf{g}(\mathbf{x}, \dot{\mathbf{x}}, \ddot{\mathbf{x}})$ except that $\dot{\mathbf{x}}^{\mathrm{T}} \mathbf{D}\ \mathbf{g}(\mathbf{x}, \dot{\mathbf{x}}, \ddot{\mathbf{x}})$ must be integrable. On the other side, this approach introduces an important drawback: only one equation is available for each force configuration. Whereas the method proposed in [103] provides n equations for each different excitation, in this case a different strategy in performing the experiments and solving the energy equation must be applied. The identification parameters in eq. (4.5) are represented by the coefficients in $\mathbf{D}$, which has to be parametrized in a proper way for the method to be practical.

4.2.2 Parameterisation of the damping matrix

As previously stated, $\mathbf{D} \in \mathbb{R}^{n \times n}$ represents a generic damping matrix of coefficients multiplied by $\mathbf{g}(\mathbf{x}, \dot{\mathbf{x}}, \ddot{\mathbf{x}})$ $\mathbb{R}^{n \times 1}$, a function of displacements, velocities or accelerations in order to obtain the damping forces. For example, viscous damping forces $\mathbf{d}_v$ can be expressed in the form

$$\mathbf{d}_v = \mathbf{C}\ \dot{\mathbf{x}} \tag{4.6}$$

where $\mathbf{C}$ is the viscous damping matrix. The Coulomb friction dissipative forces $\mathbf{d}_c$ can be expressed by

$$\mathbf{d}_c = \mathbf{D}_c \, \mathrm{sgn}(\dot{\mathbf{x}}) \tag{4.7}$$

where $\mathbf{D}_c$ represents the coefficients of friction multiplied by the normal forces, and so on. The different formulations can be used together in a model simply by adding all the sources in the energy equation as in this case

$$\int_t^{t+T} \dot{\mathbf{x}}^{\mathrm{T}} \mathbf{C} \dot{\mathbf{x}} \mathrm{d}t + \int_t^{t+T} \dot{\mathbf{x}}^{\mathrm{T}} \mathbf{D}_c \, \mathrm{sgn}(\dot{\mathbf{x}}) \mathrm{d}t = \int_t^{t+T} \dot{\mathbf{x}}^{\mathrm{T}} \mathbf{f}(t) \mathrm{d}t \tag{4.8}$$

For simplicity, consider viscous damping only and the following energy equation

$$\int_t^{t+T} \dot{\mathbf{x}}^{\mathrm{T}} \mathbf{C} \dot{\mathbf{x}} \mathrm{d}t = \int_t^{t+T} \dot{\mathbf{x}}^{\mathrm{T}} \mathbf{f}(t) \mathrm{d}t \tag{4.9}$$

Considering a fully populated viscous damping matrix, eq. (4.9) can be written as

$$\sum_{j=1,k=1}^{n} \left(c_{j,k} \int_0^T \dot{x}_j \dot{x}_k \mathrm{d}t \right) = \int_0^T \dot{\mathbf{x}}^{\mathrm{T}} \mathbf{f}(t) \mathrm{d}t \tag{4.10}$$

The number of equations available for the identification can be increased by using m different force configurations $\mathbf{f}_i(t)$ at different frequencies ω_i. The equations can then be arranged in a matrix form as

$$\mathbf{G} \, \mathbf{c} = \mathbf{e} \tag{4.11}$$

where $\mathbf{G}$ is the matrix of velocity integrals, $\mathbf{c}$ is a column vector containing the unknown damping coefficients and $\mathbf{e}$ contains the energy input by external forces as

$$\mathbf{G} = \begin{bmatrix} \int_0^{T_1} \dot{x_1}^2 \mathrm{d}t_{(1)} & \int_0^{T_1} \dot{x}_1 \dot{x}_2 \mathrm{d}t_{(1)} & \dots & \int_0^{T_1} \dot{x}_n \dot{x}_{n-1} \mathrm{d}t_{(1)} & \int_0^{T_1} \dot{x}_n^2 \mathrm{d}t_{(1)} \\ \dots & \dots & \dots & \dots & \dots \\ \int_0^{T_m} \dot{x_1}^2 \mathrm{d}t_{(m)} & \int_0^{T_m} \dot{x}_1 \dot{x}_2 \mathrm{d}t_{(m)} & \dots & \int_0^{T_m} \dot{x}_n \dot{x}_{n-1} \mathrm{d}t_{(m)} & \int_0^{T_m} \dot{x}_n^2 \mathrm{d}t_{(m)} \end{bmatrix} \tag{4.12}$$

$$\mathbf{c} = \begin{Bmatrix} c_{1,1} \\ c_{1,2} \\ \dots \\ c_{n,n-1} \\ c_{n,n} \end{Bmatrix} \qquad \mathbf{e} = \begin{Bmatrix} \int_0^{T_1} \dot{\mathbf{x}}^{\mathrm{T}} \mathbf{f}_1(t) \mathrm{d}t \\ \dots \\ \int_0^{T_m} \dot{\mathbf{x}}^{\mathrm{T}} \mathbf{f}_m(t) \mathrm{d}t \end{Bmatrix} \tag{4.13}$$

From a mathematical point of view, the identification problem in eq. (4.11) is underdetermined if matrix $\mathbf{G}$ has less rows than columns, i.e. if $m < n^2$ in the case of fully populated viscous damping matrix. At this point there are several different strategies which can be applied in order to remove the underdetermination of the problem or to reduce it as much as possible. The number m of different excitations cannot be increased unconditionally; each different test has a cost in terms of money and time and the number of frequencies where the damping can effectively be measured and at which an independent equation can be obtained is limited. For this reason, reducing the number of unknowns is an alternative way to reduce the underdetermination of the system of equations. The simplest way of doing this is assuming that the viscous damping matrix is diagonal as

$$\mathbf{C} = \mathrm{diag}(c_{i,i}) \in \mathbb{R}^{n \times n} \tag{4.14}$$

where $c_{i,i}$ is the damping coefficient at the i^{th} degree of freedom of the diagonal. In this particular case there would be only n unknowns and matrix $\mathbf{G}$ and vector $\mathbf{c}$ would be reduced to

$$\mathbf{G} = \begin{bmatrix} \int_0^{T_1} \dot{x_1}^2 \mathrm{d}t_{(1)} & \dots & \int_0^{T_1} \dot{x}_n^2 \mathrm{d}t_{(1)} \\ \dots & \dots & \dots \\ \int_0^{T_m} \dot{x_1}^2 \mathrm{d}t_{(m)} & \dots & \int_0^{T_m} \dot{x}_n^2 \mathrm{d}t_{(m)} \end{bmatrix} \quad \mathbf{c} = \begin{Bmatrix} c_{1,1} \\ \dots \\ c_{n,n} \end{Bmatrix} \tag{4.15}$$

Alternatively, the energy equation can be solved considering the symmetry of the viscous damping matrix. This would reduce the number of unknowns for the fully populated matrix from n^2 to $(n^2 + n)/2$. Moreover, a constraint on the positive definiteness of the viscous damping matrix can also be added to the system of equations to further improve the solution.

However, if the diagonal assumption could be considered oversimplistic, the solution for a fully populated matrix is probably unnecessary since matrices of dynamic systems are normally sparse and usually diagonal band matrices. For this reason a damping pattern approach is presented. The viscous damping matrix can be written as a summation of p different matrices in the form

$$\mathbf{C} = \sum_{i=1}^{p} c_i \mathbf{L}_i \tag{4.16}$$

where $\mathbf{L}_i \in \Re^{n\times n}$ is a matrix which indicates the location of the i^{th} viscous damping sources of amplitude c_i.

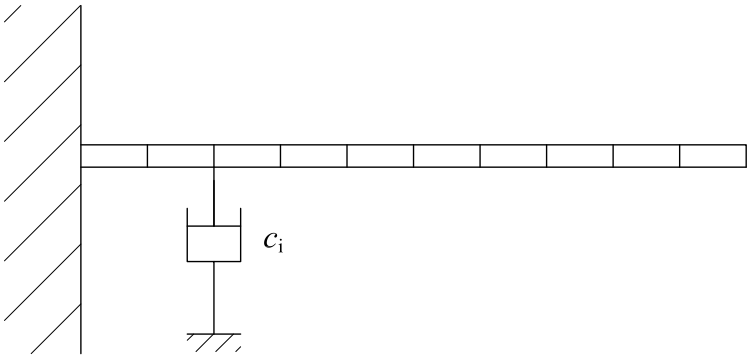

Figure 4.1: Absolute dashpot connecting DOF 2 to the ground

Consider for example a cantilever beam with ten vertical DOFs numbered from 1 to 10 starting from the clamp. In the case of an absolute dashpot connecting one degree of freedom (e.g. degree-of-freedom 2, see figure 4.1) of the structure to the ground, $\mathbf{L}_i$ takes the form

$$\mathbf{L}_i = \begin{pmatrix} 0 & 0 & 0 & \cdots & 0 \\ 0 & 1 & 0 & \cdots & 0 \\ 0 & 0 & 0 & \cdots & 0 \\ \vdots & \vdots & \vdots & \ddots & 0 \\ 0 & 0 & 0 & 0 & 0 \end{pmatrix} \tag{4.17}$$

In this case the pattern approach does not help the reduction of the number of unknowns, but helps a systematic procedure to define the damping sources in an automated way. In the case of a relative dashpot connecting two consecutive

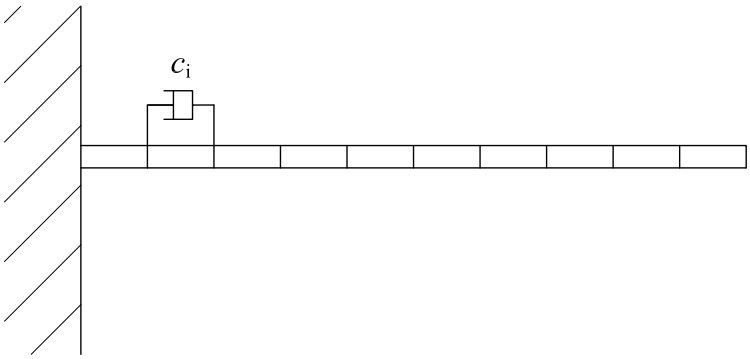

Figure 4.2: Relative dashpot connecting DOF 1 to DOF 2

degrees of freedom together (e.g degree-of-freedom 1 and 2, see figure 4.2), $\mathbf{L}_i$ takes the form

$$\mathbf{L}_i = \begin{pmatrix} 1 & -1 & 0 & \cdots & 0 \\ -1 & 1 & 0 & \cdots & 0 \\ 0 & 0 & 0 & \cdots & 0 \\ \vdots & \vdots & \vdots & \ddots & 0 \\ 0 & 0 & 0 & 0 & 0 \end{pmatrix} \tag{4.18}$$

which allows the reduction of the number of parameters to identify from 4 to 1. If the damping between two consecutive degrees of freedom is assumed to be the same for all the different couples (figure 4.3) representing, for example, the material damping between identical elements or similar connections or joints between parts of the structure, $\mathbf{L}_i$ can take the form

$$\mathbf{L}_i = \begin{pmatrix} 1 & -1 & 0 & \cdots & 0 & 0 \\ -1 & 2 & -1 & \cdots & 0 & 0 \\ 0 & -1 & 2 & \cdots & 0 & 0 \\ \vdots & \vdots & \vdots & \ddots & -1 & 0 \\ 0 & 0 & 0 & -1 & 2 & -1 \\ 0 & 0 & 0 & 0 & -1 & 1 \end{pmatrix} \tag{4.19}$$

reducing the number of non-zero unknowns, in a 10 degrees of freedom example, from 28 to 1.

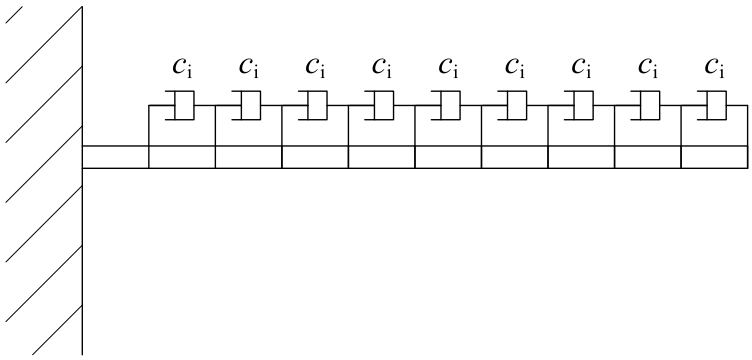

Figure 4.3: Identical relative dashpots connecting consecutive DOFs

Assuming p different possible configurations for the damping sources, the energy equation can be arranged as

$$c_1 \int_0^T \dot{\mathbf{x}}^\mathrm{T} \mathbf{L}_1 \dot{\mathbf{x}} \mathrm{d}t + c_2 \int_0^T \dot{\mathbf{x}}^\mathrm{T} \mathbf{L}_2 \dot{\mathbf{x}} \mathrm{d}t + \ldots + c_p \int_0^T \dot{\mathbf{x}}^\mathrm{T} \mathbf{L}_p \dot{\mathbf{x}} \mathrm{d}t = \int_0^T \dot{\mathbf{x}}^\mathrm{T} \mathbf{f}(t) \mathrm{d}t \tag{4.20}$$

and by exciting the structure with m excitations at different frequencies, different versions of eq. (4.20) are obtained and arranged in a matrix form

$$\begin{bmatrix} \int_0^{T_1} \dot{\mathbf{x}}^{\mathrm{T}} \mathbf{L}_1 \dot{\mathbf{x}} \mathrm{d}t & \dots & \int_0^{T_1} \dot{\mathbf{x}}^{\mathrm{T}} \mathbf{L}_p \dot{\mathbf{x}} \mathrm{d}t \\ \vdots & \vdots & \vdots \\ \int_0^{T_m} \dot{\mathbf{x}}^{\mathrm{T}} \mathbf{L}_1 \dot{\mathbf{x}} \mathrm{d}t & \dots & \int_0^{T_m} \dot{\mathbf{x}}^{\mathrm{T}} \mathbf{L}_p \dot{\mathbf{x}} \mathrm{d}t \end{bmatrix} \begin{Bmatrix} c_1 \\ \vdots \\ c_p \end{Bmatrix} = \begin{Bmatrix} \int_0^{T_1} \dot{\mathbf{x}}^{\mathrm{T}} \mathbf{f}_1(t) \mathrm{d}t \\ \vdots \\ \int_0^{T_m} \dot{\mathbf{x}}^{\mathrm{T}} \mathbf{f}_m(t) \mathrm{d}t \end{Bmatrix} \tag{4.21}$$

which can be written in the same compact form as eq. (4.11),

$$\mathbf{G}\mathbf{c} = \mathbf{e} \tag{4.22}$$

This parameterisation can considerably reduce the number of unknowns and eq. (4.22) can be solved for vector $\mathbf{c}$ using least square techniques and forcing the non-negative definiteness of the identified damping matrix at the same time. When vector $\mathbf{c}$ is calculated, the full identified viscous damping matrix can be obtained from eq. (4.16).

4.2.3 Expansion of incomplete measurements

Another common issue in damping identification and, more generally, vibration experiments is spatial incompleteness. In real experiments it is often impossible to measure accelerations, velocities and displacements at all the degrees of freedom. This happens for many reasons: a limited number of accelerometers is usually available and attaching too many accelerometers to a structure may considerably change the dynamic behaviour of the initial system by adding further mass, stiffness and damping. The amount of data acquired during a test is also limited and repeating tests and moving accelerometers all around a big structure could take several days of work. Moreover, rotational degrees of freedom are more difficult to measure than translational degrees of freedom and even if rotational accelerometers are commercially available it seems that the quality of measurement at the moment is still not as good as conventional translational accelerometers. For these reasons, matrix $\mathbf{G}$ described in the previous section cannot be fully computed since some measurements are missing. To overcome this problem there are two strategies: model reduction and modal expansion [113]. Model reduction consists of reducing the number of degrees of freedom in the

analytical model to the number of degrees of freedom measured in experiments, using techniques such as Guyan static reduction or dynamic reduction. Modal expansion consists in expanding the measured data to the number of degrees of freedom of the analytical model.

It has been stated before that one of the advantages of the energy method is the fact that an analytical model is not necessary but in chapter 3 the importance of having information about the location of damping (MDOF spatial identification) rather than a single scalar for each mode (modal damping) has also been considered. In order to apply the energy method and have useful information about the location of damping in large structures, modal expansion of measurements could be necessary, so stiffness and mass matrix of the analytical model are required. The chosen method for expanding the measurements uses concepts similar to the ones used by Jalali *et al.* [114]. Consider the full vector of velocities $\dot{\mathbf{x}}_f(t) \in \mathbb{R}^{n\times 1}$ necessary to compute $\mathbf{G}$ and the set of accelerations $\ddot{\mathbf{x}}_m(t) \in \mathbb{R}^{p\times 1}$ measured at p different degrees of freedom, where $p < n$. If the damping is small and the system is excited by a single frequency harmonic force close to the i^{th} natural frequency, the acceleration response of the structure may be written in the form

$$\ddot{\mathbf{x}}_f = \boldsymbol{\Phi}_i \ddot{q}_i(t) \tag{4.23}$$

where $\ddot{\mathbf{x}}_f(t) \in \mathbb{R}^{n\times 1}$ is the full vector of accelerations, $\boldsymbol{\Phi}_i \in \mathbb{R}^{n\times 1}$ is the full i^{th} mode shape of the undamped structure obtained from the analytical model and $\ddot{q}_i(t)$ is the modal acceleration. By using this approximate formulation it is possible to estimate $\ddot{q}_i(t)$ from the experimental measurements and then substitute into eq. (4.23) to obtain the complete set of data. Consider eq. (4.23) for the degrees of freedom of the incomplete measurements only

$$\ddot{\mathbf{x}}_m = \boldsymbol{\Phi}_{m_{(i)}} \ddot{q}_i(t). \tag{4.24}$$

where $\boldsymbol{\Phi}_{m_{(i)}}$ is the incomplete i^{th} mode shape in the form

$$\boldsymbol{\Phi}_{m_{(i)}} = \begin{bmatrix} \phi_1 \\ \dots \\ \phi_p \end{bmatrix} \tag{4.25}$$

containing the p measured degrees of freedom. If the excitation is harmonic at a single frequency ω_i, the response of the system will be harmonic too and generally

would contain higher harmonics due to nonlinearities. The modal coordinate $\ddot{q}(t)$ may be represented using

$$\ddot{q}_i(t) = \sum_{k=1}^{n} (A_k \sin(k\omega_i t) + B_k \cos(k\omega_i t)) \tag{4.26}$$

For simplicity, consider the linear case without higher harmonics so eq. (4.26) is reduced to

$$\ddot{q}_i(t) = A\sin(\omega_i t) + B\cos(\omega_i t) \tag{4.27}$$

By substituting eq. (4.27) in eq. (4.24), it is possible to rearrange the equation for each time instant from t_0 to t_{end} in a matrix form so that

$$\begin{bmatrix} \phi_1 \sin(\omega_i t_0) & \phi_1 \cos(\omega_i t_0) \\ \dots & \dots \\ \phi_p \sin(\omega_i t_0) & \phi_p \cos(\omega_i t_0) \\ \dots & \dots \\ \phi_1 \sin(\omega_i t_{end}) & \phi_1 \cos(\omega_i t_{end}) \\ \dots & \dots \\ \phi_p \sin(\omega_i t_{end}) & \phi_p \cos(\omega_i t_{end}) \end{bmatrix} \begin{bmatrix} A \\ B \end{bmatrix} = \begin{bmatrix} \ddot{x}_1(t_0) \\ \dots \\ \ddot{x}_p(t_0) \\ \dots \\ \ddot{x}_1(t_{end}) \\ \dots \\ \ddot{x}_p(t_{end}) \end{bmatrix} \tag{4.28}$$

Using a least squares procedure, A and B can be determined. The analytical integration of eq. (4.27) can be used to calculate the modal coordinate velocity $\dot{q}_i(t)$ and the modal coordinate displacement $q_i(t)$ as

$$\dot{q}_i(t) = \frac{1}{\omega_i}(-A\cos(\omega_i t) + B\sin(\omega_i t)) \tag{4.29}$$

$$q_i(t) = \frac{1}{\omega_i^2}(-A\sin(\omega_i t) - B\cos(\omega_i t)) \tag{4.30}$$

and to reconstruct the full vector of velocities by

$$\dot{\mathbf{x}}_f = \boldsymbol{\Phi}_i \cdot \dot{q}_i(t). \tag{4.31}$$

to be used in the calculation of $\mathbf{G}$.

4.2.4 Localisation of damping

The energy equation per se does not give direct information about the location of damping. However, each column of matrix $\mathbf{G}$ is related to a specific degree of freedom or to a specific hypothetical damping configuration $\mathbf{L}_i$. These columns are vectors which will be linearly combined through the damping coefficients c_i

to obtain the vector of external energy $\mathbf{e}$. Since the problem is often underdetermined, as previously discussed, locating the damping means understanding which columns of $\mathbf{G}$ are the most suitable to represent vector $\mathbf{e}$. One way of choosing the "best" columns is using a criterion based on the angle between vectors. This method was used by Friswell *et al.* [115] for a different application in model updating. The angle ϑ between two vectors $\mathbf{a}$ and $\mathbf{b}$ can be calculated by

$$\vartheta = \cos^{-1}\left(\frac{\mathbf{a}^{\mathrm{T}}\mathbf{b}}{\sqrt{\mathbf{a}^{\mathrm{T}}\mathbf{a}}\cdot\sqrt{\mathbf{b}^{\mathrm{T}}\mathbf{b}}}\right) \tag{4.32}$$

Among the large number of columns of matrix $\mathbf{G}$, a certain s number of columns with the smallest value of ϑ is selected. From a vector point of view, these columns are the most parallel to the vector $\mathbf{e}$ so they are the best representative in a one-dimensional approximation. After selecting these columns, the concept of angle between subspaces is introduced [116]. Consider the two matrices $\mathbf{A} \in \mathbb{R}^{n\times m}$ and $\mathbf{B} \in \mathbb{R}^{n\times q}$. An orthogonal basis for these subspaces can be obtained by the QR algorithm

$$\mathbf{A} = \mathbf{Q}_A\mathbf{R}_A \tag{4.33}$$

$$\mathbf{B} = \mathbf{Q}_B\mathbf{R}_B \tag{4.34}$$

where $\mathbf{Q}_A$ and $\mathbf{Q}_B$ are orthogonal matrices of size $n\times m$ and $n\times q$ respectively and $\mathbf{R}_A$ and $\mathbf{R}_B$ are upper triangular. If $q < m$ there will be q principal angles between the subspaces, ϑ_i, which are computed from the singular value decomposition of $\mathbf{Q}_A^{\mathrm{T}}\mathbf{Q}_B$. Thus

$$\cos(\vartheta_i) = \sigma_i(\mathbf{Q}_A^{\mathrm{T}}\mathbf{Q}_B) \tag{4.35}$$

where $\sigma_i()$ indicates the i^{th} singular value. Again, it is now possible to select a number s of subsets of two columns of $\mathbf{G}$ that have the smallest angle with $\mathbf{e}$. These subsets were created using combinations of one of the previously selected vectors with the other columns of $\mathbf{G}$. This method can then be applied for bigger subsets of three columns and so on. When the angle between these subsets and $\mathbf{e}$ is sufficiently small, the selection can be stopped and only the chosen columns, which carry spatial information, will be used to solve the energy equation. This criterion does not guarantee the correct location of the sources of damping but gives a physically meaningful location from an energy point of view and for the

range of frequencies used. In the next chapter the results of numerical simulations show that in most cases the angle criterion leads to the correct location in most cases and even when it does not, the identified location is close to the correct one and the amplitude of the damping coefficient varies accordingly to the energy dissipation.

4.2.5 Solution of the energy equation

The solution of the energy equation (4.11) is a basic linear least squares problem which can be stated as follow [117]:

Given a real $m \times n$ *matrix* $\mathbf{A}$ *of rank* $k \leq \min(m, n)$*, and given a real* m*-vector* $\mathbf{b}$*, find a real* n*-vector* $\mathbf{x}$ *minimizing the euclidean length of* $\mathbf{Ax} - \mathbf{b}$*.*

This problem can lead to six different cases:

1. $m = n$, $\mathbf{Ax} = \mathbf{b}$, $\text{rank}(\mathbf{A}) = m = n$
2. $m = n$, $\mathbf{Ax} \cong \mathbf{b}$, $\text{rank}(\mathbf{A}) = k < m = n$
3. $m > n$, $\mathbf{Ax} \cong \mathbf{b}$, $\text{rank}(\mathbf{A}) = n < m$
4. $m > n$, $\mathbf{Ax} \cong \mathbf{b}$, $\text{rank}(\mathbf{A}) = k < n < m$
5. $m < n$, $\mathbf{Ax} = \mathbf{b}$, $\text{rank}(\mathbf{A}) = m < n$
6. $m < n$, $\mathbf{Ax} \cong \mathbf{b}$, $\text{rank}(\mathbf{A}) = k < m < n$

Most of the simulations and experiments performed in this research fall into cases 5 and 6, since the number of useful single frequency harmonic excitations m is always smaller than the number of damping parameters to identify n, which are normally of the same order of the number of degrees of freedom or larger. This was deliberately done in simulations (where the number of possible force configurations can increase considerably since there are no physical constraints) in order to simulate real engineering problems on large structures with thousands of degrees of freedom which cannot be practically excited with the same amount of different force configurations. More precisely, case 5 is the most common case since matrix $\mathbf{G}$ is almost always of rank m. However, in some cases some rows

of matrix $\mathbf{G}$ were very close to being linearly dependent, especially when the two different excitations were similar in terms of frequency, amplitude and location. As it has already been mentioned, the solution can be achieved using the angle criterion and reducing the problem to the square problem (case 1) which possess a single solution or an overdetermined problem (case 3) which can be solved by pseudo-inverting matrix $\mathbf{G}$. Another way of solving the equation, which gives good results especially with real data, has been found to be the non-negative least squares algorithm (also known as NNLS in [117]) which minimise the norm of $\mathbf{Ax} - \mathbf{b}$ subject to $\mathbf{x} \geq 0$. If the damping matrix is parameterised as described in section 4.2.2, forcing $\mathbf{x} \geq 0$ (which in this case represents the vector of the damping coefficients of the dashpots physically connected to different degrees of freedom) automatically means forcing the non-negative definiteness of the damping matrix, which is what is expected from a passive structure. On the other hand forcing $\mathbf{x} \geq 0$, even if reasonable from a physical point of view, constraints the solution from a mathematical point of view so that the solution may be not exact ($\mathbf{Ax} \neq \mathbf{b}$) even for case 1 and 5. This never happened in simulations, where the added damping was viscous or in other known forms, but happened in experiments where the model for damping is assumed to be viscous but is in fact an uncertain approximation.

4.3 Energy method and inverse FRF equivalence

In the case of linear viscous damping only, the energy method provides exactly the same solution of the identification methods based on the inversion of the receptance matrix described in chapter 3. Specifically eq. (3.57) in the case where $\mathbf{D}_s$ is zero can be related to eq. (4.9), demonstrating a mathematical equivalence of the two methods despite the different kinds of measurement and processing used, with all advantages and drawbacks related. In eq. (4.9), $\mathbf{f}(t)$ can be expressed as

$$\mathbf{f}(t) = \left\{ \begin{array}{c} f_1 \\ f_2 \\ \cdots \\ f_n \end{array} \right\} \cos(\omega t) = \mathbf{f} \cos(\omega t) \tag{4.36}$$

If the system is linear as in this case, the vector of velocities $\dot{\mathbf{x}}(t)$ can be written in the following way

$$\dot{\mathbf{x}}(t) = -\omega \left\{ \begin{array}{c} \Re(x_1) \\ \Re(x_2) \\ \cdots \\ \Re(x_n) \end{array} \right\} \sin(\omega t) + \omega \left\{ \begin{array}{c} \Im(x_1) \\ \Im(x_2) \\ \cdots \\ \Im(x_n) \end{array} \right\} \cos(\omega t) \tag{4.37}$$

or in condensed form

$$\dot{\mathbf{x}}(t) = -\omega \left\{ \begin{array}{c} a_1 \\ a_2 \\ \cdots \\ a_n \end{array} \right\} \sin(\omega t) + \omega \left\{ \begin{array}{c} b_1 \\ b_2 \\ \cdots \\ b_n \end{array} \right\} \cos(\omega t) = -\omega \mathbf{a} \sin(\omega t) + \omega \mathbf{b} \cos(\omega t) \tag{4.38}$$

The two quantities inside the integrals become

$$\begin{aligned} \dot{\mathbf{x}}^{\mathrm{T}} \mathbf{C} \dot{\mathbf{x}} =& \mathbf{a}^{\mathrm{T}} \omega^2 \mathbf{C} \mathbf{a} \sin^2(\omega t) - \mathbf{a}^{\mathrm{T}} \omega^2 \mathbf{C} \mathbf{b} \sin(\omega t) \cos(\omega t) + \\ & - \mathbf{b}^{\mathrm{T}} \omega^2 \mathbf{C} \mathbf{a} \sin(\omega t) \cos(\omega t) + \mathbf{b}^{\mathrm{T}} \omega^2 \mathbf{C} \mathbf{b} \cos^2(\omega t) \end{aligned} \tag{4.39}$$

and

$$\dot{\mathbf{x}}^{\mathrm{T}} \mathbf{f} = -\omega \mathbf{a}^{\mathrm{T}} \mathbf{f} \sin(\omega t) \cos(\omega t) + \omega \mathbf{b}^{\mathrm{T}} \mathbf{f} \cos^2(\omega t) \tag{4.40}$$

and since

$$\int_0^{2\pi} \cos^2(\omega t) \mathrm{d}(\omega t) = \int_0^{2\pi} \sin^2(\omega t) \mathrm{d}(\omega t) = \pi \tag{4.41}$$

$$\int_0^{2\pi} \cos(\omega t) \sin(\omega t) \mathrm{d}(\omega t) = 0 \tag{4.42}$$

then eq. (4.9) may be cast in the simplified form

$$\mathbf{a}^{\mathrm{T}} (\omega \mathbf{C}) \mathbf{a} + \mathbf{b}^{\mathrm{T}} (\omega \mathbf{C}) \mathbf{b} = \mathbf{b}^{\mathrm{T}} \mathbf{f} \tag{4.43}$$

Now, assuming that $\mathbf{f} = \mathbf{e}_i$ where $\mathbf{e}_i$ is the i^{th} column of the identity matrix, the response to this i^{th} force input may be then expressed as

$$\mathbf{x}_i = \left\{ \begin{array}{c} h_{1i} \\ h_{2i} \\ \cdots \\ h_{ni} \end{array} \right\} \tag{4.44}$$

so that

$$\mathbf{a}_i = \Re \left\{ \begin{array}{c} h_{1i} \\ h_{2i} \\ \cdots \\ h_{ni} \end{array} \right\} \quad \mathbf{b}_i = \Im \left\{ \begin{array}{c} h_{1i} \\ h_{2i} \\ \cdots \\ h_{ni} \end{array} \right\} \tag{4.45}$$

where h_{ji} is the receptance at degree of freedom j when exciting the structure at degree of freedom i. Eq. (4.43) becomes

$$\mathbf{a}_i^{\mathrm{T}}(\omega\mathbf{C})\mathbf{a}_i + \mathbf{b}_i^{\mathrm{T}}(\omega\mathbf{C})\mathbf{b}_i = \mathbf{b}_i^{\mathrm{T}}\mathbf{e}_i \tag{4.46}$$

From the definition of receptance matrix

$$(\Re(\mathbf{H}^{-1}) + i\Im(\mathbf{H}^{-1}))(\Re(\mathbf{H})_i + i\Im(\mathbf{H})) = \mathbf{I} \tag{4.47}$$

so that

$$\Re(\mathbf{H}^{-1})\mathbf{a}_i - \Im(\mathbf{H}^{-1})\mathbf{b}_i = \mathbf{e}_i \tag{4.48}$$

$$\Re(\mathbf{H}^{-1})\mathbf{b}_i + \Im(\mathbf{H}^{-1})\mathbf{a}_i = \mathbf{0} \tag{4.49}$$

and

$$-\omega^2\mathbf{M} + \mathbf{K} = \Re(\mathbf{H}^{-1}(i\omega)) \tag{4.50}$$

$$-\omega\mathbf{C} = \Im(\mathbf{H}^{-1}(i\omega)) \tag{4.51}$$

Eqs. (4.48) and (4.49) may be cast as

$$(-\omega^2\mathbf{M} + \mathbf{K})\mathbf{a}_i - \omega\mathbf{C}\mathbf{b}_i = \mathbf{e}_i \tag{4.52}$$

$$\omega\mathbf{C}\mathbf{a}_i + (-\omega^2\mathbf{M} + \mathbf{K})\mathbf{b}_i = \mathbf{0} \tag{4.53}$$

From eq. (4.53)

$$\mathbf{b}_i = -(-\omega^2\mathbf{M} + \mathbf{K})^{-1}(\omega\mathbf{C})\mathbf{a}_i \tag{4.54}$$

and premultiplying eq. (4.52) by $\mathbf{b}_i^{\mathrm{T}}$ and combining with eq. (4.54), the following equation is obtained from the receptance matrix

$$\mathbf{a}_i^{\mathrm{T}}(\omega\mathbf{C})\mathbf{a}_i + \mathbf{b}_i^{\mathrm{T}}(\omega\mathbf{C})\mathbf{b}_i = \mathbf{b}_i^{\mathrm{T}}\mathbf{e}_i \tag{4.55}$$

which is the same as eq. (4.46) from the energy method. In chapter 3 it has been shown that methods based on the inversion of the receptance are the ones which have the best results when dealing with modal incompleteness. By demonstrating this equivalence it is stated that the energy method should perform in the same way for the case of viscous damping, with the advantage of the possibility of being applied to different types of damping too.

4.4 Closure

The theory of the damping identification method based on the balance of the energy input by external forces with the energy dissipated by damping has been presented. A damping-pattern matrix parameterisation has been proposed in order to reduce the number of unknowns of the identification problem together with a criterion based on the angle between vectors to localize the main damping sources when the problem is uderdetermined. In the case of viscous damping, the method is equivalent to methods based on the inversion of receptance which were found to be the best when dealing with modal incompleteness. In the next chapter the method will be used to identify sources of damping in several numerical simulations performed in Matlab and Simulink in order to validate the proposed theory.

Chapter 5

Numerical simulations

5.1 Introduction

Several numerical simulations have been performed in order to validate the proposed method. In this chapter a selection of the most interesting results is presented to show the advantages of the method together with some considerations on the physical meaning of the energy-equivalent identified damping, incompleteness of data and size of the model. The simulations include a ten-element cantilever beam with absolute viscous dashpots and spatial incompleteness of the measured accelerations, a similar example including Coulomb friction and a larger problem on a 196 degrees of freedom simplified aircraft wing.

5.2 Cantilever beam

The first numerical simulation consists of a ten element (22 degrees of freedom) cantilever beam clamped at one side and free to vibrate on the other side. The DOF numbering is shown in figure 5.1. The two clamped degrees of freedom are not considered so that the size of the system matrices is 20×20. The beam dimensions are $4 \times 40 \times 560$ mm and the material is aluminium.

5.2.1 Case 1: same damping coefficients

Four viscous dashpots (figure 5.2) are attached between the ground and degrees of freedom number 3, 5, 13 and 17, as the absolute dashpot described in section 4.2.2, figure 4.1. The viscous damping coefficient of the four dashpots is set to the same value of 0.1 Ns/m as shown in table 5.1. After selecting an appropriate

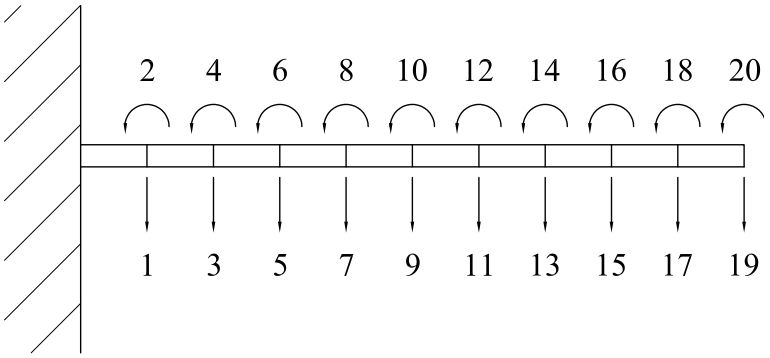

Figure 5.1: Cantilever beam and DOFs numbering

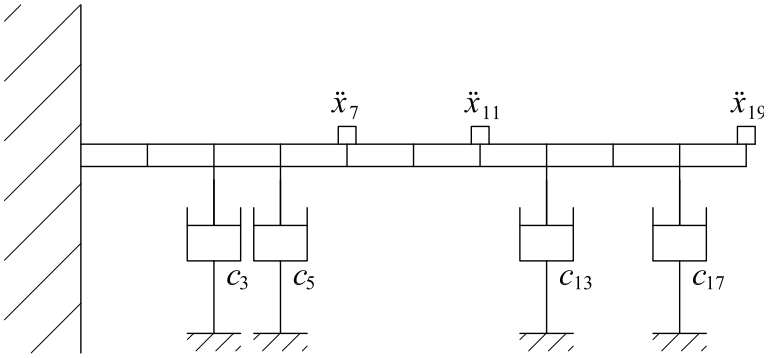

Figure 5.2: Numerical simulation: cantilever beam with four absolute viscous dashpots attached at DOF 3, 5, 13 and 17 with acceleration measurements at DOF 7, 11 and 19.

set of single frequency excitations, the signals from three accelerometers, contaminated with 5% white noise and applied on degrees of freedom 7, 11 and 19 are measured and the full vector of velocities is derived using the expansion described in section 4.2.3. A realistic damping pattern (section 4.2.2) is defined according to the engineering knowledge of the structure and the matrix $\mathbf{G}$ and vector $\mathbf{e}$ are computed to obtain the energy equation. The minimum angle criterion described

Dashpots DOF				Damping coefficients (Ns/m)			
3	5	13	17	0.1	0.1	0.1	0.1

Table 5.1: Dashpots configuration for case 1.

in section 4.2.4 is used to locate the main damping sources and the non-negative least squares algorithm [117] is used to extract the values of the equivalent damp-

ing coefficients. The first step is the selection of the force configurations used to excite the structure. Theoretically, the method would work with any set of m different excitations which leads to a well conditioned matrix $\mathbf{G}$ so the choice could fall into a sufficient number of forces applied in different places at different random frequencies. In practice changing the location of the exciting force (i.e. moving a shaker along the length of the beam) could be unnecessarily expensive and time consuming, moreover choosing random frequencies is also not the optimal selection from an engineering point of view. It has been shown in chapter 2 that the effect of damping is mainly visible in the proximity of resonances, so if the excitations are at frequencies close to those of the modes of vibration of the structure, the information held by this kind of test is likely to be more valuable when dealing with the identification of damping. In this example eight different excitations are used and consist of single frequency harmonic forces applied at DOF 19 at frequencies close to the first 8 bending modes, respectively at 10, 65, 182, 358, 593, 889, 1247 and 1671 Hz. The responses of the system excited with these forces is simulated in Simulink and the measurement of the accelerations at degrees of freedom 7, 11 and 19 is obtained. It is very important at this stage to wait for the transient to end before measuring the accelerations. If the transient is still present, the energy balance equation used for the identification is wrong since the response is not periodic and the energy of conservative forces does not vanish.

For this simple example the parameterisation consists in 20 localisation matrices as eq. (4.17), one for each degree of freedom (rotational degrees of freedom included) representing the 20 possible locations of an indefinite number of absolute dashpots. It must be considered that in a general identification problem it is not always known where the damping sources are and how many they are. In this simulation there are many issues involved: spatial incompleteness (3 accelerometers only for 20 DOFs), modal incompleteness (excitations at frequencies close to 8 out of 20 modes), uncertainty on the location and quantity of the sources of damping (20 *possible* locations for a maximum of 8 equivalent absolute viscous dashpots to identify).

After expanding the measurements and deriving velocities as explained in section

4.2.3, the integrals present in matrix $\mathbf{G}$ have to be computed. Remembering the energy matrix equation, for this case is

$$\begin{bmatrix} \int_0^{T_1} \dot{\mathbf{x}}^{\mathrm{T}}\mathbf{L}_1\dot{\mathbf{x}}\mathrm{d}t & \dots & \int_0^{T_1} \dot{\mathbf{x}}^{\mathrm{T}}\mathbf{L}_{20}\dot{\mathbf{x}}\mathrm{d}t \\ \vdots & \vdots & \vdots \\ \int_0^{T_8} \dot{\mathbf{x}}^{\mathrm{T}}\mathbf{L}_1\dot{\mathbf{x}}\mathrm{d}t & \dots & \int_0^{T_8} \dot{\mathbf{x}}^{\mathrm{T}}\mathbf{L}_{20}\dot{\mathbf{x}}\mathrm{d}t \end{bmatrix} \begin{Bmatrix} c_1 \\ \vdots \\ c_{20} \end{Bmatrix} = \begin{Bmatrix} \int_0^{T_1} \dot{\mathbf{x}}^{\mathrm{T}}\mathbf{f}_1(t)\mathrm{d}t \\ \vdots \\ \int_0^{T_8} \dot{\mathbf{x}}^{\mathrm{T}}\mathbf{f}_8(t)\mathrm{d}t \end{Bmatrix} \tag{5.1}$$

or

$$\mathbf{G}\mathbf{c} = \mathbf{e} \tag{5.2}$$

If the accelerations are assumed to be in the form

$$\ddot{x}_i(t) = a\sin(\omega_i t) + b\cos(\omega_i t) \tag{5.3}$$

where ω_i is the frequency of the excitation, velocities can be written as

$$\dot{x}_i(t) = \frac{1}{\omega_i}(-a\cos(\omega_i t) + b\sin(\omega_i t)) \tag{5.4}$$

so the integrals in $\mathbf{G}$ can be calculated analytically. Consider the expanded acceleration measurements for the i^{th} excitation in the form

$$\ddot{\mathbf{x}}_i(t) = \begin{Bmatrix} \ddot{x}_{1_i}(t) \\ \vdots \\ \ddot{x}_{20_i}(t) \end{Bmatrix} = \begin{Bmatrix} a_{1_i} \\ \vdots \\ a_{20_i} \end{Bmatrix} \sin(\omega_i t) + \begin{Bmatrix} b_{1_i} \\ \vdots \\ b_{20_i} \end{Bmatrix} \cos(\omega_i t) \tag{5.5}$$

or

$$\ddot{\mathbf{x}}_i(t) = \mathbf{a}_i\sin(\omega_i t) + \mathbf{b}_i\cos(\omega_i t) \tag{5.6}$$

so that velocities and displacements can be calculated by analytical integration as

$$\dot{\mathbf{x}}_i(t) = \frac{1}{\omega_i}\left(-\mathbf{a}_i\cos(\omega_i t) + \mathbf{b}_i\sin(\omega_i t)\right) \tag{5.7}$$

$$\mathbf{x}_i(t) = -\frac{1}{\omega_i^2}\left(\mathbf{a}_i\sin(\omega_i t) + \mathbf{b}_i\cos(\omega_i t)\right) \tag{5.8}$$

Consider now the integrals in the j^{th} column of matrix $\mathbf{G}$

$$\int_0^{T_i} \dot{\mathbf{x}}^{\mathrm{T}}\mathbf{L}_j\dot{\mathbf{x}}\mathrm{d}t \tag{5.9}$$

the period T_i for the linear case is equivalent to the period of the excitation, then

$$T_i = \frac{2\pi}{\omega_i} \tag{5.10}$$

so that the analytical solution of the integral becomes

$$\int_0^{T_i} \dot{\mathbf{x}}^{\mathrm{T}} \mathbf{L}_j \, \dot{\mathbf{x}} \, dt = \frac{\pi}{\omega_i^3} \left(\mathbf{a}_i^{\mathrm{T}} \mathbf{L}_j \mathbf{a}_i + \mathbf{b}_i^{\mathrm{T}} \mathbf{L}_j \mathbf{b}_i \right) \tag{5.11}$$

Regarding the vector of input energy $\mathbf{e}$, each force can be expressed as

$$\mathbf{f}_i(t) = \left\{ \begin{array}{c} 0 \\ \vdots \\ f_i(t) \\ 0 \end{array} \right\} \tag{5.12}$$

with $f_i(t)$ in the corresponding degree of freedom (in this case DOF 19) which can also be fit to a sinusoidal curve in the form

$$f_i(t) = r_i \sin(\omega_i t) + s_i \cos(\omega_i t) \tag{5.13}$$

so that the entries of $\mathbf{e}$ can be calculated as

$$\int_0^{T_i} \dot{\mathbf{x}}^{\mathrm{T}} \mathbf{f}_i(t) \mathrm{d}t = \frac{\pi}{\omega_i^2} \left(b_{19_i} r_i - a_{19_i} s_i \right) \tag{5.14}$$

When matrix $\mathbf{G}$ and vector $\mathbf{e}$ have been calculated, the localisation of damping through the minimum angle criterion can start. The first step is finding the smallest angle between each column $\mathbf{g}_i$ of matrix $\mathbf{G}$ and the vector $\mathbf{e}$, using the formula

$$\vartheta_i = \cos^{-1} \left(\frac{\mathbf{g}_i^{\mathrm{T}} \mathbf{e}}{\sqrt{\mathbf{g}_i^{\mathrm{T}} \mathbf{g}_i} \cdot \sqrt{\mathbf{e}^{\mathrm{T}} \mathbf{e}}} \right) \tag{5.15}$$

The smallest 5 angles are selected, corresponding to the degrees of freedom displayed in table 5.2. From this first calculation, two aspects can be observed.

DOF	ϑ_i (deg)
19	6.505
13	6.899
17	6.905
15	13.468
11	18.420

Table 5.2: Selection of smallest angles.

Firstly, the degree of freedom corresponding to the smallest angle (DOF 19) is

not where the dashpots actually are (3,5,13 and 17). This is not unexpected since the minimum angle criterion does not guarantee the correct location of the equivalent dashpots, especially when the number of equivalent dashpots selected (corresponding to the number of columns which in this first step is equal to one) is smaller than the actual number of damping sources. The second and third smallest angles correspond to two of the correct degrees of freedom (DOFs 13 and 17). Secondly, the five smallest angles are all related to translational degrees of freedom so it seems that this preliminary criterion "understands" that the dashpots are not rotational but they are actually acting on the vertical degrees of freedom. The selection of the columns could stop after the first step and the value of the damping coefficient of the equivalent dashpot at DOF 19 can be calculated by applying the non-negative least squares algorithm to

$$\left[\ \mathbf{g}_{19} \ \right] \left\{ \ c_{19} \ \right\} \approx \mathbf{e} \tag{5.16}$$

which leads to $c_{19} = 0.107$ Ns/m. From an energy point of view, this result means that a dashpot with this damping coefficient located at DOF 19 dissipates the same amount of energy as the four original dashpots (in a least square approximation sense and for the 8 modes considered). Even if the damping coefficient is small compared to the sum of the four dashpots that it is representing, it must be considered that DOF 19 is the one which possess the largest velocities in the selected range of frequencies so it will dissipate more energy than a similar dashpot attached, for example, at DOF 1. If the error between the actual energy vector $\mathbf{e}$ and the identified energy vector $\mathbf{e}_{id}$, calculated as

$$\mathbf{e}_{id} = \left[\ \mathbf{g}_{19} \ \right] \left\{ \ c_{19} \ \right\} \tag{5.17}$$

does not meet the desired requirements, the location of a second dashpot can be selected. Since the number of combinations will grow in a factorial way which becomes very costly in computation, the five best DOFs were kept and only the combination of these five DOFs with the other one are considered instead of all the possible combination of two locations. Using the definition of angle between subspace [116] described in section 4.2.4

$$\cos(\vartheta_i) = \sigma_i(\mathbf{Q}_{\mathbf{G}2}^{\mathrm{T}} \mathbf{Q}_{\mathbf{e}}) \tag{5.18}$$

where $\mathbf{G}_2$ is a matrix containing two columns of $\mathbf{G}$ selected as previously explained, it is now possible to select the combination with the smallest angle, which in this case corresponds to DOFs 13 and 19, and calculate the equivalent damping coefficients solving

$$\left[\begin{array}{cc} \mathbf{g}_{13} & \mathbf{g}_{19} \end{array} \right] \left\{ \begin{array}{c} c_{13} \\ c_{19} \end{array} \right\} \approx \mathbf{e} \tag{5.19}$$

by applying the non-negative least squares algorithm and re-checking the error between actual and identified energy. If the result is not satisfactory, the number of equivalent dashpots can be increased to three and so on until an acceptable error is obtained. The identification results for up to four equivalent dashpots (which corresponds to the actual number of dashpots attached to the structure) are summarised in table 5.3. It can be seen that the method leads to the cor-

Number of dashpots	Dashpots DOF				Damping coefficients (Ns/m)				ϑ_i (deg)
1	-	-	-	19	-	-	-	0.107	6.505
2	-	-	13	19	-	-	0.151	0.059	0.404
3	-	5	15	17	-	0.212	0.127	0.055	0.124
4	3	5	13	17	0.1	0.099	0.1	0.101	0.001
Original	3	5	13	17	0.1	0.1	0.1	0.1	-

Table 5.3: Results for case 1.

rect solution when a sufficient number of equivalent dashpots is selected for the identification (with some negligible differences due to the added noise). An interesting result is the equivalent configuration obtained using three dashpots; two of the three locations (DOFs 5 and 17) are correct and the third one (DOF 15) is relatively close to the correct location (DOF 13). The value of the coefficients is reasonable since the 0.212 Ns/m dashpot at DOF 5 could represent a sort of sum of the two 0.1 Ns/m dashpots at DOFs 3 and 5 and the remaining ones appears close to the expected values, considering that the number of identified parameters is smaller than the actual number necessary to describe the damping. This result has to be seen from an engineering point of view on larger and more complicated structures. The information extracted from the three dashpots equivalent system is valuable both for the location and the amplitude of the damping sources.

Moreover they have been obtained from incomplete data.

The energy equivalence is reflected in the damping ratio ζ. In table 5.4 a comparison of the damping ratio of the first 10 modes (using respectively 1, 2 and 3 equivalent dashpots) of the identified system versus the original system is shown.

Mode	$\zeta_{original}$	$\zeta_{eq}(1)$	Err %	$\zeta_{eq}(2)$	Err %	$\zeta_{eq}(3)$	Err %
1	1.41E-02	1.35E-02	4.09%	1.41E-02	0.14%	1.41E-02	0.13%
2	1.50E-03	2.16E-03	44.15%	1.50E-03	0.07%	1.50E-03	0.22%
3	1.02E-03	7.71E-04	24.74%	8.95E-04	12.60%	1.04E-03	1.22%
4	3.38E-04	3.94E-04	16.66%	3.05E-04	9.68%	3.41E-04	0.95%
5	1.38E-04	2.39E-04	73.13%	1.49E-04	7.97%	1.34E-04	2.90%
6	1.90E-04	1.61E-04	14.82%	1.93E-04	1.99%	1.81E-04	4.51%
7	1.14E-04	1.17E-04	2.68%	1.18E-04	4.23%	1.01E-04	11.37%
8	5.75E-05	8.85E-05	53.99%	4.88E-05	15.07%	4.84E-05	15.81%
9	1.06E-04	6.84E-05	35.49%	7.30E-05	31.11%	1.05E-04	0.51%
10	8.51E-05	4.43E-05	47.96%	6.14E-05	27.87%	8.73E-05	2.62%

Table 5.4: Damping ratios for case 1 for the first ten modes. $\zeta_{eq}(1)$, $\zeta_{eq}(2)$ and $\zeta_{eq}(3)$ respectively indicate the damping ratios of the system with 1, 2 and 3 equivalent dashpots.

The agreement between the two systems increases with the number of columns selected and it is interesting to notice how the error for the first seven modes when using only two equivalent dashpots to represent four dashpots is smaller than 10%, which in the field of damping identification is already a reasonably positive result. The method is then capable not only of obtaining valuable information about the location and the magnitude of the single source but also to keep modal values close to the exact ones.

5.2.2 Case 1a: same damping coefficients with known location

A subcase of case 1 is considering the same problem when one or more damping locations are known. For example, consider the case when the location of the dashpot at degree of freedom 3 is known. Starting from this information, a different pattern of solutions is found by forcing the presence of DOF 3 in the column selection, summarised in table 5.5.

Number of dashpots	Dashpots DOF				Damping coefficients (Ns/m)				ϑ_i (deg)
1	3	-	-	-	0.856	-	-	-	72.055
2	3	-	-	17	0.322	-	-	0.148	2.284
3	3	-	13	19	0.060	-	0.177	0.049	0.120
4	3	5	13	17	0.1	0.099	0.1	0.101	0.001
Original	3	5	13	17	0.1	0.1	0.1	0.1	-

Table 5.5: Results for case 1a.

Despite the fact that the angle between column number 3 and the energy vector is large, adding a second dashpot to the identification process immediately reduces the angle to 2.284 degrees with reasonable results in terms of location and value. This new set of possible solutions is also valid and leads to the same solution of case 1 when four equivalent dashpots are used.

Results from case 1 and case 1a represent different sets of energy equivalent solutions to the same problem, obtained using different initial information. Which one is better is difficult to judge since it depends not only on the agreement between modal damping ratios and correct locations of the sources, but also on the problem under examination. An incomplete set of dashpot locations might represent certain modes well and this could be a practical good solution, though not the physically correct one.

5.2.3 Case 2: different damping coefficients

In case 2 the dashpots and accelerometers are located at exactly the same degrees of freedom as case 1, but the value of their viscous damping coefficients is different so that there are now large sources of damping to identify together with smaller and possibly negligible ones. The values of the damping coefficients for case 2 are shown in table 5.6. The same procedure as case 1 is used with the same forces configuration and amount of noise. The results are summarised in table 5.7. In this case results are qualitatively better than in case 1 for two distinct reasons. Firstly, the location of damping is always correct even using the first approximation with only one equivalent dashpot. Secondly, the order the dashpots are selected using the minimum angle criterion is from the largest to the smallest

Dashpots DOF				Damping coefficients (Ns/m)			
3	5	13	17	0.01	0.5	0.1	1

Table 5.6: Dashpots configuration for case 2.

damping coefficient. This is a good result from an engineering point of view since

Number of dashpots	Dashpots DOF				Value of damping coefficients (Ns/m)				ϑ_i (deg)
1	-	-	-	17	-	-	-	1.084	12.557
2	-	5	-	17	-	0.581	-	1.042	1.029
3	-	5	13	17	-	0.506	0.124	0.989	0.263
4	3	5	13	17	0.01	0.5	0.1	1	0.001
Original	3	5	13	17	0.01	0.5	0.1	1	-

Table 5.7: Results for case 2.

in real problems there is not much information about the total number of sources of damping and one must decide at what level of approximation to stop. If, for example in this case the decision is to consider a two-dashpot equivalent system then the two most important sources are correctly located whereas the smallest ones are somehow included through a small increase in the value of the damping coefficients of the larger ones.

5.2.4 Case 3: Viscous and Coulomb friction

One of the advantages of the energy method is the fact that it is theoretically able to identify sources of damping that are different from viscous damping. To check if this feature works effectively, a simulation on the previous structure damped with both viscous dashpots and Coulomb friction devices (figure 5.3) has been tested. A total of six damping sources (three viscous and three Coulomb friction) have been attached to the cantilever beam. The values of the viscous damping coefficients and the values of the product F_c of the normal forces F_n and the friction coefficients μ

$$F_c = \mu F_n \tag{5.20}$$

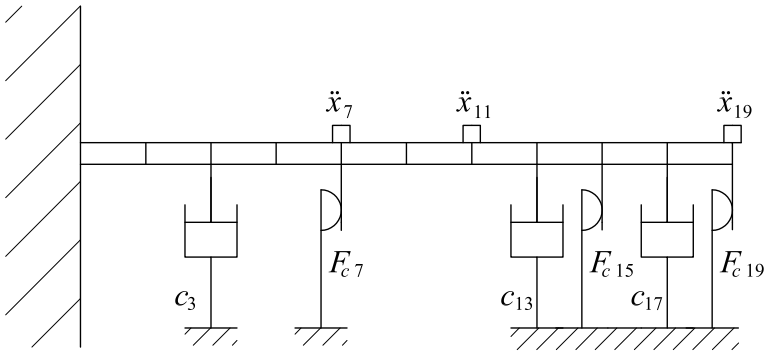

Figure 5.3: Numerical simulation: cantilever beam with three absolute viscous dashpots attached at DOF 3, 13 and 17, three Coulomb friction devices attached at DOF 7, 15 and 19 with acceleration measurements at DOF 7, 11 and 19.

as described in section 2.2.3 are displayed in table 5.8.

	Viscous damping coefficients			F_c		
DOF	3	13	17	7	15	19
Value	0.2 Ns/m	0.5 Ns/m	0.15 Ns/m	3.2 N	5.1 N	1 N

Table 5.8: Damping sources configuration for case 3.

The method works in the same way as the previous two cases with some small differences. Maintaining the same damping pattern as the previous examples for the possible location of the sources, the size of matrix $\mathbf{G}$ is doubled (8×40 instead of 8×20) since it contains the integrals of both types (viscous and Coulomb friction) in the form

$$\mathbf{G} = \begin{bmatrix} \int_0^{T_1} \dot{\mathbf{x}}^{\mathrm{T}}\mathbf{L}_1\dot{\mathbf{x}}\mathrm{d}t & \dots & \int_0^{T_1} \dot{\mathbf{x}}^{\mathrm{T}}\mathbf{L}_{20}\dot{\mathbf{x}}\mathrm{d}t & \int_0^{T_1} \dot{\mathbf{x}}^{\mathrm{T}}\mathbf{L}_1\mathrm{sgn}(\dot{\mathbf{x}})\mathrm{d}t & \dots & \int_0^{T_1} \dot{\mathbf{x}}^{\mathrm{T}}\mathbf{L}_{20}\mathrm{sgn}(\dot{\mathbf{x}})\mathrm{d}t \\ \vdots & \vdots & \vdots & \vdots & \vdots & \vdots \\ \int_0^{T_8} \dot{\mathbf{x}}^{\mathrm{T}}\mathbf{L}_1\dot{\mathbf{x}}\mathrm{d}t & \dots & \int_0^{T_8} \dot{\mathbf{x}}^{\mathrm{T}}\mathbf{L}_{20}\dot{\mathbf{x}}\mathrm{d}t & \int_0^{T_8} \dot{\mathbf{x}}^{\mathrm{T}}\mathbf{L}_1\mathrm{sgn}(\dot{\mathbf{x}})\mathrm{d}t & \dots & \int_0^{T_8} \dot{\mathbf{x}}^{\mathrm{T}}\mathbf{L}_{20}\mathrm{sgn}(\dot{\mathbf{x}})\mathrm{d}t \end{bmatrix} \tag{5.21}$$

and vector $\mathbf{c}$ is also doubled in size (it is now 40×1) in the form

$$\mathbf{c} = \left\{ \begin{array}{c} c_1 \\ \vdots \\ c_{20} \\ F_{c1} \\ \vdots \\ F_{c20} \end{array} \right\} \tag{5.22}$$

whereas the length of $\mathbf{e}$ remains unchanged (8×1) since it depends on the number of excitations only. The terms of matrix $\mathbf{G}$ have different orders of magnitude between the viscous and the Coulomb friction parts. The integrals in the first twenty columns are proportional to the squared velocities whereas the remaining columns are related to the absolute value of the velocities. This may lead to scaling problems when solving the energy equation through least squares techniques, so matrix $\mathbf{G}$ and vector $\mathbf{e}$ are normalized in order to solve the equation and subsequently the solution of the normalized equation is converted to the solution of the original equation. The integrals in the form

$$\int_0^{T_i} \dot{\mathbf{x}}^{\mathrm{T}} \mathbf{L}_j \mathrm{sgn}(\dot{\mathbf{x}}) \mathrm{d}t \tag{5.23}$$

can be solved analytically. The accelerations previously written in the form

$$\ddot{x}_i(t) = a \sin(\omega_i t) + b \cos(\omega_i t) \tag{5.24}$$

can be written as

$$\ddot{x}_i(t) = p \cos(\omega_i t - \varphi) \tag{5.25}$$

where

$$p = \sqrt{a^2 + b^2} \tag{5.26}$$

and

$$\varphi = \cos^{-1}\left(\frac{b}{p}\right) \qquad \text{if} \quad a \geq 0 \tag{5.27}$$

$$\varphi = -\cos^{-1}\left(\frac{b}{p}\right) \qquad \text{if} \quad a < 0 \tag{5.28}$$

Velocities become

$$\dot{x}_i(t) = \frac{1}{\omega_i} p \cos(\omega_i t - \varphi) \tag{5.29}$$

and assuming

$$T_i = \frac{2\pi}{\omega_i} \tag{5.30}$$

the integral combining, for example, degrees of freedom 1 and 2 will be

$$\int_0^{T_i} \dot{x}_1 \mathrm{sgn}(\dot{x}_2)\mathrm{d}t = \frac{p_1}{\omega_i} \int_0^{\frac{2\pi}{\omega_i}} \sin(\omega_i t - \varphi_1)\, \mathrm{sgn}(\sin(\omega_i t - \varphi_2))\mathrm{d}t \tag{5.31}$$

Since the function is periodic, the value of the definite integral between 0 and $2\pi/\omega_i$ is the same as the one between φ_2/ω_i and $(\varphi_2 + 2\pi)/\omega_i$. To integrate the sign function it is possible to split the integral into two parts according to

$$\mathrm{sgn}(\sin(\omega_i t - \varphi_2)) = +1 \qquad \text{for} \quad \frac{\varphi_2}{\omega_i} < t < \frac{\varphi_2 + \pi}{\omega_i} \tag{5.32}$$

$$\mathrm{sgn}(\sin(\omega_i t - \varphi_2)) = -1 \qquad \text{for} \quad \frac{\varphi_2 + \pi}{\omega_i} < t < \frac{\varphi_2 + 2\pi}{\omega_i} \tag{5.33}$$

so that

$$\int_0^{T_i} \dot{x}_1 \mathrm{sgn}(\dot{x}_2)\mathrm{d}t = \frac{p_1}{\omega_i} \left(\int_{\frac{\varphi_2}{\omega_i}}^{\frac{\varphi_2+\pi}{\omega_i}} \sin(\omega_i t - \varphi_1)\mathrm{d}t - \int_{\frac{\varphi_2+\pi}{\omega_i}}^{\frac{\varphi_2+2\pi}{\omega_i}} \sin(\omega_i t - \varphi_1)\mathrm{d}t \right) \tag{5.34}$$

which results in

$$\int_0^{T_i} \dot{x}_1 \mathrm{sgn}(\dot{x}_2)\mathrm{d}t = \frac{4p_1}{\omega_i^2} \cos(\varphi_1 - \varphi_2) \tag{5.35}$$

In a n degrees of freedom system (as in this case) for the i^{th} excitation the two vectors are defined as

$$\mathbf{p}_i = \begin{Bmatrix} p_{1_i} \\ \vdots \\ p_{n_i} \end{Bmatrix} \quad \boldsymbol{\phi}_i = \begin{Bmatrix} \varphi_{1_i} \\ \vdots \\ \varphi_{n_i} \end{Bmatrix} \tag{5.36}$$

and the matrix of phase differences cosines $\mathbf{P}_D$ as

$$\mathbf{P}_D = \begin{bmatrix} \cos(\varphi_1 - \varphi_1) & \cos(\varphi_2 - \varphi_1) & \dots & \cos(\varphi_n - \varphi_1) \\ \cos(\varphi_1 - \varphi_2) & \cos(\varphi_2 - \varphi_2) & \dots & \cos(\varphi_n - \varphi_2) \\ \dots & \dots & \dots & \dots \\ \cos(\varphi_1 - \varphi_n) & \cos(\varphi_2 - \varphi_n) & \dots & \cos(\varphi_n - \varphi_n) \end{bmatrix} \tag{5.37}$$

The analytical solution of the integral in eq. (5.23) for responses in the form of eq. (5.25) is then

$$\int_0^{T_i} \dot{\mathbf{x}}^{\mathrm{T}} \mathbf{L}_j \mathrm{sgn}(\dot{\mathbf{x}})\mathrm{d}t = \frac{4}{\omega_i^2} \mathbf{p}_i^{\mathrm{T}} \mathbf{P}_D \mathbf{L}_j \mathbf{u}_n \tag{5.38}$$

where $\mathbf{u}_n$ is the unity vector

$$\mathbf{u}_n = \left\{ \begin{array}{c} 1 \\ \vdots \\ 1 \end{array} \right\} \in \mathbb{R}^{n \times 1} \tag{5.39}$$

It is now possible to build matrix $\mathbf{G}$ analytically and to proceed to the minimum angle selection to locate the damping sources and to solve the energy equation as in the previous case. It is not known a priori if the equivalent sources to identify are related to viscous damping or Coulomb friction. In this specific case (with three viscous dashpots and three Coulomb friction devices attached to the structure) it is possible that the equivalent system could consist of six viscous dashpots as well as six Coulomb friction devices. The results of the identification are summarised in table 5.9. As in previous cases, the rotational degrees

Number of dashpots		Viscous damping DOF and coefficients (Ns/m)				Coulomb friction DOF and F_c (N)		
1	DOF	-	-	-	-	13	-	-
	Value	-	-	-	-	35.3	-	-
2	DOF	-	-	-	-	13	15	-
	Value	-	-	-	-	29.7	4.6	-
3	DOF	-	-	13	-	-	15	19
	Value	-	-	0.45	-	-	8.4	6.2
4	DOF	3	11	13	17	-	-	-
	Value	0.36	0.06	0.51	0.25	-	-	-
5	DOF	3	7	13	17	-	15	-
	Value	0.28	0.08	0.52	0.20	-	3.4	-
6	DOF	3	-	13	17	7	15	19
	Value	0.20	-	0.5	0.15	3.18	5.08	1
Original	DOF	3	-	13	17	7	15	19
	Value	0.2	-	0.5	0.15	3.2	5.1	1

Table 5.9: Results for case 3.

of freedom (which are indicated using even numbers) are never selected by the minimum angle criterion showing that the method somehow understands the direction of the damping sources. It can be seen that the two largest sources for each type are correctly located using three equivalent dashpots. Unfortunately the quality of the damping location for the Coulomb friction devices seems to

decrease when four dashpots are used. The reasons for this are not clear but it must be said that the selection is based solely on the angle between vectors from an incomplete set of data and the amount of information which can be extracted with few measurements is still remarkable. Using an appropriate number of equivalent dashpots leads to the correct solution (with small differences due to noise contamination) confirming that the equations used have been correctly formulated. The error between the identified energy vector and the original one, however, always decreases with an increasing number of equivalent dashpots.
The numerical simulation on the cantilever beam appears to be reasonably successful for the three cases proposed. The results are particularly good for case 2, where the location is always correct and the dashpots are selected from the largest to the smallest. Cases 1 and 3 behave slightly differently but a logical trend is visible and the results can be explained and justified using reasonable physics and engineering considerations. The next simulation on a larger structure aims to test the identification of relative dashpots between two different degrees of freedom when the amount of data available is considerably smaller compared to the size of the model.

5.3 Goland wing

The Goland wing (figure 5.4) is a benchmark structure in aeroelastic studies and provides a valid example for testing the damping identification method on a more complex structure than the previous cantilever beam. The finite element model of the heavy version of the Goland wing is composed of upper and lower skins, three spars, eleven ribs, three spar caps, eleven rib caps and 33 posts (1-D elements) with nominal thicknesses and areas as defined [118] in tables 5.10 and 5.11.

Parameter	Thickness (m)
Upper and lower wing skins	0.0047
Leading and trailing edge spars	0.00018
Centre spar	0.0271
Ribs	0.01058

Table 5.10: Nominal values of thicknesses for the Goland wing FEM.

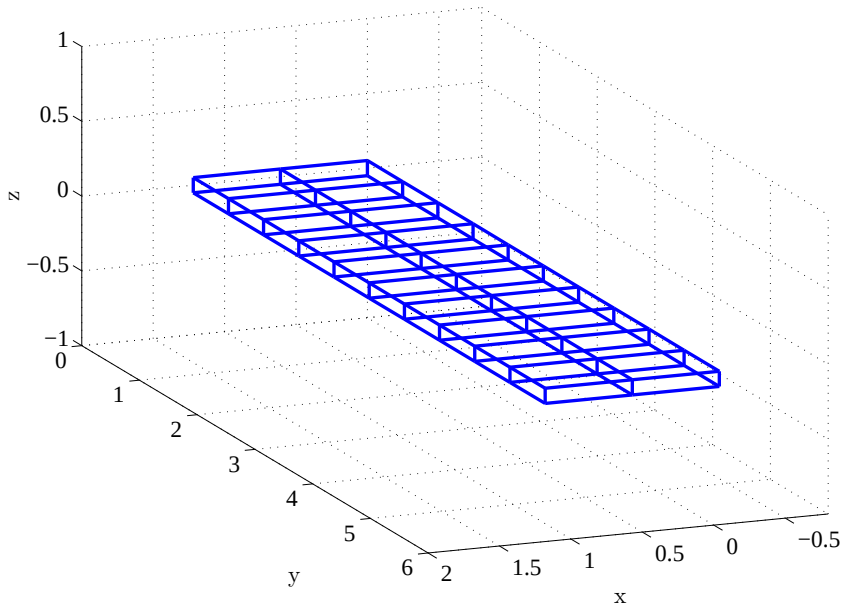

Figure 5.4: Finite element model of the heavy version of the Goland wing

Parameter	Areas (m^2)
Leading and trailing edge spar caps	0.003865
Centre spar cap	0.013898
Rib caps	0.003921
Posts	0.000074

Table 5.11: Nominal values of areas for the Goland wing FEM.

Each node of the finite element model has three degrees of freedom (translation along x, y and z axis) for a total of 198 degrees of freedom. Six nodes (at coordinate $y = 0$) are clamped reducing the size of the system matrices to 180×180. The aim of this simulation is to check the performance of the method when dealing with the identification of relative dashpots between two different degrees of freedom. In this case fourteen viscous dashpots acting on the vertical degree of freedom (z axis) of fourteen couple of consecutive nodes is applied as shown in figure 5.5. These dashpots create a damping force which is proportional to the relative velocity in the z direction of the two connected nodes. The value and the location of the dashpots have been chosen in order to spatially cover most of the wing and to obtain damping ratios ζ_i for the first ten modes in the range 0.01-0.06 (table 5.12) which is an average typical value for mechanical systems.

All dashpots have the same damping coefficient equal to 2919 Ns/m. The nodes

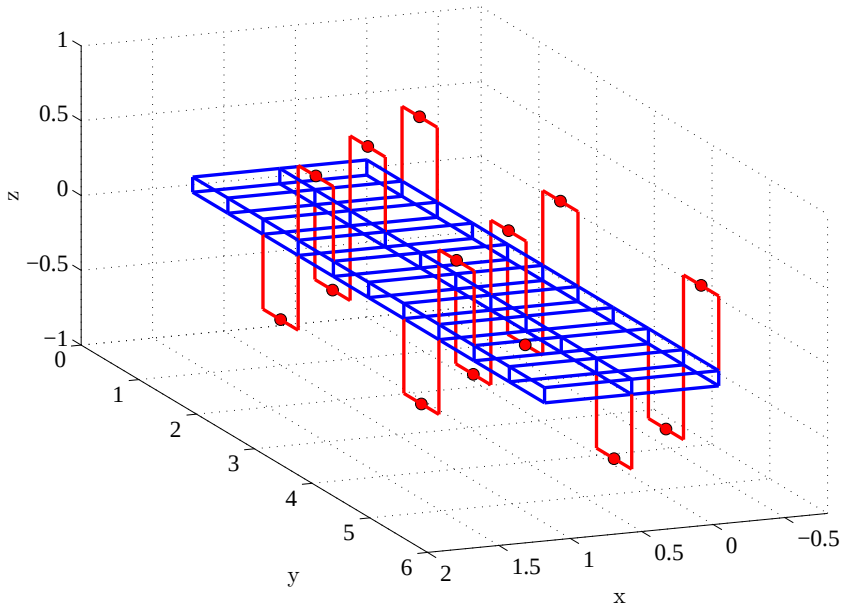

Figure 5.5: Location of viscous dashpots on the Goland wing

are numbered starting from the clamp to the free end of the upper part of the wing (node 1 to node 30, three nodes for each rib excluding the clamped one) and in the same way for the lower part of the wing (node 31 to node 60). For clarity, x and y direction degrees of freedom will not be displayed in the results so that DOFs 1 to 60 indicate the z direction only; however they have been included in the calculations. The identification method is not restricted to one-direction sources of damping; the dashpot pattern proposed is just a simple example with the purpose of showing the philosophy and the physical meaning of the equivalent spatial damping identification on large structures. The fourteen dashpots have been located between the following groups of nodes: 1-4, 5-8, 9-12, 13-16, 17-20, 21-24, 25-28, 32-35, 36-39, 40-43, 44-47, 48-51, 52-55, 56-59. It can be seen that the modal damping of mode 4 is zero; this is due to the fact that mode 4 is an in-plane mode and there is no relative displacement in the z direction.

In this example, there are no dashpots connecting the structure to the ground so the damping pattern selected for the identification is different from the one selected for the cantilever beam. In this case it is preferred to use the relative dashpot localisation matrices described by eq. (4.18). In this part of the iden-

Mode	Frequency (Hz)	ζ
1	1.967	0.0216
2	4.047	0.0092
3	9.651	0.0192
4	13.272	0.0000
5	13.450	0.0263
6	17.998	0.0233
7	23.888	0.0292
8	29.940	0.0452
9	31.017	0.0495
10	35.196	0.0569

Table 5.12: Natural frequencies and damping ratios of the first 10 modes of the Goland Wing.

tification process engineering knowledge of the structure is used to reduce the possibilities for the location of the damping sources. A set of single frequency harmonic excitations at frequencies close to those of the first five modes has been used to perform the energy-balance damping identification method. Considering that the system possess 180 modes, the information used to identify the equivalent viscous damping matrix represent a small percentage of the whole data theoretically available. This is a useful test to evaluate the behaviour in case of modal incompleteness in the data.

The response of the system excited by single frequency harmonic excitations has been simulated in Matlab by using the damping matrix described in the previous section together with the mass and stiffness matrices extracted from the MSC.NASTRAN model used in [118, 119] derived from the Goland wing model described in [120] originally developed by Goland [121]. The response can be calculated in two ways: numerically or analytically. The first way consists of using the three system matrices in a Simulink model. By applying a harmonic source to the system the differential equations of motion are solved for each time instant by using the Matlab "ode45" solver to obtain accelerations which are then numerically integrated to obtain velocities and displacements. This approach has been used in previous simulations of the cantilever beam since it allows the calculation of the response of a system with different sources of

damping (included non-viscous sources) and gives an easy visualisation of the measurements, including the transient.

However, for the application of the energy method in this specific case the approach is not convenient for two main reasons: firstly, solving a system of 180 coupled differential equations for each time instant is computationally intensive and secondly the energy method is based on the steady-state response so it is necessary to wait for the transient to end, which could take a significant amount of time and calculation depending mainly on the level of damping. Since in this case the damping is viscous and the closed form solution of the forced response of a viscously damped multi-degree-of-freedom system is available in literature [44] and has been described in section 2.3.2, the analytical solution has been used to produce the necessary data to apply the identification method, i.e. the velocities. Following a similar procedure to the one used for the cantilever beam, the results of the identification are represented in figure 5.6 The size of the red circles

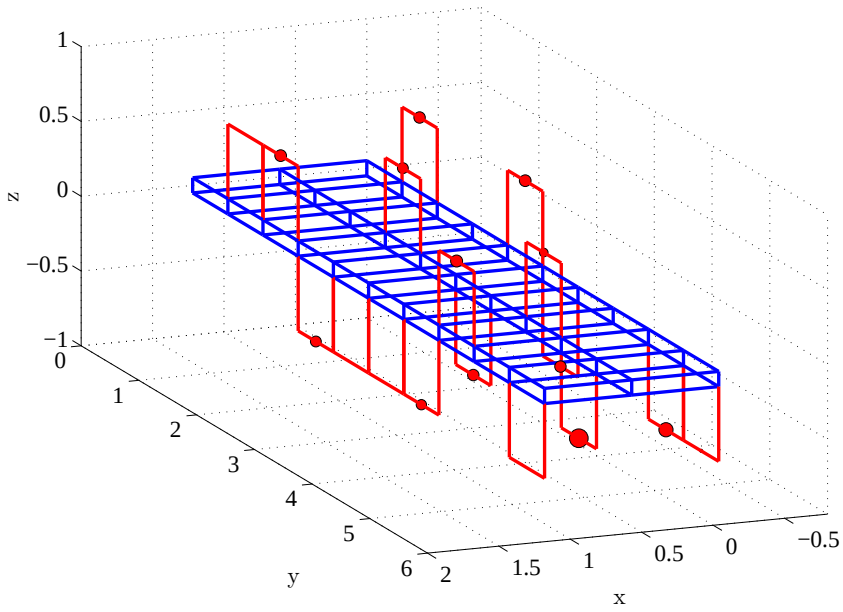

Figure 5.6: Location of the identified viscous dashpots on the Goland wing.

represent the amplitude of the damping sources with respect to the ones shown in figure 5.5. The limited amount of data used provides an identified viscous damping matrix which does not exactly represent the spatial distribution of the original dashpots but it gives an energy-equivalent result which is valid for the

five modes considered.

A relative dashpot with a viscous coefficient c located between two degrees of freedom p and q produces four entries in the viscous damping matrix. Two of these entries are off-diagonal terms located at the p^{th} column of the q^{th} row and vice versa, both equal to $-c$, whereas the other two entries are on the diagonal on the p^{th} and q^{th} row. Since the whole 180×180 matrix is difficult to display, an estimation of the quality of the damping location and identification can be extracted from the plot of the sixty terms corresponding to the vertical degrees of freedom, from the diagonal of the identified damping matrix versus the original damping matrix (figure 5.7). As already mentioned, the degrees of freedom from

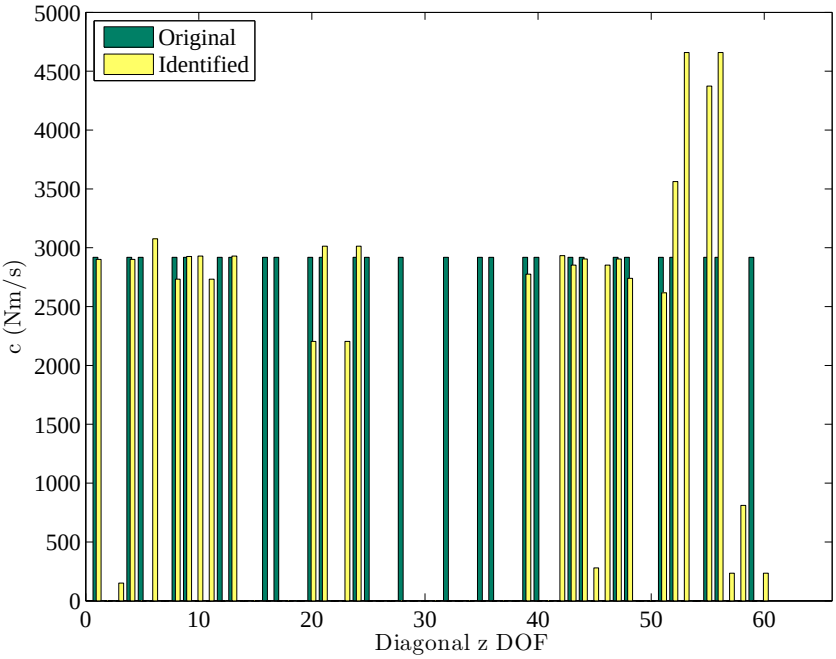

Figure 5.7: Amplitude of the diagonal elements of the identified and original damping matrices

1 to 30 represent the upper part of the wing whereas the degrees of freedom from 31 to 60 refer to the lower part. It can be seen that the identified values are of the same order of magnitude of the original values and in some cases the location is very accurate too (see for example degrees of freedom 1 and 4). There is also an almost "empty" area between degrees of freedom 25-30 in the upper part and between 31-38 in the lower part. This can be explained by the fact that the identified equivalent damping in the 1-15 upper zone is larger than the original

damping, therefore it compensates for the missing dashpots in the lower 31-38 zones whereas the big values between DOFs 50 to 60 in the lower part compensate for the missing damping in the corresponding upper part. Another factor that affects the location of damping in case of incomplete data is that some of the original dashpots could have been located between degrees of freedom which do not have large relative velocities in the range of frequencies considered. Identifying their location becomes more difficult with a limited number of measurements and other locations are preferred for the energy-equivalent model. From a modal

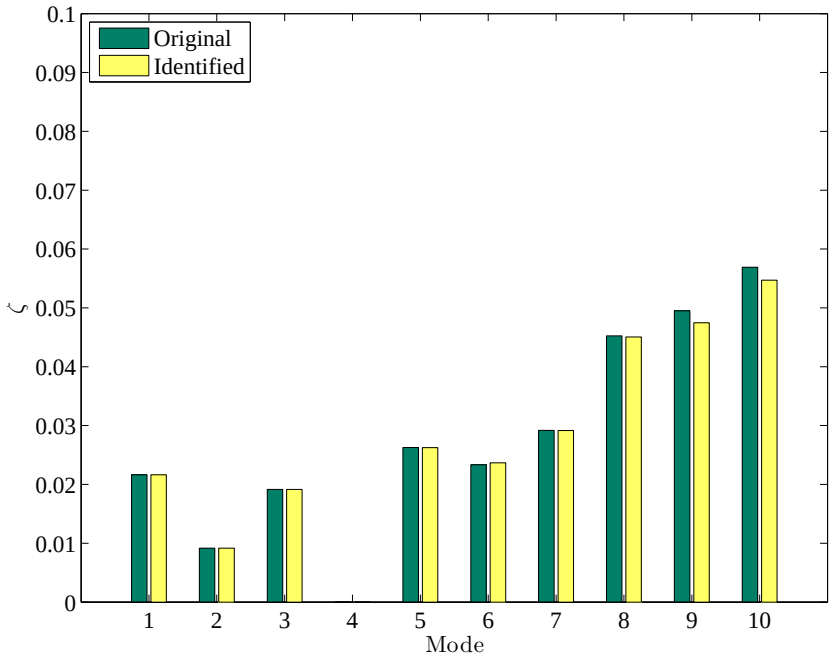

Figure 5.8: Modal damping ratio comparison for the first 10 modes.

point of view, the results are shown in figure 5.8 and table 5.13. The agreement between the modal damping coefficients of the original and identified system is very accurate for the first five modes used to perform the identification (the maximum error is -0.104%) and it is still acceptable for further modes with reasonable errors up to 4%. The energy method is then able to give a reasonable spatial pattern of dashpots with viscous damping coefficients of the same order of the original one together with a good agreement of the modal properties even on large structures using a relatively small amount of data.

Mode	ζ Original	ζ Identified	Error (%)
1	0.021636	0.021635	-0.003%
2	0.009169	0.009169	-0.001%
3	0.019158	0.019149	-0.045%
4	0.000000	0.000000	0.000%
5	0.026271	0.026243	-0.104%
6	0.023350	0.023658	1.319%
7	0.029190	0.029165	-0.086%
8	0.045236	0.045047	-0.417%
9	0.049506	0.047473	-4.107%
10	0.056917	0.054697	-3.901%

Table 5.13: Identified versus original modal damping comparison

5.4 Closure

The numerical simulations on two different structures with different damping configurations have been studied in order to evaluate the advantages and drawbacks of the method proposed. This method is a spatial identification method aimed at providing information about the location and amplitude of the sources of energy dissipation in order to link the damping to a specific region or to a specific physical phenomenon. This method seems to give valuable information in all the cases proposed. The numerical simulation on the cantilever beam appears to be reasonably successful for the three cases proposed. Particularly in case 2 the location is always correct and the dashpots are selected from the largest to the smallest. Cases 1 and 3 present some inaccuracies due to limited data and noise, but a logical trend is visible and the results can be explained using engineering considerations. In the Goland wing example, the identified damping pattern obtained possess viscous damping coefficients of the same order of magnitude as the original and the location is globally representative of the spatial distribution on the wing. From a modal damping point of view, the two systems (original and identified) are very close to each other for the first five modes used to identify the damping and remain close for further modes.

Although these results are encouraging, they are not sufficient to validate a method. Simulations can validate the mathematics behind the method and even-

tually the effect of noise or other kinds of contaminations, however they are not able to validate the relationships between the real world and the way the damping is modelled and the approximations introduced. For these reasons in the next chapter two different experiments have been designed in order to test the method on real structures with different sources of damping.

Chapter 6

Experiments

6.1 Introduction

Most of the identification methods found in the literature work very well in theory and in simulations but there are not many papers on their validation with regard to real structures, especially for the location of the sources of energy dissipation. An interesting article on the subject is written by Srikantha Phani and Woodhouse [84], who compared the performance of a number of specific identification routines on two different test structures: a three cantilever beam system and a free-free beam. In this chapter the proposed energy balance identification method is tested on two structures: an aluminium cantilever beam with nominal dimensions close to the one of the numerical simulations described in chapter 5 and a five degrees of freedom mass-spring structure. Both structures have been designed and built for the purpose of validating the method and several different damping devices (eddy current dashpots, air viscous dashpots, Coulomb friction devices) have been attached to these structures in order to locate and evaluate their damping properties.

6.2 Design of experiment 1: cantilever beam

Since the numerical simulations on the cantilever beam performed reasonably well, the idea is to repeat a similar experiment on a real structure. A sketch of the experiment is showed in figure 6.1. The cantilever aluminium beam has nineteen equidistant holes in order to have different locations for the damping devices along the length of the beam by means of small wings attached to it. The dimensions

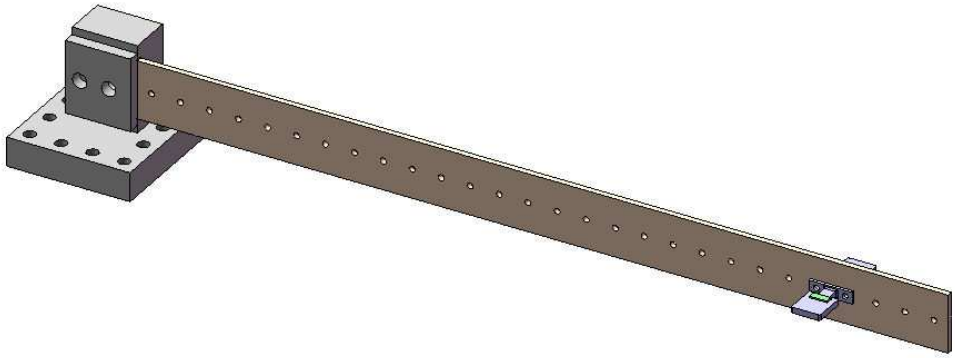

Figure 6.1: Cantilever beam experimental setup

and material of the beam have been designed so that the natural frequencies of the first ten modes are well separated from each other, in order to minimise the effect of each mode on those closest to it. The chosen material is aluminium since the damping devices that will be used on the beam include magnets and there could be unwanted interactions in case of ferromagnetic materials, even if they are located considerably far from the beam. After choosing the dimensions of the

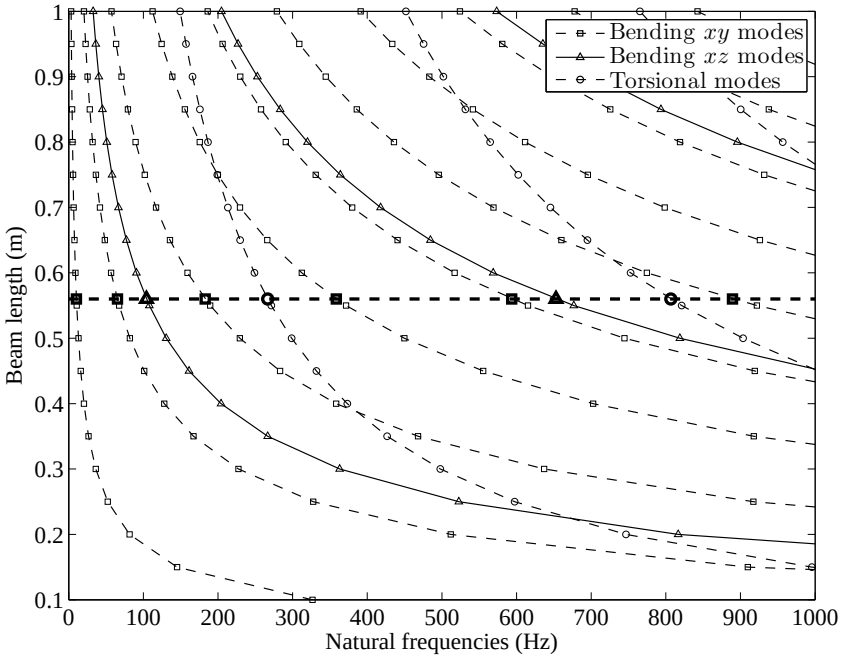

Figure 6.2: Effect of the length of the beam on natural frequencies

rectangular section of the beam (40×4 mm), an eigenvalues analysis based on a FEM of the beam (figure 6.2) was performed in order to choose the optimal length.

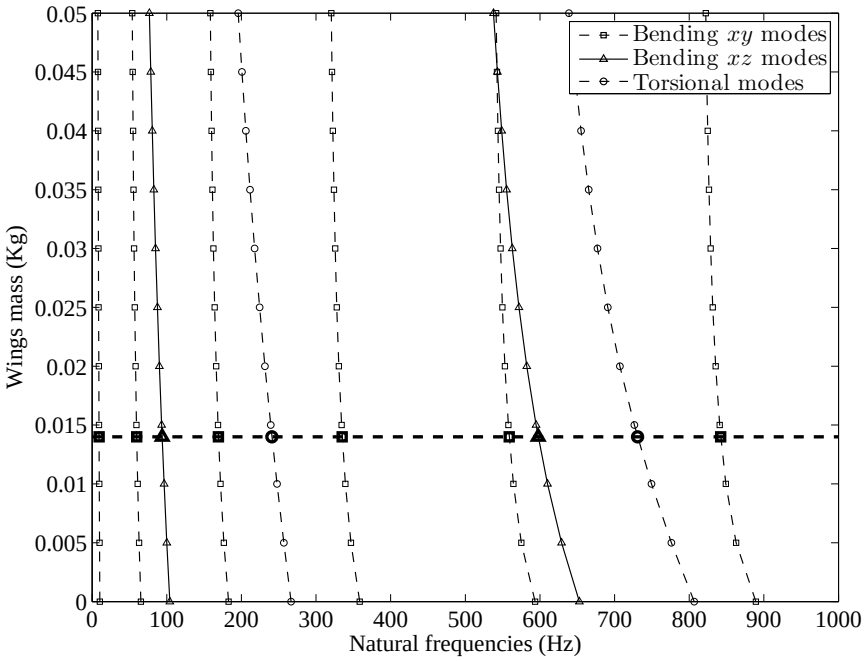

Figure 6.3: Effect of added mass on natural frequencies

An appropriate length was found to be 560 mm. The mass of the wings attached to the beam to provide damping will have an effect on the dynamics of the beam (figure 6.3) which has been considered in the design. The mass for one pair of wings at the same degree of freedom was calculated as 0.014 Kg. In table 6.1 are displayed the values of the natural frequencies of the first ten modes for three different wings configuration: the beam only without added mass (configuration 1), the beam with wings at 500 mm distance from clamp (configuration 2) and the beam with wings at 200 mm distance from clamp (configuration 3). It can be seen that frequencies are well separated and the location of the wings does not affect modes considerably if the wings are reasonably light. The shape of the wings was optimised in order to provide enough conductive material for the magnetic dashpot, described in the following section, while keeping the mass of 0.014 Kg. The beam is stiffly clamped in compression between two large steel blocks. Ten translational accelerometers are placed along the beam, five for each side and equidistant from each other; no rotational degrees of freedom are considered. Degrees of freedom are numbered from 1 to 10 starting from the clamp to the free end and a shaker, which provides the external excitation forces, is placed at

Mode	Description	ω (Hz) case 1	ω (Hz) case 2	ω (Hz) case 3
1	1^{st} bending xy	10.380	9.7256	10.536
2	2^{nd} bending xy	65.034	64.271	63.469
3	1^{st} bending xz	103.05	96.679	102.82
4	3^{rd} bending xy	181.98	182.42	177.66
5	1^{st} torsional	269.11	233.66	264.09
6	4^{th} bending xy	356.75	357.91	353.13
7	5^{th} bending xy	588.27	591.69	582.99
8	2^{nd} bending xz	628.73	623.06	606.53
9	2^{nd} torsional	809.35	754.52	684.69
10	6^{th} bending xy	885.38	885.09	873.69

Table 6.1: Natural frequencies for three different wing configurations

DOF 3 (figure 6.4). The complete experimental setup is shown in figure 6.5. On

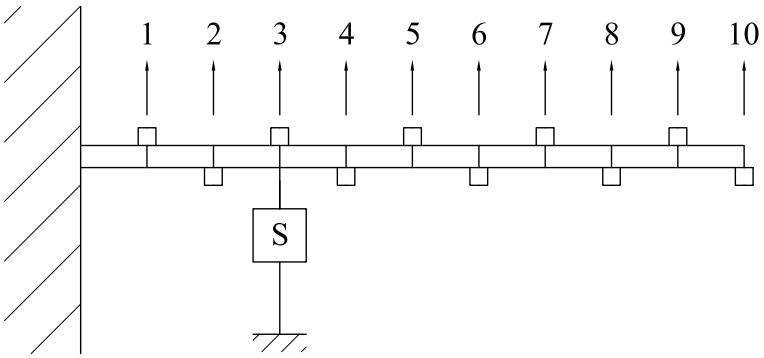

Figure 6.4: Experiment 1: DOFs numbering and location of the shaker

the left a magnetic eddy current dashpot is visible acting on DOF 9 where the two wings are attached, five accelerometers can be seen on one side of the beam whereas the other five are on the opposite side; the large white cylinder is the shaker. As previously discussed in the introduction, all structures exhibit some forms of damping. In this case there would certainly be some energy dissipation in the clamp, which cannot be considered completely ideal, and also some friction between the beam and the steel blocks of the clamp. The cables connected to the accelerometers will also dissipate some vibration as well as the material damping of the aluminium itself. However, the experiment is aimed to locate and measure the external added sources of damping which are meant to be larger than these intrinsic values which can then potentially be neglected.

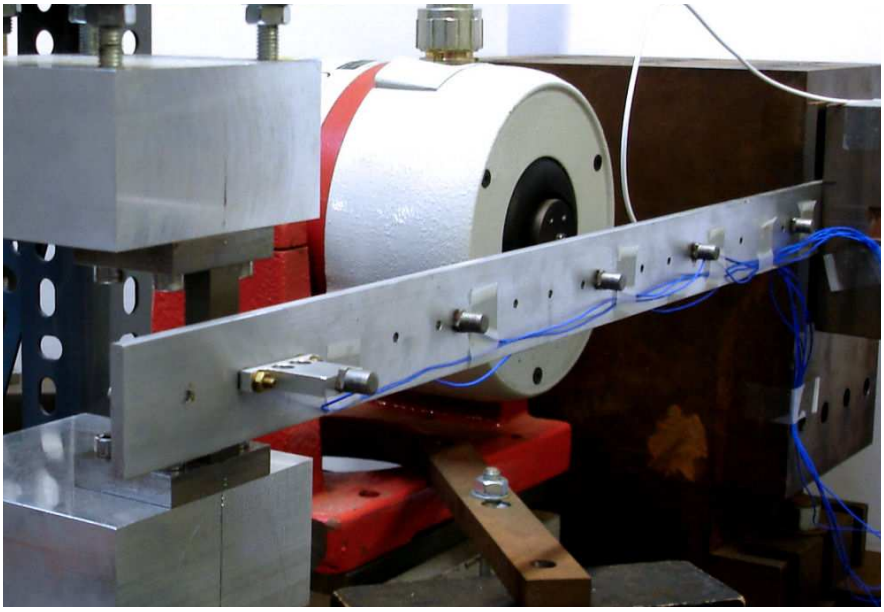

Figure 6.5: Experimental setup

6.3 Damping sources

The three different damping sources chosen for this experiment consist in eddy current dashpots, air viscous dashpots and Coulomb friction devices. The magnetic eddy current dashpots provide a damping force close to viscous damping with the advantage of not having moving parts in contact so that unwanted forms of friction are avoided. The air viscous dashpots consist in the traditional cylinder with a movable piston which creates a damping force proportional to velocity by forcing a laminar flow of air through a restriction. The Coulomb friction devices are essentially callipers which compress the wings through an adjustable normal force; different materials can be used on the contact surfaces to change the friction coefficient.

6.3.1 Magnetic eddy current dashpot

The movement of a conductor (in this case the aluminium wing) through a stationary magnetic field (figure 6.6) generates an electromagnetic force that creates a damping effect proportional to instantaneous velocities similar to pure viscous damping [12, 13]. By varying the air gap between the magnet and the conductor it is possible to vary the damping coefficient of the dashpot. This coefficient

can be estimated if the size of the magnets and conductor are known [11]. The value of the damping coefficient can be further increased by using two magnets placed on the two sides of the conductor with opposite direction of the magnetic flux density $\mathbf{B}_m$. The viscous damping coefficient of this device is proportional

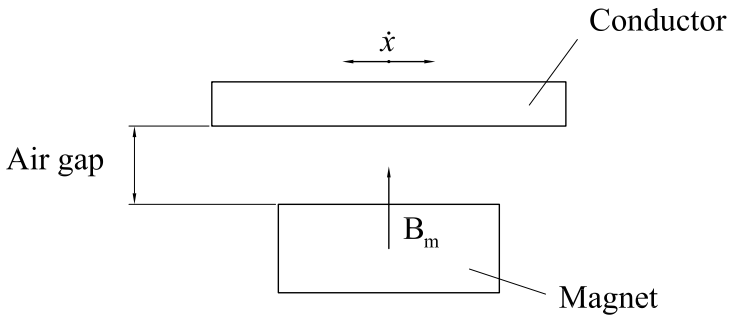

Figure 6.6: Eddy current dashpot model

to the size and geometry of the magnet and the conductor, the magnetic flux density in the direction orthogonal to the displacements, the electric resistance of the conductor and the air gap between the magnet and the conductor [11]. The

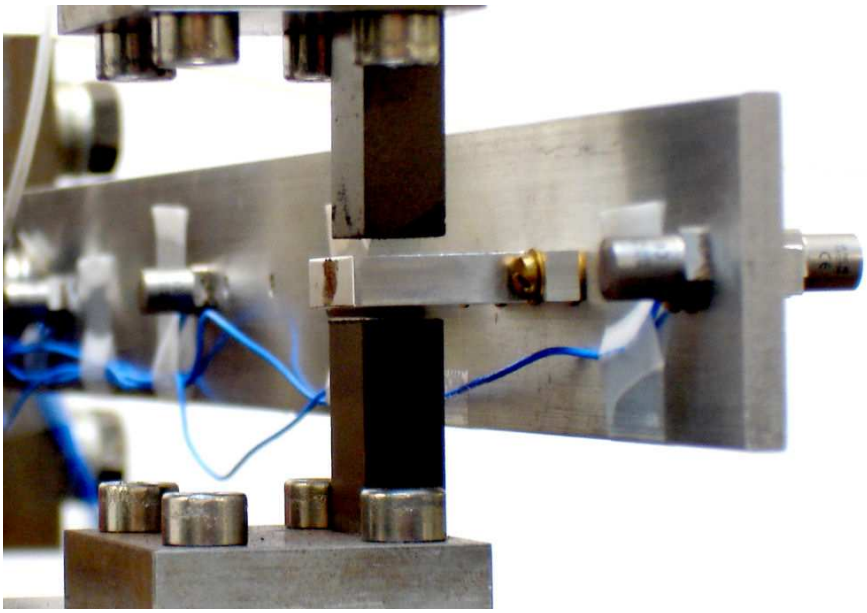

Figure 6.7: Magnetic eddy current dashpot located at DOF 9

constraint on the mass of the wings, which represent the conductor (aluminium) of the eddy current dashpot, limits the value of the damping coefficient in the

0-1.5 Ns/m range depending on the air gap between the magnet and the conductor. This value seems to be a valid compromise in order to have a light device providing viscous damping without friction.

6.3.2 Air viscous dashpot

The viscous dashpot (figure 6.8) used in the experiments is a precision air damping dashpot by Airpot® type 2KS160A2.0TX which is able to produce higher damping coefficients than the magnetic eddy current dashpot, in the 0-20 Ns/m range, with the minor disadvantage of experiencing a small amount of energy dissipation by friction due to the movable parts in contact.

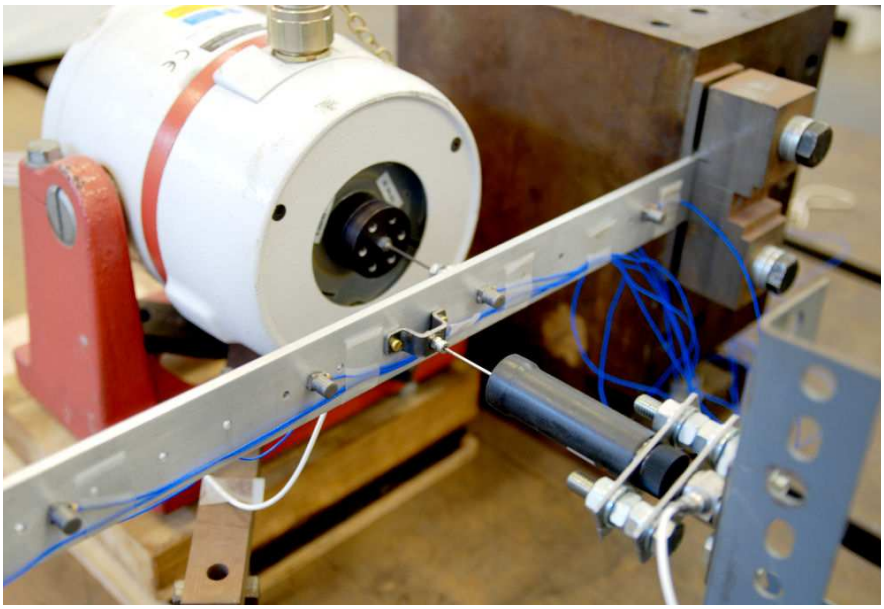

Figure 6.8: Air dashpot at DOF 4

However, this amount of energy is relatively small compared to the energy dissipated by viscous damping, so it is assumed to be negligible during the identification process. The value of the damping coefficient in this case can be varied by adjusting a screw which reduces or increases the section of the hole where the air is forced to flow through. Even if the viscous damping coefficient is theoretically constant at any frequency and this kind of dashpots are normally used to represent viscous damping, it has been found that the actual damping coefficient is not constant but it varies considerably depending on the frequency. For this reason an average value of the damping coefficient within the range of frequencies used

in the identification process has been previously estimated on the dashpot only in order to compare it with the value identified once attached to the structure.

6.3.3 Coulomb friction device

The Coulomb friction device consists of the simple system showed in figure 6.9. A calliper acts on the aluminium wing by means of a normal force obtained by turning the screw in the middle of the device creating a deflection of the two small beams. The normal force can be adjusted using the screw while films of different

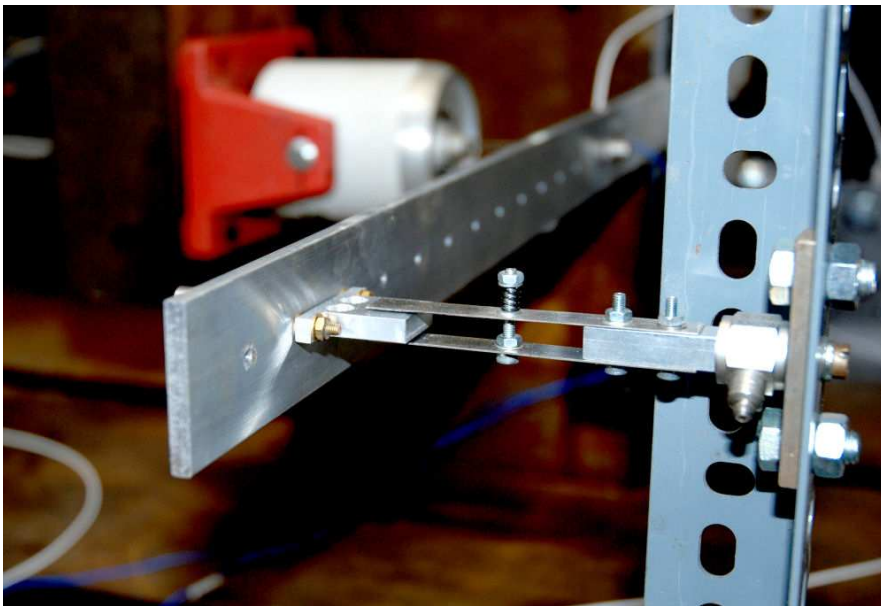

Figure 6.9: Coulomb friction device at DOF 9

materials can be applied to the wings and to the callipers to provide different combinations and different friction coefficients μ. On the back of the calliper it is possible to measure the tangential force through a load cell transducer while the normal force can be measured by static tests before starting the dynamic experiment.

6.4 Test procedure

The experimental procedure is similar to the procedure used for the numerical simulations; a preliminary Frequency Response Function of the undamped structure under investigation (the cantilever beam only) is measured in order to

choose the frequencies at which the excitations will be applied for the identification method. The choice is to use frequencies close to the ones of the first eight modes of the undamped system, where the effect of damping is more likely to appear when the additional sources will be attached. The structure is then excited using these single-frequency forces and maintaining the input energy as constant as possible in order to have similar order of magnitude in each row of matrix **G** and vector **e** in eq. (4.22). The measured data from the load cell attached to the

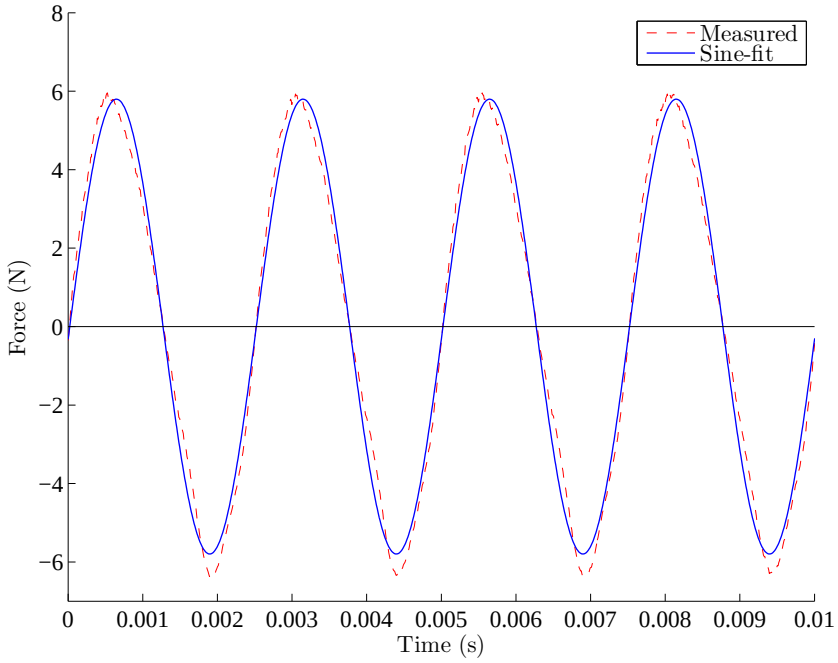

Figure 6.10: Typical measured force versus harmonic fitted force

shaker and the ten accelerometers are then fitted to a harmonic function. In this ten degree-of-freedom system, with the shaker attached at DOF 3, the measured forces vector will take the form

$$\mathbf{f}_i(t) = \begin{Bmatrix} 0 \\ 0 \\ f_i(t) \\ 0 \\ 0 \\ 0 \\ 0 \\ 0 \\ 0 \\ 0 \end{Bmatrix} \tag{6.1}$$

and $f_i(t)$ will be fitted to the harmonic function

$$f_i(t) = r_i \sin(\omega_i t) + s_i \cos(\omega_i t) \tag{6.2}$$

by estimating the two coefficients r_i and s_i using least squares techniques. A representative typical measured force versus its fitted harmonic function is shown in figure 6.10. The same procedure is done for the acceleration measurements (figure 6.11). In this example, the vector of measured accelerations will be

$$\ddot{\mathbf{x}}_i(t) = \left\{ \begin{array}{c} \ddot{x}_{1_i}(t) \\ \vdots \\ \ddot{x}_{10_i}(t) \end{array} \right\} = \left\{ \begin{array}{c} a_{1_i} \\ \vdots \\ a_{10_i} \end{array} \right\} \sin(\omega_i t) + \left\{ \begin{array}{c} b_{1_i} \\ \vdots \\ b_{10_i} \end{array} \right\} \cos(\omega_i t) \tag{6.3}$$

or

$$\ddot{\mathbf{x}}_i(t) = \mathbf{a}_i \sin(\omega_i t) + \mathbf{b}_i \cos(\omega_i t) \tag{6.4}$$

Once $\mathbf{a}_i$ and $\mathbf{b}_i$ have been estimated, velocities and displacements can be calculated by analytical integration as

$$\dot{\mathbf{x}}_i(t) = \frac{1}{\omega_i} \left(-\mathbf{a}_i \cos(\omega_i t) + \mathbf{b}_i \sin(\omega_i t) \right) \tag{6.5}$$

$$\mathbf{x}_i(t) = -\frac{1}{\omega_i^2} \left(\mathbf{a}_i \sin(\omega_i t) + \mathbf{b}_i \cos(\omega_i t) \right) \tag{6.6}$$

This harmonic fitting is not necessary but it is advantageous for many reasons. For example, the analytical integration of the harmonic-fitted accelerations is faster than using the fast Fourier transform (FFT) on all frequencies and then apply the inverse to obtain velocities and displacements. The same is valid for the integrals present in matrix $\mathbf{G}$ and vector $\mathbf{e}$. Since the excitation frequencies are known and the nonlinearities present in the system are considered negligible, it is an acceptable approximation to assume that the response is at the same frequency of the excitation. This is an important advantage since it must be considered that the amount of measured data when using this method is considerably large. A certain number of periods of the time histories with a proper resolution is needed for each accelerometer and force transducer (for each excitation frequency, for each test) which results in large files that would have taken a large amount of time to be integrated numerically. However, in order to check if the chosen approximation was reasonable, the values for the entries of matrix $\mathbf{G}$ and vector $\mathbf{e}$

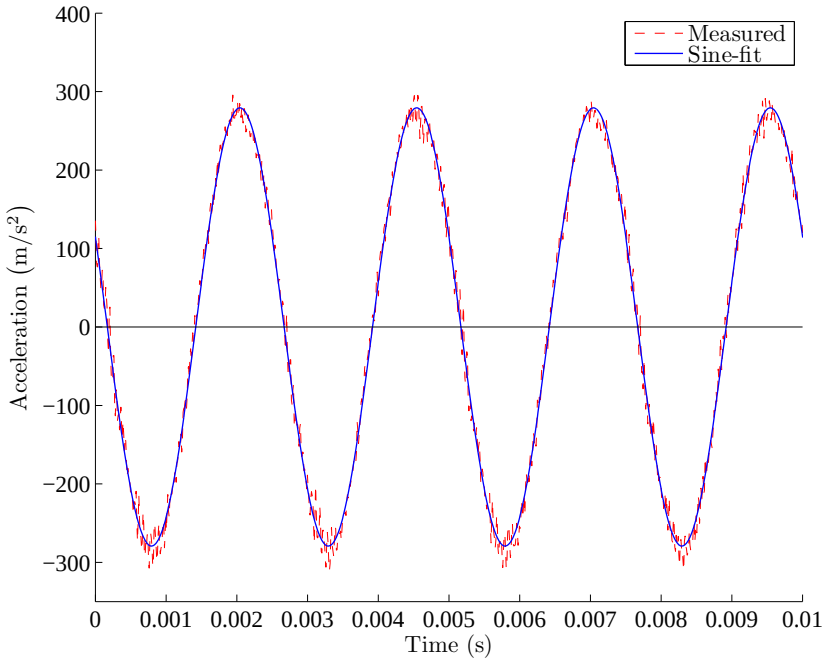

Figure 6.11: Typical measured acceleration versus harmonic fitted acceleration

in the very first experiment obtained by analytical and numerical integration have been compared. The maximum error is found to be 0.12% by using the analytical harmonic fitted solution instead of the numerical inverse-FFT integration, and for this simple ten degree-of-freedom example the ratio between the time consumed to perform the integrations using the two methods is about 1 to 250. Moreover, high frequency noise is automatically filtered by assuming a linear relationship between input force and response. Other numerical integration related problems such as the error in the trapezoid sum or phase shifts are also avoided or reduced by analytical integration.

In order to compute matrix $\mathbf{G}$ it is necessary to choose a parameterisation for the damping matrix by means of the localisation matrices $\mathbf{L}_i$ described in section 4.2.2. In this experiment the damping is going to be applied between some degrees of freedom and the ground so ten relative dashpot localisation matrices in the

form

$$\mathbf{L}_2 = \begin{pmatrix} 0 & 0 & 0 & \cdots & 0 \\ 0 & 1 & 0 & \cdots & 0 \\ 0 & 0 & 0 & \cdots & 0 \\ \vdots & \vdots & \vdots & \ddots & 0 \\ 0 & 0 & 0 & 0 & 0 \end{pmatrix} \tag{6.7}$$

have been used (eq. (6.7) refers to a dashpot connected between DOF 2 and the ground, for example). Moreover, a matrix in the form

$$\mathbf{L}_{11} = \begin{pmatrix} 1 & -1 & 0 & \cdots & 0 & 0 \\ -1 & 2 & -1 & \cdots & 0 & 0 \\ 0 & -1 & 2 & \cdots & 0 & 0 \\ \vdots & \vdots & \vdots & \ddots & -1 & 0 \\ 0 & 0 & 0 & -1 & 2 & -1 \\ 0 & 0 & 0 & 0 & -1 & 1 \end{pmatrix} \tag{6.8}$$

is used to represent dissipations between all pairs of two consecutive degrees of freedom. These energy dissipations are assumed of equal magnitude since nothing is connected between two of these DOFs and all damping is due to material damping in the aluminium, which is considered an homogeneous material. There might also be some damping due to the accelerometers' cables, which can be larger in the proximity of the clamp (DOF 1) since there are ten cables there compared to the free end (DOF 10) where only the cable of the last accelerometer is present. A total of eleven equivalent viscous damping coefficients are identified to represent the damping of the structure. Once matrix $\mathbf{G}$ and vector $\mathbf{e}$ have been calculated for each test, the identification procedure is the same as the numerical simulations in chapter 5, i.e. by applying the non-negative least squares algorithm and the minimum angle criterion.

6.5 Results for experiment 1

In this section the results of the energy equivalent damping identification are presented on different damping configurations: the undamped cantilever beam (referred as "offset damping", i.e. the intrinsic damping of the structure itself without any added source), the cantilever beam with a magnetic dashpot attached at DOF 8, the cantilever beam with an air dashpot attached at DOF 8, the

cantilever beam with a Coulomb friction device attached between at DOF 6 and the cantilever beam with two air dashpots attached at DOFs 6 and 8.

6.5.1 Case 1: undamped cantilever beam

The first experiment is performed on the undamped cantilever beam in order to estimate the offset damping due to the clamp, material damping, cables, air and everything else. The identified equivalent viscous damping matrix $\mathbf{C}_{id}$ for the range of frequencies selected ($10 \div 1000$ Hz) is

$$\mathbf{C}_{id} = \begin{bmatrix} 5.67 & -0.26 & 0 & 0 & 0 & 0 & 0 & 0 & 0 & 0 \\ -0.26 & 0.52 & -0.26 & 0 & 0 & 0 & 0 & 0 & 0 & 0 \\ 0 & -0.26 & 0.52 & -0.26 & 0 & 0 & 0 & 0 & 0 & 0 \\ 0 & 0 & -0.26 & 0.52 & -0.26 & 0 & 0 & 0 & 0 & 0 \\ 0 & 0 & 0 & -0.26 & 0.76 & -0.26 & 0 & 0 & 0 & 0 \\ 0 & 0 & 0 & 0 & -0.26 & 0.52 & -0.26 & 0 & 0 & 0 \\ 0 & 0 & 0 & 0 & 0 & -0.26 & 0.52 & -0.26 & 0 & 0 \\ 0 & 0 & 0 & 0 & 0 & 0 & -0.26 & 0.78 & -0.26 & 0 \\ 0 & 0 & 0 & 0 & 0 & 0 & 0 & -0.26 & 0.52 & -0.26 \\ 0 & 0 & 0 & 0 & 0 & 0 & 0 & 0 & -0.26 & 0.26 \end{bmatrix} \tag{6.9}$$

and it is shown in figure 6.12. Immediately visible is a large value (5.67 Ns/m) in the proximity of the clamp (DOF 1), with similar, albeit smaller, values for the rest of the beam. This result was expected since the clamp region is the most

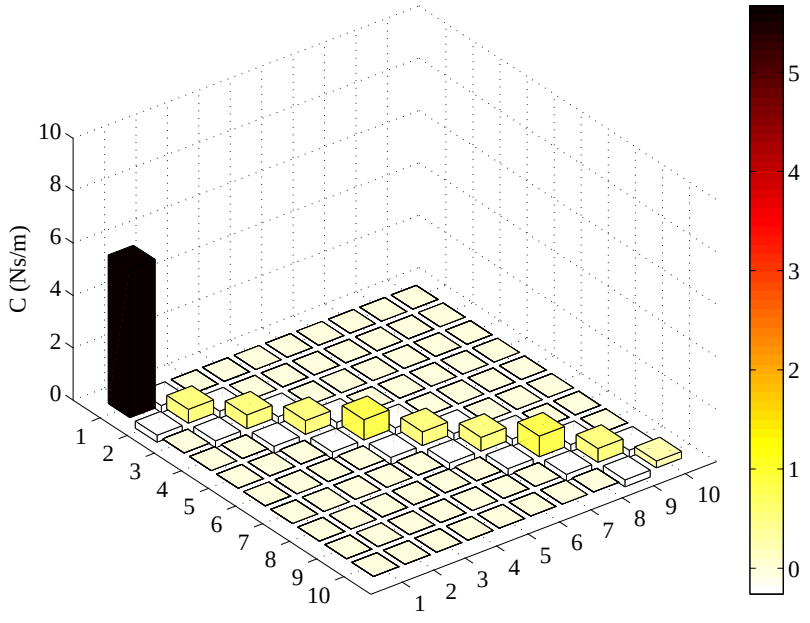

Figure 6.12: Identified damping matrix for case 1

affected by the damping due to the non-perfect boundary conditions and cables. However, the values of damping coefficients are larger than it was expected by preliminary studies during the design stage, confirming how damping is difficult to predict and to model a priori. From an energy point of view, it is not strictly valid to compare the value of the coefficients of the equivalent viscous damping matrix in order to find the largest sources of damping. The energy dissipated in a particular degree of freedom is obviously proportional to the damping coefficient but also to the velocity of that DOF. For this reason the degree of freedom with the highest damping value is not necessarily the one which dissipates most energy in a certain frequency range. It makes more sense to compare the percentage of energy dissipated in a particular degree of freedom compared to the total energy dissipated by the whole damping matrix, in the frequency range of interest, as shown in figure 6.13. In the undamped case the energy dissipated in the clamp is

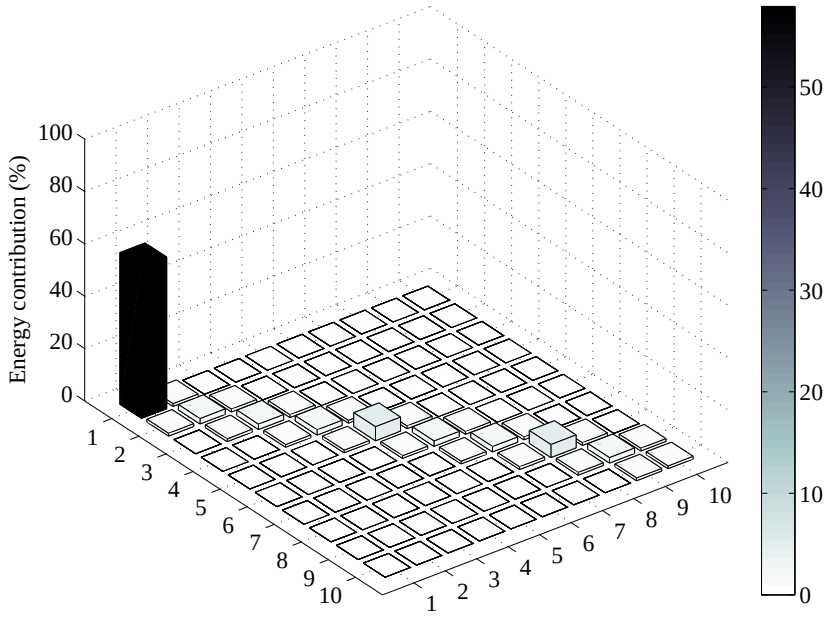

Figure 6.13: Energy DOF contribution (% of the total dissipation) of the identified damping matrix for case 1

still relatively the largest, since there are no other important external sources of damping and material damping seems to be negligible. However, in subsequent cases this way of displaying the results will help with the location of the main sources of energy dissipation. The identified damping matrix for case 1 will be

used to compare the other cases for detecting the additional damping provided by the different devices.

6.5.2 Case 2: single magnetic dashpot

The first damped experiment uses the magnetic eddy current dashpot described in section 6.3.1 as additional external source of viscous damping. Due to the constraints occurred during the design stage the maximum damping coefficient attainable with this device in the frequency range of interest, according to Nagaya and Kojima [11], is 1.5 Ns/m. This value is of the same order of magnitude (or even smaller) of the offset damping, which has been found to be larger than expected, so locating and identifying it could be challenging. The magnetic dashpot has been attached between degree of freedom 8 and the ground as shown in figure 6.14, and its viscous damping coefficient has been set to the maximum value 1.5 Ns/m. The identified damping matrix is shown in figure 6.15. The magnetic

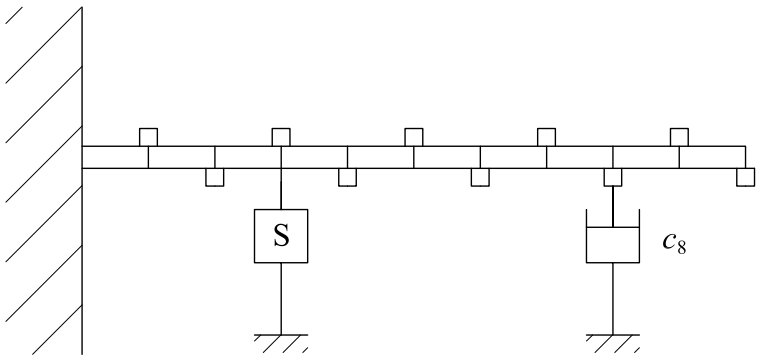

Figure 6.14: Case 2: magnetic dashpot location (DOF 8)

dashpot creates some small disturbances with respect to the matrix identified from the undamped system in figure 6.12 and even if a small value (1.17 Ns/m) is present at degree of freedom 8 (where the magnetic dashpot is actually located), the system seems to exhibit some damping of approximately the same value at DOFs 2 and 6 too, which is not present in the real system. The plot of the energy contributions in figure 6.16 shows that the clamp is no longer the main source of energy dissipation but the effect of the magnetic dashpot is still too small to be correctly located. Although the results of this first case are not particularly successful, there are some positive aspects that can be extracted from the com-

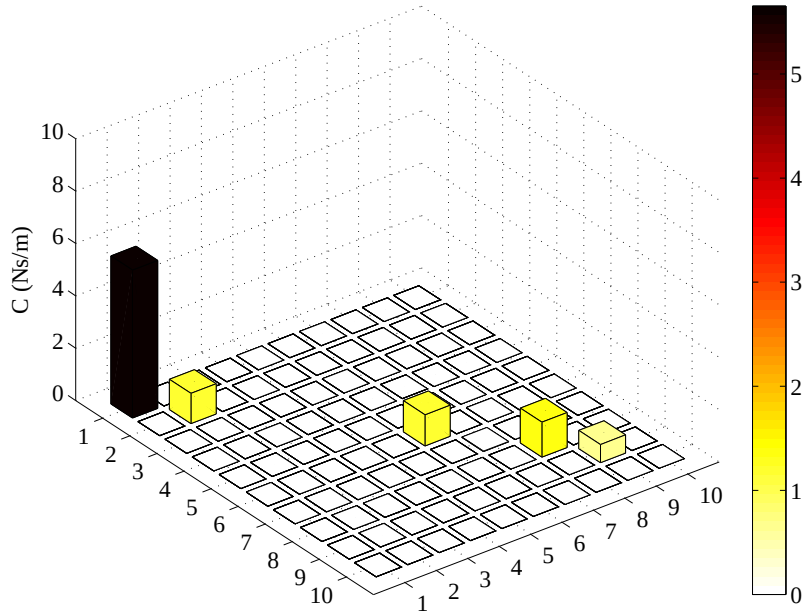

Figure 6.15: Identified damping matrix for case 2

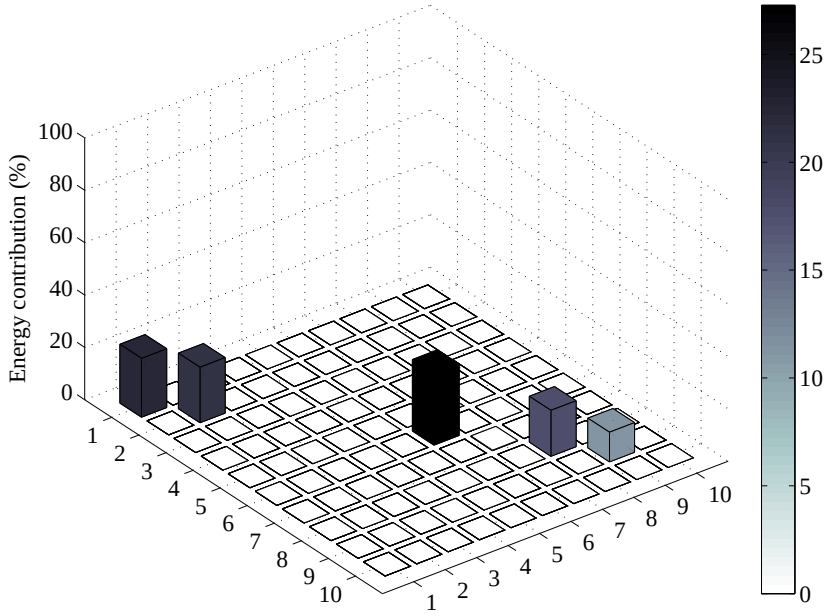

Figure 6.16: Energy DOF contribution (% of the total dissipation) of the identified damping matrix for case 2

parison of the undamped case with this lightly damped example. Firstly, the norm of the identified damping matrix which has increased from 5.6863 Ns/m to

6.1293 Ns/m showing that the added dashpot has a direct effect on the identified damping matrix in the right direction. This could look banal but considering the uncertainty and simplicity of the chosen damping model (only eleven viscous linear parameters to describe and locate all sorts of energy dissipation in a real structure) and the number of assumptions and approximations made during the handling of measured data, it was not so obvious. Secondly, though the method is not able to explicitly locate the magnetic dashpot, the general damping pattern is reasonable and confirms the presence of damping in the clamp region and the second largest value of the damping matrix at the right degree of freedom (DOF 8). A conclusion of this first experiment is that the external added damping source which was meant to be identified has been undersized during the design stage and as such the method is not particularly effective in locating it. This is because the useful information is lost within the offset damping.

6.5.3 Case 3: single air dashpot

Following the results of case 2, the choice for case 3 is to use a dashpot with a larger damping coefficient at the same degree of freedom (DOF 8). The air dashpot described in section 6.3.2 has been used, with a damping coefficient set to 5 Ns/m by a previous experiment on the daspot alone. The identified damping matrix is shown in figure 6.17. The identified damping matrix presents a peak of 4.4312 Ns/m at the location where the air dashpot is attached, some small values at DOFs 3, 4 and 7 and the usual large value in the clamp region. Despite the value of the identified damping at the location of the air dashpot being slightly lower than expected, the value of the coefficient in the clamp region (DOF 1) has increased from 5.67 Ns/m to 7.75 Ns/m. This result may look strange but it must be considered that DOF 1 is the one with smallest velocities in the frequency range under examination, so the actual increase from an energy point of view is not particularly remarkable. From the plot of the energy contributions (figure 6.18) it is now clear that the main source of dissipation is given by the added air dashpot at DOF 8. Unexpectedly, there seems to be some kind of energy dissipation at DOFs 3 and 4. These "perturbations" may occur for numerical or physical reasons: one interpretation may be related to the minimum angle selection which

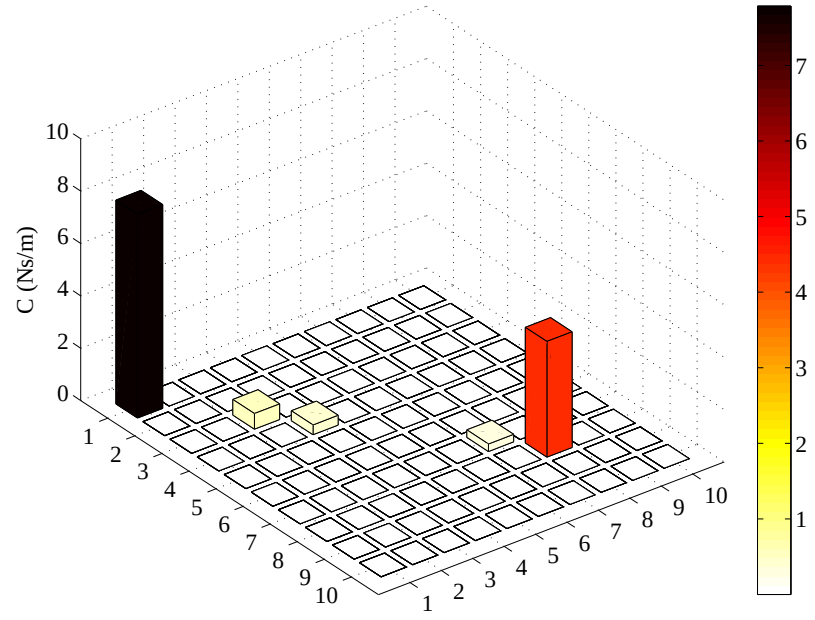

Figure 6.17: Identified damping matrix for case 3

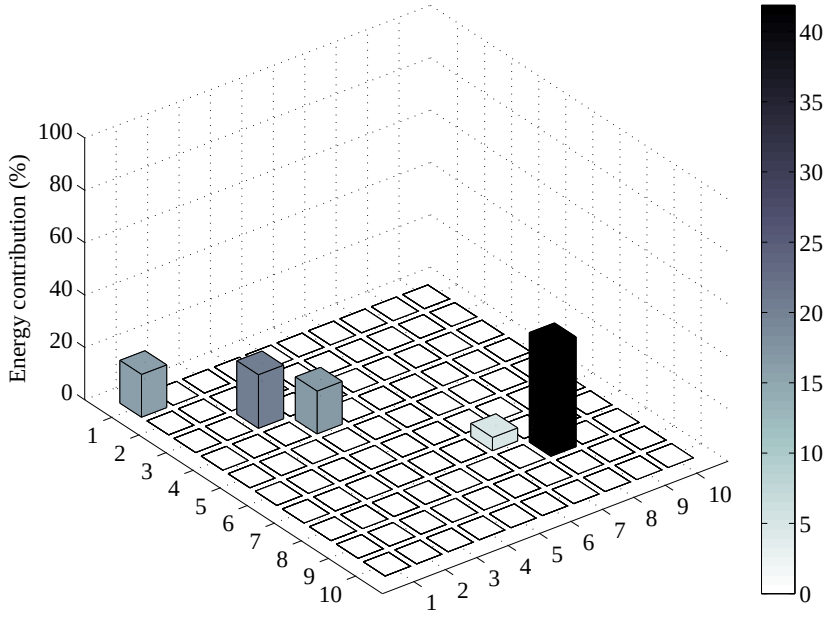

Figure 6.18: Energy DOF contribution (% of the total dissipation) of the identified damping matrix for case 3

might select the wrong column (in section 4.2.4 it is stated that the method does not guarantee a correct location but it just leads to it in most cases; even in

numerical simulations it happened to have wrong but reasonable solutions). A physical reason, instead, could be the fact that the shaker is attached at DOF 3 and it surely affects the dynamics of the structure and the damping as well. The results obtained in case 3 seem reasonably good and it appears that if the source is relatively big and the type of damping is mainly viscous, the method is able to locate the source and its magnitude effectively. In the next case a non-viscous source is attached to the system to check if an equivalent viscous damping system is able to give useful information on this different kind of source as well.

6.5.4 Case 4: single Coulomb friction device

In case 4, a Coulomb friction device such as the one described in section 6.3.3 has been attached between degree of freedom 6 and the ground, as schematically shown in figure 6.19. A thin sheet of biaxially-oriented polyethylene terephthalate

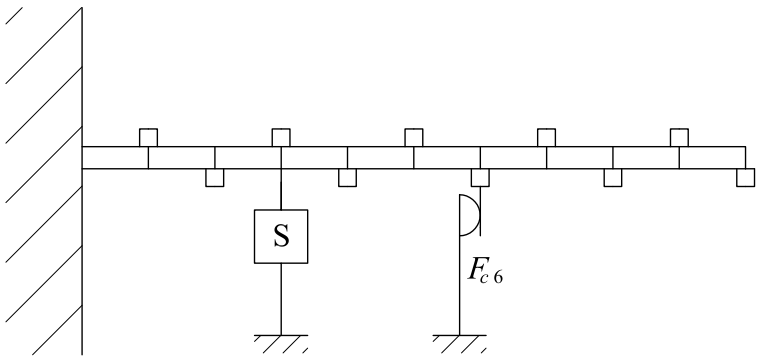

Figure 6.19: Case 4: Coulomb friction device location (DOF 6)

(boPET, commercially known as Mylar) has been placed between the callipers and the wing to obtain the desired friction coefficient. The identified damping matrix is shown in figure 6.20. Although the viscous model does not reflect the true physics of Coulomb friction as explained in section 2.2.3, the energy method is able to locate the source of damping at the right degree of freedom for this device too. An equivalent viscous damping coefficient of 3.2776 Ns/m has been obtained on the diagonal of the identified matrix corresponding to DOF 6. This viscous damping value is considered equivalent in terms of energy dissipated per

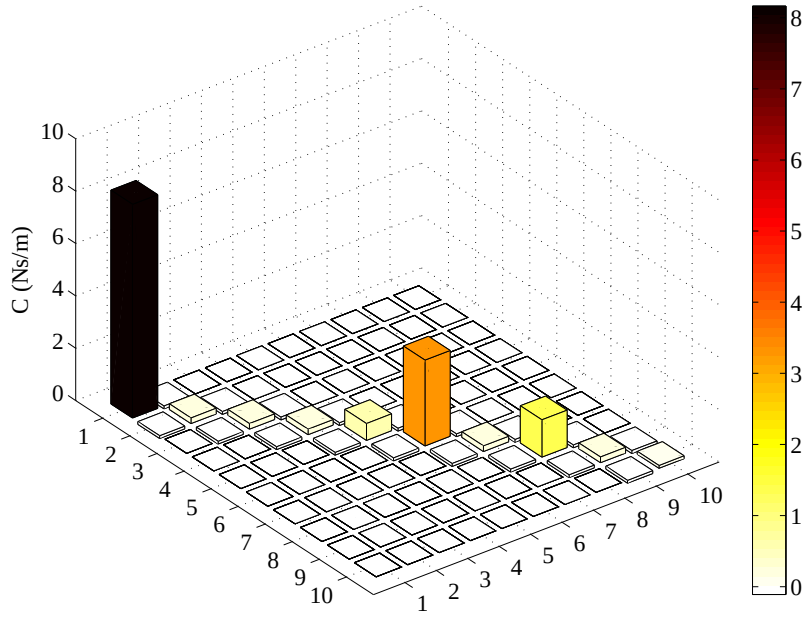

Figure 6.20: Identified damping matrix for case 4

cycle to the energy dissipated by Coulomb friction through the relationship

$$\pi c_{eq} \omega x_0^2 = 4\mu F_n x_0 \tag{6.10}$$

where ω is the frequency of vibration, x_0 is the amplitude of displacements, μ the coefficient of friction and F_n the normal force acting on the wing. The equivalent viscous damping coefficient c_{eq} is then

$$c_{eq} = \frac{4\mu F_n}{\pi \omega x_0} \tag{6.11}$$

This approximation means that the equivalent system with a viscous dashpot and damping coefficient c_{eq} dissipates the same amount of energy per cycle of the original system with Coulomb friction, but only at the specific frequency ω. In this case a range of frequencies, and not a specific value, is considered with different values of the displacement x_0 for each different excitation. The normal force F_n has been statically measured resulting as 0.8 N and the average coefficient of friction μ for the range of interest has been estimated as 0.32 using eq. (6.11). The value of the coefficient of friction between aluminium and Mylar

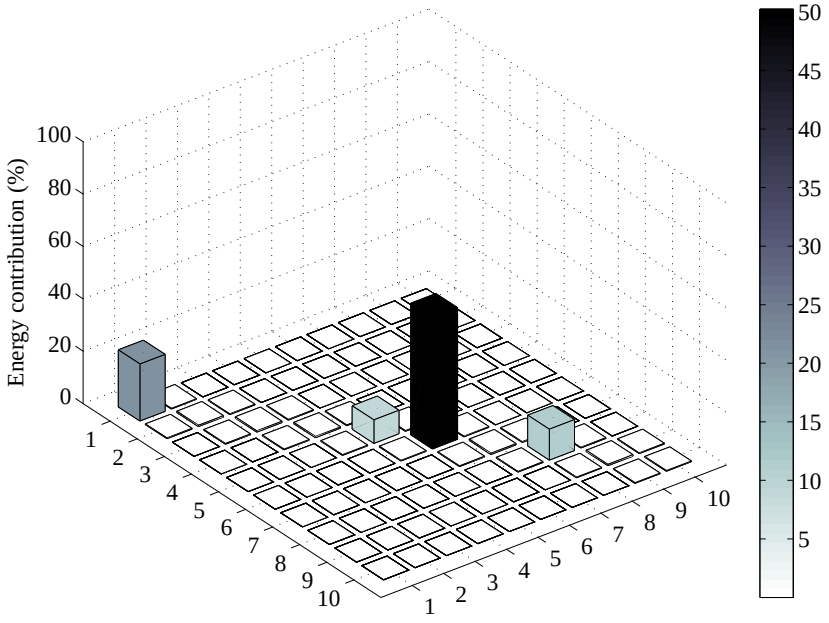

Figure 6.21: Energy DOF contribution (% of the total dissipation) of the identified damping matrix for case 4

obtained from a previous experiment on a inclined plane was 0.40. The plot of the energy contributions (figure 6.21) shows that the main source of damping is located at DOF 6, followed by the energy dissipated in the clamp, confirming a good spatial localisation as in the previous case.

6.5.5 Case 5: multiple air dashpot

The last case for the first experiment consists in two air dashpots, respectively of viscous damping coefficient 5 Ns/m and 7 Ns/m, attached at degrees of freedom 6 and 8 as schematically represented in figure 6.22 and shown in figure 6.23.
The identified damping matrix is shown in figure 6.24. As in the previous cases, the highest damping coefficient is in the clamp region, followed by DOFs 8, 6, 9 and 3. The damping coefficients of 3.2391 Ns/m and 4.8121 Ns/m are lower than expected for the two air dashpots but some of the energy input in the system is dissipated by the "wrong" equivalent dashpots at DOFs 9 and 3. The method seems to perform reasonably well with multiple sources of damping; the localisation seems particularly effective and even if the amplitude is not always precise, it is still representative of the relative magnitude between the different

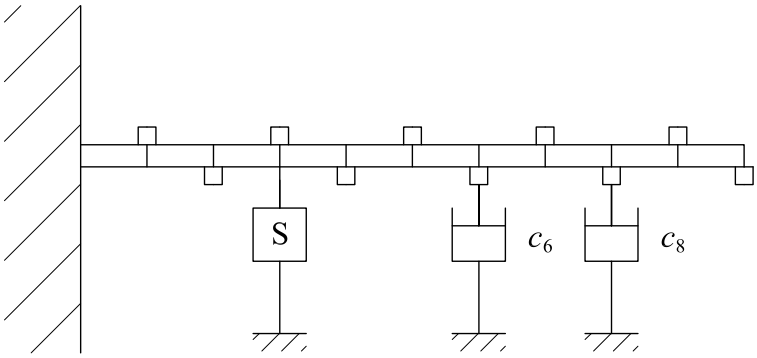

Figure 6.22: Case 4: Multiple air dashpots location (DOF 6 and 8)

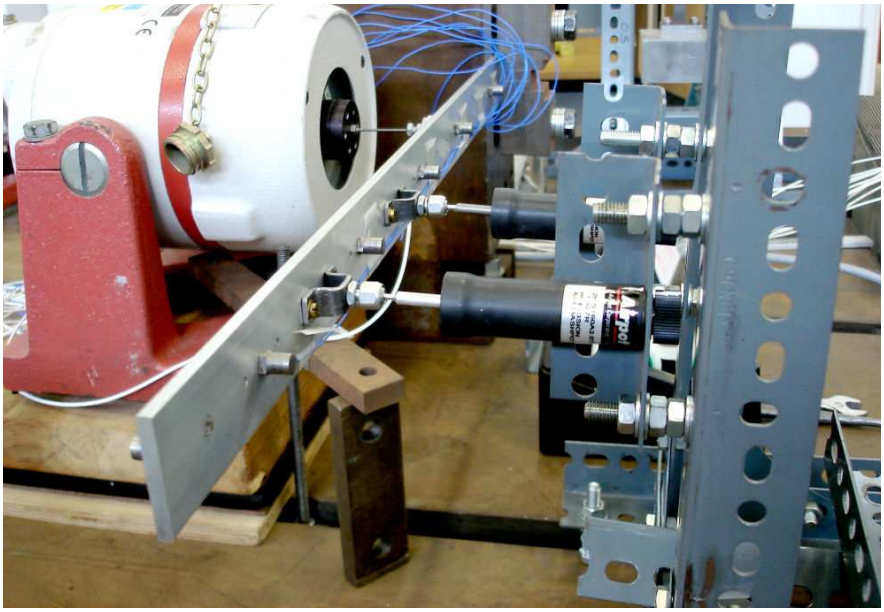

Figure 6.23: Case 5: air dashpots at DOF 6 and 8

energy dissipations.

By looking at the energy contributions (figure 6.25), it can be seen how the energy dissipated by the dashpot at DOF 8 is split into two equivalent dashpots at DOFs 8 and 9. Since nothing is attached to the beam at DOF 9, this is probably one of the numerical perturbations mentioned for case 3. However, figure 6.25 clearly shows the regions where the damping sources are effectively acting on the structure.

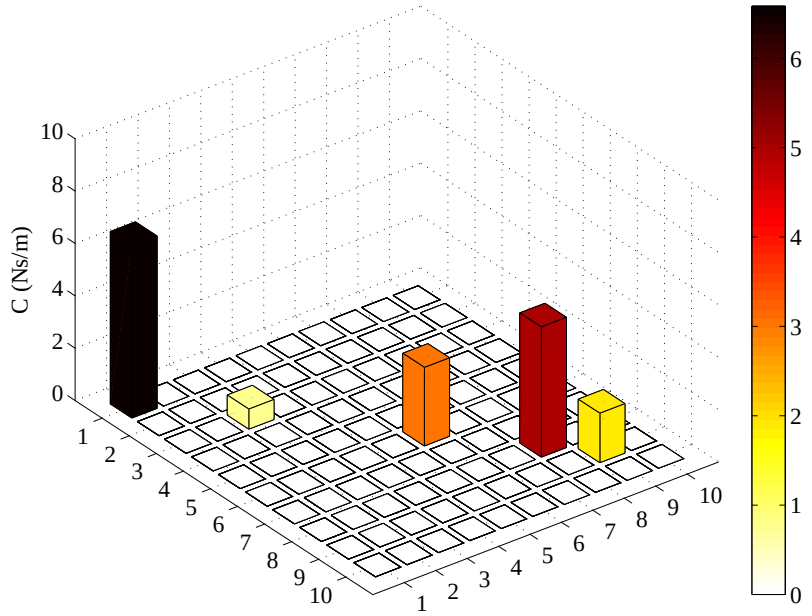

Figure 6.24: Identified damping matrix for case 5

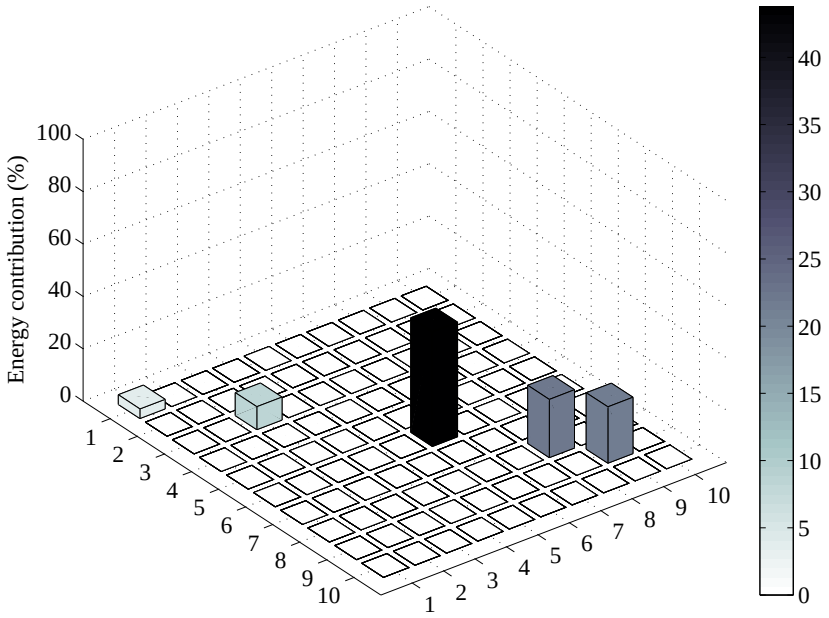

Figure 6.25: Energy DOF contribution (% of the total dissipation) of the identified damping matrix for case 5

6.6 Conclusions for experiment 1

The first experiment was meant and designed to validate the damping identification energy method, especially regarding the location of absolute dashpots

connected between the structure and the ground. The results obtained are encouraging: despite the simple linear eleven-parameters model which has been used to describe all the energy dissipations present in the system, the method gives valuable information about the location and amplitude of the sources of damping with a reasonably simple procedure. By measuring the time responses of only eight different excitations for each case and without building any FEM of the structure under examination, the results are sufficiently accurate to give a good general idea of the critical regions for damping.

Some important practical issues which are worth mentioning were encountered during the performance of the experiments. The first issue regards some problems which occurred with standard accelerometers at low frequencies. What appeared from this experiment is that standard equipment normally used for vibration tests may experience small phase lag at frequencies below 15 Hertz. Damping identification is extremely affected by phase lag since damping itself is the cause of the normal phase delays present in real systems. For methods based on time history as the energy method in particular, this may easily lead to wrong results so low frequency signals have to be checked carefully before applying the method and high performance accelerometers may become necessary when the range of frequencies of interest is in the low region. In this experiment, with a range of frequency approximately between 10 to 1000 Hz, the first bending mode of the beam is around 12 Hz so it is possible either to ignore the first mode or to excite the structure at a slightly higher frequency (around 15-16 Hertz) if the damping is still effective at that frequency.

Another practical issue encountered during the experiment is the difficulty to build a dashpot which behaves as a viscous dashpot with constant damping coefficient in the range of frequencies of interest. The values used to compare with the results of the identification are the average of the values at the different frequencies used in the experiments. The damping coefficient, even for the air dashpot which is the typical example used in all vibration books to illustrate viscous damping, is far from being constant in the range from 10 to 1000 Hz with variations sometime larger than 100%. Viscous damping is then a purely mathematical approximation which is often sufficient for engineering needs but

not accurately representative of reality.

Given the good results of the first experiment, a second experimental setup has been designed to test the method on the identification of relative dashpots between different degrees of freedom of a structure with a limited frequency range to avoid the two problems just mentioned.

6.7 Design of experiment 2: five masses system

The second experiment consists of a five degree-of-freedom system as schematically shown in figure 6.26. Five masses $(m_1, \ldots, m_5)$ are connected to the

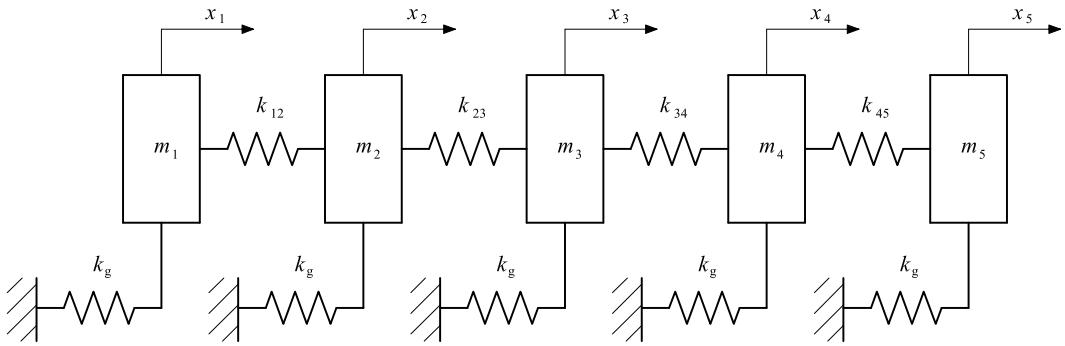

Figure 6.26: Experiment 2: Scheme and DOF numbering

ground with five nominally identical springs of stiffness k_g and four other springs $(k_{12}, \ldots, k_{45})$ connecting each mass to the next one. The values of masses and stiffnesses of springs have been chosen in order to have the frequency of the first mode higher than 20 Hz to avoid the phase lag problem at low frequencies encountered in the first experiment.

Moreover, the five degree-of-freedom system differs from the cantilever beam since it can be considered a discrete system with a finite number of modes (five) instead of a continuous system with an infinite number of modes. The system has been designed so that the frequencies of the five modes are in a limited range of frequencies between 20 to 80 Hz, well separated from each other, so that the damping coefficients of the sources of energy dissipation that will be attached to it will not vary too much in that range.

From a practical point of view, the spring connecting the masses to the ground

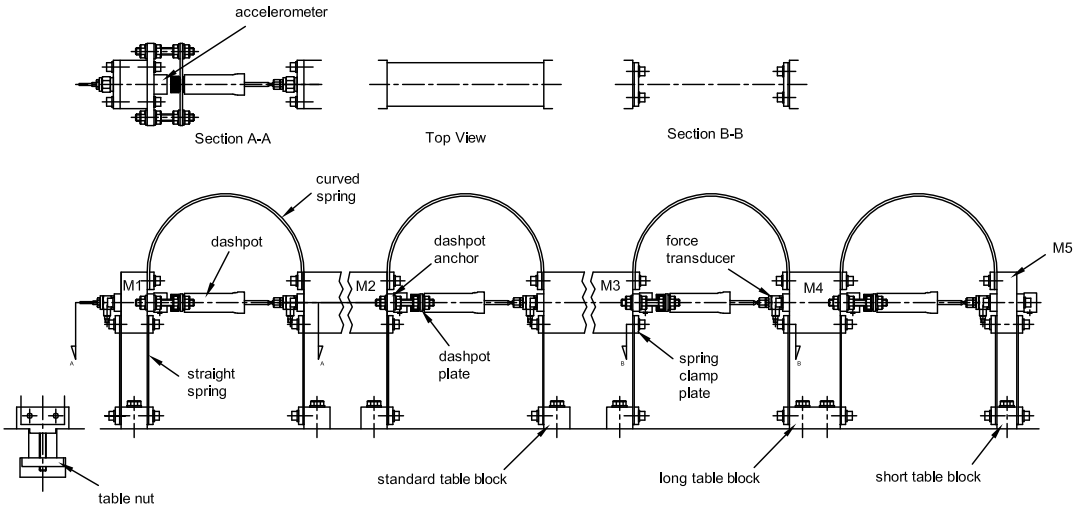

Figure 6.27: Experiment 2 design

consist of two identical vertical beams for each mass, connected to a steel block clamped to the ground. The relative springs between two masses are instead curved arc springs fixed to the upper part of each mass. Between the two spring attachments there is the necessary space for the attachment of damping devices (figure 6.27). The chosen mass and stiffness values are shown in table 6.2, leading to the five natural frequencies shown in table 6.3.

Parameter	Value
m_1	1.727 Kg
m_2	5.122 Kg
m_3	8.213 Kg
m_4	2.609 Kg
m_5	1.339 Kg
k_g	94263 N/m
k_{12}	75136 N/m
k_{23}	67744 N/m
k_{34}	75466 N/m
k_{45}	83396 N/m

Table 6.2: Mass and stiffness values for experiment 2

These frequencies will slightly change when the damping devices will be attached to the system because of the added mass of the dashpot itself, the added damping and a small increase in stiffness too. However the damping devices are considerably lighter than the five masses and the variation expected in terms of frequency

Mode	Frequency (Hz)
1	21.88 Hz
2	32.13 Hz
3	42.48 Hz
4	52.44 Hz
5	64.36 Hz

Table 6.3: Natural frequencies for experiment 2

when attaching these devices should not exceed 2 Hz. The experimental setup for experiment 2 is shown in figure 6.28. The measured Frequency Response Function

Figure 6.28: Experimental setup

of the undamped system is shown in figure 6.29. The five natural frequencies are well spaced from each other and in the predicted range. The localisation matrices chosen for this example consist of five absolute dashpot localisation matrices as eq. 6.7, representing the energy dissipations present in the connections between the five masses and the ground, plus four relative dashpot localisation matrices in the form

$$\mathbf{L}_{1,2} = \begin{pmatrix} 1 & -1 & 0 & \cdots & 0 \\ -1 & 1 & 0 & \cdots & 0 \\ 0 & 0 & 0 & \cdots & 0 \\ \vdots & \vdots & \vdots & \ddots & 0 \\ 0 & 0 & 0 & 0 & 0 \end{pmatrix} \tag{6.12}$$

representing, for example, the equivalent dashpot between degrees of freedom 1 and 2 for a total of nine parameters to identify.

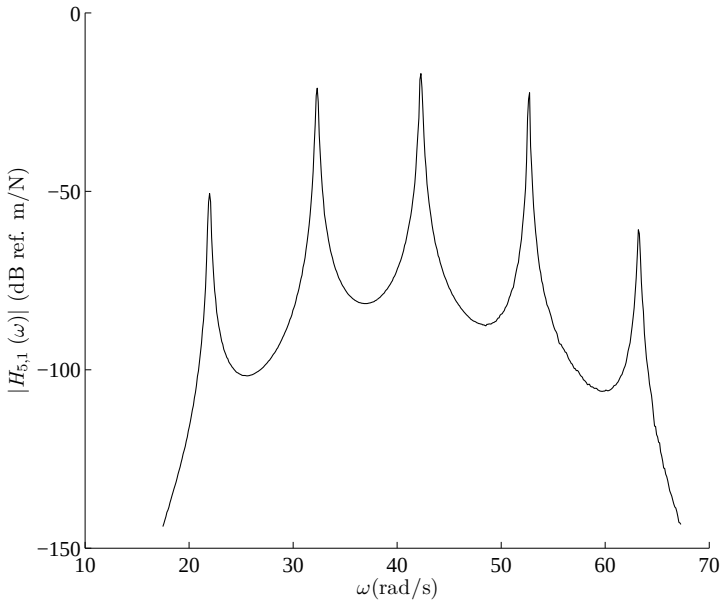

Figure 6.29: Experiment 2: FRF of the undamped system

6.8 Test procedure

The test procedure is practically identical to the one used for experiment 1. The main difference is that in this case only five different frequencies are used and a preliminary analysis on the Frequency Response Function is performed in order to select the most relevant frequencies to use in the process before starting the identification procedure.

Since the added dashpots will be located between two degrees of freedom, it is important to know the mode shapes in order to understand if a particular mode is affected or not by the presence of an added dashpot. Consider the five mode shapes displayed in figure 6.30; depending on the location of the added dashpots each mode could be relevant or not to the identification procedure. If, for example, a dashpot is placed between degrees of freedom 4 and 5, the most relevant information will be obtained by exciting the structure at frequencies close to the fifth mode (figure 6.30(e)), since it is the one with the largest relative displacement between the two DOFs, whereas in all the other four modes the two DOFs move together in the same direction. For the same reason, mode 2 (figure 6.30(b)) will be more important when trying to locate sources of damping between DOFs 2 and 3. Mode 4 (figure 6.30(d)), instead, is clearly a local mode

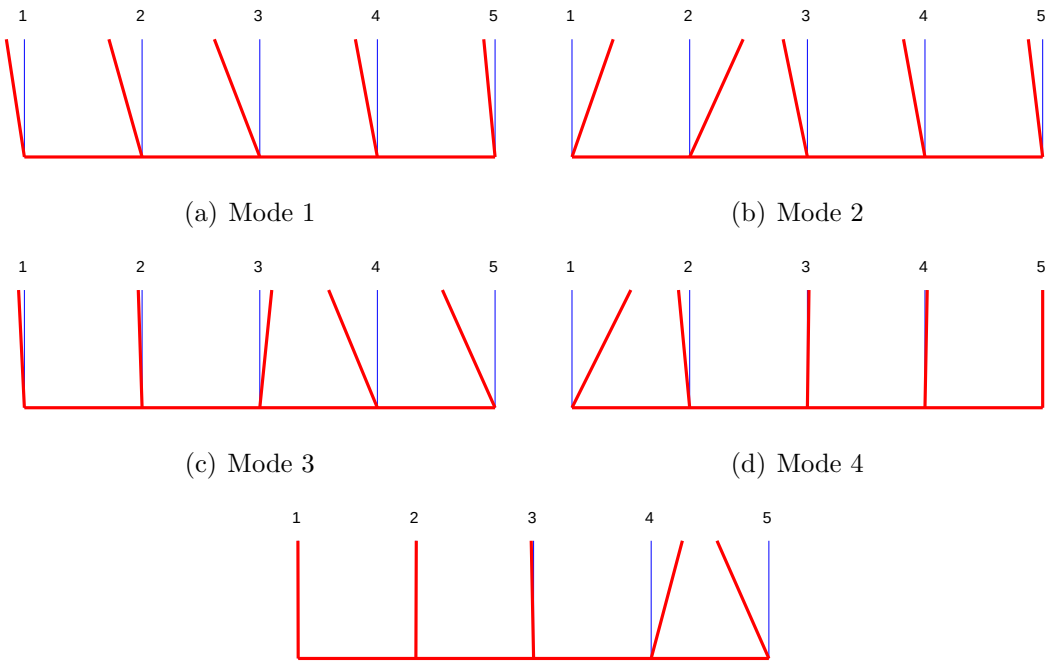

(a) Mode 1

(b) Mode 2

(c) Mode 3

(d) Mode 4

(e) Mode 5

Figure 6.30: Mode shapes for experiment 2

regarding mainly DOFs 1 and 2. Using data obtained from mode 4 in order to identify damping between DOFs 3 and 4 or 4 and 5 could actually make the identification results worse introducing useless information in the energy equation and reducing the accuracy of the identified parameters.

In the next section a selection of the most interesting results on the identification of damping on the five degree-of-freedom system is presented. Results include the undamped system, the system with single and multiple air dashpots and a combined air dashpot and Coulomb friction device system.

6.9 Results for experiment 2

6.9.1 Case 1: undamped system

The first test has been performed in order to measure the offset damping present in the structure which will be compared to the other cases with additional external sources of damping. Several excitations at different frequencies close to the ones of the first five modes have been applied to degree of freedom 5 and the accelerations at all five DOFs have been measured to apply the energy method. The energy

equivalent viscous damping matrix for the undamped system is

$$\mathbf{C}_{id} = \begin{bmatrix} 2.0413 & 0 & 0 & 0 & 0 \\ 0 & 4.0066 & -1.9652 & 0 & 0 \\ 0 & -1.9652 & 4.0066 & 0 & 0 \\ 0 & 0 & 0 & 2.3693 & -0.3280 \\ 0 & 0 & 0 & -0.3280 & 2.3693 \end{bmatrix} \tag{6.13}$$

and it is shown in figure 6.31. The values of the equivalent viscous damping

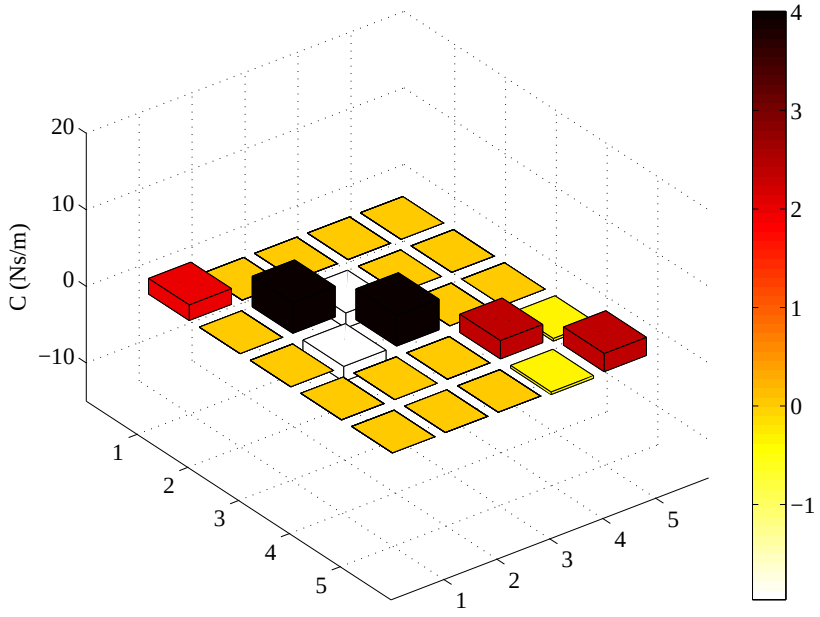

Figure 6.31: Identified damping matrix for the undamped system

coefficient on the diagonal are between 2 to 4 Ns/m and there seems to be a small amount of energy dissipation between DOFs 2 and 3. The identified damping matrix can be used together with the mass and stiffness matrices derived from the values in table 6.2 to obtain the damping ratio ζ of the identified system which can be compared with the damping ratio obtained directly from the acquisition system using the half-power bandwidth method (section 3.2.2). The results of this comparison are shown in table 6.4. Values are not too different for modes from 2 to 5 whereas mode 1 appears to be more damped in the energy equivalent identified system. However, each identification method contains different assumptions and the energy method provides information that are not available using the half-power bandwidth method alone. Since the half-power method is well established

Mode	ζ_{hp}	ζ_{id}	Err %
1	0.0020	0.0030	+50%
2	0.0024	0.0025	+4%
3	0.0023	0.0019	-17%
4	0.0015	0.0017	+13%
5	0.0021	0.0020	-5%

Table 6.4: Comparison of damping ratios for case 1 obtained by half-power bandwidth method (ζ_{hp}) versus energy spatial identification method (ζ_{id}).

in engineering and widely used in many applications, it could eventually be used to adjust the results obtained by the energy method by scaling the amplitudes of the identified damping coefficients once the location is determined.

6.9.2 Case 2: single air dashpot

In the first case with added damping, an air dashpot (figure 6.32) with a viscous damping coefficient of 4 Ns/m has been attached between DOFs 4 and 5 as additional source of damping. By using data obtained from excitations in the full

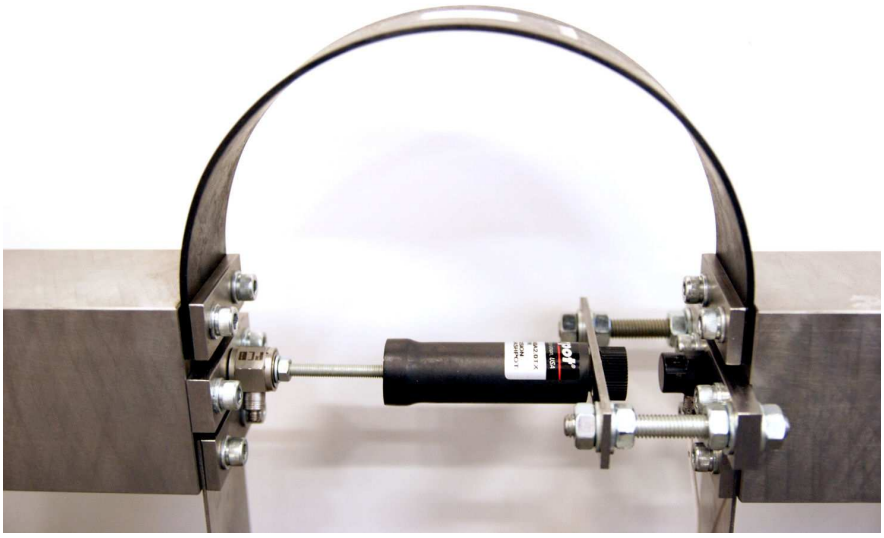

Figure 6.32: Viscous dashpot between DOFs 4 and 5

frequency range of the first five modes in the identification process, the results are not satisfactory both for the location and for the amplitude of the identified

damping sources. Looking at mode shapes in figure 6.30, a possible reason could be the fact that adding a dashpot between DOFs 4 and 5 almost does not affect the first four modes but strongly affects the fifth mode. Data obtained from excitations at frequencies in the range between 20 to 55 Hz does not contain much information about the added damping and does not give any useful contribution to the energy equations regarding the identification. Actually this data could be considered damaging to the method. Another way of looking at this aspect is considering the Frequency Response Function of the undamped system versus the FRF of the system with the added dashpot in figure 6.33. The two FRFs

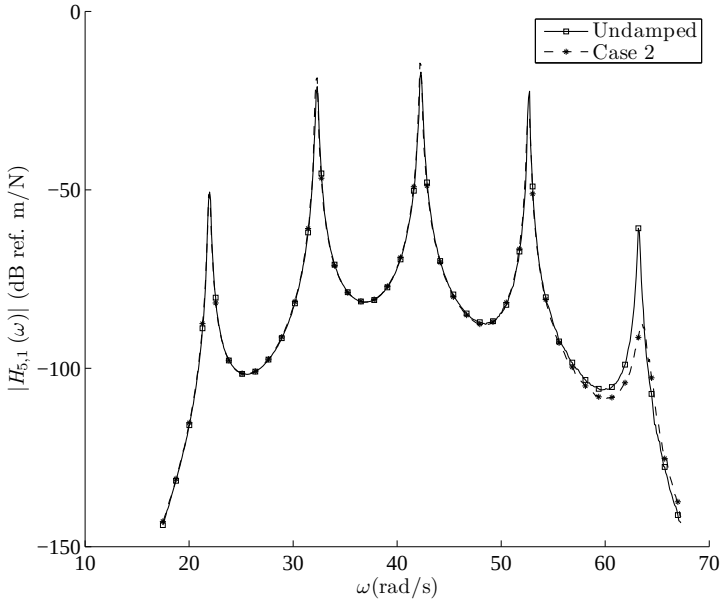

Figure 6.33: Experiment 2: FRF of the undamped system versus case 2

practically overlap for the first four modes and the effect of damping is only visible for the fifth mode.

For this reason, instead of using all the data available, only a selection of significant excitations in the range from 55 to 70 Hz is used to apply the method. The identified equivalent viscous damping matrix for case 2 becomes

$$\mathbf{C}_{id} = \begin{bmatrix} 0.8165 & 0 & 0 & 0 & 0 \\ 0 & 1.6026 & -0.7861 & 0 & 0 \\ 0 & -0.7861 & 1.8751 & -2.1476 & 0 \\ 0 & 0 & -2.1476 & 6.3098 & -3.3457 \\ 0 & 0 & 0 & -3.3457 & 4.1622 \end{bmatrix} \tag{6.14}$$

and it is shown in figure 6.34. In the damping matrix is immediately noticeable an

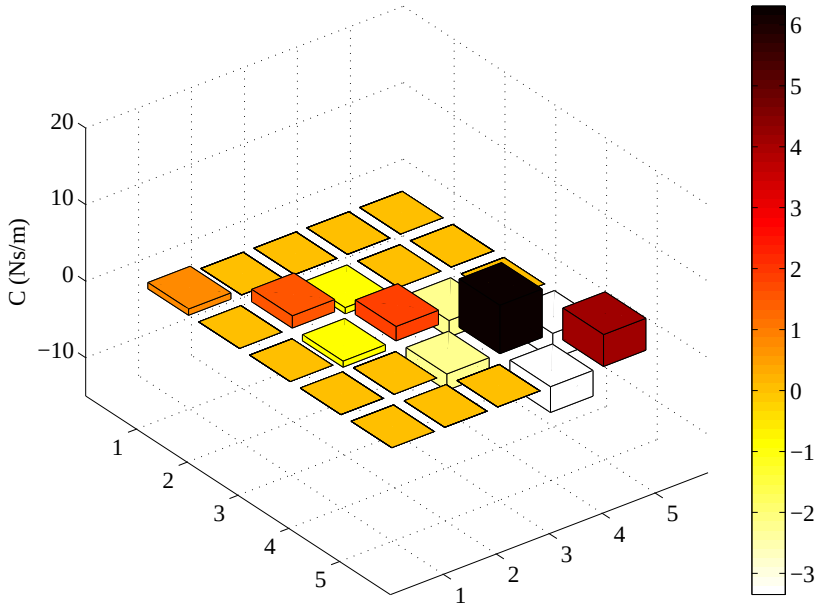

Figure 6.34: Identified damping matrix for case 2

increasing of the damping coefficients in the region where the dashpot is attached (between DOFs 4 and 5). The value of the damping coefficient of the added dashpot is slightly lower than expected (3.3457 Ns/m instead of 4 Ns/m) but reasonably close and correctly located. Some of the offset damping changed, but the identified damping pattern is representative of the real system.

6.9.3 Case 3: multiple air dashpots

In the second damped example two air dashpots of viscous damping coefficient respectively equal to 15 and 4 Ns/m have been applied between DOFs 2 and 3 and between DOFs 4 and 5. By looking at the mode shapes, the first dashpots seems to be especially effective on mode 2 where DOFs 2 and 3 are moving in opposite directions with large relative displacements and velocities. By looking at the comparison between the Frequency Response Function of the undamped system versus case 3 (figure 6.35), the frequency ranges affected by the added dashpots seems to be between 25 and 38 Hz and between 55 to 70 Hz again. There appears to be a small effect on modes 3 and 4 too with a slight shift for the natural frequencies due to the added masses of dashpots. The identified

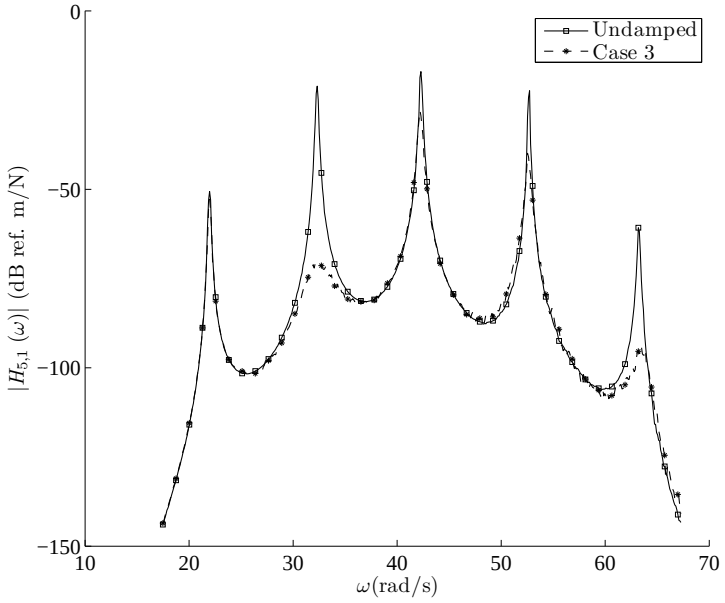

Figure 6.35: Experiment 2: FRF of the undamped system versus case 3

equivalent viscous damping matrix for case 3 becomes

$$\mathbf{C}_{id} = \begin{bmatrix} 2.0413 & 0 & 0 & 0 & 0 \\ 0 & 21.7735 & -19.7321 & 0 & 0 \\ 0 & -19.7321 & 21.7735 & 0 & 0 \\ 0 & 0 & 0 & 7.5764 & -5.5351 \\ 0 & 0 & 0 & -5.5351 & 7.5764 \end{bmatrix} \tag{6.15}$$

and it is shown in figure 6.36. The identification is representative of the real system, both regarding the location and the relative amplitude (the damping coefficient of the dashpot between DOFs 2 and 3 is larger than the one of the dashpot between DOFs 4 and 5). The damping coefficient values are close to the previously measured ones and considering each single dashpot individually, the error is around 30%. The dashpot between DOFs 4 and 5 is then moved between DOFs 3 and 4 (case 3b) to check if the identification method is able to detect the change in the location maintaining the same amplitude. The new location particularly affects mode 3, as it can be seen from the FRF in figure 6.37. The identified equivalent viscous damping matrix for case 3b becomes

$$\mathbf{C}_{id} = \begin{bmatrix} 2.0543 & 0 & 0 & 0 & 0 \\ 0 & 16.4224 & -14.3811 & 0 & 0 \\ 0 & -14.3811 & 25.8219 & -9.3995 & 0 \\ 0 & 0 & -9.3995 & 11.7689 & -0.3280 \\ 0 & 0 & 0 & -0.3280 & 2.3693 \end{bmatrix} \tag{6.16}$$

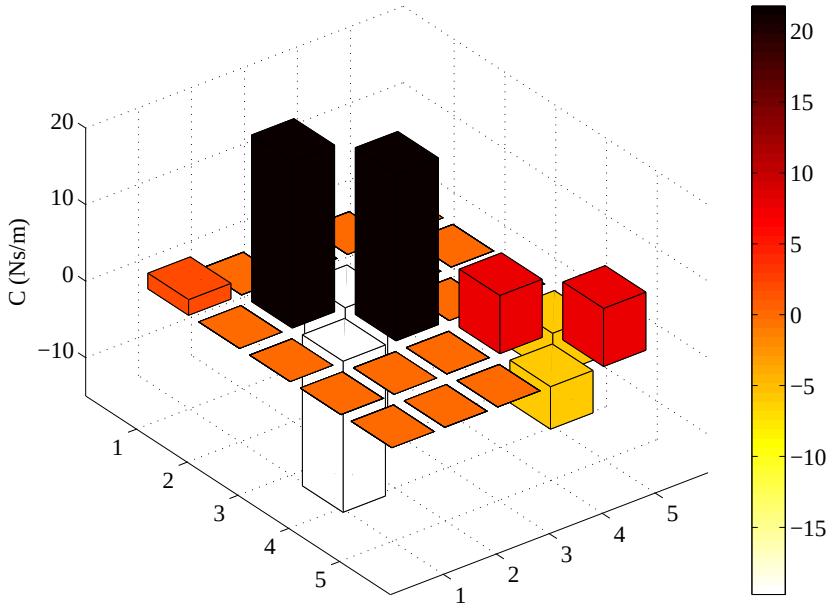

Figure 6.36: Identified damping matrix for case 3

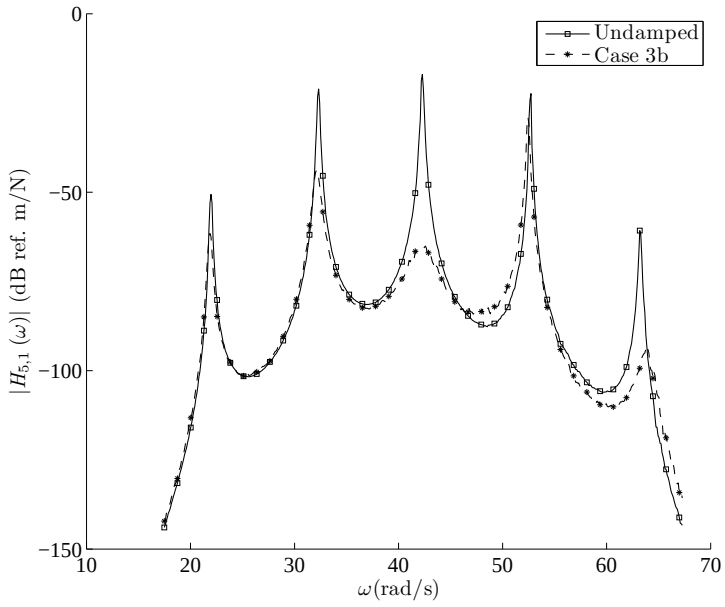

Figure 6.37: Experiment 2: FRF of the undamped system versus case 3b

and it is shown in figure 6.38. The two dashpots are correctly located but the damping coefficients merged together with a transfer of energy from the largest to the smallest. In case 3 it was expected to find two damping coefficients of respectively 15 and 4 Ns/m but the results obtained were 19.73 and 5.53 Ns/m

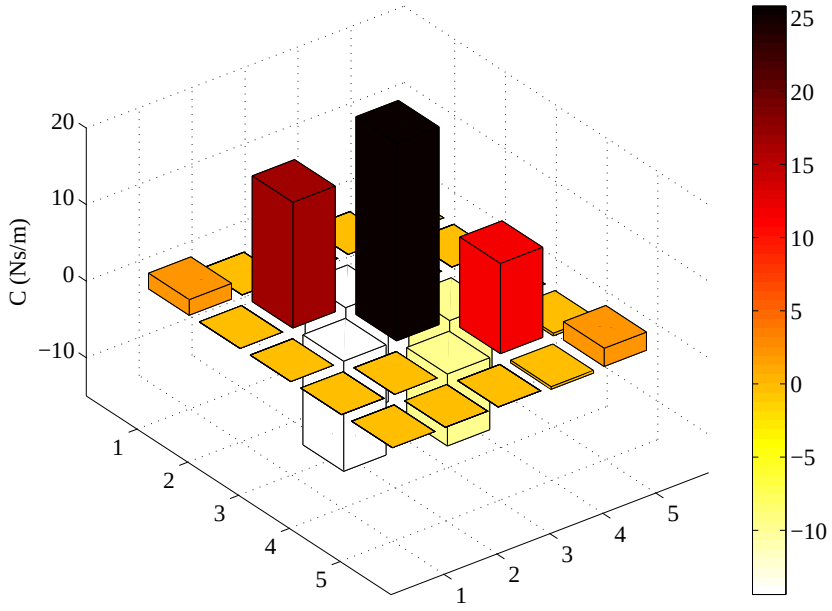

Figure 6.38: Identified damping matrix for case 3b

with some variations of the offset damping. In case 3b, again the expectation was to obtain 15 and 4 Ns/m but the results was 14.38 and 9.40 Ns/m. The validity of these results depends on many factors and the level of accuracy requested by the specific application of the method. Qualitatively speaking, the damping pattern looks reasonably close to the real system and to usual viscous damping models used to represent these systems. One question which could arise is how these equivalent systems are capable of predicting physical phenomena which are closely related to damping. If the identification is performed in order to detect the regions of a structure where the energy is mostly dissipated, this method can give valuable information; if the identification aims to give, for example, a precise value of frequency at which an instability will happen, then more accurate and expensive approaches may be necessary.

6.9.4 Case 4: combined viscous and friction dashpots

The last case consists of the system with combined viscous and friction dashpots. The viscous dashpot is the same as case 3 located between DOFs 2 and 3 of damping coefficient 15 Ns/m whereas the Coulomb friction device (figure 6.39) is

located between DOFs 3 and 4 with a coefficient of friction of 0.4 and a normal force of 0.9 N. The FRF is similar to the one of case 3b, so the same frequency

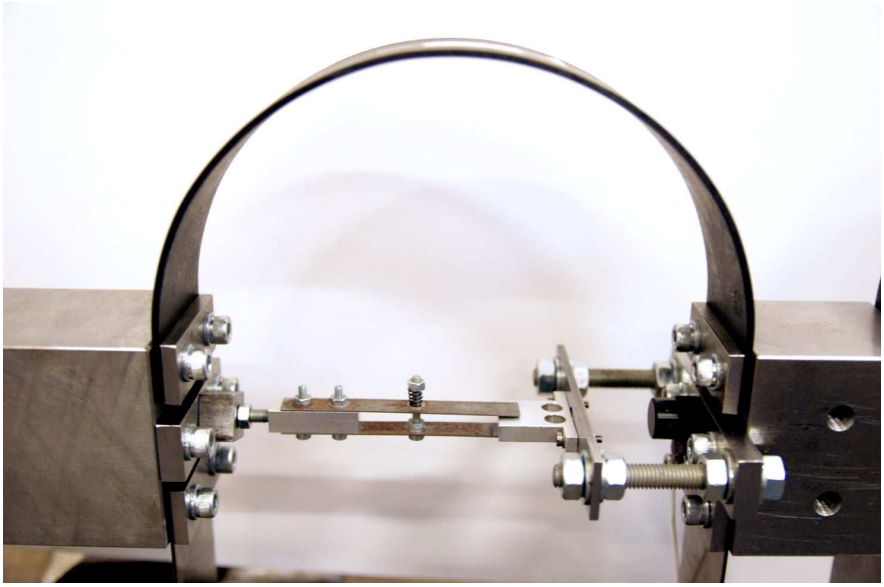

Figure 6.39: Coulomb friction device between DOFs 3 and 4

range is used to perform the identification. The identified equivalent viscous damping matrix for case 4 is

$$\mathbf{C}_{id} = \begin{bmatrix} 2.9881 & -2.3757 & 0 & 0 & 0 \\ -2.3757 & 14.6754 & -11.6874 & 0 & 0 \\ 0 & -11.6874 & 19.3396 & -7.0399 & 0 \\ 0 & 0 & -7.0399 & 9.3596 & -1.7073 \\ 0 & 0 & 0 & -1.7073 & 2.3197 \end{bmatrix} \tag{6.17}$$

and is shown in figure 6.40. The identified viscous dashpot has a damping coefficient of 11.68 Ns/m instead of the expected 15 Ns/m and the equivalent viscous dashpot representing the Coulomb friction device has a damping coefficient of 7.03 Ns/m. From eq. (6.11) the value of the coefficient of friction can be derived for the frequency of mode 3, where the Coulomb friction device is mostly effective, obtaining

$$\mu = \frac{c_{eq}\pi\omega x_0}{4F_n} = \frac{7.03 \cdot \pi^2 \cdot 2 \cdot 50 \cdot 0.0003}{4 \cdot 0.9} = 0.5782 \tag{6.18}$$

The value is higher than the expected 0.4, compensating the lower value for the viscous dashpot. This last case was initially meant to validate the energy method with Coulomb friction included in the analytical model, as explained in section 5.2.4. The good results obtained in numerical simulations were not

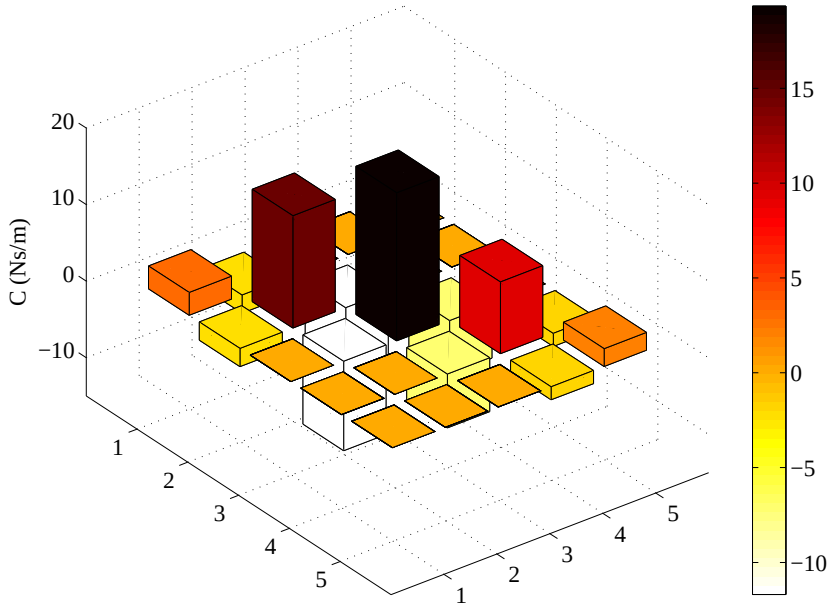

Figure 6.40: Identified damping matrix for case 4

exactly replicated in the experiments. Possible reasons include the analytical model chosen to represent friction as well as the conditioning of matrix **G** when different mathematical models are included and the effect of nonlinearities. This dissertation is not intended to address issues such as nonlinearities at this stage but they might be part of future work on the subject.

6.10 Conclusions for experiment 2

Results extracted from experiment 2 reflect the general performances obtained from the previous experiment: good location of the damping sources when appropriate data is used with realistic values for the equivalent viscous damping coefficients. The choice of the localisation matrices seems to be very important in order to obtain the right results. If too many parameters are chosen to represent the damping matrix, a large number of measurements is required and the method becomes less advantageous. Engineering knowledge is required to choose the most important parameters to identify, the best force configurations, the range of frequencies to excite the structure and the interpretation of the results obtained. At the moment the method is not very effective in distinguishing between different

sources of damping but it quantitatively performed well in capturing the energy equivalent dissipations.

6.11 Closure

The energy balance identification method proposed in chapter 4 has been tested on two different structures: an aluminium cantilever beam and a five degrees of freedom mass-spring structure. The results obtained are interesting from an engineering point of view since they provide useful information both on the location and on the amplitude of the main sources of damping. The method does not require expensive instrumentation more than any other modal test, it is reasonably fast and seems suitable for many engineering applications where energy dissipation is a major issue. In the last chapter the most important outcomes of the research are summarised, with particular interest on the possible applications of the energy method in other fields and future work.

Chapter 7

Conclusions and future work

7.1 Summary of the contributions made

The oscillation of elasto-mechanical systems involves the exchange of kinetic and potential energies as well as the dissipation of energy by damping. Methods are generally well established for modelling the inertial and stiffness properties of most systems but often there remains considerable doubt on how the damping behaviour should be represented. The most common method is to assume viscous damping, which is attractive computationally because it results in systems of second-order differential equations with solutions which are readily available by well understood techniques. However, viscous damping is a mathematical approximation of a large number of physical phenomena involving friction, radiation, air pumping, fluid interactions, electronic mechanisms, dislocations, relaxation on grain boundaries, irreversible intercrystal heat flux, viscoelasticity, eddy currents and ferromagnetic hysteresis. Whether this approximation is valid or not depends on the application, the level of accuracy required and the nature of the problem under examination. This dissertation addresses the problem of spatial damping identification in multi degree-of-freedom systems, with particular attention to practical issues arising from real structures and measurements.

An extensive literature review of the main viscous damping matrix identification methods has been presented. Some useful considerations on the philosophy and performance of the existing methods have been provided. Methods have been classified into three main categories depending on the input used to perform the identification, i.e. methods based on the Frequency Response Function, modal parameters and time-domain measurements. In particular, attention has been

focused on three fundamentally different approaches; the closed-form solution developed by Lancaster [87], methods based on inverting the measured matrix of receptances and first-order perturbation methods. Interesting considerations include an alternative way of deriving Lancaster's formula from the second-order matrix pencil, addressing the problem of inverting the matrix of receptances by showing the effect of modal incompleteness as well as the error introduced by pseudo inversion in the first-order perturbation method. The three methods have been compared by a numerical simulation and all three approaches have been found to be capable of closely reproducing the complex eigenvalues within the frequency range of the data obtained by modal truncation. However, the perturbation method seems to be highly affected by modal incompleteness whereas the other two methods lead to reasonably good results with the limited frequency range measurements available.

From the several methods available in literature, a method based on the balance between the energy input by external forces and the energy dissipated by damping mechanisms proposed by Liang [103] has been considered. It is particularly interesting for some of the advantages it presents with respect to the other methods. This method can potentially be used to identify different kinds of damping (and not only with viscous damping) and it seems to perform well when dealing with the modal incompleteness of measurements; however it also has some disadvantages: it assumes a diagonal mass matrix and knowledge of the full stiffness matrix and some coefficients of damping. In order to avoid these disadvantages but maintain the versatility and performance of the method a different energy approach has been proposed. The improved method does not require any mass or stiffness information if measurements at the degrees of freedom of interest are available. This advantage has a cost in terms of the number of equations available for each measurement, which is reduced. For this reason some techniques are proposed in order to improve the identification by addressing issues such as the damping matrix parameterisation, the spatial incompleteness of measurements and the underdetermination of the system of equations.

The method has been tested on different numerical simulations, including cases with sources of damping different from viscous damping such as Coulomb friction,

and it obtained good results when dealing with random noise and modal and spatial incompleteness too. The method seems able to replicate the location and the amplitude of damping accurately and provides a useful tool to detect the main sources of energy dissipations. The identified damping matrix is equivalent from an energy point of view to damping of the actual system in the frequency range of interest. This does not always means that the two systems (original and identified) are identical but the general damping pattern and values have consistently been found to be reasonably similar and representative of the actual system. The method can be set to a certain level of approximation depending on the number of parameters and on the complexity of the damping functions used; it has been found that if a low approximation level is used the method seems to detect the largest sources of energy dissipation first, whereas the smallest (and possibly negligible) require a more accurate model.

Given the good results in the numerical simulations two different experiments have been designed and tested in order to validate the method on real structures. The two structures consist of an aluminium cantilever beam with nominal dimensions close to the one of the numerical simulations and a five degrees of freedom mass-spring structure. Different damping devices (eddy current dashpots, air viscous dashpots, Coulomb friction devices) have been attached to these structures in order to locate and evaluate their damping properties. The results obtained are interesting from an engineering point of view since they provide useful information both on the location and on the amplitude of the main sources of damping. The method does not require expensive instrumentation, it is reasonably fast and seems suitable for many engineering applications where the energy dissipation is a major issue. The choice of the damping matrix parameterisation seems to be very important in order to obtain the right results. If too many parameters are chosen to represent the damping matrix, a large number of measurements are required and the method is not advantageous. Engineering knowledge is required to choose the most important parameters to identify, the best force configurations, the range of frequencies to excite the structure and the interpretation of the results obtained.

The most important outcomes of this research consist of the critical analysis of

some of the existing spatial damping identification techniques, the definition of an improved method which has been successfully validated by numerical simulations and provided good results in real problems as well as demonstrated by two experiments. The method can still be improved on many aspects; some suggestions and ideas for future work are proposed in the next section.

7.2 Suggestions for future work

Several ideas have arisen from the development and testing of the energy method proposed in this dissertation. The results obtained both from numerical simulations and experiments are encouraging but there is always the possibility for further improvements. One of the weak points of the method concerns the amplitude of the identified damping sources. Whereas the location has been accurate in most cases (if the right parameterisation and the correct range of frequency are selected) the values of the damping coefficients have often been found to be different from what was expected, with errors sometimes larger than 100%. One idea is to use the information given by other well-established modal damping identification methods, such as the half-power bandwidth method, to properly "scale" the results once the location has been identified. If the modal damping ratio is known it is possible to calculate the energy dissipated by a certain mode and therefore the energy dissipated in the frequencies of interest by modes involved in that range. This information can then be used in the energy spatial identification to improve the results. Alternatively, an equivalent modal energy method can be derived from the spatial method proposed in this thesis simply by writing the energy equations in terms of modal parameters instead of spatial coordinates. This has not been done, since it is not pertaining to spatial damping identification, but it can be an interesting extension of the proposed technique which can lead to improved results.

Another idea regards the application of the energy method to other fields. A possibility is to consider damage or defect detection; most of these phenomena result in energy dissipation in the region surrounding the defect which can eventually be detected by a specific version of the energy method. In this case more

accurate measurements might become necessary but the principles of the method remain valid. The same thing is true for damage detection: even if established techniques are already available, the energy method could help by looking at the same problem from a different angle which might be advantageous in some cases.
An improvement that has to be considered regards the non-viscous sources of damping. Although in numerical simulations the method has proven to be successful, the same thing cannot be said for real experiments where the results were not particularly accurate where the Coulomb friction model has been introduced into the energy equations. The best results have been obtained when using the viscous damping model only and subsequently deriving the friction coefficient rather than including it in the equations in the first place. This way of solving the energy equations can be further improved by introducing different solving algorithms or adding other important information. However, it must be kept in mind that the initial purpose of the method was to give readily usable information for engineering design with a simple but effective method. The parameterisation of the damping matrix also plays an important role in the identification process and further investigation could lead to improved results.
Another aspect which can be improved is the implementation of the identification method in standard modal analysis software and instrumentation. At present one of the most common techniques to dynamically define a system and measure damping is to excite the structure by random signals in the frequencies of interest or by a hammer test to obtain the Frequency Response Function and then using the half-power bandwidth method to estimate the modal damping ratio. Using the energy method as it has been developed in this dissertation, where time domain measurements and single frequency excitations are needed, will result in more time-consuming and expensive tests if the interest is in both dynamic properties (FRF) and damping at the same time.
The last suggestion is to properly investigate whether the equivalent viscous damping approximation is sufficient for a specific application or not. Obtaining similar natural frequencies and mode shapes between the real and identified systems does not mean that the identified system is able to predict any phenomenon occuring in the real system. All non-linear events are practically deleted by the

viscous damping approximation in the model so each case has to be studied separately with particular attention to the nature of the problem.

7.3 List of publications

The major outcomes of this research may be found in the following references.

Journal papers

- M. Prandina, J.E. Mottershead and E. Bonisoli, An assessment of damping identification methods, Journal of Sound and Vibration **323** (3-5), 2009, pages 662-676.

- M. Prandina, J.E. Mottershead and E. Bonisoli, Damping identification in multiple degree-of-freedom systems using an energy balance approach, J. Phys.: Conf. Ser., **181**, 2009, 012006.

Conference papers

- M. Prandina, J.E. Mottershead and E. Bonisoli, Location and identification of damping parameters, IMAC XXVII Conference and Exposition on Structural Dynamics, Orlando, Florida, USA, 2009.

- G.A. Vio, M. Prandina and G. Dimitriadis, Damping identification in a non-linear aeroelastic structure, abstract accepted in the ISMA 2010 International Conference on Noise and Vibration Engineering, Leuven, Belgium, 2010.

Bibliography

[1] L. Gaul. The influence of damping on waves and vibrations. *Mechanical Systems and Signal Processing*, 13(1):1–30, 1999.

[2] I. Newton. *Philosophiæ naturalis principia mathematica*. Henderson & Saplding, London, 1687.

[3] R. Hooke. *Lectiones Cutlerianæ or A collection of lectures: physical, mechanical, geographical and astronomical*. Printed for John Martyn, London, 1679.

[4] S.H. Crandall. The role of damping in vibration theory. *Journal of Sound and Vibration*, 11(1):3–18, 1970.

[5] J.E. Ruzicka and T.F. Derby. *Influence of damping in vibration isolation*. The Shock and Vibration Information Center, United States Department of Defense, Naval Research Laboratory, Washington, D.C., 1971.

[6] S.D. Poisson. Mémoire sur les équations générales de l'équilibre et du mouvement des corps solides élastiques et des fluides. *Journal de l'cole Polytechnique*, 13:139, 1831.

[7] G.G. Stokes. *On the effect of the internal friction of fluids on the motion of pendulums*. Pitt press, Cambridge, 1851.

[8] J.C. Maxwell. On the viscosity or internal friction of air and other gases. *Philosophical Transactions of the Royal Society of London*, 156:249–268, 1866.

[9] Lord Rayleigh. *The theory of sound - Second edition revised and enlarged*. Macmillan and co., New York, 1896.

[10] D.J. Mead. *Passive vibration control*. Wiley, Chichester, 1998.

[11] K. Nagaya and H. Kojima. Shape characteristics of a magnetic damper consisting of a rectangular magnetic flux and a rectangular conductor. *Bulletin of JSME*, 25(206):1306–1311, 1982.

[12] K. Nagaya, H. Kojima, Karube Y., and Kibayashi H. Braking forces and damping coefficients of eddy current brakes consisting of cylindrical magnets and plate conductors of arbitrary shape. *IEEE Transactions on Magnetics*, 20(6):2136–2145, 1984.

[13] H.A. Sodano, J.-S. Bae, D.J. Inman, and W.K. Belvin. Concept and model of eddy current damper for vibration suppression of a beam. *Journal of Sound and Vibration*, 288:1177–1196, 2005.

[14] N.W. Hagood and A. Von Flotow. Damping of structural vibrations with piezoelectric materials and passive electrical networks. *Journal of Sound and Vibration*, 146(2):243–268, 1991.

[15] F. Dell'Isola, C. Maurini, and M. Porfiri. Passive damping of beam vibrations through distributed electric networks and piezoelectric transducers: prototype design and experimental validation. *Smart Materials and Structures*, 13:299–308, 2004.

[16] F. Sadek, B. Mohraz, A.W. Taylor, and R.M. Chung. Method of estimating the parameters of tuned mass dampers for seismic applications. *Earthquake Engineering and Structural Dynamics*, 26:617–635, 1997.

[17] N.A. Alexander and F. Schilder. Exploring the performance of a nonlinear tuned mass damper. *Journal of Sound and Vibration*, 319:445–462, 2009.

[18] R. Stanway, J.A. Rongong, and N.D. Sims. Active constrained-layer damping: A state-of-the-art review. *Proceedings of the Institution of Mechanical Engineers. Part I: Journal of Systems and Control Engineering*, 217(6):437–456, 2003.

[19] G. Gatti, M.J. Brennan, and P. Gardonio. Active damping of a beam using a physically collocated accelerometer and piezoelectric patch actuator. *Journal of Sound and Vibration*, 303:798–813, 2007.

[20] A. Preumont. *Vibration control of active structures : an introduction (2nd ed.)*. Kluwer Academic Publishers, Dordrecht, 2002.

[21] C. Paulitsch, P. Gardonio, and S.J. Elliott. Active vibration damping using self-sensing, electrodynamic actuators. *Smart Materials and Structures*, 15:499508, 2006.

[22] B.J. Lazan. Energy dissipation mechanisms in structures, with particular reference to material damping. In *Structural Damping edited by J.E. Ruzicka*, American Society of Mechanical Engineers, pages 1–34, New York, 1959. Pergamon Press.

[23] A. Muszynska. Tlumienie wewnetrzne w ukladach mechanicznuch (Internal damping in mechanical systems). In *Dynamika Maszyn (Dynamics of Machines)*, Polish Academy of Sciences, pages 164–212, Warsaw, 1974. Ossolineum.

[24] A.D. Nashif, D.I.G. Jones, and J.P. Henderson. *Vibration damping*. John Wiley & Sons, New York, 1985.

[25] B.J. Lazan. *Damping of materials and members in structural mechanics*. Pergamon, New York, 1968.

[26] C.W. Bert. Material damping: an introductory review of mathematical models, measures and experimental techniques. *Journal of Sound and Vibration*, 29(2):129–153, 1973.

[27] F.R. Eirich. *Rheology. Theory and applcations*. Academic Press, New York, 1956.

[28] R.C. Koeller. Applications of fractional calculus to the theory of viscoelasticity. *ASME Journal of Applied Mechanics*, 51:299–307, 1984.

[29] A. Schmidt and L. Gaul. Finite element formulation of viscoelastic constitutive equations using fractional time derivatives. *Nonlinear Dynamics*, 29:37–55, 2001.

[30] D.R. Bland. *The theory of linear viscoelasticity*. Pergamon Press, Oxford, 1960.

[31] W.N. Findley, J.S. Lai, and K.Onaran. *Creep and relaxation of nonlinear viscoelastic materials, with an introduction to linear viscoelasticity*. North-Holland series in applied mathematics and mechanics, Amsterdam, 1976.

[32] C.F. Beards. The damping of structural vibration by controlled interfacial slip in joints. *ASME Journal of Vibration, Acoustics, Stress and Reliability in Design*, 105:369–372, 1983.

[33] E.E. Ungar. Energy dissipation at structural joints; mechanisms and magnitudes. Technical report, Flight Dynamics Laboratory, Report FDL-TDR-14-98, 1964.

[34] E.E. Ungar. The status of engineering knowledge concerning the damping of built-up structures. *Journal of Sound and Vibrations*, 26:141–154, 1973.

[35] L. Goodman. A review of progress in analysis of interfacial slip damping. In *Structural Damping edited by J.E. Ruzicka*, American Society of Mechanical Engineers, pages 1–34, New York, 1959. Pergamon Press.

[36] J. Lenz and L. Gaul. The influence of microslip on the dynamic behaviour of bolted joints. In *Proceedings of the 13th International Modal Analysis Conference, Nashville*, pages 248–254, 1995.

[37] L. Gaul and J. Lenz. Nonlinear dynamics of structures assembled by bolted joints. *Acta Mechanica*, 125:169–181, 1997.

[38] M. Groper. Microslip and macroslip in bolted joints. *Experimental Mechanics*, 25(2):171–174, 1985.

[39] W.D. Iwan. On a class of models for the yielding behaviour of continuous composite systems. *ASME Journal of Applied Mechanics*, 89:612–617, 1967.

[40] D.J. Segalman. An initial overview of iwan modeling for mechanical joints. Technical report, Sandia National Laboratories, Albuquerque, New Mexico, Report No. SAND2001-0811, 2001.

[41] K.C. Valanis. Fundamental consequences of a new intrinsic time measure. plasticity as a limit of the endochronic theory. *Archive of Mechanics*, 32:171–191, 1980.

[42] H. Wentzel. Modelling of frictional joints in dynamically loaded structures: a review. Technical report, KTH Solid mechanics, Royal Institute of technology, 2006.

[43] Y.K. Wen. Equivalent linearization for hysteretic systems under random excitation. *ASME Journal of Applied Mechanics*, 47:150–154, 1980.

[44] N.M.M. Maia, J.M.M. Silva, J. He, N.A.J. Lieven, R.M. Lin, G.W. Skingle, W.M. To, and A.P.V. Urgueira. *Theoretical and experimental modal analysis*. Research Studies Press, Taunton, 1997.

[45] D.J. Ewins. *Modal testing: theory and practice*. Research Studies Press LTD, Letchworth, Hertfordshire, England, 1984.

[46] W.T. Thomson and M.R. Dahleh. *Theory of vibration with applications*. Prentice-Hall, Englewood Cliffs, N.J., 1998.

[47] L.S. Jacobsen. Steady forced vibration as influenced by damping. *Transactions of the American Society of Mechanical Engineers*, 52(1):169–181, 1930.

[48] J. Woodhouse. Linear damping models for structural vibration. *Journal of Sound and Vibration*, 215(3):547–569, 1998.

[49] A.L. Kimball and D.E. Lovell. Internal friction in solids. *Phys. Rev.*, 30(6):948–959, 1927.

[50] T. Theodorsen and I.E. Garrick. Mechanism of flutter. a theoretical and experimental investigation of the flutter problem. Technical report, N.A.C.A. Report No. 689, Langley Field, Virginia, 1940.

[51] R.E.D. Bishop and D.C. Johnson. *The mechanics of vibration*. Cambridge University Press, 1960.

[52] S.H. Crandall. The hysteretic damping in vibration theory. In *Proceedings of the Institution of Mechanical Engineers*, volume 205, pages 23–28, London, U.K., 1991.

[53] B.M. Fraijs de Veubeke. Influence of internal damping on aircraft resonance. In *AGARD manual on elasticity*, volume 1. AGARD, 1960.

[54] T.K. Caughey. Vibration of dynamics systems with linear hysteretic damping. In *Proceedings of Fourth US National Congress of Applied Mechanics*, New York, 1962. ASME.

[55] S.H. Crandall. Dynamic response of systems with structural damping. In *Air, space and instruments, Draper Anniversary Volume*, pages 183–193, New York, 1963. McGraw-Hill.

[56] S. Adhikari. *Damping models for structural vibration*. PhD thesis, University of Cambridge, 2000.

[57] R.E.D. Bishop and W.G. Price. A note on hysteretic damping of transient motions. In *Random vibration - status and recent developments*, pages 39–45, Amsterdam, 1986. Elsevier.

[58] G.B. Muravskii. On frequency independent damping. *Journal of Sound and Vibration*, 274:653–668, 2004.

[59] G.B. Muravskii. Frequency independent model for damping. In *Proceedings of the 25th Israel Conference on Mechanical Engineering*, pages 230–232, Haifa, Israel, 1994.

[60] N.B. Do, A.A. Ferri, and O.A. Bauchau. Efficient simulation of a dynamic system with LuGre friction. *Journal of Computational and Nonlinear Dynamics*, 2(4):281–289, 2007.

[61] A.J. Morin. New friction experiments carried out at Metz in 1831-1833. In *Proceedings of the French Royal Academy of Sciences*, volume 4, pages 1–128, 1833.

[62] R. Stribeck. Die wesentlichen eigenschaften der gleit- und rollenlager. Technical report, VDI-Zeitschrift 46, 1902.

[63] J.E. Mottershead and R. Stanway. Identification of nth-power velocity damping. *Journal of Sound and Vibration*, 105(2):309–319, 1986.

[64] I. Podlubny. *Fractional differential equations*. Academic Press, San Diego, CA, 1999.

[65] I. Podlubny. Geometric and physical interpretation of fractional integration and fractional differentiation. *Fractional Calculus and Applied Analysis*, 5(4):367 – 386, 2002.

[66] P.G. Nutting. A new general law of deformation. *Journal of the Franklin Institute*, 191:679–685, 1921.

[67] R.A. Fraser, W.J. Duncan, and A.R. Collar. *Elementary matrices*. Cambridge University Press, 1946.

[68] L. Meirovitch. *Analytical methods in vibrations*. Macmillan Publishing, New York, 1967.

[69] W.T. Thomson, C. Calkins, and P. Caravani. A numerical study of damping. *Earthquake Engineering and Structural Dynamics*, 3:97–103, 1974.

[70] F. Ma S.M. Shahruz. Approximate decoupling of the equations of motion of linear underdamped system. *ASME Journal of Applied Mechanics*, 55:716–720, 1988.

[71] S.R. Ibrahim and A. Sestieri. Existence and normalisation of complex modes in post experimental modal analysis. In *Proceedings of the 13th IMAC*, pages 483–489, Nashville TN, 1995.

[72] T.K. Caughey. Classical normal modes in damped linear systems. *ASME Journal of Applied Mechanics*, 27:269–271, 1960.

[73] T.K. Caughey and M.E.J. O'Kelly. Classical normal modes in damped linear systems. *ASME Journal of Applied Mechanics*, 32:583–588, 1965.

[74] M. Link. Using complex modes for model updating of structures with non-proportional damping. In *Proceedings of the International Conference on Noise and Vibration Engineering ISMA 2006*, Belgium, 2006. University of Leuven.

[75] J.-W. Liang and B.F. Feeny. Balancing energy to estimate damping parameters in forced oscillators. *Journal of Sound and Vibration*, 295:988–998, 2006.

[76] F.-L. Huang, X.-M. Wang, Z.-Q. Chen, X.-H. He, and Y.-Q. Ni. A new approach to identification of structural damping ratios. *Journal of Sound and Vibration*, 303:144–153, 2007.

[77] J.-W. Liang. Identifying coulomb and viscous damping from free-vibration acceleration decrements. *Journal of Sound and Vibration*, 282:1208–1220, 2005.

[78] C. Meskell. A decrement method for quantifying nonlinear and linear damping parameters. *Journal of Sound and Vibration*, 296:643–649, 2006.

[79] W. Li. Evaluation of the damping ratio for a base-excited system by the modulations of responses. *Journal of Sound and Vibration*, 279:1181–1194, 2005.

[80] C.H. Lamarque, S. Pernot, and A. Cuer. Damping identification in multi-degree-of-freedom systems via a wavelet-logarithmic decrement - part 1: Theory. *Journal of Sound and Vibration*, 235(3):361–374, 2000.

[81] J. Slavic, I. Simonovski, and M. Boltezar. Damping identification using a continuous wavelet transform: application to real data. *Journal of Sound and Vibration*, 262:291–307, 2003.

[82] W.J. Staszewski. Identification of damping in mdof systems using time-scale decomposition. *Journal of Sound and Vibration*, 203(2):283–305, 1997.

[83] A. Srikantha Phani and J. Woodhouse. Viscous damping identification in linear vibration. *Journal of Sound and Vibrations*, 303:475–500, 2007.

[84] A. Srikantha Phani and J. Woodhouse. Experimental identification of viscous damping in linear vibration. *Journal of Sound and Vibrations*, 319:832–849, 2009.

[85] M. Prandina, J.E. Mottershead, and E. Bonisoli. An assessment of damping identification methods. *Journal of Sound and Vibration*, 323(3-5):662 – 676, 2009.

[86] D.F. Pilkey and D.J. Inman. A survey of damping matrix identification. In *Proceedings of the 16th IMAC*, pages 104–110, Santa Barbara CA, 1998.

[87] P. Lancaster. Expression of damping matrices in linear vibrations problems. *Journal of the Aerospace Science*, 28:256, 1961.

[88] S.Y. Chen, M.S. Ju, and Y.G. Tsuei. Estimation of mass, stiffness and damping matrices from frequency response functions. *ASME Journal of Vibration and Acoustic*, 118(1):78–82, 1996.

[89] J.-H. Lee and J. Kim. Development and validation of a new experimental method to identify damping matrices of a dynamic system. *Journal of Sound and Vibration*, 246(3):505–524, 2001.

[90] C.P. Fritzen. Identification of mass, damping and stiffness matrices of mechanical systems. *ASME Journal of vibration, acoustics, stress, and reliability in design*, 108:9–16, 1986.

[91] A. Berman and A.W.G. Flannelly. Theory of incomplete models of dynamic structures. *AIAA Journal*, 9(8):1481–1487, 1971.

[92] A. Berman. System identification of structural dynamic models - theoretical and practical bounds. In *AIAA conference*, volume 84-0929, pages 123–129, 1984.

[93] P. Lancaster. Inversion of lambda-matrices and application to the theory of linear vibrations. *Arch. Rational Mech. Anal.*, 6:105–114, 1960.

[94] P. Lancaster and U. Prells. Inverse problems for damped vibrating systems. *Journal of Sound and Vibration*, 283:891–914, 2005.

[95] F. Zhang. *The Schur Complement and Its Applications*. Springer, 2005.

[96] D.F. Pilkey, G. Park, and D.J. Inman. Damping matrix identification and experimental verification. In *Proceedings of the SPIE's 6th Annual International Symposium on Smart Structures and Materials*, volume 3672, pages 350–357, Newport Beach CA, 1999.

[97] S.R. Ibrahim. Dynamic modeling of structures from measured complex modes. *AIAA Journal*, 21(6):898–901, 1983.

[98] A. Berman, F.S. Wei, and K.W. Rao. Improvement of analytical models using modal test data. In *Proceedings of the AIAA/ASME/ASCE/AHS 21st SDM Conference*, Seattle, 1980.

[99] C. Minas and D.J. Inman. Identification of a nonproportional damping matrix from incomplete modal information. *Journal of Vibration and Acoustics*, 113:219–224, 1991.

[100] S. Adhikari and J. Woodhouse. Identification of damping: part 1, viscous damping. *Journal of Sound and Vibration*, 243(1):43–61, 2001.

[101] A.W. Lees. Use of perturbation analysis for complex modes. In *Proceedings of the 17th International Modal Analysis Conference, Kissimmee*, pages 779–784, 1999.

[102] S. Adhikari and J. Woodhouse. Identification of damping: part 3, symmetry-preserving methods. *Journal of Sound and Vibration*, 251(1):477–490, 2001.

[103] J.-W. Liang. Damping estimation via energy-dissipation method. *Journal of Sound and Vibration*, 307:349–364, 2007.

[104] P. Caravani and W.T. Thomson. Identification of damping coefficients in multidimensional linear systems. *ASME Journal of Applied Mechanics*, 41:379–382, 1974.

[105] J.G. Beliveau. Identification of viscous damping in structures from modal information. *ASME Journal of Applied Mechanics*, 41:379–382, 1976.

[106] J. Fabunmi, P. Chang, and J. Vorwald. Damping matrix identification using the spectral basis technique. *ASME Journal of vibration, acoustics, stress, and reliability in design*, 110:332–337, 1988.

[107] T.K. Hasselman. A method of constructing a full modal damping matrix from experimental measurements. *AIAA Journal*, 10:526–527, 1972.

[108] L. Starek and D.J. Inman. A symmetric inverse vibration problem for non-proportional underdamped systems. *ASME Journal of Applied Mechanics*, 64:601–605, 1997.

[109] J.H. Wang. Mechanical parameter identification with special consideration of noise effect. *Journal of Sound and Vibration*, 125(1):151–167, 1988.

[110] M.E. Gaylard. Identification of damping matrices: an autocorrelation-style technique. In *Proceedings of the conference on identification in engineering systems*, pages 225–237, 1996.

[111] J.E. Mottershead and C.D. Foster. An instrument variable method for the estimation of mass, stiffness and damping parameters from measured frequency response functions. *Mechanical Systems and Signal Processing*, 2(4):379–390, 1988.

[112] M.J. Roemer and D.J. Mook. Mass, stiffness, and damping matrix identification: an integrated approach. *ASME Journal of Vibration, Acoustics, Stress and Reliability in Design*, 114(3):358–363, 1992.

[113] M.I. Friswell and J.E. Mottershead. *Finite element model updating in structural dynamics*. Kluwer Academic Publishers, Dordrecht, 1995.

[114] H. Jalali, H. Ahmadian, and J.E. Mottershead. Identification of nonlinear bolted lap-joint parameters by force-state mapping. *International Journal of Solids and Structures*, 44:8087–8105, 2007.

[115] M.I. Friswell, J.E. Mottershead, and H. Ahmadian. Combining subset selection and parameter constraints in model updating. *Transactions of the ASME, Journal of Vibration and Acoustics*, 120(4):854–859, 1998.

[116] A. Bjorck and G.H. Golub. Numerical methods for computing angles between linear subspaces. *Mathematics of Computation*, 27(123):579–594, 1973.

[117] C.L. Lawson and R.J. Hanson. *Solving least squares problems*. Prentice-Hall Series in Automatic Computation, Englewood Cliffs, 1974.

[118] H.H. Khodaparast, J.E. Mottershead, and K.J. Badcock. Propagation of structural uncertainty to linear aeroelastic stability. *Computers and Structures*, 88(3-4):223–236, 2010.

[119] K.J. Badcock, H. Haddad Khodaparast, S. Marques, and J.E. Mottershead. Cfd based aeroelastic stabilty predictions under the influence of structural uncertainty. In *50th Structural Dynamics and Materials Conference*, AIAA-2009-2324, Palm Springs, 2009. American Institute of Aeronautics and Astronautics.

[120] P.S. Beran, N.S. Knot, F.E. Eastep, R.D. Synder, and J.V. Zweber. Numerical analysis of store-induced limit cycle oscillarion. *Journal of Aircraft*, 41(6):1315–1326, 2004.

[121] M. Goland. The flutter of a uniform cantilever wing. *Journal of Applied Mechanics*, 12(4):197–208, 1945.